



HAL
open science

Contribution of deep convection on the intensification of Mediterranean cyclones

Stavros Ntafis

► **To cite this version:**

Stavros Ntafis. Contribution of deep convection on the intensification of Mediterranean cyclones. Meteorology. Institut Polytechnique de Paris, 2020. English. NNT : 2020IPPAX106 . tel-03153343

HAL Id: tel-03153343

<https://theses.hal.science/tel-03153343>

Submitted on 26 Feb 2021

HAL is a multi-disciplinary open access archive for the deposit and dissemination of scientific research documents, whether they are published or not. The documents may come from teaching and research institutions in France or abroad, or from public or private research centers.

L'archive ouverte pluridisciplinaire **HAL**, est destinée au dépôt et à la diffusion de documents scientifiques de niveau recherche, publiés ou non, émanant des établissements d'enseignement et de recherche français ou étrangers, des laboratoires publics ou privés.



Contribution de la convection profonde à l'intensification des cyclones méditerranéens

Thèse de doctorat de l'Institut Polytechnique de Paris
préparée à École Polytechnique

École Doctorale de l'Institut Polytechnique de Paris (ED IPP) n°626
Spécialité de doctorat: Mécanique des fluides et des solides, acoustique

Thèse présentée et soutenue à Palaiseau, le 14 décembre 2020, par

Stavros Dafis

Composition du Jury :

Phillippe Drobinski Directeur de recherche, CNRS (LMD)	Président
Nadia Fourrié Directrice de recherche, CNRS (CNRM)	Rapporteuse
Jean-Pierre Chaboureau Physicien, CNRS (OMP)	Rapporteur
Heini Wernli Professeur, ETH (IAC)	Examineur
Mario-Marcello Miglietta Directeur de recherche, CNR (ISAC)	Examineur
Konstantinos Lagouvardos Directeur de recherche, NOA (IERSD)	Examineur
Chantal Claud, Directrice de recherche, CNRS (LMD)	Directrice de thèse

Acknowledgments

This thesis was funded partly by the Direction générale de l'armement - Ministère des Armées (DGA) and partly by the National Observatory of Athens (NOA) - Institute for Environmental Research and Sustainable Development (IERSD). The conducted numerical simulations with WRF model were supported by computational time granted from the National Infrastructures for Research and Technology S.A. (GRNET S.A.) in the National HPC facility - ARIS - under project IDs "HDMEDICANES" and "HDMEDICANES2". In addition, the author acknowledges EUMETSAT for the provision of METEOSAT and MetOp satellite data, NASA for the provision of NOAA satellite data and the Copernicus Climate Change Service (C3S) Climate Data Store for the provision of ERA5 reanalysis data.

The author recognizes the important assistance of his supervisor Chantal Claud and the advisors Konstantinos Lagouvardos and Vassiliki Kotroni. The author is also thankful to Heini Wernli and Emmanouil Flaounas for the invitation to visit the Institute of Atmospheric and Climate Science at ETH, Zurich and for their invaluable comments on this work. Finally, the author of this thesis extends his gratitude to numerous colleagues at the Laboratory of Dynamic Meteorology at the Polytechnic School of Paris, École Normale Supérieure, and the National Observatory of Athens, and special thanks go to the members of the jury for their constructive comments on earlier versions of this manuscript.

Preface

The basis of this research stemmed from my passion for meteorology that has been growing ever since I can remember myself. I have been fascinated by the weather a long time before I installed my first weather station at our house's rooftop in Volos in 2005 and my dream to study Meteorology came true a few years later. During my undergraduate studies at the University of Ioannina, I realized that there are several open questions in the field of Atmospheric Sciences and scientific research is the only way to provide answers to this fairly new discipline. Thus, I decided to pursue answers to many questions we have on Mediterranean Tropical-like Cyclones and I am glad that this thesis successfully addressed some of them.

In truth, I could not have completed this thesis without the support of several wonderful people. First of all, I would like to extend my deepest gratitude to my supervisor, Chantal Claud who was always there for me, providing patient advice and guidance throughout the research process. Secondly, this project could not have even started without the relentless support of Konstantinos Lagouvardos and Vassiliki Kotroni. Next, I would like to sincerely thank two colleagues and friends for the provision of their expertise and the great amount of assistance: Jean-François Rysman who has provided me with practical help and valuable advice while conducting this research project, and I cannot leave aside our endless and constructive discussions on Mediterranean Cyclones with Emmanouil Flaounas and his advice on how to learn to live with our numerical residuals! Last, I would like to highlight the unwavering moral support of my family and my life partner, Artemis, and their love and understanding that I received during my Ph.D. studies.

Stavros Dafis

Contents

Contents	4
Introduction	6
1.1 Nomenclature of Mediterranean Tropical-Like Cyclones (MTLCs)	6
1.2 Climatological studies of MTLCs	9
1.3 Intensification mechanisms of MTLCs	13
1.4 Questions addressed in this thesis and thesis plan	20
Observations of deep convection during Mediterranean tropical-like cyclones	21
2.1 Introduction	21
2.2 Data and methods	23
2.2.1 The Advanced Microwave Sounding Unit (AMSU-B) and the Microwave Humidity Sounder (MHS).....	23
2.2.2 Deep convection detection based on AMSU-B/MHS.....	25
2.2.3 Meteosat SEVIRI.....	27
2.2.4 Deep convection detection based on SEVIRI.....	28
2.2.5 Cyclone tracking and atmospheric reanalysis.....	30
2.3 Results	32
2.3.1 Introduction of the article “Remote sensing of deep convection within a tropical-like cyclone over the Mediterranean Sea”.....	32
2.3.2 Article “Remote sensing of deep convection within a tropical-like cyclone over the Mediterranean Sea”.....	34
2.3.3 Introduction of the article “Insights into the convective evolution of Mediterranean tropical-like cyclones”.....	41
2.3.4 Article “Insights into the convective evolution of Mediterranean tropical-like cyclones”	42
2.4 Summary and Discussion	65
Assessment of the contribution of diabatic processes in the intensification of Mediterranean tropical-like cyclones	68
3.1 Introduction	68
3.2 Data and methods	69
3.2.1 The numerical model (WRF).....	69
3.2.2 Online potential vorticity tracers in WRF.....	79
3.2.3 Pressure tendency equation.....	82
3.3 Results	86
3.3.1 Model set-up and case studies.....	86
3.3.2 Definition of tropical-like phase.....	91

3.3.3 MTLC pressure tendencies	94
3.3.4 The evolution of vertical PV structures	102
3.3.5 Connecting the PV evolution with cyclone intensity	115
3.3 Summary and discussion	124
<i>Conclusions and future work</i>.....	<i>130</i>
4.1 Questions addressed in this thesis.....	130
4.2 Future work	132
<i>Appendix 1</i>	<i>136</i>
The Manual Tracking procedure	136
The convective evolution of MTLCs and ERA-5 performance	138
<i>Appendix 2</i>	<i>144</i>
Synoptic and mesoscale analysis during the MTLCs.....	144
<i>Abbreviations</i>	<i>160</i>
<i>References</i>.....	<i>162</i>

Chapter 1

Introduction

1.1 Nomenclature of Mediterranean Tropical-Like Cyclones (MTLCs)

An intense depression either tropical or extra-tropical is called “cyclone” with the latter being characterized by frontal activity influenced by baroclinic instability in mid and high latitudes. Baroclinic instability occurs when atmospheric conditions permit the conversion of potential energy stored within horizontal temperature gradients into kinetic energy in the form of cyclonic eddies. The presence of baroclinic instability is not a sufficient condition for the production of eddy kinetic energy, since an additional mechanism is needed to transport the heat in the direction of cold air. The structure of typical mid-latitude cyclones is based on this poleward transport of heat and the equatorward transport of cold air masses, during the interaction of troughs and ridges in the presence of baroclinic instability, while Tropical Cyclones (TCs) have different generation mechanisms. The majority of extra-tropical cyclones are cold-core cyclones and deep convection (DC) is mostly active near fronts, while in TCs deep convection is profound close to the centre of the depression. Cyclones which exhibit both tropical and extratropical characteristics during their lifetime are called “Subtropical Cyclones” and develop in the sub-tropics and mid-latitudes 20°N – 40°N (Evans and Guishard, 2009; González-Alemán et al., 2015; Bentley et al., 2016; 2017) or 20°S – 40°S (Evans and Braun, 2012; Dowdy et al., 2019), where TCs can also develop. TCs with maximum sustained winds close to the surface of less than 17 m s^{-1} are called tropical depressions (TDs). TCs with higher than 17 m s^{-1} sustained surface wind speeds are called “tropical storms”. If the 1-minute sustained surface wind speed exceeds 33 m s^{-1} then the TC is called a “hurricane” in North Atlantic and North-East Pacific or a “typhoon” in Northwest Pacific Ocean.

The Mediterranean Tropical-Like Cyclones (MTLCs) are mesoscale (scale of the order of a few hundred kilometers) cyclones developing in the Mediterranean basin with encompassing features of both TCs and extra-tropical cyclones (Figs. 1.1 and 1.2). The tropical-like characteristics include the cloud-free eye and the spirally distributed cloud bands around a front-less cyclone, with DC close to the cyclone centre (Shapiro and Keyser, 1990; Emanuel, 2005; Miglietta and Rotunno, 2019). MTLCs develop first as typical extratropical cyclones in baroclinic environments and then experience tropical transition (TT) through tropospheric heating (Davis and Bosart, 2003; 2004). A key contributor to the large variability of structures seen in MTLCs is the influence of diabatic heating by convection. The fluxes of heat and moisture from the sea towards the atmosphere can result in a large latent heat release within developing MTLCs. However, it is also known that

latent heat release can interact with the baroclinic dynamics in a strongly non-linear way (Kuo et al., 1991; Stoelinga, 1996).

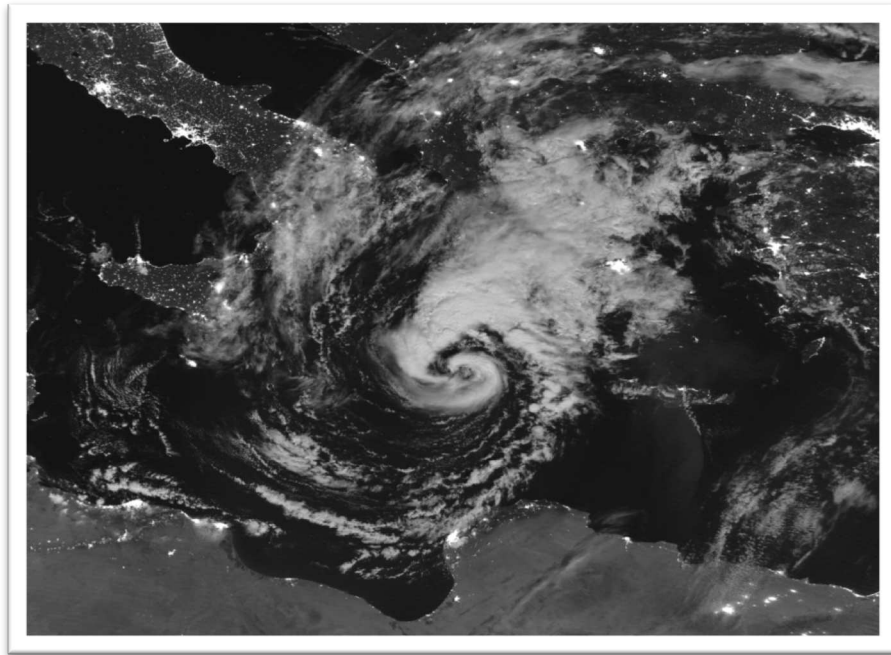


Fig. 1.1 Satellite image of the MTLC ZORBAS on 29 September 2018.

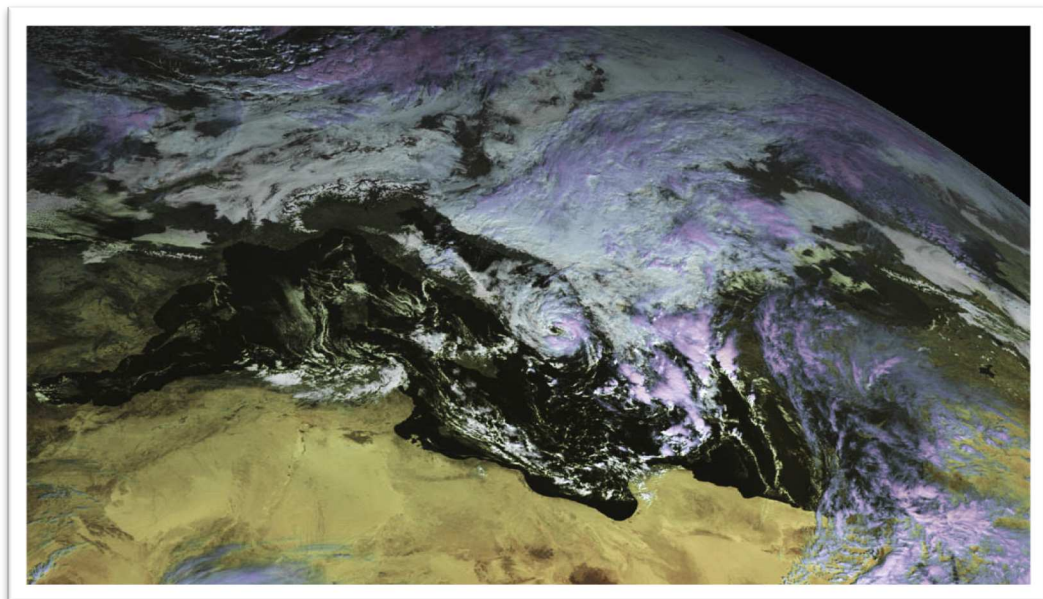


Fig. 1.2 Satellite image of the MTLC NUMA on 18 November 2017.

The generally accepted model for the formation of an MTLC is the development of a low-level cyclone as a response to an upper-level potential vorticity (PV) anomaly and a surface baroclinic zone, a process that is observed in the majority of Mediterranean cyclones. As a second stage, the low-level PV anomaly generated by diabatic processes becomes important and interacts with the baroclinicity at low levels (Miglietta et al., 2017). Vertical motions are induced by this anomaly embedded in baroclinic shear. This contributes to the further generation of low-level PV through latent heat release in moist ascent, related to the intensification

mechanism proposed by Montgomery and Farrell (1992). More recent numerical studies have addressed the impact of the diabatic production of latent and sensible heat release in the mid-troposphere through convection on warm seclusions in the Mediterranean (Tous and Romero, 2013; Mazza et al., 2017), similar to other cyclogenetic areas (e.g., Posselt and Martin, 2004). Moreover, despite the presented conceptual framework for the formation of MTLCs, additional factors dictate their geneses, such as the presence and intensity of DC, the differential surface friction, and the uneven topography of the Mediterranean basin which further complicate any attempt to categorize the cyclones within strict boundaries. A possible definition for an MTLC would be: *“An intense mesoscale maritime secluded cyclone which experiences intense tropospheric heating by convective activity and exhibits a front-less structure with gale-force wind speeds close to the centre of the depression.”*

A long-term and still active debate about the Mediterranean tropical-like cyclones (MTLCs or “medicanes”, a contraction of the words “Medi-terranean” and “hurri-canes”) is based on the different mechanisms responsible for their development which have links to extratropical and tropical-cyclone theory (Shapiro and Keyser, 1990; Emanuel, 2005). The contributions of baroclinic and diabatic processes are not well understood and despite several studies trying to quantify the contribution of convection in the intensification of MTLCs, no consensus has emerged.

Winstanley (1970) was probably the first to investigate an MTLC as a deep Mediterranean cyclone just north of Libya on 23 September 1969 which was responsible for severe flash floods in Tunisia and Algeria, with nearly 600 casualties and 250.000 people were left homeless. The convective and persistent nature of precipitation was highlighted, as well as the presence of a quasi-symmetrical cloud-free centre (an “eye”) visible in satellite images (see their Fig. 7c) giving evidence for a warm-core cyclone with an axisymmetric structure. The first reference to warm-core cyclones in the Mediterranean was introduced by Ernst and Matson (1983) while a few years later, Rasmussen and Zick (1987) studied a sub-synoptic warm-core vortex and compared the environment and the cyclone dynamics with polar lows (intense cyclones forming at high latitudes). They used the first Meteosat satellite data to observe DC around the cyclone and argued that DC was most pronounced at the early stages of the cyclone, before the formation of an “eye”. Figure 1.3 shows the formation of an MTLC in the Ionian Sea on 26 and 27 January 1982 and at the same time, a polar low was active in the Norwegian Sea. This NOAA-17 satellite swath with a coincidence of an MTLC and a polar low is the only one known in the satellite era and provides a unique opportunity to compare the size and structure of these two types of intense cyclones.

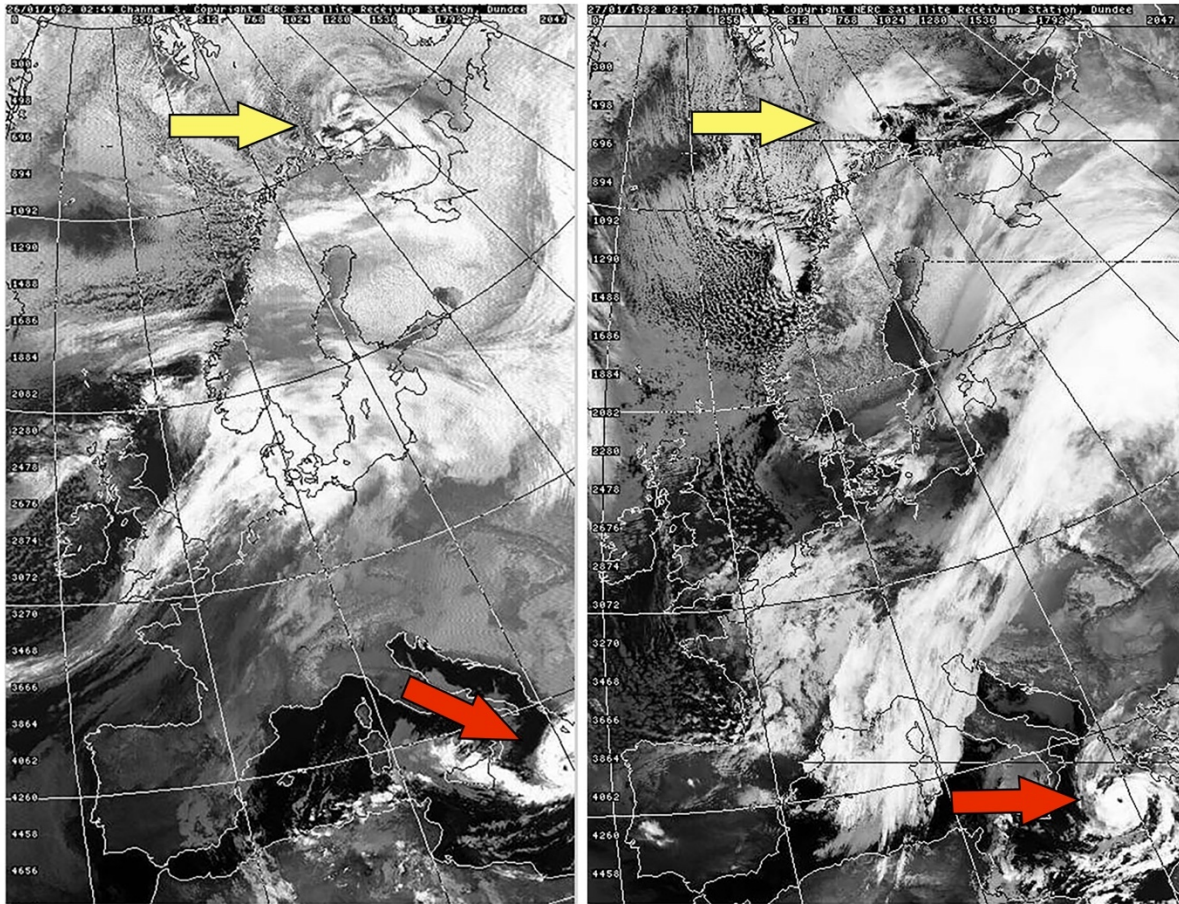


Fig. 1.3 Satellite images of a polar low (yellow arrow) and an MTLC (red arrow) on 26 (left) and 27 (right) January 1982. Images courtesy of Dundee University's satellite receiving station.

Very few studies exist in the literature dedicated to the convective evolution and the environments of MTLCs from an observational point of view. Claud et al. (2010), Miglietta et al. (2013) used a combined approach with satellite-based infrared and microwave diagnostics to show that DC occurrence in MTLCs peaks several hours before the maximum strength of the cyclones, showing a longer time lag than in strong extratropical Mediterranean cyclones (Galanaki et al., 2016) and more similar characteristics with TCs. Other studies have tried to explain the convective structure of these cyclones with numerical simulations (e.g., Lagouvardos et al., 1999; Pytharoulis et al., 2000; Emanuel, 2005; Tous and Romero, 2012; Carrió et al., 2017) and provide similar results.

1.2 Climatological studies of MTLCs

Due to the lack of a clear definition of MTLCs, most of the climatological studies suffer from subjective criteria and most of them are based on numerical modeling, because in-situ observations are scarce for the vast majority of the documented cyclones. Using historical infrared (IR) Meteosat satellite data Tous and Romero (2012) identified 12 MTLCs with a lifetime of at least 6 hours between 1982-2003. They also provided the first insights into the thermodynamic environment at the MTLCs' genesis areas and compared the synoptic meteorological conditions with other extratropical cyclones using the European Center for Medium-Range Weather Forecasts (ECMWF) reanalysis ERA-40 dataset (Uppala et al., 2005). The main

result of their study was that the large-scale environment of MTLCs was very similar to the ones known to be associated with tropical cyclones, i.e. the diabatic contribution to the surface-level equivalent potential temperature, even though with much lower SSTs than in the tropics, but higher than 15°C. Another attempt for a satellite-based climatology of subtropical cyclones in Europe was made by Holzer and Groenenemeijer (2014), but was limited to satellite imagery provided by the first generation of Meteosat satellites between 1982-2006 and was not extended afterwards. The authors of this study employed the manual Dvorak technique (Dvorak, 1975) in order to identify tropical-like cyclones in the European coasts of Eastern Atlantic, the Mediterranean Sea and the Black Sea, and found 81 cyclones as “suspected” MTLCs out of which 47 were eventually classified as MTLCs. They also suggested a classification of the detected systems according to their appearance in the satellite imagery. A more recent climatological study by Nastos et al. (2018) used satellite imagery with subjective criteria (such as the visual inspection of cloud patterns) to detect MTLCs in the period 1969-2014 and found 63 events with an average number of 1.4 ± 1.3 events per year.

The long-term objective climatological study by Cavicchia et al. (2014a) employed a dynamical downscaling technique of the NCEP/NCAR reanalysis dataset (Kalnay et al., 1996) and used a cyclone-detection algorithm (Cavicchia and von Storch, 2012) to systematically record the development of MTLCs between 1948 and 2011. The objective criteria for detecting MTLCs in the numerical simulations include a) the definition of a pressure gradient at the sea-level pressure fields around a minimum, b) the symmetry and warm-core structure of the cyclones using phase-space diagrams (Hart, 2003) and c) a 10 m wind speed threshold. They found that MTLCs occur with a very low frequency of about 1.6 per year in the whole Mediterranean basin (Fig. 1.4a) with a total number of 99 detected MTLCs during the studied period. Their main genesis sites are the Western Mediterranean (0.75 ± 0.95 per season) and the region between the Ionian Sea and the North African coast (0.32 ± 0.50 per season), with an uncorrelated variability between the two basins. The seasonality of occurrence is characterized by a peak at the beginning of winter with a comparable number of events in fall, much fewer events in spring and only 2 events in summer (Fig. 1.4b). In addition, the year-to-year variability is large but there is no significant climatic trend in the studied period ($+0.015$ events per year). In the Ionian Sea, most of the MTLCs were found in late fall with a sharp peak of activity in January, while in Western Mediterranean a comparable number of MTLCs was found in the fall and winter, with many events in spring. Finally, their study provided information about the environmental factors present during the MTLCs’ genesis and highlighted the presence of cold temperature anomalies in the upper troposphere and high moisture in the lower troposphere that increases the atmospheric instability, and along with weak wind shear and high low-level vorticity create a favorable environment for TT in the Mediterranean, even though the SSTs are much lower than in the tropics.

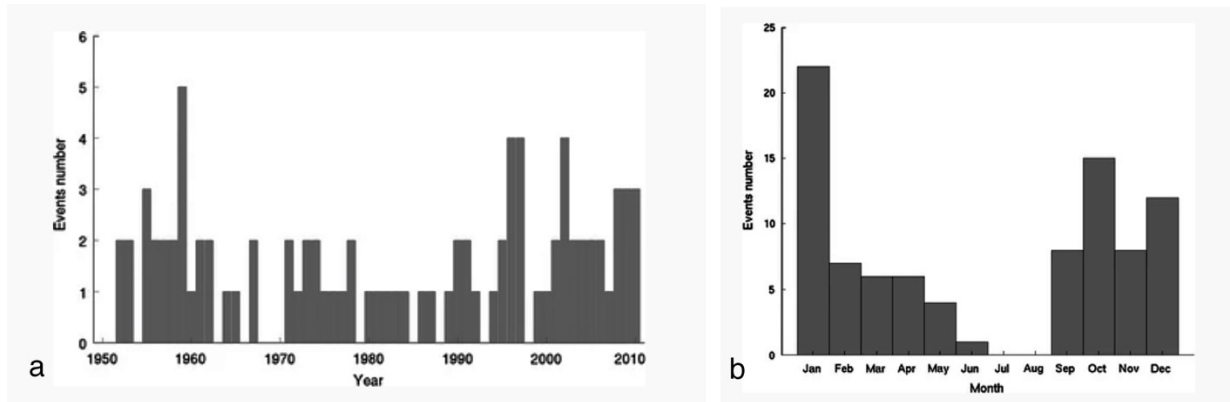


Fig. 1.4 Number of medicanes per year (a) and per month (b) during the period 1948-2011 based on the NCEP/NCAR reanalysis dataset (source: Cavvichia et al., 2014a)

A more recent numerical study by Ragone et al. (2018) used a downscaling technique of the ERA-Interim reanalysis dataset (Dee et al., 2011) by using a limited-area numerical model in high-resolution mode (11-4 km) to detect MTLCs in the period 1979-1998. By applying a prototype cyclone tracking algorithm to 4 numerical configurations, they found a frequency of occurrence of between 0.47 ± 0.15 and 1.38 ± 0.25 per year, depending on the different microphysical schemes used in each set-up (Fig. 1.5). Moreover, they highlighted the pronounced differences in the total simulated life-time of the MTLCs in the different runs, with the longest-lasting events ranging between 4 and 6.5 days in duration. They also used a modified version of the cyclone phase diagram (Hart, 2003) to detect the warm-core cyclones in their simulations, but the most critical parameter was the sea-level pressure gradient (G) which varied between $0.5 \times 10^{-2} \text{ hPa km}^{-1}$ and $3.5 \times 10^{-2} \text{ hPa km}^{-1}$ and had a great impact on the analyzed MTLCs' trajectories with about 0.47 - 9.9 events per year (Ragone et al., 2018, their Fig. 3). By applying a constant G of $3.21 \times 10^{-2} \text{ hPa km}^{-1}$ they found an occurrence of about 1.3-1.4 events per year, slightly lower than in Cavicchia et al. (2014a). Similar results were presented in Zhang et al. (2020) study, with 1.5 events per year and no linear trend, but with the highest number of events in winter rather than in fall as the previous studies have shown. They used the ECMWF ERA-5 dataset (Hersbach et al., 2020) at 31 km spatial resolution and detected 59 MTLCs between 1979-2017, with 0-4 events per year, and also studied the spatial and temporal evolution of precipitation fields.

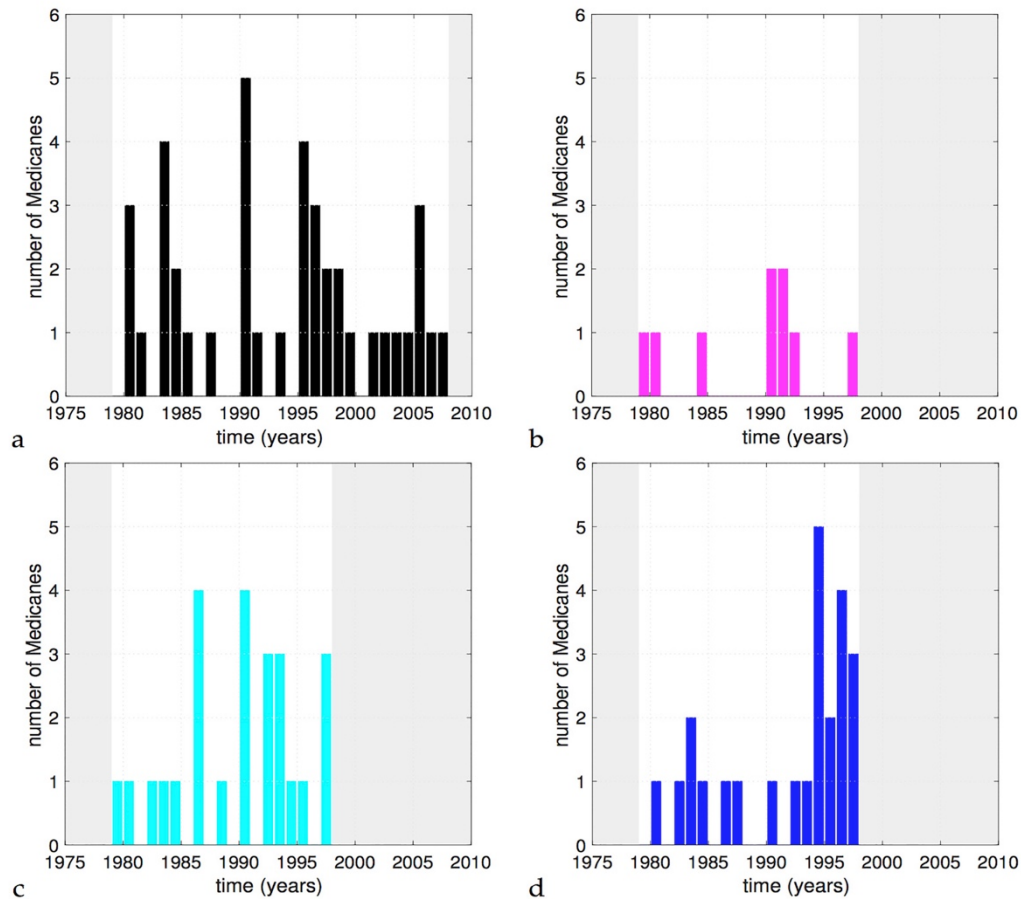


Fig. 1.5 Time-series of the number of detected medicanes between 1979-2008 in historical numerical simulations of 4 WRF configurations with boundary conditions by ERA-Interim (source: Ragone et al., 2018)

The ability of Regional Climate Models (RCMs) to simulate MTLCS, using 29 multi-model ensembles of RCM simulations from EURO-CORDEX (Jacob et al., 2014) and Med-CORDEX (Ruti et al. 2015) projects, was discussed in Gaertner et al. (2018). Some of these simulations are air-sea coupled and with a spectrum of spatial resolutions between 10 and 50 km. The large ensemble of RCM simulations provides the uncertainty linked to differences in model configurations and the treated physical processes (e.g., oceanic mixed layer depth and surface fluxes in the air-sea coupled runs) but all in all, the simulated MTLCS often do not coincide in date with the observed ones and most of the low-resolution simulations underestimate the observed frequency of about 1-1.5 medicanes/year. The high-resolution simulations show an improvement, with values generally closer to the observed values. The strong underestimation of the high-intensity MTLCS in the 50 km simulations (with values between 0 and 0.2 MTLCS per year) is not corrected by many of the high-resolution simulations. Moreover, intensity changes are strongly model-dependent, and increased resolution alone does not improve the intensity of the simulated medicanes. Another interesting result is that the genesis areas of MTLCS in these simulations are found around Italy, in contrast with previous studies placing them more to the west and in the Ionian Sea.

A few additional studies have been dedicated to climatic projections and the risks associated with MTLCS in the warming climate. Romero and Emanuel (2013) applied a statistical-deterministic approach to

thousands of synthetic storms in climatic projections, and they concluded that there is a high risk that future MTLCs will be more violent but with a lower frequency of occurrence. The scientific consensus about the potential increase in the hazards associated with MTLCs due to their projected higher intensity in a warmer climate has also been discussed in the results of Cavicchia et al. (2014b), Walsh et al. (2014), Tous et al. (2016), Romera et al. (2017) and González-Alemán et al. (2019).

In summary, the climatological studies of MTLCs have provided important information about the spatial and temporal distribution of these cyclones. Some of them have investigated the environmental factors conducive for the development of MTLCs but there are key limitations associated with the numerical models used. The ambiguity associated with the atmospheric reanalysis coarse resolution and the application of subjective techniques raise concerns about how well these models simulate actual MTLCs, and no study has addressed so far this important topic. Moreover, there is not a systematic investigation of the different processes in the intensification of the MTLCs in historical numerical simulations and whether the models are able to capture the full evolution of their lifetime. Unfortunately, there has not yet been a systematic comparison between the simulated events and the observed MTLCs.

1.3 Intensification mechanisms of MTLCs

a) Conceptual models and baroclinic instability

The Norwegian Cyclone Model introduced by the Bergen School of Meteorology (Bjerkness and Solberg, 1922) was the first one to describe the life cycle and dynamics of extratropical cyclones and it originated from detailed analyses of synoptic weather charts and surface observations. This conceptual model served as the textbook for cyclone development for almost 70 years before being updated by the Shapiro-Keyser model (Shapiro and Keyser, 1990) who used both observations and numerical analyses. The founders of the theoretical models of cyclones and fronts knew that not all cyclones fall into strict boundaries, for example, they observed re-intensifying occluded cyclones and tried to explain their dynamics. Large-scale environmental conditions conducive to intense extratropical cyclones in Europe include an unusually strong baroclinic zone associated with an intense jet stream over an extensive longitudinal sector of the North Atlantic (e.g., Pinto et al., 2009). This is particularly true for extreme cyclones, which typically originate off the east coast of North America and propagate towards northern Europe, while secondary developments over the south-eastern North Atlantic are often more “low-level” forced (Dacre and Gray, 2009). The latter suggests a more important contribution from latent heating to the rapid cyclogenesis in line with ideas of the so-called Diabatic Rossby Waves or Vortices (Parker and Thorpe, 1995; Wernli et al., 2002; Moore and Montgomery, 2004).

Godske et al. (1957) studied two kinds of cyclone re-generation (intensification) which were considered challenging to weather forecasting: a thermodynamic intensification with similarities to the development of tropical cyclones, and the non-frontal trough intensification, or the back-bent occlusion, of strong cyclones. The latter kind was associated with the strongest surface winds observed in the European Atlantic coasts. It was found that these cyclones evolve as the Shapiro-Keyser frontal model and that the strong

winds develop by a secondary, mesoscale (~ 500 km) cyclogenesis closely linked to the seclusion process. The time scale of the intensification is shorter than a day, starting with what is called the seclusion trough at the tip of the back-bent warm front. As the cold air secludes the warm core, the disturbance develops into a separate secluded low. The release of latent heat connected to the back-bent warm front was found to play an important role in forming the seclusion.

Figure 1.6 illustrates the four stages of cyclone development in the Norwegian and the Shapiro-Keyser models. In both conceptual models, stages I and II show the cyclone beginning as an initial small perturbation on a stationary front within a low-level baroclinic zone, the cyclonic circulation advects cold air equatorward and warm air poleward of the cyclone centre, thereby forming cold and warm fronts, respectively. There are clear differences between the models regarding stages III and IV when in the Norwegian model (Fig. 1.6a) an occluded front is formed as the faster moving cold front catches up with the warm front ahead (Schultz et al., 1998), while in the Shapiro-Keyser model (Fig. 1.6b) the cold front is orientated approximately perpendicular to the warm front (the T-bone front). Finally, a bent-back front develops in the latter model, forming a warm-core seclusion, unlike the Norwegian model where the seclusion does not appear and the cold front is closely tight to the propagating warm front.

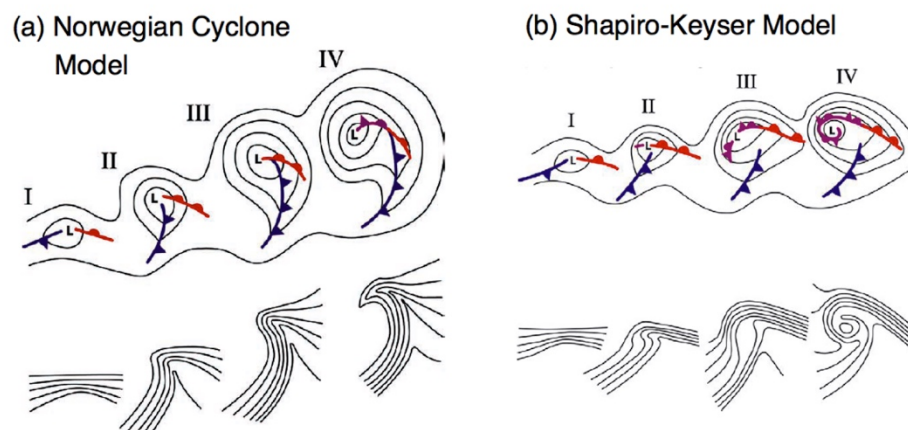


Fig. 1.6 The Norwegian conceptual model of cyclone development (a) and the Shapiro-Keyser model (b) in the presence of baroclinic instability. The lower panels show lower-tropospheric potential temperature while the top panels show lower-tropospheric geopotential heights (black contours) and associated warm (red contours), cold (blue contours), and occluded (purple contours) fronts. (adapted from Schulz et al., 1998)

The three-dimensional structure of a mid-latitude cyclone can be described by the interactions of three main airflows or ‘conveyor belts’: a) the warm conveyor belt (WCB), b) the cold conveyor belt (CCB) and c) a dry intrusion (Carlson, 1980). The WCB is a band of rising warm and moist air which originates at low levels within the warm sector of a cyclone and moves poleward ahead of the cold front, ascending over the warm front where it can often split into two branches: one branch turns cyclonically, forming part of the upper-level cloud head, while the other turns anti-cyclonically joining the westerly jet flow (Carlson, 1980; Browning & Roberts, 1994; Browning, 2004). The WCBs can ascend high into the troposphere, transporting warm, moist air which then forms clouds and precipitation (Browning, 1986). While these airflows usually create comma-

cloud patterns and indicate the presence of baroclinic instability, the dominance of deep convection in spiral clouds close to the cyclone centre is indicative of a hurricane-like structure.

In contrast with Northwest Europe, cyclone occurrence in the Mediterranean has a relatively small annual cycle over the whole basin which reflects the different seasonality in the separate cyclogenetic regions (Trigo et al., 2002). For example, the Western Mediterranean has a more pronounced seasonality than the eastern basin, with a peak of cyclone activity in spring over the southern parts, close to the coast of Africa, in summer over the Iberian Peninsula, while a smoother annual cycle is found in the Black Sea. The seasonality of occurrence is not equated with cyclone strength, as for example, over the Gulf of Genoa cyclones occur over the whole year, but they are particularly deeper, and bring more severe weather in autumn and in winter than in summer, when they are more frequent. Nevertheless, there is a general consensus that the most intense Mediterranean cyclones are closely connected with intruding upper-level tropospheric systems that trigger baroclinic instability (Fita et al., 2006; Claud et al., 2010; Flaounas et al., 2015). After the development of these cyclones, baroclinic forcing may further intensify them, but also DC close to their center begins as a response to large-scale ascent (Prezerakos et al., 2006; Lagouvardos et al., 2007) which also indicates a hurricane-like structure as mentioned before.

The MTLCs consist of a small fraction of intense Mediterranean cyclones which deviate from the classical conceptual models and exhibit characteristics of cyclones with both extratropical (e.g., frontal activity) and tropical characteristics (e.g., warm core structure and deep convective clouds in spiral forms and/or a central cloud-free “eye”). In a very limited number of them, structures similar to hurricanes have been observed with remarkable axisymmetric cloud structures. Nevertheless, all of these cyclones emerge first as extratropical systems that experience intensification periods and hybrid characteristics (extratropical and tropical). Both baroclinic instability and convection act in synergy to intensify MTLCs (Fita et al., 2006; Chaboureau et al., 2012; Miglietta et al., 2017) but the processes that play the primary role at each of their development stages and intensification periods, remain an open question.

b) The Wind-Induced Surface Heat Exchange (WISHE) theory

Another approach to investigate the mechanisms that lead to a cyclone intensification is to study the air-sea fluxes. In order to explain the intensification of marine cyclones, Emanuel (1986) suggested a theory that was first named the “Air-Sea Interaction Instability” (ASII) but later was renamed “Wind-Induced Surface Heat Exchange” (WISHE). According to this theory, the intensification and maintenance of TCs depend exclusively on the self-induced heat transfer from the ocean. A positive feedback occurs because fluxes of heat and moisture from the ocean to the atmosphere increase with increasing wind speed. DC is assumed to distribute the boundary layer heat through the troposphere over much shorter time-scales than the changes to the large-scale environment. The heating rate of a warm-core cyclone can thus be estimated by the surface heat fluxes. In addition, according to Emanuel and Rotunno (1989), in order for an axisymmetric vortex to be intensified by WISHE, an initial and large-amplitude perturbation must exist, and its radius of the maximum wind speed must be small compared to the Rossby radius of deformation. This condition ensures that the

maximum heating rate is located close to the warm-core and tropospheric heating is controlled by the distribution of surface fluxes. If the maximum heating is located further away than the Rossby radius of deformation, the heating will not induce the intensification of the low-level vortex (van Delden, 1989). The requirement of a pre-existing surface cyclone to initiate a tropical-like intensification in MTLCs is always fulfilled according to the observations.

Even though the MTLCs develop over unfavorable sea-surface temperatures (SST) (15 - 23°C) (Tous and Romero, 2013) for tropical cyclones, studies have recently shown that TCs formed by an TT can develop over colder than 26°C SSTs (Trenberth, 2005; McTaggart-Cowan et al., 2015). Early studies on MTLCs concluded that low-level instability controlled by surface heat fluxes may be an important factor of intensification (Reed et al., 2001), and that the latent heat extraction from the sea is essential for the heating of the troposphere (Homar et al., 2003). Some other studies investigated the relative importance of surface heat extraction versus the latent heat release during the lifetime of several MTLCs by using adjoint models or factor separation techniques (Reed et al., 2001; Homar et al., 2003; Carrió et al., 2017) and concluded that the low-level latent heat release during the developing and mature stages of MTLCs is necessary to maintain their structure and intensity. As surface fluxes may strongly depend on the SST, a change of the oceanic surface conditions may, in theory, impact the development of a MTLC. Several sensitivity studies have investigated the impact of a uniform SST change during a MTLC event, for instance, to anticipate the possible effect of the warming of Mediterranean surface waters due to climate change. Consistent tendencies were obtained in different MTLC case studies (Homar et al., 2003; Miglietta et al., 2011; Pytharoulis, 2018; Noyelle et al., 2019). Warmer (colder) SSTs lead to more (less) intense cyclones even though changes of SST by less than 2°C result in no significant changes in the track, duration, or intensity of the cyclones. Like in the tropical cyclones, the latent heat fluxes always dominate the surface enthalpy processes (the sensible heat flux represents 25% to 30% of the turbulent heat fluxes prior to the tropical transition and 15% to 20% during the mature phase; Pytharoulis, 2018).

To complicate things further, Moscatello et al. (2008b) showed that the role of surface enthalpies in feeding the cyclonic circulation proved important during the early and mature stages of a MTLC that developed in September 2006, whereas its role was marginal during the intensification period. Also, later studies showed that the impact of surface fluxes on MTLCs is case-dependent (Tous and Romero, 2013; Miglietta and Rotunno, 2019). The latter study compared the MTLC of October 1996 and December 2005 to investigate the relative role of the WISHE mechanism and baroclinic processes. In the case of October 1996, the warm core of the cyclone was formed by latent heat release originating from the sea-surface heat fluxes, whereas for the December 2005 case the surface enthalpy fluxes played only a marginal role to the warm-core formation, which was attributed to a tropospheric seclusion.

c) Potential Vorticity thinking

All the cyclones can be conceptualized as the outcome of potential vorticity (PV) anomalies in different atmospheric levels which are attributed to different atmospheric processes (Chagnon et al., 2013; Martínez-Alvarado et al., 2016; Büeler and Pfahl, 2017; Attinger et al., 2019). The PV framework explains a wide range

of dynamical phenomena in planetary fluids, primarily due to the conservation and invertibility properties of this tracer (Hoskins et al., 1985). Ertel's PV (Rossby, 1940; Ertel, 1942) is conserved in adiabatic, inviscid flow, enabling its treatment as a passive tracer in such motions. In addition, due to its invertibility, wind and mass fields can be obtained knowing only the scalar PV, given appropriate boundary and balance conditions. TC and sub-tropical cyclone circulations exist far from the adiabatic, inviscid limit in which PV is conserved as a Lagrangian tracer, but the study of PV evolution in these storms has nevertheless provided insights on their intensification and motion (Kepert, 2010).

A first climatology dedicated to the vertical structures of PV of North Atlantic explosive deepening extratropical cyclones was presented by Wang and Rogers (2001). They showed that an upper-level PV anomaly first approaches the surface cyclones during their deepening phase and a low-level PV generation starts shortly before the cyclones attain maximum intensity. A coherent cyclonic circulation is achieved when both PV anomalies align close to the cyclone centre, extending all the way from the tropopause to the surface, resulting in a “PV-tower” development. Another study by Lim and Simmonds (2007) showed that the most intense and explosive extratropical cyclones in Southern Hemisphere have a larger vertical tilt compared to “normal” cyclones, a feature that assists in releasing baroclinic energy in favor of the development of these cyclones. Another important result from their study was that the maximum intensity of the surface cyclones preceded that at 500 hPa, which highlights the importance of surface fluxes and the diabatically produced low-level PV anomalies. Dacre and Gray (2009) found that the PV at 1 km height at the time of maximum intensity of Atlantic extratropical cyclones was higher in the cyclones generated in the western parts of North Atlantic than for the eastern North Atlantic cyclones. Moreover, the climatological study for the vertical structure of PV in the Northern Hemisphere cyclones between 1989 and 2009 by Čampa and Wernli (2012) showed a large regional variability of PV, but on average, more intense cyclones are associated with more prominent low-tropospheric and upper-tropospheric positive PV anomalies. They also highlighted the fact that the strongest ocean cyclones experience a marked intensification period during increasing positive low/upper-level PV anomalies, prior to the minimum sea-level pressure (SLP).

Figure 1.7 shows schematically how a PV streamer is eroded above a low-level occlusion during the intensification of a surface cyclone (Posselt and Martin, 2004). First, the “open wave” stage (a): Heating is concentrated along the cold front and in the vicinity of the developing surface depression. Second, the formation of an occlusion (b): Persistent diabatic erosion in the northwest quadrant of the cyclone deforms the upper tropospheric PV contour northwest of the surface cyclone. Tropopause-level flow is also deformed in that vicinity. Third, the fully occluded stage (c): Cyclone is removed from the peak of the surface warm sector. Heating is no longer proximate to the ‘notch’ in the upper-tropospheric PV and tropopause-level flow controls intensification of the notch through negative PV advection in the upper troposphere.

The evolution of PV and vorticity during most of the MTLCS is expected to be strongly controlled by the vertical and radial distribution of diabatic heating (Eliassen, 1951). Diabatic heating is commonly classified into convective and stratiform profiles in organized convection in general (Houze, 2014) and TCs in particular (Houze, 1989; Fritz et al., 2016). Deep convective clouds are characterized by low-level convergence and

upper-level divergence, with maximum heating in the mid-troposphere diabatically generating PV in the lower troposphere and destroying it in the upper troposphere (Fig. 1.8). Stratiform clouds are characterized by mid-level convergence and upper- and lower-level divergence. In these stratiform clouds, condensation and freezing heat the upper troposphere while melting and evaporation cool the lower layers, with positive PV diabatically generated in the mid-troposphere and destroyed at upper and lower levels (Houze, 1997).

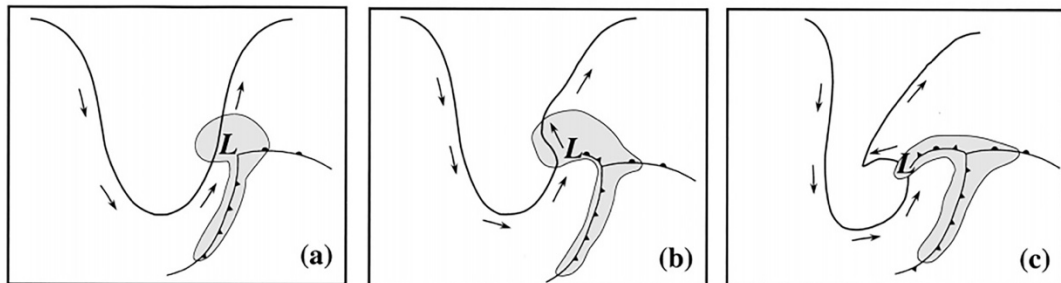


Fig. 1.7 Schematic illustrating the synergy between diabatic erosion of PV and negative advection of PV at the tropopause during occlusion. Grey shading represents the erosion of tropopause PV by diabatic heating associated with the cyclone, the surface position of which is marked by the 'L'. Traditional surface frontal symbols indicate surface frontal locations. The thick solid line represents the PV=2 PVU isopleth near or at the tropopause. Arrows represent the tropopause-level flow associated with the upper-tropospheric PV feature. (source: Posselt and Martin, 2004)

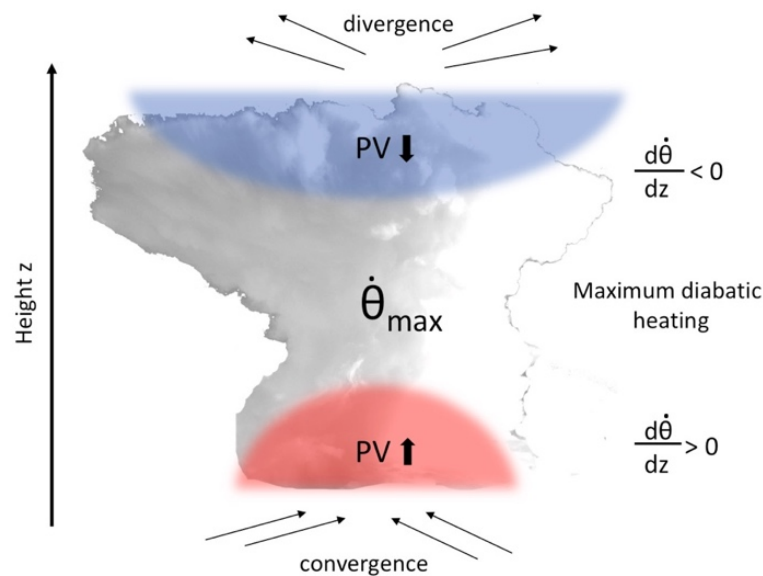


Fig. 1.8 Conceptual illustration of diabatic heating rates $\frac{d\dot{\theta}}{dz}$ and PV modification during deep convection.

Characterizing and understanding the distribution of PV in MTLCs is important because PV has been mentioned to play a pivotal role in their intensification and modulates the upper-level forcing. While conservation equations of both absolute vorticity and PV can be used to describe the motion of MTLCs, a PV

budget presents a more compact description, especially in baroclinic environments (Shapiro, 1996; Chan et al., 2002; Chan, 2005) and this approach is used in our study. Many studies have been dedicated to the study of PV evolution in TCs, while little attention has been given to extratropical cyclones and in particular to MTLCs. Some recent studies have concluded that during their life cycle, MTLCs can rely either on purely diabatic processes or on a combination of baroclinic and diabatic processes (Mazza et al., 2017; Fita and Flaounas, 2018; Miglietta and Rotunno, 2019). The importance of PV streamers and their key role in the development of MTLCs has been confirmed in several cases. Chaboureau et al. (2012) investigated the TT of an MTLC in the Ionian Sea in September 2006 and found that a PV tower with a vertical extent of more than 600 hPa resulted in an explosive deepening of the cyclone at the left exit of a mid-level jet stream. While low-level PV was formed at the early stages of this cyclone due to orographic forcing and diabatic heating, it interacted with the upper-level PV reservoir forming the PV-tower only when the jet stream arrived in the vicinity of the cyclone. Similar results for this MTLC were presented in the study of Miglietta et al. (2017) which showed that this case was the only one among 14 MTLCs that developed an intense PV-tower extending from the surface to the lower stratosphere. For the rest of their cases, the low-level PV remained distinct from the upper-level intruding PV near the tropopause. A mid-level PV maximum between 700-800 hPa was also found during the MTLC QENDRESA in November 2014, resulting from diabatic heating during deep convection in the studies of Cioni et al. (2018) and Bouin and Brossier (2020).

Early studies of the evolution of PV in TCs using axisymmetric, isentropic models found mature TCs to have a deep maximum in PV throughout the troposphere and a minimum at the tropopause (e.g., Schubert and Alworth, 1987; Möller and Smith, 1994; Hausman et al., 2006). This PV structure of mature TCs was corroborated by observations, which found large values of PV throughout the lower and middle troposphere within the TC eyewalls and low values aloft (Shapiro and Franklin, 1995; Wu and Kurihara, 1996). The influence of large-scale flows, such as upper-level baroclinic troughs, on TC intensification has been investigated by examining their interaction with PV anomalies (Bosart and Bartlo, 1991; McIntyre, 1993; Molinari et al., 1998). When precipitating vortices are subject to a vertically sheared environment, the diabatic evolution of PV can also be used to understand aspects of their motion and tilting (Raymond and Jiang, 1990), and their possible amplification through baroclinic processes (de Vries et al., 2010; Cohen and Boos, 2016). Tory et al. (2006) found diabatically-generated PV at both lower and middle levels during TC formations, and Yuan and Wang (2014) found mid-level PV maxima. Raymond (2012) argued that the mid-level PV maxima and accompanying warm-over-cold thermal structures aided further cyclone intensification. Ritchie and Holland (1997) suggested that the increase in PV during merging of mesoscale vortices in cyclone spin-up increases the vertical depth of the vortex and leads to the formation of a low-level vortex. Hurley and Boos (2015) found that monsoon TDs in multiple monsoon regions appeared as mid-level PV maxima in an atmospheric reanalysis, with the peak PV centred near 500 hPa and a secondary maximum near 700–800 hPa. Similar results for mid-level PV maxima have been found for MTLCs in Miglietta et al. (2017).

1.4 Questions addressed in this thesis and thesis plan

The present work focuses on the diabatic processes during DC activity in MTLCs in order to better understand the processes leading to cyclone intensification periods which are among the most challenging phenomena in meteorology. A major gap in the literature about the organization of DC during MTLCs has motivated us to investigate the structure and intensity of DC, and how it is connected with environmental shear and changes in vortex tilt. Moreover, we further explore the vertical and horizontal distribution of PV during MTLCs with a different approach by using a PV budget technique and we compare the results with previous studies.

The most important scientific questions discussed in this dissertation are:

- How is deep convection organized during the MTLCs? How do the vertical wind shear and the Mediterranean topography affect the DC activity during MTLCs and how does the vortex vertical structure changes during intense DC? Does the DC activity follow the diurnal solar cycle as in TCs?
- Which MTLCs experience thermodynamic (diabatic) intensification? What is the relative contribution of diabatic processes in the amplification of the MTLCs? How do the vertical PV structures evolve during the lifetime of the MTLCs and when do they attain bottom-heavy diabatic PV?
- Can we place the MTLCs near the end of the Mediterranean cyclones continuum or do they need a separate classification? Do the MTLCs have more similarities with intense extratropical and subtropical cyclones or TCs?

Eventually the answers to these questions will contribute towards a definition for the MTLCs and will provide a better understanding to the MTLCs' dynamics and raise further questions for future studies.

This dissertation is organized into this Introduction chapter (Chapter 1), a chapter detailing two main aspects of this work, about how to observe deep convection during MTLCs and the associated tools and methodology (Chapter 2). Nine MTLCs between 2005 and 2018 have been considered in Chapter 2, based on different criteria about their duration and structure evolution. Satellite retrievals are analysed in detail to characterize the evolution of these MTLCs. Comparisons are made to studies in other oceans about tropical and subtropical cyclones with special focus on vortex structure (tilt) and vertical wind shear influences on the evolution of DC, computed by atmospheric reanalysis data. Chapter 3 presents and discusses numerical simulations about the diabatically-induced intensification of MTLCs. The impact of the location and intensity of diabatic heating in the intensification of MTLCs is shown, and a PV budget technique along with pressure tendency equations are utilized to verify the conclusions of Chapter 2. Changes of MTLC intensity and strength to the location of diabatic heating in relationship to the upper-level configuration and low-level fluxes are also discussed. Finally, a summarizing chapter (Chapter 4) discusses the main findings of this dissertation and provides insights into future studies.

Chapter 2

Observations of deep convection during Mediterranean tropical-like cyclones

2.1 Introduction

This chapter presents an observational study of the evolution of DC during MTLCs. Satellite imagery is most of the time the only source of information in the absence of conventional in-situ observations in the Mediterranean Sea. For that reason, brightness temperature data at different wavelengths is used. It is important to study the evolution of DC since it is associated with strong upward vertical motions and strong latent-heat release, and it typically occurs within a region of consolidating low/mid-level spin, it plays a key role in the vorticity dynamics of cyclogenesis. As it will be illustrated in the following paragraphs, a few instances of DC develop a closed “eye” during the MTLCs, as cloudy remnants with small orbital periods are wrapped around the centre of the cyclones. The mesocyclones developing close to the eye of the TCs can engender large surface-pressure falls (e.g., Hendricks et al., 2004) but similar observations are presented in this study during MTLCs.

The rapid advances in remote sensing of the Earth from space the past two decades have made it possible to observe cyclones worldwide with great details and with an increasing spatial and temporal resolution (Tourville et al., 2015). Even though the temporal availability of polar-orbiting satellites in the mid-latitudes is limited to a few overpasses per day, they complement the geostationary satellites which provide rapid-scans of the atmosphere. The most commonly used approach to indicate the presence, the intensity and the fractional coverage of deep convective clouds is based on the use of infrared (IR) brightness temperature (BT) provided by geostationary satellites in high temporal and spatial resolution. Moreover, the microwave (MW) satellite imagery from polar-orbiting satellites has the ability to detect and measure liquid and frozen hydrometeors, even at the lowest parts of the troposphere.

- **Definition of deep convection**

Deep convection is the thermally-driven turbulent mixing that moves air parcels from the lower to the upper troposphere. The deep moist convection occurs when air is lifted to saturation and achieves positive buoyancy, such that it may rise high in the troposphere or even up to the lower stratosphere. The initiation of moist DC requires that air parcels reach their level of free convection (LFC) and subsequently remain positively buoyant over a significant upward vertical motion. Thus, convective available potential energy

(CAPE) is a necessary, albeit insufficient, condition for convection initiation (Markowski and Richardson, 2010). The presence of an LFC and CAPE requires a relatively steep lower to middle tropospheric lapse rate (larger than the moist adiabatic lapse rate) and high tropospheric moisture. Air typically requires some forced ascent in order to reach the LFC, owing to the presence of at least some convective inhibition (CIN). Deep moist convection is commonly initiated along air mass boundaries such as synoptic fronts, drylines, outflow boundaries, and sea breezes. Convective storms can also be initiated by orographic circulations driven by the heating of elevated or sloped terrain, and by forced lifting by ducted gravity waves. Synoptic-scale dynamics often prime the mesoscale environment for convective initiation, for example, by providing large-scale ascent to unstable low-level air masses, a common mechanism which tends to reduce CIN and deepen the low-level moist layer. On the other hand, synoptic-scale dynamics also can inhibit convection initiation by leading to subsidence, which has the opposite effects. Large-scale vertical motions (e.g., quasigeostrophic upward motions) often lead to widespread convective initiation and deep convection.

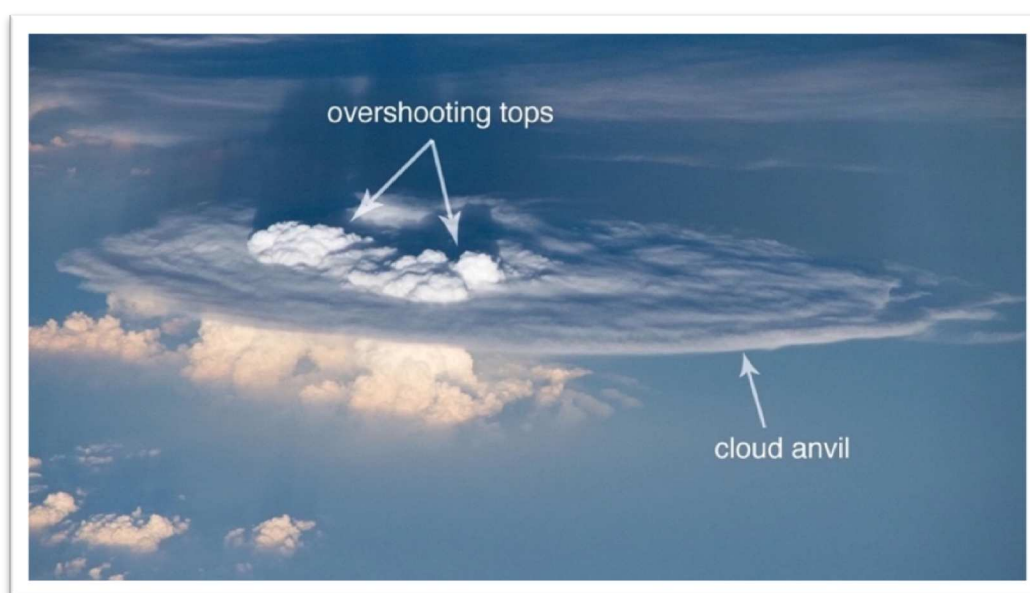


Fig. 2.1 Deep moist convection with overshooting tops as seen from space. The cloud anvil indicates the level of neutral buoyancy or in other words, the position of thermal tropopause. Overshooting tops above strong updrafts penetrate the tropopause and rise in the lower stratosphere. Image courtesy of the International Space Station (ISS) (ESA/NASA).

The core of deep convective storms usually acquire strong upward momentum within the strong updrafts, where vertical velocities reach values comparable or even stronger than downdrafts, where CAPE is high. The air parcels will rise into these updrafts as long as they are less dense and therefore more buoyant than the surrounding environment. They will slow down only when they reach a very stable layer in the atmosphere, i.e. the tropopause. The faster the parcels rise, the longer it take to slow down and stop, bringing moisture into high altitude. This is the physical explanation for the occurrence of overshooting tops (COV) above the thunderstorm's anvil, where the strongest updrafts, and with the greatest momentum, create a dome-like protrusion (Fig. 2.1). COV is often formed above the core of DC, so it is a good indicator to track the core of a thunderstorm. Not all convective clouds do penetrate the tropopause, but all of them can contribute to the

warming of the middle troposphere through condensational heating and release of latent heat. COV has been known to be associated with severe weather around the globe (e.g., Adler et al., 1985; Brunner et al., 2007) and climatological studies of Bedka et al. (2010) and Rysman et al. (2016) have shown the high frequency of COV in the Mediterranean basin.

2.2 Data and methods

2.2.1 The Advanced Microwave Sounding Unit (AMSU-B) and the Microwave Humidity Sounder (MHS)

The passive microwave sounders are considered to be one of the most essential tools to observe the atmosphere and they are of primary importance in many aspects of observational and numerical studies (Bormann and Bonavita, 2013). Their ability to probe the atmosphere even in cloudy conditions and provide information about the vertical profiles of both temperature and humidity (Suskind et al., 1984; Gloersen and Barath, 1977) is unique among the spaceborne instruments currently in Earth's orbit. They have been widely used for detecting deep moist convection and convective rainfall in the atmosphere (e.g., Hong et al., 2005; Funatsu et al., 2007; Laviola and Levizzani, 2011; Alhammoud, et al., 2014; Kidd et al., 2016; Rysman et al., 2016; 2018 among others). Nowadays, the passive microwave sounders probe the atmosphere from 20 to 200 GHz with their channels centered in the oxygen bands (for temperature profiles) and in the water vapor bands (for humidity profiles) and they were first put in orbit in 1975. The 5-channel Scanning Microwave Spectrometer (SCAMS) (Staelin et al., 1975) was the first scanning radiometer on-board Nimbus-6 (launched in June 1975) to measure temperatures over the ocean surfaces, water vapor and liquid water. A few years later and since 1978, the 4-channel Microwave Sounding Unit (MSU) was used operationally on-board the TIROS-N (NOAA series) satellites and provided a global coverage, probing between 50 and 60 GHz with a spatial resolution of about 250 km. There were 9 MSUs launches between 1978 and 1994 (NOAA-14 was the last one) and since 1998 the Advanced Microwave Sounding Unit (AMSU) (Vangasse et al., 1996) has replaced the MSU, providing higher spatial resolution and additional channels. For the platforms launched after May 2005, the 5-channel Microwave Humidity Sounder (MHS) (Bosignori, 2007) replaces the observations of AMSU-B and they both provide a temporal resolution of about 3-4 hours over the Mediterranean.

The AMSU-B and MHS instruments measure the upwelling microwave radiation with very similar frequencies: two window channels at 89 and 150 GHz (AMSU-B)/157 GHz (MHS) and three channels in the water vapor absorption line at 183.31 ± 1 , 183.31 ± 3 , and 183.31 ± 7 (AMSU-B)/190.3 GHz (MHS) (Table 2.1). Their swath width is approximately of 1650 km, their nadir resolution is 16 km for AMSU-B and 17 km for MHS, and their viewing angles go up to about 50° . The first AMSU-B was launched in 1998 on-board the National Oceanic and Atmospheric Administration 15 (NOAA-15) polar orbiting satellite and since then, seven more instruments have been launched, in 2001 (AMSU-B/NOAA-16), in 2002 (AMSU-B/NOAA-17), in 2005 (MHS/NOAA-18), in 2006 (MHS/Meteorological Operational Satellite A (MetOp-A)), in 2009 (MHS/NOAA-19), in 2012 (MHS/MetOp-B), and in 2018 (MHS/MetOp-C). In this study, we use BT measurements between 2005 and 2018 in order to detect deep convective cloud systems during MTLCS and Fig. 2.2 shows the time-

series of satellite availability during this period. At least 4 AMSU-B/MHS passes per day are available during each MTLC analysed in this study.

Radiometer	Channel	Frequency (GHz)
AMSU-B	1	89.0±0.9
	2	150.0±0.9
	3	183.31±1.0
	4	183.31±3.0
	5	183.31±7.0
MHS	1	89.0
	2	157.0
	3	183.31±1.0
	4	183.31±3.0
	5	190.31

Table 2.1 The radiometric characteristics of AMSU-B and MHS microwave humidity sounders for the high-frequency channels. The rows for channels 3, 4 and 5 which are used in this study are highlighted with a blue shade.

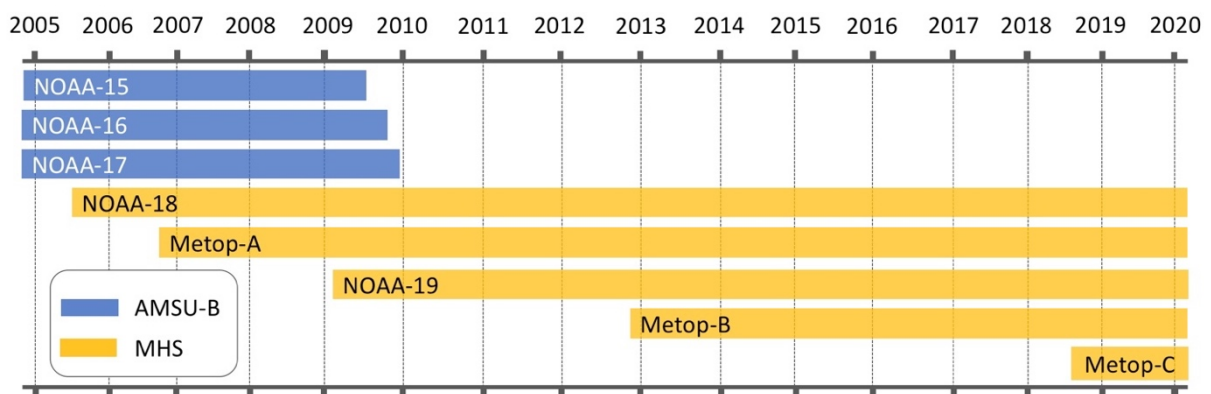


Fig. 2.2 Time-series of the availability of satellites which carry microwave humidity sounders between 2005 and 2020 and are used in this study (apart from Metop-C).

The Earth's surface emissivity, the water vapor and the liquid/frozen hydrometeors affects the microwaves (e.g., Mugnai and Smith, 1988; Mugnai et al., 1990; Petty, 1995; Panegrossi et al., 1998; Stephens and Kummerow, 2007). The passive microwave retrievals of AMSU-B and MHS have been extensively studied the past few decades (e.g., Ferraro et al., 2000; Bennartz and Bauer, 2003; Hong et al., 2005; Laviola and Levizzani, 2011, among others). The weighting functions of AMSU-B and MHS peak at the ground level for the window channels, and between 2 and 8 km height (inside the troposphere) for the water vapor channels in mid-latitudes (Karbou et al., 2005). The radiation measured by the AMSU-B and MHS depends on: the emission of the surface and/or the atmosphere and the emission, absorption and scattering by atmospheric components (water vapor, cloud liquid water, rain and frozen hydrometeors). Thus, the BT retrievals depend on the surface properties, on the vertical profiles of water vapor/temperature and on the density, phase, shape, size distribution and altitude of hydrometeors.

2.2.2 Deep convection detection based on AMSU-B/MHS

MW imagery has been extensively used for the detection of DC in TCs around the globe (e.g., Chen and Houze, 1997; Yang and Slingo, 2001; Machado et al., 2002; Wilcox, 2003; Tian et al., 2004; Hong et al., 2006a; Wu and Ruan, 2016). DC and COV detection for the needs of our study is realized by using BTs from the water vapor channels 183.31 ± 1 GHz (BT_3), 183.31 ± 3 GHz (BT_4), and $183.31 \pm 7 / 190.3$ GHz (BT_5) of AMSU-B and MHS which are sensitive to the water vapor and the scattering from hydrometeors. In particular, they are very sensitive to high density frozen hydrometeors (such as graupel and hail). They are almost insensitive to low-level clouds and surface properties (i.e., temperature and surface emissivity, except for very dry and cold conditions (Laviola and Levizzani, 2011)). Because the BT_5 channel probes deeper in the atmosphere, it is also sensitive to rain and cloud liquid water (Bennartz and Bauer, 2003). The DC detection algorithm of Hong et al. (2005) is used to detect areas covered with deep convective clouds, which has been extensively used and validated in the Mediterranean (e.g., Funatsu et al., 2007; 2018; Rysman et al., 2016; 2017) and it is computed as follows:

$$\begin{aligned} BT_3 - BT_5 &\geq T_0 \\ \text{and } BT_3 - BT_4 &\geq T_0 \\ \text{and } BT_4 - BT_5 &\geq T_0 \quad (\text{Eq. 2.1}) \end{aligned}$$

where $T_0 = 0.04761 - 0.01678 \theta + 0.00599 \theta^2$ where θ is the viewing angle. This diagnostic has been primarily developed to detect DC in the tropics but it has been validated in the Mediterranean region by Funatsu et al. (2007) and Rysman et al. (2015).

COV can be detected by the microwave sounders by applying a more strict relation between the aforementioned BT differences. We apply the Hong et al. (2005) criteria for BT differences, first developed with AMSU-B data for tropical storms, which have also been evaluated for the Mediterranean using the MHS (Rysman et al., 2015; Flaounas et al., 2016):

$$BT_3 - BT_5 \geq BT_3 - BT_4 \geq BT_4 - BT_5 \geq T_1 \quad (\text{Eq. 2.2})$$

where $T_1 = 0$ K for $\theta \leq 30^\circ$ and $T_1 = 7$ K for $35^\circ \geq \theta > 30^\circ$. A demonstration of DC and COV detections is shown in Fig. 2.3 where data from RASTA (RAdar SysTEM Airborne) 95 GHz Doppler airborne cloud radar (Delanoë et al., 2013) were collocated with SEVIRI BTs and MHS DC-COV diagnostics. Time series of radar reflectivity (dBZ), MHS BTs (K) and DC-COV diagnostics are shown in Fig. 2.3b when the airplane crossed the core of a storm during the Intensive Observational Period 1 (IOP1) of the international project ‘‘Hydrological cycle in the Mediterranean Experiment (HyMeX) (Ducrocq et al., 2014).

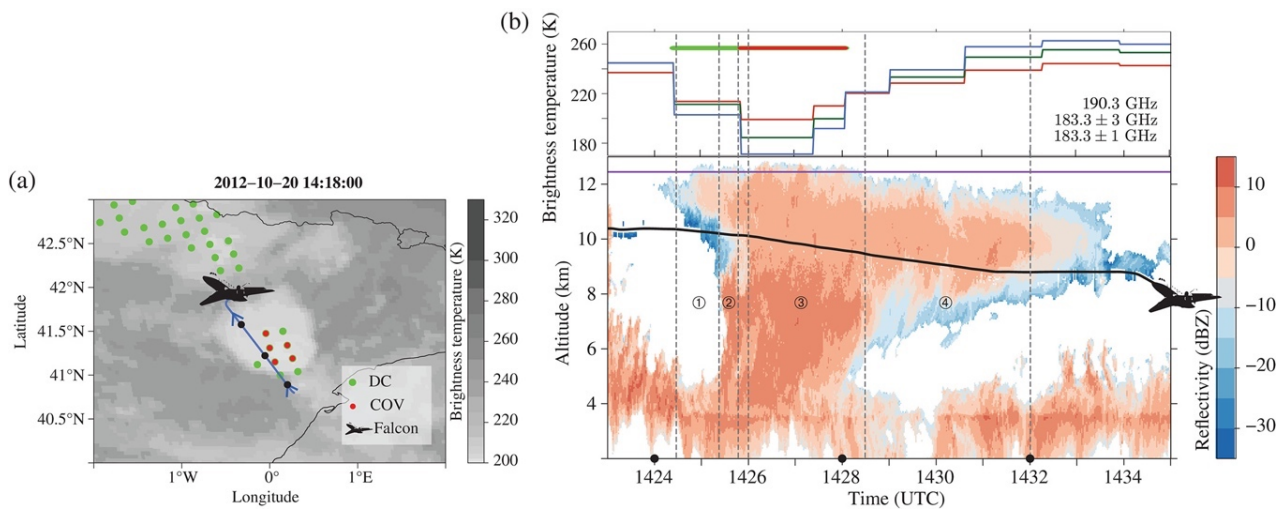


Fig. 2.3 (a) Brightness temperatures from the MSG-SEVIRI IR10.8 channel at 1418 UTC on 20 October 2012. (grey shading), the track of the research aircraft Falcon 20 (blue line), and DC and COV events (green and red spots respectively). (b) Dark red (183.31 ± 1 GHz), dark green (183.31 ± 3 GHz) and dark blue (190.3 GHz) lines show the MHS brightness temperatures from NOAA-18 satellite at 1418 UTC for grid points closest to the flight track. DC and COV events are symbolised by thick green and red lines respectively. (c) Reflectivity from airborne radar (colour shading), the track of Falcon 20 (black line), and tropopause height (purple line). Black dashed lines have been added to highlight several segments of the cloud discussed in the text. Black points are displayed along flight track at 1424, 1428 and 1432 UTC.

(source: Rysman et al., 2015)

In addition, the algorithm for detecting intense rainfall (MR) developed by Funatsu et al. (2007) (Eq.2.3) is used:

$$BT_3 - BT_5 \geq T_0, \text{ (Eq. 2.3)}$$

where and $T_0 = -8$ K. Funatsu et al. (2007) showed that the T_0 value corresponds to a rain rate greater than 10 mm (3h)⁻¹ in the Mediterranean but rain from low-level clouds can be missed using this diagnostic.

2.2.3 Meteosat SEVIRI

The Meteosat Second Generation (MSG) satellite series provide continuous observations of the Earth's full disc since 2002. The first one of this series, the MSG-1 satellite also named Meteosat-8, was launched in August 2002, the MSG-2, named Meteosat-9, started operation in December 2005 and two more satellites were launched in 2012 (Meteosat-10 or MSG-3) and in 2015 (Meteosat-11 or MSG-4). MSG-4 is currently the prime satellite in Meteosat service and positioned over the equator at 0° longitude. Each Meteosat scene encompasses Europe, Africa, Near East and partly South America. Each MSG satellite carries the Spinning Enhanced Visible and Infrared Imager (SEVIRI), a multi-spectral imager (Sobrino and Romaguera, 2004). SEVIRI has eight spectral channels in the infrared (IR) (channels Nb 5-12 in Table 2.2), three channels in the solar spectrum, and a broadband high resolution visible channel (HRV) used for observations of clouds and surface temperatures, water vapor or ozone.

Channel Nb	Channel Name	Central Wavelength (μm)
1	VIS0.6	0.6
2	HRV	0.75
3	VIS0.8	0.8
4	NIR1.6	1.6
5	IR3.9	3.9
6	WV6.2	6.2
7	WV7.3	7.3
8	IR8.7	8.7
9	IR9.7	9.7
10	IR10.8	10.8
11	IR12.0	12.0
12	IR13.4	13.4

Table. 2.2 Spectral channel characteristics of SEVIRI providing the official EUMETSAT names and central wavelengths (μm). The rows for channels 6 and 10 which are used in this study are highlighted with a blue shade.

All spectral regions are affected by the absorption in the atmosphere. However, in ranges of atmospheric windows the Earth's atmosphere is largely or partially transparent. Water vapor is responsible for atmospheric effects on BT in the whole spectral range with different intensity. Other gases absorb the radiance only in some selected parts of spectral range. The BT can be interpreted as a weighted average temperature of the atmospheric layers where the absorbing gases are present. From the 12 spectral channels available in Table 2.2, in order to detect the presence of DC in the troposphere, the special focus is placed on two channels with different physical interpretation for clouds: a) the IR10.8 channel which is strongly affected by the presence of hydrometeors and provides the BT of cloud tops and the surface, and b) the WV6.2 channel which provides information for the upper-tropospheric moisture content.

2.2.4 Deep convection detection based on SEVIRI

Most observational studies on DC occurrence define a threshold for IR10.8 BTs between 230-240 K under which is assumed to observe DC (e.g., Chen and Houze, 1997; Yang and Slingo, 2001; Machado et al., 2002; Wilcox, 2003; Tian et al., 2004; Hong et al., 2006; Wu and Ruan, 2016). One major drawback adopting this method is the lack of discrimination between high-level clouds (i.e., cirrus, cirrostratus) and convective clouds, especially in their developing stage. In order to detect DC and COV using SEVIRI in this thesis, a similar method to Olander and Velden (2009) is used. This method relies on the channel differencing between the water vapor channel WV6.2 and the window channel IR10.8 (ΔBT) of SEVIRI pixels used at the nominal spatial resolution of about 3 km. Typically during clear-sky conditions, the IR10.8 channel has a peak spectral response close to or at the surface of the Earth, while the WV6.2 channel peaks at about 350 hPa (Fig. 2.4), thus ΔBT is typically negative. In the presence of opaque and convective clouds, this spectral response can change significantly and even reverse. During intense DC, important amounts of WV can be transported in the upper troposphere or lower stratosphere where it is reemitted at higher temperatures in the WV6.2 channel than in the window channel (Schmetz et al., 1997). Positive ΔBT ($WV6.2 - IR10.8 > 0$) values are attributed to convection penetrating the tropopause and is attributed to COV but it is not always collocated with the core of the updrafts, since WV can remain in the lowest stratosphere for several hours (Setvak et al., 2007; Chung et al., 2008; Bedka et al., 2010).

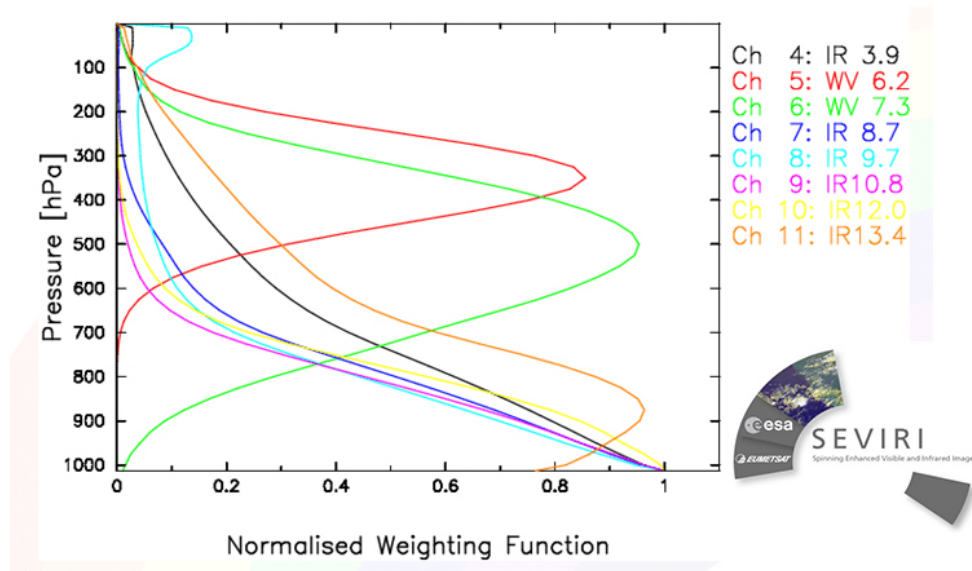


Fig. 2.4 Normalized weighting functions of SEVIRI channels for clear sky conditions. (source: eumetrain.org)

In order to detect the DC in IR data, pixels accounted as containing deep convective clouds must meet the criterion of ΔBT greater or equal to -10 K. SEVIRI pixels with ΔBT values above -10 K will be referred to as “DCPIXELS”. The -10 K ΔBT threshold was chosen to be representative of DC after additional analysis of collocating SEVIRI data with DC diagnostics calculated with passive microwave data. An example is shown in Fig. 2.5 where SEVIRI DCPIXELS and passive microwave diagnostics from MHS on-board MetOp-B are overlapped during the MTLZ ZORBAS on 28 September 2019. False-color areas covered by DCPIXELS and MHS diagnostics agree on the presence of DC over the Mediterranean within 200 km from ZORBAS’ centre. The differences between the two diagnostics are mostly attributed to the different scanning footprints of the two instruments, with 3 km grid increment for SEVIRI and about 16 km for MHS and the time lag between the two scans (about 3 minutes). The right panel of Fig. 2.5b-c provides the BT values of Fig. 2.5a where values of IR10.8 BTs of up to 246 K correspond to DCPIXELS in contrast to previous studies defining the DC thresholds between 230-240 K. Adding the WV6.2 channel to the analysis, we add information about the vertical extent of water-vapor in the troposphere and lower stratosphere, increasing the detection confidence for the presence of DC.

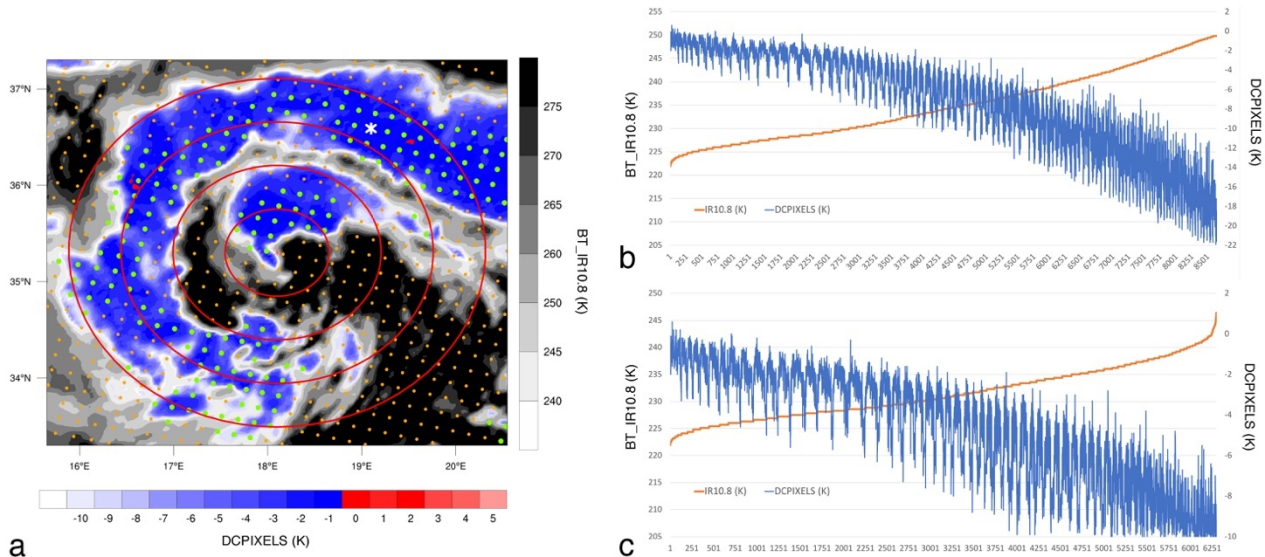


Fig. 2.5 (a) Infrared brightness temperature (BT) from channel IR10.8 (K) (grey) and DCPIXELS (K) (blue and red) derived from SEVIRI Meteosat-11 satellite during MTLC ZORBAS on 28 September 2018 at 0830 UTC. Overlapped dots: diagnostics for deep convection (MWDC) from the microwave sounder MHS on-board MetOp-B (green), convective overshooting (COV) (white asterisks) and the scanning footprint (orange) at 0833 UTC. The red circles enclose disks within 200 km from the centre of the cyclone, plotted every 50 km, the red asterisk shows the cyclone centre and the coastline is shown with an orange solid line. (b) BT values of IR10.8 (orange line) and DCPIXELS (blue line) shown in (a), sorted for all IR10.8 BTs in the domain and (c) for DCPIXELS greater than -10 K.

2.2.5 Cyclone tracking and atmospheric reanalysis

- Cyclone tracking based on satellite observations

Due to the limited conventional meteorological observing networks in the Mediterranean, most of the time, satellites are the only source of information about cyclones. Several studies about how to manually track subsynoptic low-pressure systems with satellite imagery have been published (e.g., Harold et al., 1999, Verezhenskaya et al., 2017) while for the MTLCs similar techniques for Meteosat imagery have been used to assess the ability of numerical models to reproduce the actual cyclone tracks (e.g., Lagouvardos et al., 1999, Fita and Flaounas, 2018 among others). The mesoscale cyclones chosen for this study have well-defined cyclonic curvatures in the satellite imagery or closed circular patterns, and each case was treated explicitly (e.g., QENDRESA in Fig. 2.6). SEVIRI onboard Meteosat provides a high temporal and spatial resolution to track the cyclonic curvature of cloud systems around the cyclone center. Multiple loops were analyzed every 5 or 15 minutes according to the availability of infrared brightness temperature or visual imagery starting when cyclonic circulation was visible until the last time step when the cloud circulation could indicate the presence of a surface cyclone. When available, polar-orbiting satellite data (brightness temperature and DC diagnostics) were utilized and they were crucial in determining the convective-free cyclone centers, especially when a cloud canopy was covering most of the domain. A few more examples of how the manual tracking of the MTLCs is performed are illustrated in Appendix 1.

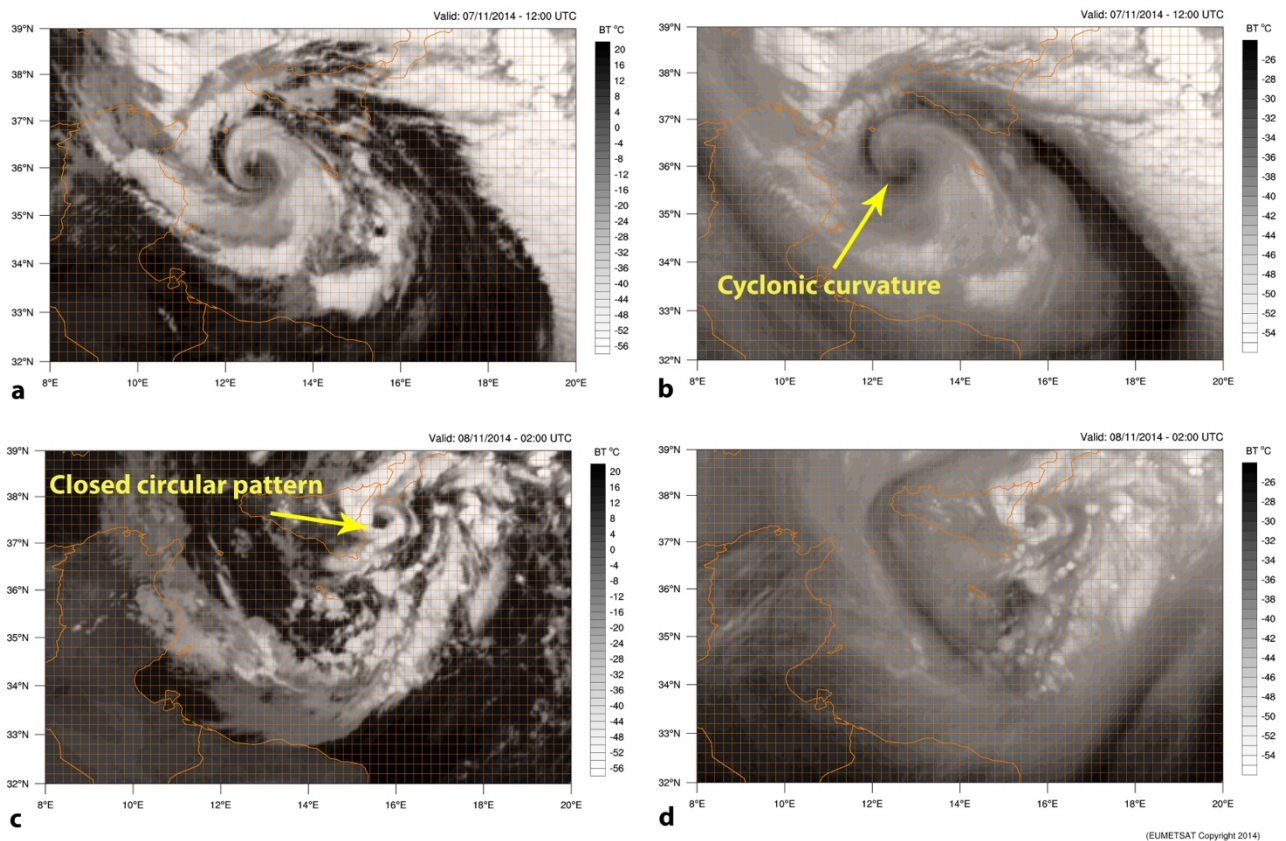


Fig. 2.6 Brightness temperature (BT) ($^{\circ}\text{C}$) derived from SEVIRI on-board Meteosat-9 from channels IR10.8 (left) and WV6.2 (right) at (a-b) 1200 UTC 7 November and (c-d) 0200 UTC 8 November 2014 during the MTLQ QENDRESA.

- Atmospheric reanalysis ERA5

The ERA5 reanalysis project is the most modern global reanalysis dataset and with the highest spatial and temporal resolution, thus it was chosen to be used in the current thesis for the computation of wind shear and vortex tilt during the studied MTLQs discussed in this chapter, and as the forcing dataset for the initial and boundary conditions in the numerical study presented in Chapter 3. The atmospheric reanalysis is a dataset created after assimilating historical atmospheric observational data spanning an extended period of time within a numerical model, using a consistent assimilation scheme. The past observational data are reprocessed in the reanalysis assimilation with the same technique throughout the historical period in order to construct consistent time-series, because otherwise the dataset would suffer from inconsistencies due to the numerical model's updates if only operational analysis is used. A reanalysis project is considered to be the best fit of a numerical model to the available data, taking into account the errors in the model and the observational data. Nevertheless, reanalysis often incorporate important observation errors and limitations, such as degradation of satellite instruments and some numerical variables (outputs) are not constrained by observations such as precipitation and evapotranspiration. There are two types of atmospheric reanalysis: a) global and b) regional. The latter, are high-resolution reanalysis datasets for specific geographical regions and are often based on a regional weather forecasting model that uses boundary conditions from a global reanalysis. The most widely

used global reanalyses are the ECMWF reanalyses (ERA40, ERA-Interim and ERA5) (Hersbach et al., 2020), the Modern-Era Retrospective analysis for Research and Applications (MERRA-2, Gelaro et al., 2017), the NCEP/NCAR Reanalysis and the Japanese 25/55-year Reanalysis (JRA-25/55) (Onogi et al., 2007).

The fifth-generation ECMWF atmospheric reanalysis (ERA5) is an atmospheric reanalysis of the global climate and is the latest reanalysis product of ECMWF. It provides hourly data on many atmospheric, land-surface and sea-state parameters together with estimates of uncertainty, as well as short (18-hour) forecasts initialized twice a day at 0600 and 1800 UTC. The ERA5 dataset covers the period 1981 – 2020 and is available on a regular latitude-longitude grid at $0.28^\circ \times 0.28^\circ$ resolution (31 km in the Mediterranean) with atmospheric parameters on 37 levels. ERA5 was produced using 12-hour window (0900-2100 UTC and 2100 – 0900 UTC) 4D-Var assimilation in CY41R2 of ECMWF's Integrated Forecast System (IFS) with 137 hybrid sigma/pressure (model) levels in the vertical with the top level at 0.01 hPa. Atmospheric data are available on these levels and they are interpolated to 37 pressure, 16 potential temperature and 1 potential vorticity level(s). "Surface or single level" data are also available, containing 2-D parameters such as precipitation, 2-m temperature, top of atmosphere radiation and vertical integrals over the entire atmosphere. The IFS is coupled to a soil model (the Tiled ECMWF Scheme for Surface Exchanges over Land (TESSEL)- Balsamo et al., 2009), the parameters of which are also designated as surface parameters, and an ocean wave model (the Nucleus for European Modelling of the Ocean (NEMO), <http://www.nemo-ocean.eu/>).

2.3 Results

2.3.1 Introduction of the article “Remote sensing of deep convection within a tropical-like cyclone over the Mediterranean Sea”

Between 6 and 9 November 2011, the MTLC ROLF develops in West Mediterranean Sea, and it is accompanied by active and long-lasting DC activity. After two days of convective activity close to the center of the depression, ROLF reaches its maximum intensity in the early morning on 8 November 2011. The evolution of DC and lightning activity during the MTLC ROLF are studied in detail in the following article, using convective diagnostics from infrared and microwave data together for the first time during in a MTLC. By calculating the occurrence of DC and overshooting tops (OT) from brightness temperatures derived from both the microwave sounder MHS and the infrared channels of SEVIRI, the temporal and spatial distribution of DC within 200 km from ROLF's centre is mapped and compared with different types of cyclones. Interestingly, the detected lightning activity is not correlated well with the observed DC activity, but most of the lightnings are detected about a day before the maximum intensity of the cyclone. In contrast, the DC activity with the most OT detections close to the cyclone center has a peak a few hours before the maximum intensity of ROLF. During the dissipation of the cyclone, and for about 24 hours after the maximum cyclone intensity, DC activity is detected only to the eastern and northern parts of ROLF while it is approaching the southern coasts of France in the Gulf of Lion on 9 November 2011, and despite the detections of OTs, lightning activity is very scarce, at least the cloud-to-ground lightnings that are more easily detected by the ground-based detection

system used. Results show that the convective evolution of ROLF shares more similar characteristics with TCs than other intense extratropical Mediterranean cyclones.

2.3.2 Article “Remote sensing of deep convection within a tropical-like cyclone over the Mediterranean Sea”

Received: 31 January 2018 | Revised: 6 April 2018 | Accepted: 9 April 2018

DOI: 10.1002/asl.823

Atmospheric Science Letters 

RESEARCH ARTICLE

Remote sensing of deep convection within a tropical-like cyclone over the Mediterranean Sea

Stavros Dafis¹  | Jean-Francois Rysman^{1,2}  | Chantal Claud¹  | Emmanouil Flaounas³ 

¹LMD/IPSL, CNRS UMR 8539, École Polytechnique, Université Paris Saclay, ENS, PSL Research University, Sorbonne Universités, Palaiseau, France

²Institute of Atmospheric Sciences and Climate (ISAC)—National Research Council (CNR), Rome, Italy

³National Observatory of Athens, Institute for Environmental Research and Sustainable Development, Athens, Greece

Correspondence

Stavros Dafis, LMD/IPSL, CNRS UMR 8539, École Polytechnique, Université Paris Saclay, ENS, PSL Research University, Sorbonne Universités, Palaiseau, France.
Email: sdafis@lmd.polytechnique.fr

Funding information

Earth2Observe, Grant/Award Number: 603608; Centre National d'Études Spatiales; ANR-MUSIC project, Grant/Award Number: 14-CE01-0014; Direction générale de l'armement—Ministère des Armées (DGA)

The Mediterranean basin occasionally hosts tropical-like cyclones named “Medicane”. Medicane may have intensity comparable to hurricanes in terms of wind speeds along with an axisymmetric cloud structure. Although these events can be particularly violent, very few studies so far have investigated the distribution and temporal evolution of deep convection within these cyclones. In this study, the characteristics and lifetime of deep convection and lightning activity surrounding the core of the longest-lasting and probably the most intense Medicane ever recorded in terms of wind speed (Rolf, November 2011) are presented by all available means of microwave and infrared satellite retrievals and a lightning detection system. Results showed that deep convective clouds penetrated the lowest stratosphere and were wrapped around the cyclone centre during the intensification period. Lightning activity was mostly active about a day before the maximum strength of the cyclone studied and it was not temporarily correlated with the most intense deep convection activity. Overall, this study reveals that spatial and temporal distribution of deep convection and lightning activity around the centre of Rolf show more similarities with Tropical Cyclones than intense Mediterranean cyclones.

KEYWORDS

convection, lightning, Medicane, Mediterranean, satellite, tropical-like cyclone

1 | INTRODUCTION

The risk assessment related to the formation of intense tropical-like cyclones (TLC) or the so-called “Medicane” over the Mediterranean Sea is crucial in order to limit the socioeconomic damages mostly in islands and coastal areas (Michaelides *et al.*, 2017). Even though cyclones that attain characteristics of tropical cyclones in the Mediterranean is a debatable issue, a Medicane can be defined as an intense, maritime warm-core cyclone that forms in the Mediterranean basin with a cloud-free eye formation and surface winds above gale force. Very few studies exist so far regarding surface or 3D observations of Medicanes and the main reason is that these systems very rarely make landfall and thus, our

understanding of the role of deep convection within these systems is limited to satellite retrievals. Lagouvardos *et al.* (1999) investigated the case of a TLC between Sicily and Greece in 1995 using infrared imagery and documented the presence of deep convection (DC) prior to TLC genesis, as well as the weak baroclinic instability contribution to the evolution of the cyclone, by using a mesoscale model. Luque *et al.* (2007) analysed satellite retrievals to construct the trajectories of three Medicanes between 1995 and 2005 and estimated precipitation features from microwave measurements. They concluded that the temporal evolution of Medicanes consists of three stages: the pre-eye, the stationary phase and the itinerant phase. Claud *et al.* (2010) used NOAA/MetOp satellite observations to investigate three

This is an open access article under the terms of the Creative Commons Attribution License, which permits use, distribution and reproduction in any medium, provided the original work is properly cited.

© 2018 The Authors. *Atmospheric Science Letters* published by John Wiley & Sons Ltd on behalf of the Royal Meteorological Society.

Atmos Sci Lett. 2018;19:e823.
<https://doi.org/10.1002/asl.823>

wileyonlinelibrary.com/journal/asl2 | 1 of 7

Medicanes and showed that convection and precipitation areas are large in the early stage of the cyclones, but significantly reduced afterwards. Convection maximum was found just after the upper-level trough, located upstream of cold mid-tropospheric air, when Medicanes reached their maximum intensity. Miglietta *et al.* (2013) studied 14 TLC in the Mediterranean and showed that deep convection, heavy rainfall and intense lightning activity preceded the maximum wind speed.

There is no common measure for the intensity of a cyclone, yet it usually inferred in the literature as the period when cyclones reach their minimum sea-level pressure (SLP) or their maximum wind speeds (e.g., Claud *et al.*, 2010; Miglietta *et al.*, 2013). Deep convection, rainfall and latent heat release play a crucial role in the intensification of tropical cyclones, as studies that use satellite techniques and high resolution models, show around the globe (e.g., Homar *et al.*, 2003; Zagrodnik and Jiang, 2014). The source of energy for tropical cyclones is the release of latent heat due to condensation in moist convection. For developing tropical storms, such convection is quite disorganized relative to the cyclonic wind field. Nonetheless, a portion of the heat released in these convective updrafts is transformed into energy of two forms: the kinetic energy of the quasi-symmetric wind field and the convective available potential energy associated with the warm core, which is necessary to hold the cyclonic wind field in hydrostatic and gradient wind balance. Even though studies show that typical baroclinic cyclones in the Mediterranean basin present a similar life cycle (Flaounas *et al.*, 2015), Medicanes exhibit rather peculiar characteristics, resembling TCs.

In this study the lifetime of deep convection of the 6 to November 9, 2011 TLC in NW Mediterranean Sea is studied and compared to similar studies referring to tropical storms and hurricanes around the globe. It is the first study that introduces the use of convective overshooting top detection from infrared satellite observations, along with microwave diagnostics, providing a unique insight to the evolution of deep convection of Medicanes Rolf.

2 | DATA AND METHODS

2.1 | Satellite diagnostics

In order to investigate the evolution of deep moist convection around the TLC during the period 6 to November 9, 2011, the cross-scanning microwave sounder MHS (Microwave Humidity Sounder), on-board NOAA and MetOp polar orbiting satellites were used. In particular, three documented diagnostics, already validated in the Mediterranean basin, were calculated: “Convective Overshooting” (COV), “Deep Convection” (DC) and “Moderate Rainfall” (MR) (Hong *et al.*, 2005; Funatsu *et al.*, 2007; 2018; Rysman *et al.*, 2016; 2017). The detection is performed using a

combination of three humidity sounding channels around 183 GHz. Microwave radiation in these bands is sensitive to the presence of frozen hydrometeors, such that the deeper (more convective) the cloud, the lower the brightness temperatures.

In addition to microwave observations, brightness temperatures (TB) derived from SEVIRI infrared channels 10.8 μm (IR) and 6.2 μm (WV) on-board Meteosat-9 (MSG-2) geostationary satellite were used to calculate the occurrence of overshooting tops (OT), based on the technique proposed by Schmetz *et al.* (1997). Overshooting tops are defined by the positive brightness temperature difference (ΔTB) between WV and IR, as the WV spectral response peak is about 350 hPa and it is typically colder than IR which has a maximum spectral response near the surface. The OT diagnostic was calculated every 15 min from 6 November 00:00 UTC until 9 November 12:00 UTC.

Note that SEVIRI's spatial resolution is 3 km, while MHS has a near nadir instantaneous field of view of approximately 16 km, that is relatively large when compared to typical updrafts, thus the observed brightness temperatures represent a combination of effects over a relatively large area. Finally, microwave diagnostics are available five times per day, while geostationary data every 15 min.

2.2 | Lightning detection

The characteristics of global lightning activity of the TLC were studied by using data from the European Cooperation for Lightning Detection (EUCLID), a long-range detection system that detects both cloud-to-ground (CG) and intra-cloud (IC) lightning flashes. Schultz *et al.* (2016) evaluated the location accuracy and detection efficiency of EUCLID system in the northwest Mediterranean basin using a 9-yr dataset of observations (2006–2014). Results showed that the location error of EUCLID is of the order of 100–500 m for CG flashes and the detection efficiency is in the order of 70% for CG flashes and about 20% for IC flashes.

3 | EVOLUTION OF THE TLC BETWEEN THE SIXTH AND NINTH OF NOVEMBER 2011

3.1 | Synoptic conditions

Satellite images derived from SEVIRI, specifically from High Resolution Visible (HRV) channel (3.6 μm), between 6 and November 9, 2011 at 12:00 UTC and the estimated track of the TLC are shown in Figure 1. Track positions were produced by the National Oceanic and Atmospheric Administration (NOAA) and the National Environmental Satellite Data and Information Service (NESDIS). Prior to November 6, Balearic Islands were under the influence of an extensive cold-core low pressure system and its profound

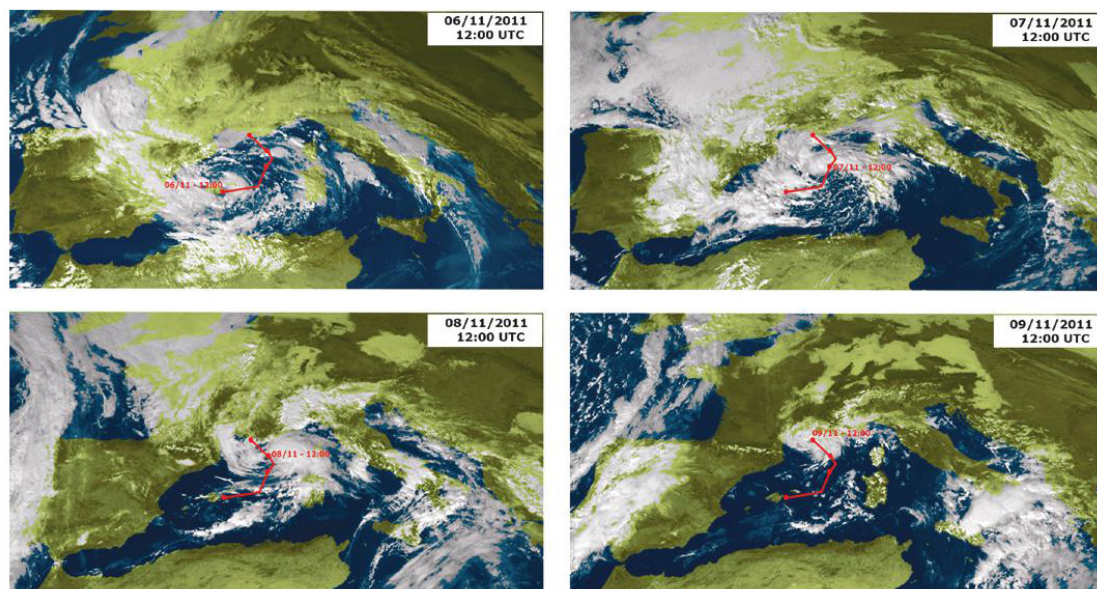


FIGURE 1 Satellite images derived from SEVIRI, high resolution visible (HRV) channel ($3.6 \mu\text{m}$) on-board Meteosat second generation (MSG-2) and cyclone track estimation by NOAA/NESDIS between 6 and November 9, 2011 at 12:00 UTC

cold front reached the northwest coasts of Italy causing tremendous flash floods with 11 confirmed fatalities (information from European Severe Weather Database—ESWD—Dotzek *et al.*, 2009).

The Integrated Forecast System (IFS) analysis data were employed to study an extensive upper-level trough with a slightly positive tilted axis entering the West Mediterranean basin on November 6, 2011, associated with advection of substantial Potential Vorticity (PV) and a jet streak at 300 hPa (not shown). At the surface, a low-pressure system evolved into a baroclinic environment near the Balearic Islands, where deep layer shear was gradually weakening and a weak steering flow at 850 hPa assisted in the formation of a banding convective structure close to the centre of the cyclone (Figure 1). Several studies have shown the significant role of low (high) vertical wind shear regarding the intensification (filling) of the tropical cyclones (e.g., DeMaria and Kaplan, 1994).

On 7 November, the system revealed tropical characteristics such as a warm quasi-symmetric core and convective bands were now wrapped around the centre and became better organized, especially on 8 November (Figure 1). Sea surface temperature (SST) fluctuated from 18°C to 22°C throughout the studied period (buoy reports from NOAA) and ASCAT non-contaminated wind data revealed sustained wind speeds up to 40 kts in the northwest quadrant of the system within 50 km radial distance from the cyclone centre (not shown). It was then the first time since NOAA/NESDIS started monitoring the system, and by using the Dvorak classification technique, classified the TLC as a T3.0 system in

the afternoon of November 8, because convection persisted for an adequate time atop the centre of the cyclone (personal communication with A. Schwartz and M. Turk from NOAA/NESDIS). The peak cyclone intensity took place between 00:00 UTC and 03:00 UTC on November 8 when the minimum sea-level pressure (SLP) was estimated at 991 hPa (NOAA/NESDIS and Miglietta *et al.*, 2013). During the afternoon of November 9, Rolf made landfall in Southeast France (Figure 1), weakened rapidly and was losing its structure. At that time ground meteorological stations reported wind gusts of less than 30 kts in Toulon and Marseille.

3.2 | Evolution of convection characteristics

In Figure 2a, brightness temperature derived from WV6.2 SEVIRI channel and overlapped microwave diagnostics within a 20-min time window, show the convective bands surrounding the centre of the cyclone at 01:15 UTC on November 8. The IR10.8 channel provides insight into the deep convective clouds at the same time (Figure 2b). Convective bands were wrapped around the cyclone centre and microwave diagnostics provide a clear evidence for deep convection development in contrast to IR channel that may provide misleading information about the actual deep moist convection areas due to high-level clouds (e.g., Cirrus canopy) (Olander and Velden, 2009).

Despite the differing fields of view, scan geometries and temporal resolution, of COV and OT, Figure 2 shows that COV values occur roughly at the same location as OT for

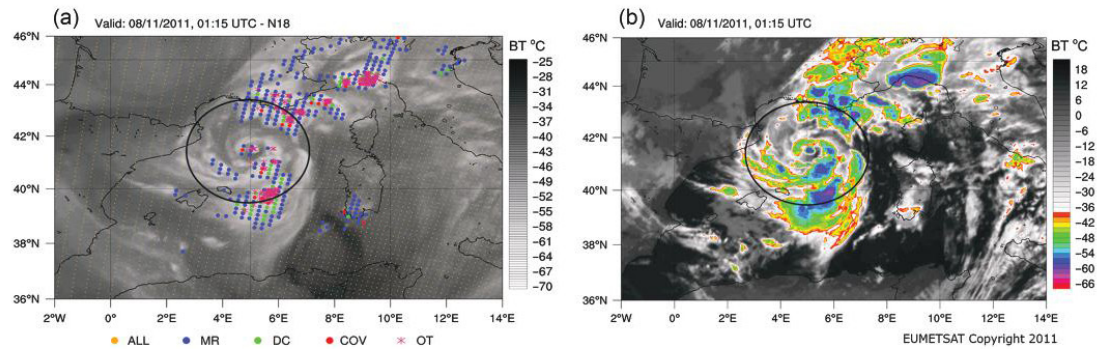


FIGURE 2 (a) Brightness temperature from water vapour (WV6.2) SEVIRI channel overlapped with microwave diagnostics moderate rainfall (MR) (blue), deep convection (DC) (green) and convective overshooting (COV) (red). ALL dots (yellow) refer to the scanning footprint of microwave humidity sounder (MHS) on NOAA 18 satellite. (b) Brightness temperature (false-colour) derived from InfraRed (IR10.8) SEVIRI channel for November 8, 2011 at 01:15 UTC. The circles enclose an area within 200 km from the centre of the Mediane

the same scanning period, giving confidence in the methodology.

The spatial distribution of flashes detected within a radial distance of 200 km from the centre of the TLC, bounded by 25 km annular rings, is shown in Figure 3. Flashes were found at all quadrants, but the maximum density was located northwest of the cyclone centre, with a sum of 2492 flashes from 12:00 UTC November 6 until 12:00 UTC November 9. Moreover, the maximum 1-hr flashing rate was recorded between 23:00 UTC on 6 November and midnight of November 7, about 27 hr before the maximum intensity of the TLC. The study performed by Miglietta *et al.* (2013) showed the highest lightning frequency about 20 hr before the peak of the EUCLID flashes. This could be due to (a) the larger investigated area compared to our study where we focus only to the most intense part of the cyclone and (b) to the efficiency of the lightning detections used, in particular the efficiency of EUCLID to detect IC flashes.

Lightning temporal patterns of the TLC resembled those of tropical cyclones in the oceans rather than Mediterranean cyclones. Galanaki *et al.* (2016) showed that intense cyclones associated with lightning activity present their highest lightning activity on average about 6 hr prior to the maximum intensity, whilst similar studies for tropical cyclones and hurricanes show a temporal lag of 24–30 hr before their maximum intensity (Price *et al.*, 2009; Zhang *et al.*, 2012).

Even though the maximum lightning activity was detected during the late night on 6 November, microwave diagnostics revealed a more active convective activity in terms of DC, MR and COV during the second half of November 7, a few hours before the maximum intensity of the cyclone. In Figure 4 the occurrence of MR, DC and COV is provided, calculated five times per day, approximately at 01:15, 02:15, 13:15, 14:15 and 20:30 UTC. IFS analysis provided the maximum wind speed and SLP data every 3 hr, although the minimum SLP which was estimated by NOAA/NESDIS at 03:00 UTC on 8 November

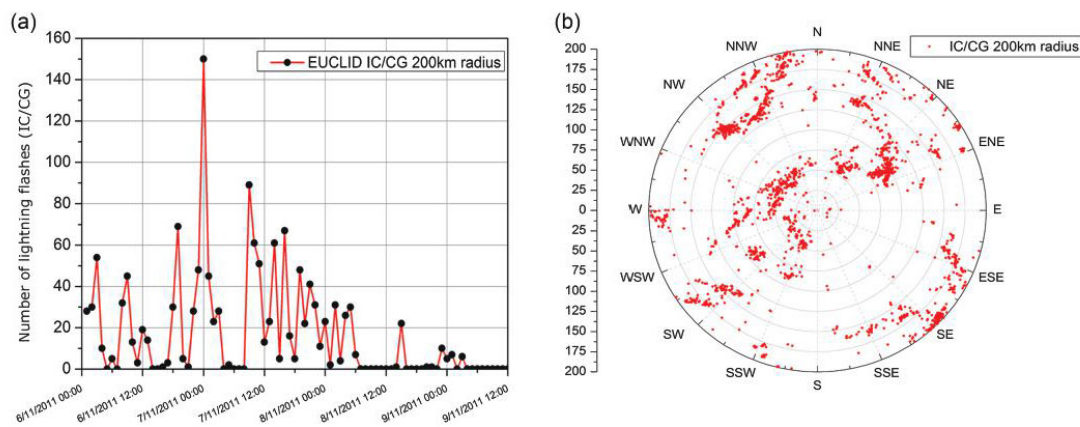


FIGURE 3 (a) Hourly lightning flashes (CG & IC) as detected by the EUCLID system. (b) Azimuthal distribution of lightning flashes in the tropical-like cyclone within a distance of 200 km from cyclone centre between 00:00 UTC on 6 November and 12:00 UTC on November 9, 2011

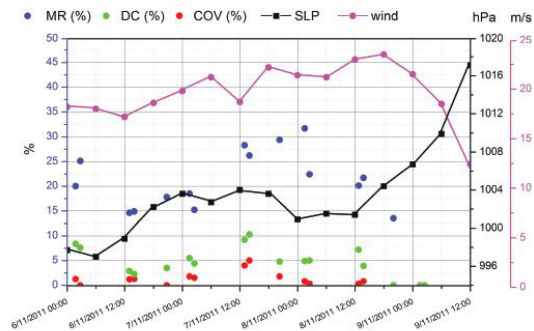


FIGURE 4 Scatterplot of microwave satellite diagnostics occurrence in % for deep convection (DC) (green dots), moderate rainfall (MR) (blue dots), convective overshooting (COV) (red dots) five times per day. Sea-level pressure (SLP—black line) and maximum wind speed (magenta line) were derived from IFS analysis data every 3 hr, between 6 and November 9, 2011

(991 hPa), was underestimated by IFS. The peak of MR occurrence coincided with the maximum intensity of the TLC between 00:00 UTC and 03:00 UTC on 8 November (Miglietta *et al.*, 2013), while DC and COV were mostly detected about 12 hr before that period.

Figure 5 shows the azimuthal distribution of microwave and infrared diagnostics. On 6 November, deep convection is mostly detected further from the cyclone centre (>200 km from the core). On 7 and 8 November, the eyewall region and inner rain-band region precipitation features (<200 km from the core), as defined by MR diagnostic, produce more deep convection (DC) and overshooting tops (COV & OT) than the outer rain-band regions.

There are several examples of asymmetric convection patterns in developing tropical cyclones that have been seen or inferred in observations (e.g., Simpson *et al.*, 1998; Lonfat *et al.*, 2004; Reasor *et al.*, 2005) which are linked with the intensification of tropical storms. The aforementioned studies suggest that DC is distributed mostly close to the

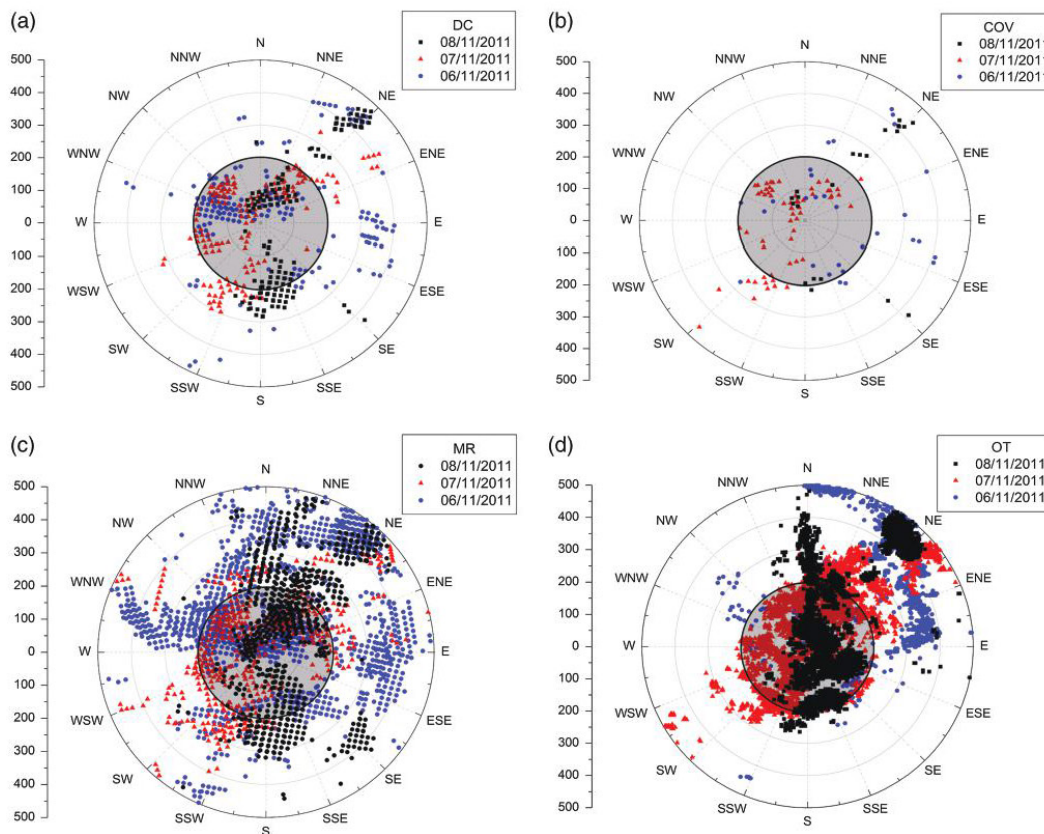


FIGURE 5 Azimuthal distribution of microwave and infrared diagnostics deep convection (DC) (a), convective overshooting (COV) (b), moderate rainfall (MR) (c) and overshooting tops (OT) (d) in the tropical-like cyclone within a distance of 500 km from cyclone centre between 6 and November 8, 2011 (no detection for 9 November). Gray circles show areas within 200 km from the cyclone centre

centre of the tropical cyclones, within 200 km radial distance, rather than at the outer rain-bands like in the Mediterranean cyclones (fronts). The evolution of DC during Rolf has more similarities with tropical cyclones studied over the oceans, rather than their baroclinic Mediterranean counterparts in terms of spatial and temporal characteristics.

4 | SUMMARY

In this paper, we combined, for the first-time, diagnostics from geostationary and polar orbiting satellites to study the evolution of a TLC in the Mediterranean Sea. Our technique provides a unique insight on deep moist convection of the most long-lasting and probably the largest (widest) TLC in the Mediterranean Sea between 6 and November 8, 2011. Lightning activity and convection during this Medicanic deviated from the typical life-cycle of Mediterranean (baroclinic) cyclones and resembled Tropical Cyclones or Hurricanes as studies have documented their behaviour along the storm tracks of the globe.

Our main results are as follows:

- Deep convective clouds penetrating the lowest stratosphere and heavy rainfall peak 0–12 hr before the maximum strength of the cyclone studied, close to the cyclone centre as the cyclone was intensifying on November 8, 2011. In contrast, maximum lightning activity was observed about 27 hr before the minimum SLP with a significant temporal lag between the peak of lightning activity and the maximum DC/COV occurrence.
- Deep convection during a TLC in the Mediterranean was studied in conjunction with OT and DC/COV, providing new insights for the spatial and temporal evolution of deep convection which, along with lightning activity, exhibit more similarities with tropical cyclones over the oceans than with intense Mediterranean cyclones.

Increasing advances in remote sensing enhance our ability to observe moist physical processes, and therefore to evaluate the potential for a depression to undergo a transition to a TLC, based mostly on an estimate of the azimuthally distribution of convection. The observational techniques proposed will be used in more TLC case studies to draw more general conclusions on the convective characteristics of Medicanes. The results of this study will have useful application on validating numerical simulations of TLCs which are planned by the authors in the near future.

ACKNOWLEDGEMENTS

This study was partially sponsored by the Earth2Observe project under grant agreement number 603608, ANR-14-CE01-0014 MUSIC project, the Centre National d'Études Spatiales (CNES) and the Direction générale de

l'armement—Ministère des Armées (DGA). The authors would like to thank A. Schwartz and M. Turk for providing the observational data from NOAA NESDIS. We are also thankful to E. Defer and Meteorage (<http://www.meteorage.fr/>) for making available the lightning data. Meteosat data were retrieved from the Earth Observational Portal of EUMETSAT. MHS data were obtained through the French Mixed Service Unit project ICARE/Climserv/Aeris.

ORCID

Stavros Dafis  <http://orcid.org/0000-0002-1513-1930>

Jean-Francois Rysman  <https://orcid.org/0000-0002-0460-3920>

Chantal Claud  <https://orcid.org/0000-0001-7613-9525>

Emmanouil Flaounas  <https://orcid.org/0000-0001-9769-7817>

REFERENCES

- Claud, C., Alhammoud, B., Funatsu, B.M. and Chaboureau, J.P. (2010) Mediterranean hurricanes: large-scale environment and convective and precipitating areas from satellite microwave observations. *Natural Hazards and Earth System Sciences*, 10, 2199–2213.
- DeMaria, M. and Kaplan, J. (1994) A statistical hurricane intensity prediction scheme (SHIPS) for the Atlantic basin. *Weather Forecasting*, 9, 209–220.
- Dotzek, N., Groenemeijer, P., Feuerstein, B. and Holzer, A.M. (2009) Overview of ESSL's severe convective storms research using the European severe weather database ESWD. *Atmospheric Research*, 93, 575–586.
- Flaounas, E., Raveh-Rubin, S., Wernli, H., Drobinski, P. and Bastin, S. (2015) The dynamical structure of intense Mediterranean cyclones. *Climate Dynamics*, 44, 2411–2427.
- Funatsu, B.M., Rysman, J.F., Claud, C. and Chaboureau, J.P. (2018) Deep convective clouds distribution over the Mediterranean region from AMSU-B/MHS observations. *Atmospheric Research*, 207, 122–135.
- Funatsu, B.M., Claud, C. and Chaboureau, J.P. (2007) Potential of advanced microwave sounding unit to identify precipitating systems and associated upper-level features in the Mediterranean region: case studies. *Journal of Geophysical Research*, 112, D17113. <https://doi.org/10.1029/2006JD008297>.
- Galanaki, E., Flaounas, E., Kotroni, V., Lagouvardos, K. and Argiriou, A. (2016) Lightning activity in the Mediterranean: quantification of cyclones contribution and relation to their intensity. *Atmospheric Science Letters*, 17, 510–516.
- Homar, V., Romero, R., Stensrud, D., Ramis, C. and Alonso, S. (2003) Numerical diagnosis of a small, quasi-tropical cyclone over the western mediterranean: dynamical vs. boundary factors. *Quarterly Journal of the Royal Meteorological Society*, 129, 1469–1490.
- Hong, G., Heygster, G., Miao, J. and Kunzi, K. (2005) Detection of tropical deep convective clouds from AMSU-B water vapor channels measurements. *Journal of Geophysical Research*, 110, D05205. <https://doi.org/10.1029/2004JD004949>.
- Lagouvardos, K., Kotroni, V., Nickovic, S., Jovic, D. and Kallos, G. (1999) Observations and model simulations of a winter sub-synoptic vortex over the Central Mediterranean. *Meteorological Applications*, 6, 371–383.
- Lonfat, M., Marks, F.D., Jr. and Chen, S.S. (2004) Precipitation distribution in tropical cyclones using the tropical rainfall measuring mission (TRMM) microwave imager: a global perspective. *Monthly Weather Review*, 132, 1645–1660.
- Luque, Á., Fita, L., Romero, R. and Alonso, S. (2007) Tropical-like Mediterranean storms: an analysis from satellite. In: *2007 Joint EUMETSAT/AMS Conference, Amsterdam, NL*.
- Michaelides, S., Karacostas, T., Sánchez, J.L., Retalis, A., Pytharoulis, I., Homar, V., Romero R Zanís, P., Giannakopoulos, C., Bühlge, J., Ansmann, A., Merinod, A., Melcón, P., Lagouvardos, K., Kotroni, V., Bruggeman, A., López-Moreno, J.L., Berthet, C., Katragkou, E., Tymvios, F., Hadjimitsis, D.G., Mamouri, R.E. and Nisantzi, A. (2017) Reviews and perspectives of high impact atmospheric processes in the Mediterranean. *Atmospheric Research*, 208, 4–44.

- Miglietta, M.M., Laviola, S., Malvaldi, A., Conte, D., Levizzani, V. and Price, C. (2013) Analysis of tropical-like cyclones over the Mediterranean Sea through a combined modeling and satellite approach. *Geophysical Research Letters*, 40, 2400–2405.
- Olander, T.L. and Velden, C. (2009) Tropical cyclone convection and intensity analysis using differenced infrared and water vapor imagery. *Weather and Forecasting*, 24, 1558–1572.
- Price, C., Asfur, M. and Yair, Y. (2009) Maximum hurricane intensity preceded by increase in lightning frequency. *Nature Geoscience*, 2, 329–332.
- Reasor, P.D., Montgomery, M.T. and Bosart, L.F. (2005) Mesoscale observations of the genesis of hurricane Dolly (1996). *Journal of the Atmospheric Sciences*, 62, 3151–3171.
- Rysman, J.F., Claud, C., Chaboureau, J.P., Delanoë, J. and Funatsu, B.M. (2016) Severe convection in the Mediterranean from microwave observations and a convection-permitting model. *Quarterly Journal of the Royal Meteorological Society*, 142, 43–55.
- Rysman, J.F., Claud, C. and Delanoë, J. (2017) Monitoring deep convection and convective overshooting from 60° S to 60° N using MHS: a Cloudsat/CALIPSO-based assessment. *IEEE Geoscience and Remote Sensing Letters*, 14, 159–163.
- Schmetz, J., Tjemkes, S., Gube, M. and Van de Berg, L. (1997) Monitoring deep convection and convective overshooting with Meteosat. *Advances in Space Research*, 19, 433–441.
- Schultz, W., Diendorfer, G., Pedeboy, S. and Poelman, D.R. (2016) The European lightning location system EUCLID – part 1: performance analysis and validation. *Natural Hazards and Earth System Sciences*, 16, 595–605.
- Simpson, J., Halverson, J.B., Ferrier, B.S., Petersen, W.A., Simpson, R.H., Blakeslee, R. and Durden, S.L. (1998) On the role of “hot towers” in tropical cyclone formation. *Meteorology and Atmospheric Physics*, 67, 15–35.
- Zagrodnik, P.J. and Jiang, H. (2014) Rainfall, convection and latent heating distribution in rapidly intensifying tropical cyclones. *Journal of the Atmospheric Sciences*, 71, 2789–2809.
- Zhang, W.J., Zhang, Y.J., Zheng, D. and Zhou, X.J. (2012) Lightning distribution and eyewall outbreaks in tropical cyclones during landfall. *Monthly Weather Review*, 140, 3573–3586.

How to cite this article: Dafis S, Rysman J-F, Claud C, Flaounas E. Remote sensing of deep convection within a tropical-like cyclone over the Mediterranean Sea. *Atmos Sci Lett*. 2018;19:e823. <https://doi.org/10.1002/asl.823>

2.3.3 Introduction of the article “Insights into the convective evolution of Mediterranean tropical-like cyclones”

After the observational study performed on the MTLC ROLF and the results that show important differences in the temporal and spatial distribution of DC against the typical extratropical cyclones in the Mediterranean, an extended study on a larger sample of MTLCs is needed. For this reason, 9 MTLCs between 2005 and 2018 are chosen to be investigated in detail, after searching for many previously documented MTLCs in the literature. First, since the second generation of Meteosat satellites (MSG) provides homogenous observations of brightness temperature since 2002 with a time step of 15 minutes, we started searching for closed cloud curvatures and circular cloud patterns (see more in paragraph 2.2.5) during previously documented MTLCs (e.g., Miglietta et al., 2013). Unfortunately, most of the time, satellite imagery in the IR spectrum does not provide cloud patterns able to indicate a continuous manual track of the MTLCs, except for the presented 9 cases in this study. Moreover, the chosen 9 MTLCs have a duration of more than one diurnal cycle and most of them have an important impact on the affected areas. In addition, since the emphasis of this thesis is put on the MTLCs that develop in the Eastern Mediterranean, 7 out of the 9 MTLCs presented here develop or spend their mature phase in Central-Eastern Mediterranean.

One major challenge to perform such an analysis was the detection of the DC activity based on observations in the infrared spectrum, with satellite data derived from SEVIRI (see paragraph 2.2.2) and the visual analysis of thousands of satellite pixels into compact graphs in order to better discriminate the areas with very active DC activity versus the areas with limited DC. After several trials, the best method was the construction of radial plots (polar coordinates) with an azimuthal distribution of DCPIXELS calculated every 30 minutes, and time-radius plots of the sum of azimuthally distributed DCPIXELS. A second challenge was the computation of vortex tilt, a variable which has never been computed before for the MTLCs and with only a few studies having considered it before in studies for cyclones in general. Taking into account the relatively shallow warm cores of the MTLCs, the maxima of relative vorticity at 950 and 500 hPa are computed from ERA5 numerical fields, and the vortex tilt is calculated based on their relative displacement. Finally, the vertical wind shear between 850 and 300 hPa is computed in order to investigate the relationship between DC organization and the magnitude of DC activity with the magnitude and direction of vertical wind shear. The vertical wind shear is closely connected with baroclinic environments and previous studies have implied its negative correlation with DC activity and MTLC intensity (e.g., Tous and Romero, 2013). To this end, the following scientific article shows the evolution of the vortex tilt, vertical wind shear and the distribution of DCPIXELS during 9 MTLCs. Furthermore, it proposes a classification of the MTLCs in 3 groups according to the position of intense DC activity related to the vertical wind shear and the changes in intensity of the surface cyclones.

2.3.4 Article “Insights into the convective evolution of Mediterranean tropical-like cyclones”

Received: 18 February 2020 | Revised: 24 August 2020 | Accepted: 25 August 2020

DOI: 10.1002/qj.3896

Quarterly Journal of the
Royal Meteorological Society 

RESEARCH ARTICLE

Insights into the convective evolution of Mediterranean tropical-like cyclones

Stavros Dafis^{1,2}  | Chantal Claud¹ | Vassiliki Kotroni² | Konstantinos Lagouvardos² | Jean-François Rysman¹¹LMD/IPSL, CNRS UMR 8539, École Polytechnique, Université Paris Saclay, ENS, PSL Research University, Sorbonne Universités, Palaiseau, France²National Observatory of Athens, Institute for Environmental Research and Sustainable Development, Athens, Greece**Correspondence**Stavros Dafis, LMD/IPSL, CNRS UMR 8539, École Polytechnique, Université Paris Saclay, ENS, PSL Research University, Sorbonne Universités, UPMC Univ Paris 06, Palaiseau, France.
Email: sdafis@lmd.polytechnique.fr**Funding information**

Direction générale de l'armement - Ministère des Armées; National Observatory of Athens

Abstract

This study aims at understanding how deep convection is organized and contributes to the intensification of nine Mediterranean tropical-like cyclones which developed between 2005 and 2018. Through a multi-satellite approach, a combination of infrared and microwave diagnostics provides insights into the temporal and spatial evolution of deep convection. ERA5 reanalysis complements the remote-sensing observations and is used to compute the vertical wind shear and vortex tilt to investigate their interactions with deep convection. Results show that vertical wind shear and topography have an important impact on the organization of deep convection and the symmetry of the cyclones. Only a fraction of these cyclones experienced intense convective activity close to their centres and we show that persistent deep convection in the upshear quadrants led to intensification periods. Convective activity solely in the downshear quadrants was not linked to intensification periods, while short-lived hurricane-like structures develop only during symmetric convective activity, leading to cyclone intensification in some of the cases. Finally, a classification of the Mediterranean tropical-like cyclones is proposed based on the evolution of deep convection and their intensification periods.

KEYWORDS

deep convection, Mediterranean, remote-sensing, subtropical cyclones, tropical-like cyclones, wind shear

1 | INTRODUCTION

The Mediterranean Sea is a well-known hot-spot for cyclogenesis with hundreds of cyclones of variable structure, lifetime and intensity forming every year (Petterssen, 1956; Trigo *et al.*, 1999; Ulbrich *et al.*, 2012; Flaounas *et al.*, 2015; Lionello *et al.*, 2016). Potential vorticity (PV) streamers, which intrude high-PV stratospheric air into the lower

atmosphere, and intense cyclogenesis have been proven as important precursors of strong Mediterranean cyclones (Raveh-Rubin and Flaounas, 2017) even though their size, intensity and lifetime are inferior to other extratropical cyclones (Čampa and Wernli, 2012). A small fraction of these cyclones exhibit characteristics similar to tropical cyclones (TCs), for example, a deep warm core, an axisymmetric structure with a windless centre (the “eye”) and

sustained wind speeds close to hurricane-force strength. Mediterranean Tropical-Like Cyclones (MTLCs) can pose a serious threat to populated coastal areas by producing all kinds of severe weather, but also resulting in heavy dust transport from Africa towards Europe (Fita and Flaounas, 2018) and leading to sea-surface changes which can last for several days or weeks. These changes include the rapid decrease of sea-surface temperature (Noyelle *et al.*, 2019) or phytoplankton blooms with comparable magnitude to hurricane cases (Kotta and Kitsiou, 2019). Climatological studies suggest that in a warming climate, even though the number of occurrence of MTLCs will remain stable, their intensity may increase dramatically as well as their lifetime (Cavicchia and von Storch, 2012; Walsh *et al.*, 2014; Romera *et al.*, 2017; Romero and Emanuel, 2017; González-Alemán *et al.*, 2019).

A long-term and still active debate about this group of Mediterranean tropical-like cyclones (MTLCs or “medicanes”) is based on the different mechanisms responsible for their development which have links to extratropical and tropical cyclone theory (Shapiro and Keyser, 1990; Emanuel, 2005; Miglietta and Rotunno, 2019). The contributions of baroclinic and diabatic processes are not well understood and despite several studies trying to quantify the contribution of convection in the intensification of MTLCs, no consensus has emerged. In particular, it is difficult to assess the relative importance of convection versus baroclinic instability because MTLCs develop first as typical extratropical cyclones in baroclinic environments and then experience tropical transition (TT) through tropospheric heating (Davis and Bosart, 2003). A key contributor to the large variability of structures seen in MTLCs is the influence of diabatic heating by convection. The fluxes of heat and moisture from the sea to the atmosphere can result in a large latent-heat release within developing MTLCs. However, it is also known that latent-heat release can interact with the baroclinic dynamics in a strongly nonlinear way (Kuo *et al.*, 1991; Stoelinga, 1996). The generally accepted model for the formation of an MTLC is the development of a low-level cyclone as a response to an upper-level PV anomaly and a surface baroclinic zone, a process that is observed in the majority of Mediterranean cyclones. As a second stage, the low-level PV (LPV) anomaly generated by diabatic processes becomes important and interacts with the baroclinicity at low levels (Miglietta *et al.*, 2017). Vertical motions are induced by the LPV anomaly embedded in baroclinic shear. This contributes to the further generation of LPV through latent-heat release in moist ascent, related to the intensification mechanism proposed by Montgomery and Farrell (1992). More recent numerical studies have addressed the importance of the diabatic production of latent- and sensible-heat release in

mid-troposphere through convection during warm seclusions in the Mediterranean (Tous and Romero, 2013; Mazza *et al.*, 2017), similar to other cyclogenetic areas (e.g. Posselt and Martin, 2004). Moreover, despite the presented conceptual framework for the formation of MTLCs, additional factors dictate their genesis, such as the presence and intensity of deep convection (DC), the differential surface friction and the uneven topography of the Mediterranean which complicate further any attempt to categorize the cyclones within strict boundaries.

Very few studies exist in the literature dedicated to the convective evolution and the environments of MTLCs from an observational point of view. Claud *et al.* (2010), Miglietta *et al.* (2013) and Dafis *et al.* (2018) used a combined approach with infrared and microwave diagnostics to show that DC occurrence in MTLCs peaks several hours before the maximum strength of the cyclones, showing a longer time lag than in strong extratropical Mediterranean cyclones (Galanaki *et al.*, 2016) and more similar characteristics with TCs. Other studies have tried to explain the convective structure of these cyclones with numerical simulations (e.g. Lagouvardos *et al.*, 1999; Pytharoulis *et al.*, 2000; Emanuel, 2005; Tous *et al.*, 2012; Carrió *et al.*, 2017). Winstanley (1970) was probably the first to investigate an MTLC as a deep Mediterranean cyclone just north of Libya on 23 September 1969 which was responsible for severe flash floods in Tunisia and Algeria, with nearly 600 casualties and 250,000 people left homeless. The convective and persistent nature of precipitation was highlighted, as well as the presence of a quasi-symmetrical cloud-free centre (an “eye”) visible in satellite images (see their figure 7c) giving evidence for a warm-core cyclone with an axisymmetric structure. The first reference to warm-core cyclones in the Mediterranean was introduced by Ernst and Matson (1983) while a few years later, Rasmussen and Zick (1987) studied a sub-synoptic warm-core vortex and compared the environment and the cyclone dynamics with polar lows. They used the first Meteosat satellite data to observe DC around the cyclone and argued that DC was most pronounced at the early stages of the cyclone, before the formation of an “eye”. Claud *et al.* (2010) studied the convective evolution and precipitation of three MTLCs in the west and central Mediterranean and showed that deep convective clouds and rainfall preceded the maximum intensity of the cyclones. Miglietta *et al.* (2013) also came to similar results by investigating 14 MTLCs with a combined satellite-monitoring and modelling approach. The evolution of DC and lightning activity of the MTLC “ROLF” in 2011 was studied by Dafis *et al.* (2018), who showed that the convective evolution of the cyclone shares more similar characteristics with TCs than intense extratropical Mediterranean cyclones.

The rapid advances in remote sensing of the Earth from space in the past two decades have made it possible to observe cyclones worldwide in great detail and with an increasing spatial and temporal resolution (Tourville *et al.*, 2015). Even though the temporal availability of polar-orbiting satellites in the midlatitudes is limited to a few overpasses per day, they complement the geostationary satellites which provide rapid-scans of the atmosphere. The most commonly used approach to indicate the presence, the intensity and the fractional coverage of deep convective clouds is based on the use of infrared (IR) brightness temperature (BT) provided by geostationary satellites in high temporal and spatial resolution. Most authors (e.g. Chen and Houze, 1997; Yang and Slingo, 2001; Machado *et al.*, 2002; Wilcox, 2003; Tian *et al.*, 2004; Hong *et al.*, 2006; Wu and Ruan, 2016) define a threshold for IR10.8 μm BTs between 230 and 240 Kelvin under which it is assumed DC will be observed. One major drawback in adopting this method is the lack of discrimination between high-level clouds (e.g. cirrus, cirrostratus) and convective clouds, especially in their developing stage. Moreover, the analysis of microwave (MW) satellite imagery from polar-orbiting satellites which have the ability to detect and measure liquid and frozen hydrometeors, even in the lowest parts of the troposphere, has also been utilized by several studies to detect DC (Hong *et al.*, 2005; 2008; Claud *et al.*, 2010; Harnos and Nesbitt, 2011; Alvey *et al.*, 2015; Harnos and Nesbitt, 2016; Rysman *et al.*, 2016; 2017; Fischer *et al.*, 2018).

The current study uses a novel approach to investigate the DC evolution of nine MTLCs spanning between 2005 and 2018, through a multi-satellite approach with an objective of better understanding the contribution of convection to the intensification of these cyclones. Moreover, the European Centre for Medium-range Weather Forecasts (ECMWF) ERA5 reanalysis is utilized, combined with satellite retrievals, to investigate the influence of vertical wind shear (VWS) on convective and cyclone asymmetries, and to explore the steering mechanisms of DC during the different stages of their evolution. Section 2 contains a brief discussion of the nine MTLCs studied, the manual tracking method, as well as the satellite data used for detecting DC and the ERA5 data. In Section 3, we describe how DC is organized in MTLCs and what the role of VWS is in the structural response of the cyclones and the position of DC activity. The main findings and possible future work are discussed in Sections 4 and 5 respectively. Supporting information Appendix S1 provides a more detailed description of the manual tracking procedure and *in situ* observations during the MTLCs, with special focus on ERA5 performance in reproducing the cyclones' intensity.

2 | DATA AND METHODS

2.1 | Cases and tracks

Given the lack of a clear definition for the MTLCs and the lack of a general consensus about the number of cyclones that experience TT in the Mediterranean, let alone the absence of an analogous dataset to the Tropical Cyclone Best Track, the choice of the most representative MTLCs is not trivial. For the present study, nine previously identified MTLCs have been chosen between 2005 and 2018 among other cases in the literature (e.g. Miglietta *et al.*, 2013) with a variable size, intensity and duration, because for them the manual tracking of the cyclone centre could be performed with high confidence. In addition, the study period was chosen to start in 2005 when the second generation of Meteosat satellites was available, providing spatial and temporal homogeneity to the satellite data. More details about the manual tracking and how the trajectories were built are presented in Supporting information S1 in Appendix S1.

Table 1 presents the nine selected case-studies of MTLCs spanning between 2005 and 2018, with dates and duration indicating the periods for which a manual tracking of the cyclones was performed, whereas their total lifetime, mostly as extratropical cyclones at earlier stages, was longer (Di Muzio *et al.*, 2019). For the manual tracking of the cyclones, the High-Resolution Visible (HRV) and the IR channels of the Spinning Enhanced Visible and Infrared Imager (SEVIRI) were used, available every 5 min through the Rapid Scanning Service (RSS) or every 15 min (RSS is available since 2008). The maximum cyclone intensity, for both the maximum wind speed and the minimum sea-level pressure (SLP) was derived either from *in situ* observations or ERA5 reanalysis data. The distance that cyclones covered during their lifetime and their mean propagation speed were estimated by the manual satellite-tracking. Additional information about the ERA5 performance, compared to the *in situ* observations used, can be found in Supporting information S2 in Appendix S1.

Figure 1 shows the cyclone-centre position according to the hourly ERA5 reanalysis based on SLP minimum location and the observed tracks. For most of the cases, the mean cyclone position error in ERA5 is less than 50 km, except for *Med2006* and *ROLF* when the model was not able to accurately reproduce the cyclone track. It is worth mentioning that the model was able to reproduce the erratic loops of the cyclones (e.g. *Med2005* and *QEN-DRESA* in Figure 1), a feature that was not simulated in previous reanalysis datasets (e.g. NCEP and ERA-Interim, see Pytharoulis *et al.* (2017)).

TABLE 1 An overview of the nine MTLCs used for this study, showing the duration of the manual tracking in hours, the maximum 10 m wind speed ($\text{m}\cdot\text{s}^{-1}$) and SLP (hPa) either by *in situ* observations or derived by ERA5 (asterisked)

	Dates (duration hr)	Max 10 m wind ($\text{m}\cdot\text{s}^{-1}$)	Min SLP (hPa)	Distance covered (km)	Mean propagation speed ($\text{m}\cdot\text{s}^{-1}$)
Med2005	15 December 2005 (44)	40	979	1850	11.5
Med2006	26 September 2006 (15)	40	986	350	10.4
Med2007	16 November 2007 (24)	20*	998	470	5.6
ROLF	06–09/11/2011 (60)	21	991	960	4.5
ILONA	22 January 2014 (26)	17	990	440	4.8
QENDRESA	07–08/11/2014 (26)	43	978	660	7.4
TRIXIE	31 October 2016 (60)	31	999	972	4.5
NUMA	19 November 2017 (54)	30	998	711	3.7
ZORBAS	29 September 2018 (48)	33	987	933	5.5

Note: The distance covered (km) by the cyclones and the mean propagation speed ($\text{m}\cdot\text{s}^{-1}$) were calculated from the manual tracking.

2.2 | Detecting deep convection with SEVIRI and AMSU-B/MHS

In order to detect DC using SEVIRI, a similar method to Olander and Velden (2009) is used. This method relies on the channel differencing between the water vapour channel $\text{WV}6.2\ \mu\text{m}$ and the window channel $\text{IR}10.8\ \mu\text{m}$ (ΔBT) of SEVIRI pixels used at the nominal spatial resolution of about 3 km. Typically during clear-sky conditions, the $\text{IR}10.8$ channel has a peak spectral response close to or at the surface of the Earth, while the $\text{WV}6.2$ channel peaks at about 350 hPa, thus ΔBT is typically negative. In the presence of opaque and convective clouds, this spectral response can change significantly and even reverse. During intense DC, important amounts of WV can be transported in the upper troposphere or lower stratosphere where it is re-emitted at higher temperatures in the $\text{WV}6.2$ channel than in the window channel (Schmetz *et al.*, 1997). Positive ΔBT ($\text{WV}6.2 - \text{IR}10.8 > 0$) values are attributed to convection penetrating the tropopause but not necessarily collocated with cloud overshoots (Setvak *et al.*, 2007; Chung *et al.*, 2008; Bedka *et al.*, 2010), as WV can remain in the lowest stratosphere for several hours. Not all convective clouds do penetrate the tropopause, but all of them can contribute to the warming of the middle troposphere through condensational heating and release of latent heat. In order to detect the DC in IR data, pixels accounted as containing deep convective clouds must meet the criterion of ΔBT greater than or equal to $-10\ \text{K}$. The $-10\ \text{K}$ ΔBT threshold was chosen to be representative of DC after additional analysis of collocating SEVIRI data with DC diagnostics calculated with passive microwave data.

The three humidity sounding channels around 183 GHz provided by the cross-scanning Microwave

Humidity Sounder (MHS) and the Advanced Microwave Sounding Unit (AMSU-B) on board National Oceanic and Atmospheric Administration (NOAA) and Meteorological Operational (MetOp) polar-orbiting satellites are sensitive to frozen hydrometeors and thus can detect DC. More specifically, the DC detection algorithm of Hong *et al.* (2005) was used to detect areas covered with deep convective clouds, which has been extensively used and validated in the Mediterranean (e.g. Funatsu *et al.*, 2007; 2018; Rysman *et al.*, 2016; 2017; Dafis *et al.*, 2018). For the current study, we make use of three diagnostics for detecting convective clouds: the Deep Convection (DC), the Moderate Rainfall (MR) and the Convective Overshooting (COV) (Hong *et al.*, 2005; Funatsu *et al.*, 2007). Both DC and COV indicate deep convective clouds while MR corresponds to intense convective rainfall (Funatsu *et al.*, 2007; Alhammoud *et al.*, 2014). The DC detections are always included in the MR, and COV indicates areas with very strong DC activity with overshooting tops. From now on, in order to define areas covered by DC, the SEVIRI ΔBT values above $-10\ \text{K}$ will be referred to as “DCPIXELS”, and the MR - DC diagnostics calculated from MW sounder retrievals combined will be referred to as “MWDC”.

2.3 | Calculating vertical wind shear with ERA5

The VWS was calculated using the ERA5 gridded analyses ECMWF provided by the Copernicus Climate Data Store. The ERA5 dataset is available hourly on a $0.25^\circ \times 0.25^\circ$ latitude–longitude grid and with 37 vertical pressure levels. The calculations to derive the vertical deep-layer shear (DLS) follow Hanley *et al.* (2001), and Corbosiero and Molinari (2002), for example, by computing the mean

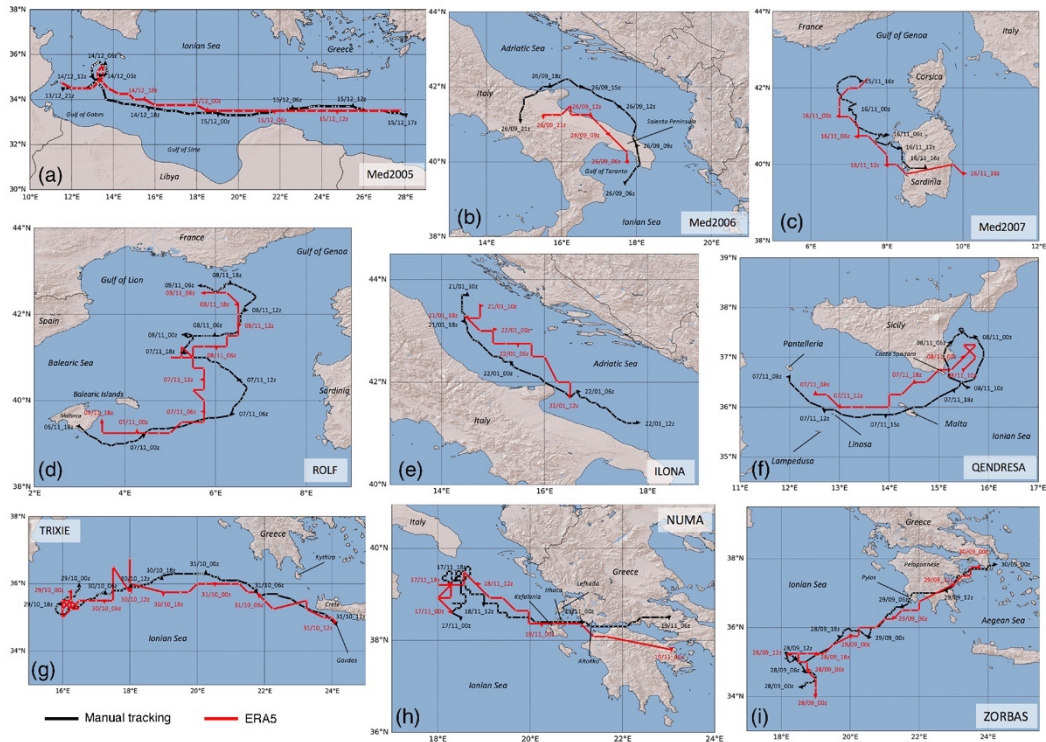


FIGURE 1 The nine observed cyclone tracks (black) plotted every 30 min (position with white dots) and the tracks based on the position of minimum SLP from ERA5 plotted every 1 hr (red). The main geographical features mentioned in the text are annotated. Hour is dd/mm_hhZ (UTC) [Colour figure can be viewed at [wileyonlinelibrary.com](https://onlinelibrary.com)]

wind components on a cylindrical area-weighted average between 850 and 300 hPa every 1 hr over a radius of 200 km. However, given the smaller extent of the MTLCS, the radius of the cylinder was chosen to be much smaller than the aforementioned studies for the TCS, as well as the upper-level boundary for the computation of DLS which is lower (i.e. 300 hPa), in order to avoid pressure levels in the stratosphere above the Mediterranean during autumn and winter months. Moreover, the gridded analyses were not interpolated on the observed storm tracks given the small average position errors between the ERA5 and the observed storm-centre positions (Figure 1). For the current study, the terminology regarding shear will be as follows: the direction of the DLS vector will be referred to as downshear and the opposite direction as upshear. Moreover, in order to assess the impact of DLS on the cyclone structure, the vortex tilt was defined as the horizontal displacement between the local maxima of 950 and 500 hPa cyclonic circulations within 200 km of the cyclone centre every 1 hr. Even though ERA5 has higher spatial resolution than previous reanalysis datasets, it may not

be fully adequate to realistically simulate the structure and intensity of the MTLCS (Zhang *et al.*, 2020) and even numerical simulations with higher spatial resolution provide different results regarding the structure and intensity of MTLCS (e.g. Ragone *et al.*, 2018). Nevertheless, ERA5 is able to reproduce the cyclone trajectories better than previous reanalyses in terms of deviation from observed tracks, and simulates the formation of warm-core structures within the MTLCS studied. Additional analyses for the nine studied MTLCS were also performed to derive the vertical extent of the vortex core axis (not shown) to check the calculations of ERA5 vortex tilt.

3 | RESULTS

3.1 | An overview of deep convection activity in MTLCS

By collecting the DCPIXELS detected by SEVIRI every 30 min, we can estimate the occurrence of DC during

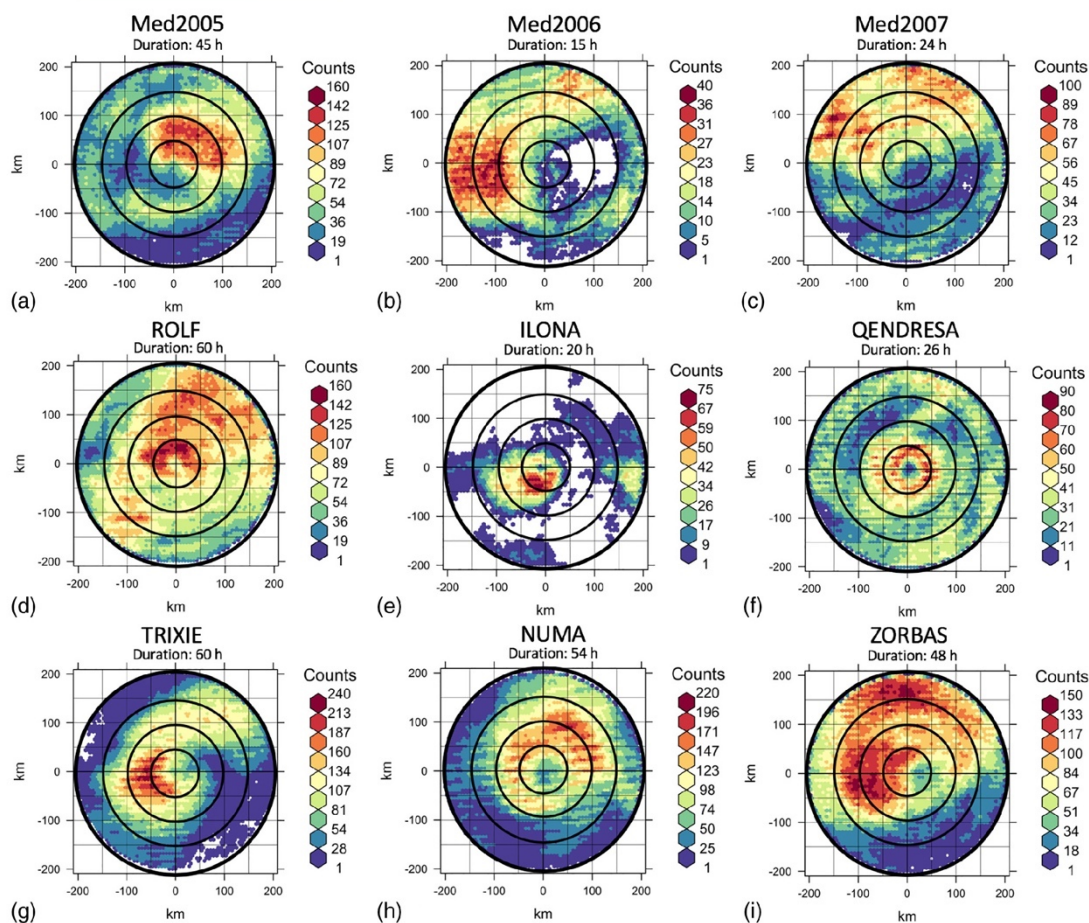


FIGURE 2 Composite azimuthal distribution of aggregated DCPIXELS using the complete lifetime of each MTL. The shade is the relative occurrence of DC for each individual case (note that the legend is not the same for each case). Top: (a) *Med2005*, (b) *Med2006* and (c) *Med2007*. Middle: (d) *ROLF*, (e) *ILONA* and (f) *QENDRESA*. Bottom: (g) *TRIXIE*, (h) *NUMA* and (i) *ZORBAS* [Colour figure can be viewed at wileyonlinelibrary.com]

the manual tracking of the cyclones. Figure 2a-i show the counts of DCPIXELS within 200 km radius from the MTLs' centres detected during the whole periods of manual tracking as if we follow the cyclones from above (bird's-eye view). In addition, Figure 3a-i provide an overview of the temporal evolution of DC occurrence by aggregating the DCPIXELS around the cyclones. These two graphs summarize the DC activity and allow a comparison for the spatial distribution and temporal evolution of DC.

Starting with *Med2005*, DC was present in all four quadrants, but mostly concentrated in the north part of the cyclone during the first 5 hr of manual tracking, from 13 December 2005, 2100 UTC (Figures 2a and 3a). An

important weakening of DC was noticeable in the following 12 hr, especially close to the cyclone centre (Figure 3a). This period was characterized by a strong deepening and intensification of the cyclone according to ERA5 and to the study of Fita and Flaounas (2018). The remaining 28 hr until the end of cyclone life, the cyclone was moving fast eastwards and DC was concentrated within the first 100 km, at the north-northeastern parts (Figure 2a), having two peaks around 1700 UTC 14 December and 0700 UTC 15 December 2005 (Figure 3a). In the morning of 15 December 2005, brief periods of semicircular patterns of DC around the centre resulted in a cloud-free area with a radius of 20 km from the centre. After 15 December 2005, 1500 UTC, DC was not present within 100 km from the

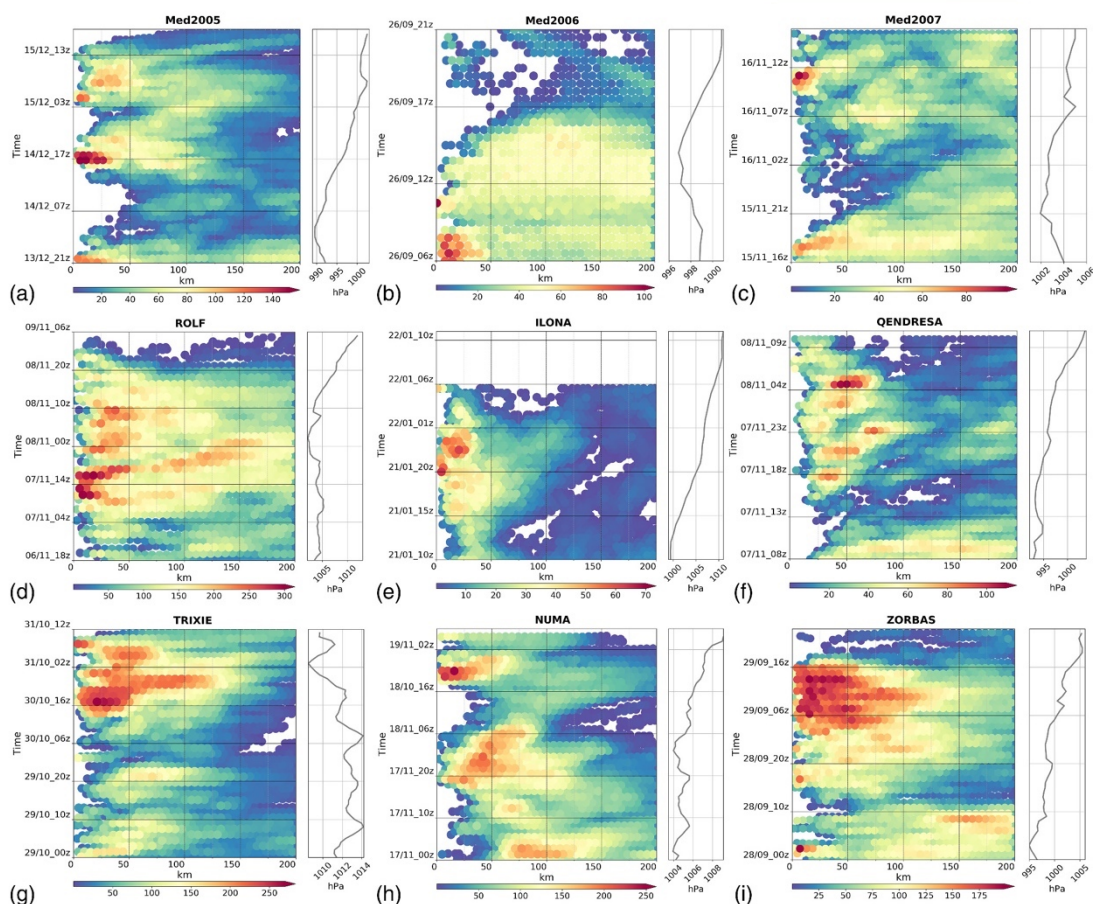


FIGURE 3 Composite distribution of aggregated DCPIXEL normalized by the distance from the cyclone centre every 30 min and time series of SLP minima by ERA5 every 1 hr (black line). The shade is the relative occurrence of DC for each individual case (note that the legend is not the same for each case). Top: (a) *Med2005*, (b) *Med2006* and (c) *Med2007*. Middle: (d) *ROLF*, (e) *ILONA* and (f) *QENDRESA*. Bottom: (g) *TRIXIE*, (h) *NUMA* and (i) *ZORBAS* [Colour figure can be viewed at wileyonlinelibrary.com]

cyclone centre and only shallow clouds were detected by the IR channels of SEVIRI (BTs higher than 245 K) until 1800 UTC east of 27°E (Figure 1a).

The *Med2006* case had a much shorter lifetime and smaller size than *Med2005*, but the greater impact in terms of damage onshore (Moscatello *et al.*, 2008a; Davolio *et al.*, 2009). The manual tracking of the cyclone using SEVIRI was possible after 26 September 2006, 0600 UTC, when it was embedded in a cold front producing a strong line of convection (Chaboureau *et al.*, 2012). Figure 3b shows that when the cyclone was in the Gulf of Taranto between 0600 UTC and 0900 UTC (Figure 1b), that is, between 0600 and 0900 UTC 26 September 2006 (Figure 3b), DC was concentrated close to the centre. When the MTLIC moved onshore between 0900 UTC and

1000 UTC, DC gradually weakened, especially close to the cyclone centre. When the cyclone left the coasts of Salento Peninsula and entered the Adriatic Sea after 1000 UTC, DC was almost absent within the first 50 km from the centre (e.g. 1700 UTC in Figure 3b). DC remained active between 50 km and 200 km from the centre, with a peak of occurrence in the west side of the cyclone (Figure 2b) between 1400 and 1600 UTC (Figure 3b) but the eastern side was free of DC within 50–150 km radius (Figure 2b) as a dry slot from east-southeast was evident in the WV6.2 channel of SEVIRI (not shown). In the HRV channel, an eye-like structure was visible between 1200 and 1800 UTC but no DC was detected, as the cloud-top IR10.8 BTs were warmer than 250 K. Eventually, the cyclone reached the mainland of Italy again at 1800 UTC and gradually dissipated.

On 15 November 2007, an Alpine lee cyclogenesis occurred in the Gulf of Genoa, and the surface cyclone (Med2007) experienced TT while moving south towards Sardinia, according to McTaggart-Cowan *et al.* (2010). The tracking of the cyclone in our study, started on 15 November 2007, 1600 UTC at 42.2°N, 7.35°E, about 150 km north-west from Corsica (Figure 1c). During the first 4 hr until 2000 UTC, DC was important in the northern and western parts of the cyclone, even close to the centre (Figures 2c and 3c), but in the following 7 hr until 0300 UTC, DC was not detected within the first 50 km from the cyclone centre (Figure 3c). In fact, DC was only pulsating far away from the centre and only in the northern parts, close to the coasts of France. The first 50 km from the cyclone centre remained DC-free until the early morning on 16 November 2007, when a new round of convective activity with isolated storm cells began after 0600 UTC (Figure 3c) when the cyclone was approaching Sardinia (Figure 1c). The cyclone centre remained offshore but within 20 km of the west coasts of Sardinia until 1400 UTC, with small and scattered convective clouds being found in all quadrants. The cyclone lost its structure moving onshore after 1500 UTC and the manual tracking was not possible after 1600 UTC 16 November 2007.

The cyclone “*ROLF*” was the longest-lasting and probably the most intense case of MTLC until 2011 according to Dafis *et al.* (2018). Tracking of the cyclone started on 6 November 2011, 1800 UTC when it was over Mallorca (Figure 1d), when DC was very active close to the cyclone centre, as well as further away, covering the largest part of the Balearic Sea. DC continued to be active until the peak of occurrence on 7 November 2011 between 1300 UTC and 1700 UTC (Figure 3d). Figure 2d shows that DC was mostly detected close to the cyclone centre, in almost all quadrants, with storm initiation close to the centre and cyclonic outward expansion of convective clouds (i.e. between 0600 and 2300 UTC 7 November 2011 in Figure 3d). After the maximum intensity of the cyclone on 8 November 2011, 0300 UTC according to ERA5, DC remained very active mostly in the southern and eastern parts. In the morning of 8 November 2011 (Figure 3d), a large mesoscale convective system (MCS) developed in the eastern parts of the cyclone and it was wrapped cyclonically into the circulation, lasting for nearly 12 hr. This MCS is responsible for the high number of DCPIXELS in Figure 2d in the northern flank of the cyclone. After 1800 UTC 8 November 2011, DC gradually disappeared from the satellite detections and until 9 November 2011, 0600 UTC, only a cyclonic circulation of shallow clouds was evident in the satellite imagery.

The MTLC case of “*ILONA*” is described thoroughly in Cioni *et al.* (2016). In the present study, the manual tracking of the cyclone was not possible during its whole

lifetime given the absence of a well-defined cyclone centre. The manual tracking started on 21 January 2014, 1000 UTC when the cyclone was over the Adriatic Sea, and its centre was at 43.7°N, 14.5°E (Figure 1e) where a TT took place according to Cioni *et al.* (2016). The size of this MTLC was exceptionally small compared to the rest of the studied cyclones, with DC being detected only within 100 km from the centre and being mostly active within the first 25 km (Figures 2f and 3f) with a constant cyclone weakening according to ERA5. The cyclone remained offshore, east of the coasts of Italy, until its complete dissipation on 22 January, 1200 UTC when it was not possible to be tracked any more with the satellite imagery.

On 7 November 2014, an MTLC that developed in the Strait of Sicily was very well covered by surface stations and a radar system (Cioni *et al.*, 2018; Pytharoulis, 2018). The MTLC “*QENDRESA*”, named by the Free University of Berlin, reached the highest intensity in terms of maximum wind speed (43 m s^{-1}) and lowest measured SLP (978 hPa) among the rest of the MTLCs (Table 1). The manual tracking started on 7 November 2014, 0800 UTC when the cyclone was over the island of Pantelleria (Figure 1f) and the pre-existing DC was propagating outward, far away from the centre. In the following 8 hr until the cyclone reached Malta, DC was not detected within the first 25 km and barely detected between 25 and 50 km from the cyclone centre, and it was short-lived and scattered further away (i.e. until 1600 UTC 7 November 2014 in Figure 3f). While the cyclone was crossing Malta at 1600 UTC, DC was initiated and wrapped around the cyclone and was most active close to the cyclone centre (Figure 2f). Almost all the detected DCPIXELS were found within the first 100 km from the cyclone centre until the dissipation of the cyclone east of the coasts of Sicily on 8 November 2014 (Figure 1f).

The MTLC “*TRIXIE*” was one of the longest-lasting cases, with the manual tracking lasting 60 hr between 29 October 2016, 0000 UTC and 31 October, 1200 UTC (Figure 1g). *TRIXIE* was about 180 km southeast of Sicily at 36.0°N, 16.5°E on 29 October 2016, 0000 UTC when a closed cyclonic circulation was visible in the satellite imagery. Several rounds of DC activity were detected in the first 30 hr of the tracking, with storms starting to develop close to the centre and expanding outwards cyclonically (i.e. between 0000 UTC 29 October and 0600 UTC 30 October 2016 in Figure 3g). The most intense DC activity started after 1200 UTC 30 October 2016 (Figure 3g) and lasted for about 21 hr until 31 October 2016, 0900 UTC. DCPIXELS were mostly detected in the western parts of the cyclone and covered a large part of the cyclone periphery (Figure 2g), especially between 2100 UTC 30 October and 0300 UTC 31 October 2016 when a small cloud-free “eye-like” structure was developed in the cyclone centre

and a short intensification period was evident in ERA5 analysis (Figure 3g).

The cyclone that developed in the south Ionian Sea on 16 November 2017 and experienced TT the following day on 17 November 2017 (Marra *et al.*, 2019) was named “NUMA” by the Free University of Berlin. The tracking of the cyclone started on 17 November 2017, 0000 UTC when the cyclone centre was about 150 km east from the coasts of Calabria region and south from Salento Peninsula (Figure 1h). In general, ERA5 underestimated the intensity of the cyclone, showing higher SLP values than *in situ* observations (see Supporting information S2 in Appendix S1). During the first 8 hr of the manual tracking, the first 50 km from the centre were free of DC and almost totally cloud-free. The cyclone remained almost stationary in the north Ionian Sea for more than 20 hr (Figure 1h) and DC was mostly active within 100–150 km from the cyclone centre (Figure 3h). Moreover, DC had a marked preference for the northeastern quadrant of the cyclone, evident by a high count of DCPIXELS (Figure 2h). When NUMA started moving towards Greece on 18 November 2017, 1200 UTC about 9 hr after reaching the maximum intensity according to ERA5, a burst of DC activity was detected in the east-northeast part, as shown by the peak of DC activity close to the centre in Figure 3h after 1600 UTC. The final stage of the cyclone was characterized by an intense MCS north from the centre when it was crossing the Gulf of Patras between 0100 and 0400 UTC 19 November 2017 (Figure 1h). Interestingly, the DC activity of NUMA followed the diurnal solar circle, with a peak of DC activity a few hours after the local sunset and a minimum of DCPIXELS count around noon, on both 17 and 18 November 2017.

The last case of our study is the MTLC “ZORBAS” that developed between 28 and 30 September 2018. The manual tracking of the cyclone started on 28 September 2018, 0000 UTC when the cyclone was in the south Ionian Sea, at 34.2°N, 18.6°E (Figure 1i). DC activity was almost always close to the centre, except for a short period between 0900 and 1200 UTC 28 September 2018 (Figure 3i). Later on the same day, a convective cell that was first detected at 1400 UTC evolved into a large MCS that lasted for almost 10 hr, until 0000 UTC 29 September 2018. This storm initiated close to the centre (Figure 3i) and was wrapped around the cyclone, with the maximum DCPIXELS occurrence found in the southwest quadrant (Figure 2i). While ZORBAS was approaching Greece in the early morning of 29 September 2018, a large MCS developed in the northwest quadrant and remained active until the cyclone reached the coasts of Greece at 1200 UTC. ERA5 was not able to realistically capture the cyclone intensification during the high DC activity in the early morning of 29 September 2018 (see Figure 3i and Supporting information S2 in Appendix S1).

3.2 | Vertical wind shear influences

The next step in order to understand the distribution of DC in the selected MTLCs is to identify environmental factors dictating the cyclone evolution. VWS has been proven to be an important factor for the development, intensification and dissipation of TCs (Corbosiero and Molinari, 2002; Zeng *et al.*, 2010; Li *et al.*, 2016). Strong VWS may inhibit the genesis or intensification of a TC as the vertical axis of the vortex is tilted which can lead to a decreased and less symmetric convective activity and eventually dissipation of the cyclone (DeMaria, 1996; Frank and Ritchie, 2001). Even though studies of the impact of VWS on cyclones may explain particular processes and mechanisms associated with the evolution of the TCs, only a few studies focused on the Mediterranean have taken VWS into account (e.g. Tous and Romero, 2013; Cavicchia *et al.*, 2014). To our knowledge, no detailed analysis about the VWS and the vortex tilt, that influence the evolution of convection in MTLCs, exists in the literature.

In order to study the influence of VWS on DC in the selected MTLCs, a shear-relative framework was employed, rotating the DCPIXELS around the storm centres according to the DLS vector provided by ERA5 every 1 hr so that the DLS vector was pointing due north. Figure 4 shows the counts of DCPIXELS within a 200 km radius from the MTLCs’ centres rotated relative to the DLS vector direction. Compared to Figure 2, DCPIXELS are concentrated mostly in the downshear left quadrant in agreement with similar studies on TCs (e.g. Corbosiero and Molinari, 2002; 2003; Stevenson *et al.*, 2014; Li *et al.*, 2016). The influence of DLS is mostly evident for the MTLCs *Med2005*, *ROLF* and *TRIXIE*, while for *Med2007*, *NUMA* and *ZORBAS* comparable DC activity is found in the upshear left quadrants. The downshear and upshear left preference near the core of the cyclones suggest that the strong helical nature of updraughts, due to very small orbital periods, plays a role in shifting the maximum convective activity counter-clockwise from updraught initiation downshear.

In addition, the intensity of DLS seems to play an important role in organizing DC, especially when it exceeds $10 \text{ m}\cdot\text{s}^{-1}$. This effect is shown in Figure 5 for MTLCs *ROLF*, *TRIXIE*, *NUMA* and *ZORBAS* which experienced more than $10 \text{ m}\cdot\text{s}^{-1}$ DLS for several hours during their lifetime and their maximum intensity was estimated after a prolonged period of strong DC. The biggest impact of strong DLS on DC in the vicinity of the cyclone centre compared to the analysis for all values of DLS speed in Figure 4 was found on *NUMA* and *ZORBAS* (cf. Figure 4 with Figure 5), where DC was mostly found in the downshear left quadrant in a strongly sheared environment. The peak of DC in the upshear quadrants for these four MTLCs

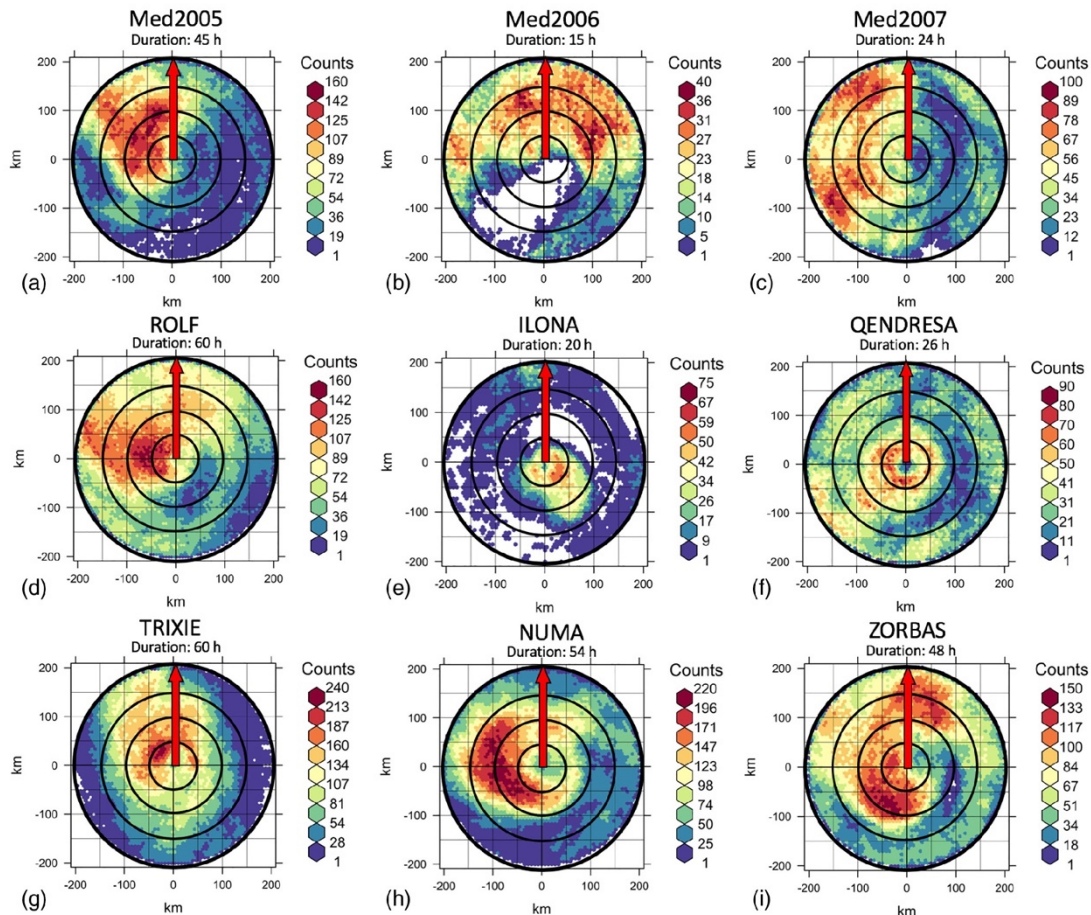


FIGURE 4 Composite azimuthal distribution of aggregated DCPIXELS rotated with respect to the DLS vector. The shade is the relative occurrence of DC for each case (note that the legend is not the same for each case). Top: (a) *Med2005*, (b) *Med2006* and (c) *Med2007*. Middle: (d) *ROLF*, (e) *ILONA* and (f) *QENDRESA*. Bottom: (g) *TRIXIE*, (h) *NUMA* and (i) *ZORBAS*. The red arrow shows the direction of the DLS vector pointing due north [Colour figure can be viewed at wileyonlinelibrary.com]

coincided with the activity of the long-lasting MCSs close to the cyclone centre discussed in Section 3.1 and Supporting information S2 in Appendix S1. In order to show the impact of strong DLS on the position of DC, we kept the DCPIXELS only for the periods with DLS stronger than $10 \text{ m}\cdot\text{s}^{-1}$ in Figure 5. The mean values of DLS for constructing Figure 5 were 13.5 , 12.4 , 11.9 and $10.9 \text{ m}\cdot\text{s}^{-1}$ for *ROLF*, *TRIXIE*, *NUMA* and *ZORBAS*, with maximum DLS values 25.5 , 15.0 , 15.9 and $14.3 \text{ m}\cdot\text{s}^{-1}$ respectively.

To investigate these patterns further, the DC detections within the last 6 hr before the time of maximum cyclone intensity were rotated with respect to the DLS vector, regardless of the DLS speed (Figure 6). During the intensification period of the long-lasting MTLCs (except

for *Med2005*), persistent DC activity was detected in the upshear quadrants of the cyclones and it was concentrated close to the centre. In the upshear parts of a cyclone, especially during strong DLS, subsidence and dry air intrusions are expected to inhibit DC (Reasor *et al.*, 2004; Riemer *et al.*, 2010; Tang and Emanuel, 2010). Most probably this is the reason why during strong DLS with values higher than $15 \text{ m}\cdot\text{s}^{-1}$ and up to $28 \text{ m}\cdot\text{s}^{-1}$ in *Med2005*, DC was barely detected in the upshear quadrants (not shown). Studies on TCs have shown that the presence of DC in the upshear quadrants within 100 km from the cyclone centre is associated with intensification periods due to the high efficiency of symmetric convection in converting diabatic heating to kinetic energy (Nolan *et al.*, 2007;

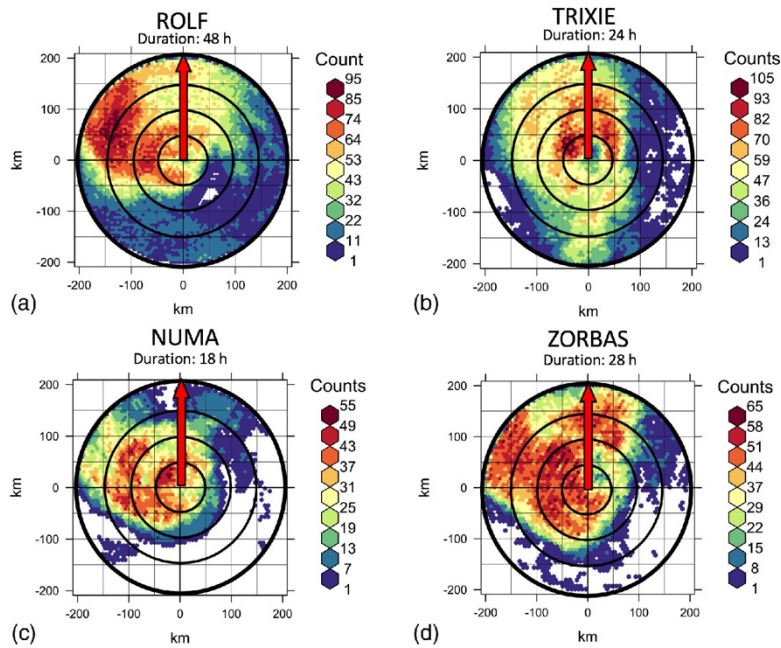


FIGURE 5 As in Figure 4 but for DLS values greater than $10 \text{ m}\cdot\text{s}^{-1}$. The shade is the relative occurrence of DC for each case (not normalized) of (a) *ROLF*, (b) *TRIXIE*, (c) *NUMA* and (d) *ZORBAS*. The red arrow shows the direction of the DLS vector pointing due north [Colour figure can be viewed at wileyonlinelibrary.com]

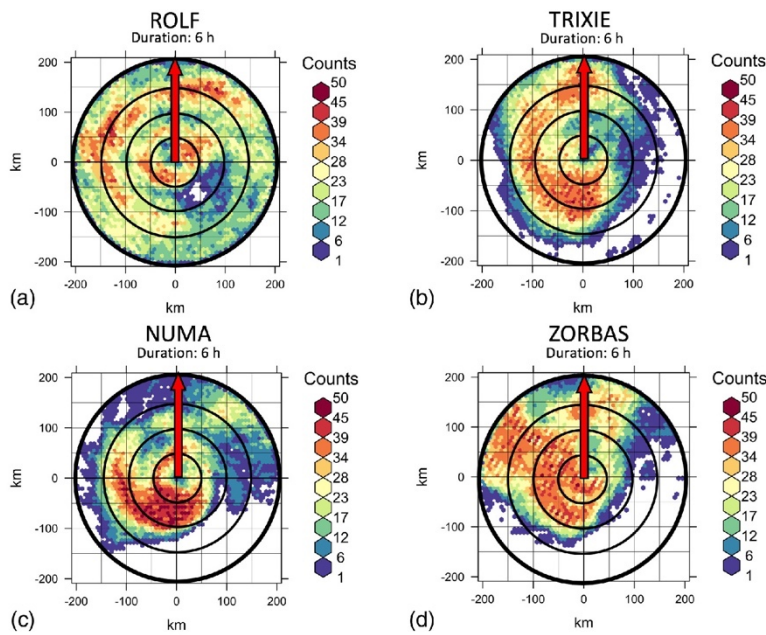


FIGURE 6 As in Figure 4 but for the 6 hr period before the maximum intensity of the cyclones and for all DLS speed values. The shade is the relative occurrence of DC for each case of (a) *ROLF*, (b) *TRIXIE*, (c) *NUMA* and (d) *ZORBAS*. The red arrow shows the direction of the DLS vector pointing due north [Colour figure can be viewed at wileyonlinelibrary.com]

Harnos and Nesbitt, 2011; 2016; Fischer *et al.*, 2018). Similar results are presented for these MTLCs, during weak to moderate DLS. The DLS during these periods was stronger than $8 \text{ m}\cdot\text{s}^{-1}$ with mean DLS values of $12.9 \text{ m}\cdot\text{s}^{-1}$ for *ROLF*, $10.6 \text{ m}\cdot\text{s}^{-1}$ for *TRIXIE*, $10.0 \text{ m}\cdot\text{s}^{-1}$ for *NUMA* and $10.6 \text{ m}\cdot\text{s}^{-1}$ for *ZORBAS*, and maximum values of 13.2, 11.7, 10.7 and $11.1 \text{ m}\cdot\text{s}^{-1}$ respectively (Figure 6). These values are within the VWS speed values discussed in Cavicchia *et al.* (2014) and Tous and Romero (2013) for older case-studies on MTLCs.

3.3 | Influences of deep convection and wind shear on the cyclone structure and intensity

In order to show how the cyclone structure changes due to the presence of VWS and DC, and understand the spatial and temporal differences in DC evolution and intensity changes among the selected MTLCs, the vortex tilt is computed and discussed in detail. Observations show that *Med2005*, *Med2007* and *QENDRESA* share a few common characteristics in terms of DC and VWS evolution, especially at the incipient stage of their tropical-like characteristics, while during *ROLF*, *TRIXIE*, *NUMA* and *ZORBAS* the DC activity had different evolution. According to the distance from the cyclone centre, associative relationships between DC activity, vortex tilt and cyclone intensification are presented, and finally the MTLCs are grouped in three categories. Figure 7 shows the first proposed group of MTLCs consisted of the cases *Med2005*, *Med2007* and *QENDRESA* for which the maximum intensity of the cyclones was found at the early stages of their development and during very weak DC activity, mostly away from the cyclone centre. Moreover, the VWS was weakening during this period of deepening, despite the absence of DC.

The maximum intensity of *Med2005* was estimated in the early morning of 14 December 2005 (Figure 3a) when there were no detections of DCPIXELS close to the core of the cyclone ($<50 \text{ km}$) (Figures 7a and 8a and Supporting information S2 in Appendix S1). After reaching the minimum SLP (Figure 3a), the cyclone experienced strong DLS after 1500 UTC 14 December 2005 and DC started to develop close to the centre with a short period of limited DC in the early morning of 15 December (Figure 8a). The vortex tilt was limited, less than 70 km and most of the time less than 50 km , despite more than $20 \text{ m}\cdot\text{s}^{-1}$ DLS (Figures 7b,c and 8a). DCPIXELS were mostly initiated and detected downshear left, with rare detections upshear left (e.g. Figure 7b), where the azimuthal location of DC was shifted towards the vortex tilt vector (Figure 7b,c). Whether the actual role of the vortex tilt is to organise DC upshear or if the upshear vortex tilt is a response to

vorticity generation associated with DC cannot be currently answered with the data used in this study. A possible explanation about the cyclonic rotation of the vortex tilt left of the shear vector between 0900 and 1300 UTC 15 December (Figure 8a) is the cyclonic rotation of the mid-level vortex as a response to the strong DLS, in order to reduce the vortex tilt (Jones, 1995; Reasor *et al.*, 2004). Similarly to Fita and Flaounas (2018), ERA5 SLP was constantly increasing on 14 and 15 December (Figure 3a) leading to cyclone filling and dissipation. Miglietta and Rotunno (2019) argue that *Med2005* may not have experienced a typical TT and the deep warm-core formation was mainly a result of baroclinic processes, such as a warm seclusion. The observations of DC evolution also suggest that during the period of maximum cyclone intensity, the absence of DC complicates the explanation of the mid/upper-level warming of the cyclone found in ERA5 and in Fita and Flaounas (2018).

Similarly to *Med2005*, the minimum SLP of MTLC *Med2007* was estimated at early stages on 15 November 2007 during very weak and scattered DC activity (Figures 3c, 8c and 7d). DLS decreased about $10 \text{ m}\cdot\text{s}^{-1}$ during DC activity before the maximum intensity of the cyclone (see Supporting information S2 in Appendix S1), before 2000 UTC 15 November and the vortex tilt was rather strong, up to 100 km downshear right. After 0400 UTC 16 November, DCPIXELS detections started to increase close to the cyclone centre but DC was scattered and short-lived (e.g. Figure 7e), in contrast to the outer MCSs developing within $100\text{--}200 \text{ km}$ from the centre (e.g. Figure 7e,f). The vortex tilt decreased below 50 km during DC activity and progressively turned from the upshear right to the downshear right quadrant (Figure 8c) as the cyclone was approaching the coasts of Sardinia. Figure 4c shows that the DLS vector seems to divide the DC-active left quadrants from the less DCPIXELS-covered right ones, indicating updraught motions on the left and downward motions to the right of the wind shear vector. This apparent DC organization may have a connection to a strongly baroclinic environment, as does the constant DLS vector pointing northeast (Figure 8c), but further analysis is needed to verify this claim.

QENDRESA is the last MTLC of this group, for which DC and SLP evolution followed a similar pattern to *Med2005* and *Med2007*, but the cyclone intensity was much stronger. The minimum SLP was estimated on 7 November 2014, 1700 UTC by ERA5 (Figure 3f) and in accordance with Cioni *et al.* (2018) and Carrió *et al.* (2017) (see also Supporting information S2 in Appendix S1). In the previous 9 hr the DC activity close to the centre was very weak (Figures 3f and 8f) and high BTs ($>250 \text{ K}$) were detected by SEVIRI (Figure 7g), while DLS was weakening with values below $10 \text{ m}\cdot\text{s}^{-1}$ (Figure 8f). Pytharoulis (2018)

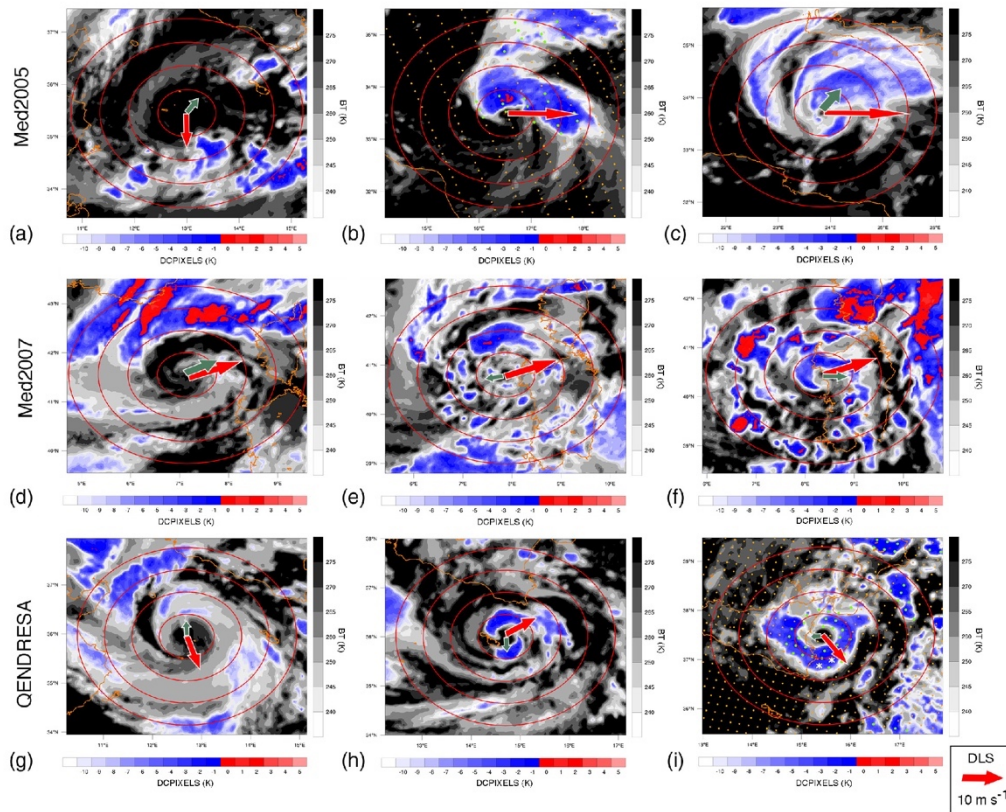


FIGURE 7 Infrared brightness temperature (BT) from channel IR10.8 (K) (grey) and DCPIXELS (K) (blue and red) derived from SEVIRI Meteosat satellites. Overlapped dots: Diagnostics from microwave sounders for deep convection (MWDC) (green), convective overshooting (COV) (white asterisks) and the scanning footprint (orange) within 15 min from SEVIRI scans. The red circles enclose disks the magnitude and direction of DLS (red) and the vortex tilt (green – proportional to radius). Top: During *Med2005* (a) on 14 December 2005 at 1100 UTC, (b) at 2000 UTC (AMSU-B NOAA-17), and (c) on 15 December 2005 at 0900 UTC. Middle: During *Med2007* (d) on 15 November 2007 at 2230 UTC, (e) on 16 November 2007 at 0500 UTC, and (f) at 1230 UTC. Bottom: During *QENDRESA* (g) on 7 November 2014 at 1200 UTC, (h) at 1700 UTC, and (i) on 8 November 2014 at 0400 UTC (MHS NOAA-18) [Colour figure can be viewed at wileyonlinelibrary.com]

attributed the weakening of DLS to DC activity, but we show that there was a continuous weakening even when only shallow convection was detected (i.e. BTs warmer than 245 K) (Figures 7g and 8f). Just before 1600 UTC, the cyclone reached Malta when DC initiation was detected close to the centre (Figures 1f and 7h). This sudden DC initiation over Malta may be attributed to surface friction and the low-level mass convergence (Wakimoto and Black, 1994), while no significant change to the DLS intensity took place to tilt the cyclone (Figure 8f). The vortex tilt remained at less than 50 km during the lifetime of the cyclone and for this reason, its direction fluctuated constantly (Figure 8f), mostly found to the right of the DLS vector pointing south-southeast during the DC activity.

The sharp changes of vortex tilt are more frequent during weak tilting and vertical alignment of the vortices where the mid-level vortex does not change much in position but shifts in direction. The weak vortex tilt cannot directly be connected with the organization of DC in the southern parts of the cyclone during the night of 7 November 2014 and the morning on 8 November 2014 (Figures 7h–i and 8f). It is worth mentioning that in the early morning of 8 November 2014, COV detections by MHS (Figure 7i) indicated the presence of very deep updraughts between 50 and 100 km from the cyclone centre and DLS reached a minimum after a prolonged period with DC activity (Figure 8f) while the cyclone was weakening fast. Previous studies have shown that shallow convection is detected

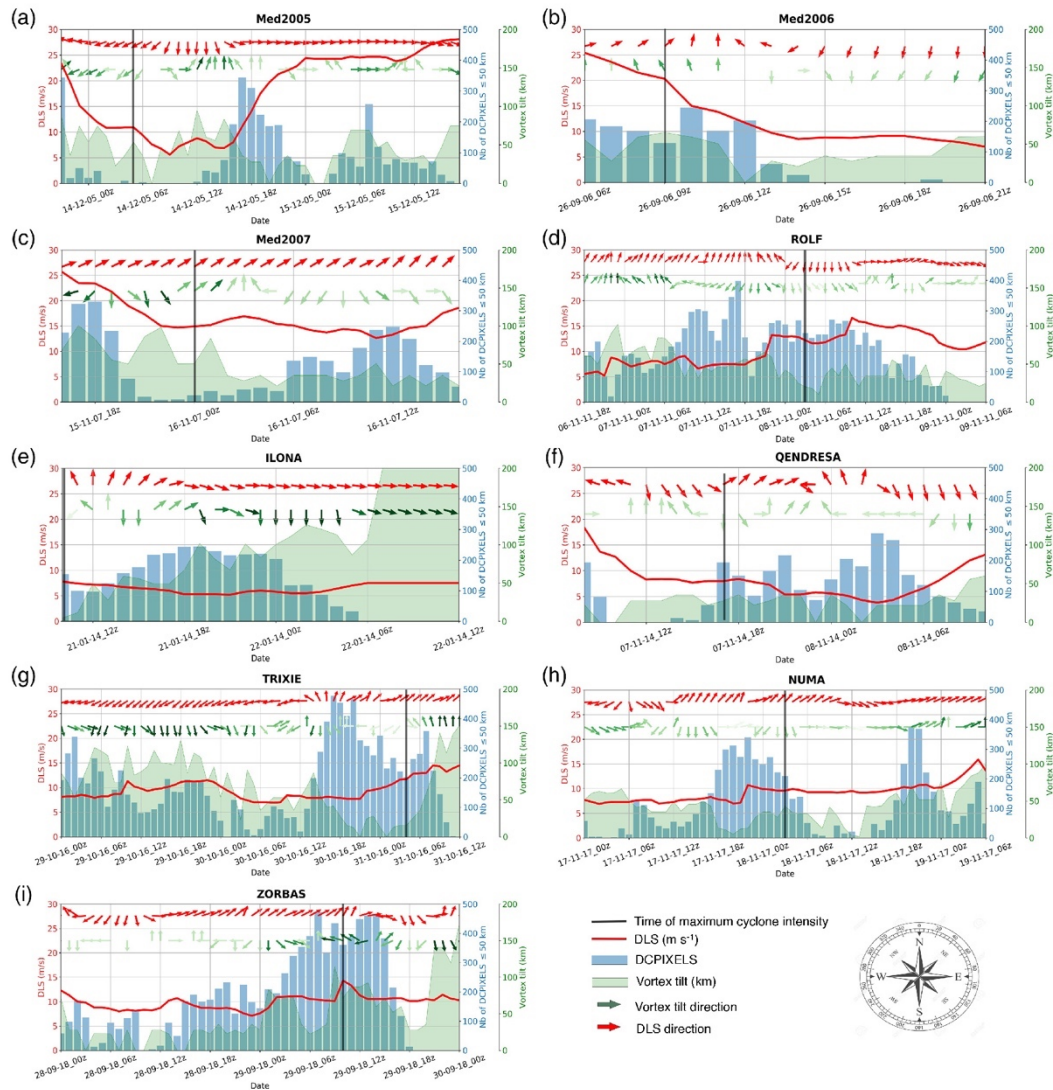


FIGURE 8 Time-series for (a) *Med2005*, (b) *Med2006*, (c) *Med2007*, (d) *ROLF*, (e) *ILONA*, (f) *QENDRESA*, (g) *TRIXIE*, (h) *NUMA* and (i) *ZORBAS*, of area-weighted average DLS magnitude (m s^{-1}) calculated by ERA5 analysis within 200 km radius (red line), DLS direction (red arrows), counts of DCPIXELS (blue bars) within 50 km radius from cyclone centre, and the vortex tilt (km) (green shading) and direction (green arrows) calculated by ERA5 analysis every 1 hr. The black line indicates the time of maximum cyclone intensity. See the text for more details. Hour is dd-mm-yy_hhz (UTC) [Colour figure can be viewed at wileyonlinelibrary.com]

during the tropical-like phase of MTLCs (Claud *et al.*, 2010; Miglietta *et al.*, 2013; Cioni *et al.*, 2016; Marra *et al.*, 2019).

A second group of MTLCs can be formed with cyclones which lasted more than 1 diurnal cycle and experienced significant DC activity prior to their maximum intensity: *ROLF*, *TRIXIE*, *NUMA* and *ZORBAS*. These MTLCs were also discussed in Section 3.2 as DC was more symmetric

compared to the rest of the cases, and covered a larger part of the cyclones' periphery. In addition, the long-lasting and intense DC activity may have played an important role in their intensification later than their genesis time, a clear distinction from the first group.

ROLF was one of the longest-lasting MTLCs until 2011 and the synoptic conditions that led to its formation can

be found in previous studies by Miglietta *et al.* (2013) and Dafis *et al.* (2018). The cyclone followed a northeast direction starting from the Balearic Islands on 6 November 2011, following the direction of DLS (Figure 8d). DLS was weaker than $10 \text{ m}\cdot\text{s}^{-1}$ until 2200 UTC 7 November and the vortex tilt was mostly found upshear (Figures 8d and 9b) and more than 200 DCPIXELS per hour were detected in all quadrants within 50 km radius from the centre (Figure 8d). With the gradual increase of DLS on 8 November, the vortex tilt was reduced and turned downshear left as DCPIXELS, MWDC and COV were constantly generated downshear left and right (e.g. Figure 9c), and DCPIXELS were moving fast counter-clockwise to the upshear left quadrant. While persistent MCSs were found upshear before the maximum intensity of *ROLF* at 0300 UTC 8 November (Figure 3d and Supporting information S2 in Appendix S1), the downshear convection was followed by cyclone weakening, despite the more vertical alignment of the cyclone and the comparable number of DCPIXELS (Figure 8d).

TRIXIE resulted in severe weather events in southern Greece on 31 October 2016. According to ERA5, the SLP during *TRIXIE* was fluctuating between 1,010 and 1,014 hPa on 29 and 30 October 2016 (Figure 3g). A strongly tilted structure is evident during the same period (Figure 8g) with the vortex tilt downshear and pulsating storms close to the cyclone centre (Figure 9d). The vortex tilt was gradually decreasing between 2100 UTC 29 October and 1200 UTC 30 October but also the DC activity and DLS were weakening (Figures 3g and 8d). After 1200 UTC 30 October a sudden shift of DLS direction coincided with a burst of DC close to the centre, producing very strong updraughts as indicated by the detections of COV in Figure 9e. Even though a direct causality cannot be addressed here, the upshear-shift of the vortex tilt and the increased DC activity at the same time must be closely related, such that the simultaneous decreasing vortex tilt could be attributed to vorticity generation by diabatic heating. The persistent DC activity close to the centre was followed by a strong cyclone deepening during the night of 30 October and early morning of 31 October according to ERA5 (Figure 3g) and *in situ* observations (see Supporting information S2 in Appendix S1). Similarly to *ROLF*, MCSs had a clear preference for the upshear left quadrants before the maximum intensity of the cyclone at 0300 UTC 31 October (Figures 3g and 9f).

NUMA had two distinct periods of strong DC activity close to the centre. The first one between 1200 UTC 17 November and 0600 UTC 18 November 2017 was directly associated with an MCS in the upshear left quadrant which was detected by numerous DCPIXELS (Figure 9h) and COV for more than 12 hr when DLS was weaker or slightly stronger than $10 \text{ m}\cdot\text{s}^{-1}$ and the vortex tilt was less than

50 km (Figure 8h). Also during this period, the maximum intensity of the cyclone was estimated by ERA5 as for Marra *et al.* (2019). The DC activity was clearly closer to the centre compared to the first 12 hr of the tracking, even though MWDC and COV were detected in the outer parts of the cyclone periphery (e.g. Figure 9g). During the incipient decrease of DC activity between 0600 and 1500 UTC 18 November the cyclone started weakening and the vortex tilt reached a minimum. The DLS speed was steady during this period and changed direction from northeast to southeast (Figure 8h). The second round of strong DC activity after 1500 UTC was detected during an increasing vortex tilt downshear as the cyclone was approaching west Greece (Figures 8h and 9i). The DCPIXELS were first detected downshear and then were cyclonically wrapped around the centre until the landfall of the cyclone in Greece where severe weather events were reported (see Supporting information S2 in Appendix S1).

During the first 12 hr of *ZORBAS'* manual tracking, DC was pulsating and organized in two distinct bands (e.g. Figure 9j) when the vortex tilt was less than 50 km (Figure 8i). After 1400 UTC 28 September 2018, an MCS in the upshear left quadrant was constantly detected upshear by numerous DCPIXELS and MWDC for more than 10 hr. After 0000 UTC 29 September, an increasing vortex tilt upshear was calculated as the DLS was slightly increasing, and DC activity started to increase close to the centre (Figure 8i). As the cyclone was approaching Greece on 29 September, ERA5 showed a constant filling of the cyclone but *in situ* observations indicated a deepening (see Supporting information S2 in Appendix S1 for more details) as the DC was wrapped cyclonically around the centre in all quadrants (Figures 3i, 8i and 9l). The maximum intensity of the cyclone was estimated around 1000 UTC before it made landfall in south Greece, when DC activity showed a maximum in the downshear and upshear left quadrants (Figures 8i and 9l).

The third proposed group consists of the short-lasting MTLCS *Med2006* and *ILONA*. Their size was much smaller than the rest of the cyclones discussed in this study (Figure 2b,e) and DC activity was weak or not detected for several hours during their lifetime (Figures 3b,e and 8b,e). During *Med2006*, many DCPIXELS were detected downshear during very strong DLS exceeding $15\text{--}20 \text{ m}\cdot\text{s}^{-1}$ (Figure 8b) but surprisingly, the estimated vortex tilt was weak. On the contrary during *ILONA*, DLS was weaker than $10 \text{ m}\cdot\text{s}^{-1}$ and the vortex tilt was found downshear and upshear right, tilted more than 100 km (Figure 8e) during DC activity close to the centre. Both cyclones were embedded within larger cyclonic systems (Chaboureaud *et al.*, 2012; Cioni *et al.*, 2016) and the short-lasting DC activity downshear close to the centre of *Med2006* (Figure 2b) and the upshear right quadrants of *ILONA*

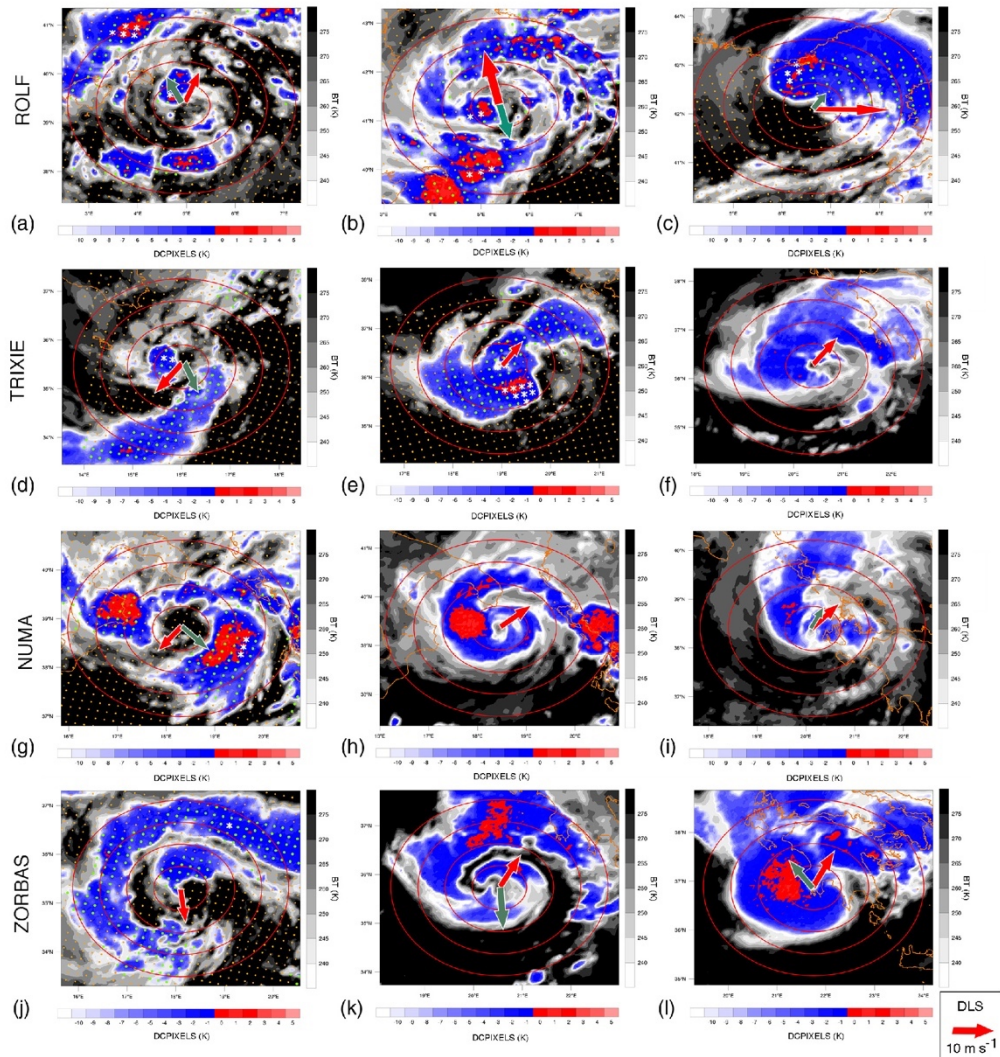


FIGURE 9 As in Figure 7 but for *ROLF* (a) on 7 November 2011 at 0230 UTC (NOAA-18 MHS) and (b) at 2030 UTC (MetOp-A MHS), (c) on 8 November 2011 at 1330 UTC (NOAA-18 MHS); for *TRIXIE* (d) on 29 October 2016 at 0900 UTC (MetOp-A MHS), (e) on 30 October at 1930 UTC (MetOp-A MHS), (f) on 31 October 2016 at 0100 UTC; for *NUMA* (g) on 17 November 2017 at 0300 UTC (NOAA-19 MHS) and (h) at 2230 UTC, (i) on 18 November 2017 at 2200 UTC; and for *ZORBAS* (j) on 28 September 2018 at 0830 UTC (NOAA-18 MHS), (k) on 29 September 2018 at 0100 UTC, and (l) at 0930 UTC [Colour figure can be viewed at wileyonlinelibrary.com]

(Figure 2e) were not associated with cyclone intensification periods (Figures 3e and 8e).

4 | DISCUSSION

The complexity of the developing MTLCs precludes the clear presence of a dominant simple mechanism for

growth; however, we tried to investigate the evolution of DC during their lifetime and extract some new and useful information. *In situ* data are still too sparse to observe the formation process and resolve the interior cyclone structure. Two very recent studies by Fita and Flaounas (2018) and Miglietta and Rotunno (2019) have raised the question to what extent the MTLCs are self-sustained vortices and if they should be categorized according to their

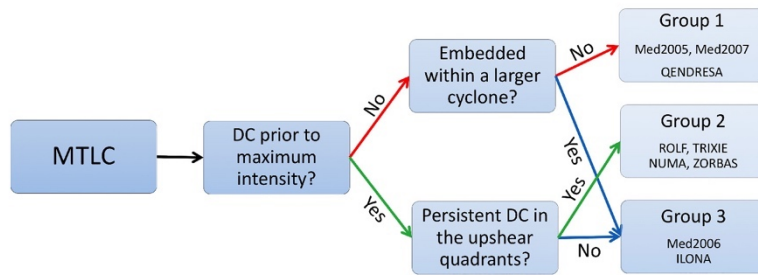


FIGURE 10 Decision tree classifier for MTLCs according to DC evolution [Colour figure can be viewed at wileyonlinelibrary.com]

precursors, stages of evolution and contribution of diabatic processes. The first paper suggests that due to the hybrid structure of the MTLCs and the process of TT, these cyclones should be treated as subtropical cyclones which can form in other oceans of the globe between 20°N and 40°N (Evans and Guishard, 2009; González-Alemán *et al.*, 2015; Bentley *et al.*, 2016; 2017) or 20°–40°S (Evans and Braun, 2012; Dowdy *et al.*, 2019). The latter paper suggests the categorization of MTLCs into three groups, based on (a) the presence of baroclinic instability and a dominant warm-seclusion process, (b) intensity of air–sea interactions and diabatic heating, and (c) the interaction of the cyclone with upper-level PV anomalies. In the present study, our observations seem to confirm that such a categorization of the MTLCs is possible. We divided the nine case-studies into groups with respect to their convective evolution and their intensification periods (Figure 10). Results show that the first group of MTLCs, *Med2005*, *Med2007* and *QENDRESA*, experienced their maximum intensity after a prolonged period of a weak DC activity close to their centres. For these cases we show that the DLS decreased during the absence of DC and the cyclone maximum intensity was observed before the organization of DC close to the centre. In addition, the spatial extent of organized DC close to the centre is much smaller than for the cases of *ROLF*, *TRIXIE*, *NUMA* and *ZORBAS*. The location of heat sources in a barotropic vortex strongly affects the strength and the structure of the cyclone. This is well analysed by numerous previous studies which also deal with the transformation of an extratropical vortex into a TC, either by naming it “diabatic intensification” (Montgomery and Farrell, 1992) or TT (Davis and Bosart, 2004). This first group of MTLCs seems to have intensified into a baroclinic environment where DC possibly had a secondary role to their TT, while DC developed later close to the centre due to either environmental shear or interactions with topography. Topography is likely an important factor for their development and further intensification, either due to influences of mid/upper-level disturbances such as the PV-banner southwest of the Alps for the *Med2007* case (McTaggart-Cowan *et al.*, 2010), the

interaction with the dry environment and Saharan dust for the case of *Med2005* (Fita and Flaounas, 2018), or the direct landfall of *QENDRESA* in Malta and Sicily (see Supporting information S2 in Appendix S1).

The second group consists of long-lasting MTLCs which have experienced an occlusion at their early stage with or without significant DC contribution, but their intensification is observed later, after intense DC activity close to their centre (Figure 10). This group can be compared with the weak Atlantic baroclinically induced TCs discussed in the studies of Davis and Bosart (2003; 2004), which usually reach intensities below Category 2 in the Saffir–Simpson Hurricane Wind Scale. During most of their lifetime, DC is scattered and numerical studies on barotropic cyclones with asymmetrically distributed DC have shown a limited positive but mostly negative effect on the intensification of TCs (e.g. Nolan and Grasso, 2003). But MTLCs develop in the midlatitudes between 30° and 45°N where the conversion of heat energy released by DC close to the cyclone centre can lead to a net kinetic energy increase with a much higher efficiency rate than in the Tropics (Nolan *et al.*, 2007, their figure 21). Moreover, values of VWS higher than 10 m·s⁻¹ do not seem to inhibit their TT and intensification as previous studies have suggested, but even promote the development of DC close to the centre either downshear or towards the direction of the vortex tilt, similar to studies on TCs (e.g. Corbosiero and Molinari, 2002; Stevenson *et al.*, 2014).

Studies on extratropical cyclones in the Atlantic have shown that TT becomes unlikely when the VWS magnitude exceeds 10 m·s⁻¹ (DeMaria *et al.*, 2001), while Gallina and Velden (2002) have found that VWS inhibits further intensification of the Atlantic TCs if it exceeds 7–8 m·s⁻¹. The negative impact of VWS in the formation or intensification of TCs has also been studied through the ventilation theory which explains how dry and cool air from the upper/mid-troposphere decreases the equivalent potential temperature near the core of the cyclones (Tang and Emanuel, 2010). The loss of latent heat in the upper levels of the core can result in an increase of sea-level pressure, and thus a dissipation (Gray, 1968;

Frank and Ritchie, 2001). On the contrary, Bracken and Bosart (2000) after studying Atlantic tropical cyclogenesis found that weak VWS is necessary for developing depressions to further intensify and become TCs, as it promotes synoptic-scale ascent. In the current study, not only do the MTLCs survive in a strongly sheared environment, but the cyclones of this group can also intensify. In addition, observations of long-lasting DC that was wrapped in the upshear quadrants of the cyclones leading to axisymmetric diabatic heating of the warm core during moderate DLS and a tilted vortex could suggest a mechanism similar to the vortex resiliency explained in Reasor *et al.* (2004). The symmetric DC close to the core of the TCs has been connected to rapid intensification periods (e.g. Fischer *et al.*, 2018). Interestingly, we have not observed a significant effect of DC activity on the decrease of DLS compared to studies in the Tropics and subtropics. Only the extratropical precursor of *TRIXIE* was quite similar to Hurricane *Michael* in 2000 (Davis and Bosart, 2003), which was at first an intense extratropical cyclone when the weakening of DLS occurred within the precursor baroclinic environment with the synergy of DC activity and baroclinic processes. For Hurricane *Michael*, the decrease of DLS was due to both a nonconservative redistribution of PV along the vorticity vector and to the diabatically induced upper-tropospheric outflow during DC activity. An impressive anticyclonic upper-level outflow was evident in *TRIXIE*, but the complex interaction of *TRIXIE* with Mediterranean topography and the upper-tropospheric configuration complicate the interpretation of the DLS evolution. Numerical simulations should be conducted to support this observation and explore the influence of upper-tropospheric troughs and PV anomalies on the MTLCs' evolution similar to Fischer *et al.* (2017).

In the third suggested group of MTLCs (Figure 10), a small fraction of cyclones can be included, mostly due to the rare circumstances that need to take place at the same time. Strong or weak surface baroclinity and upper-level PV anomalies can create subsynoptic vortices, embedded into a larger cyclonic feature, but DC seems to play a secondary role in their intensification, perhaps because of the limited lifetime or due to other environmental factors, such as strong ventilation by VWS. Such an example is the case of *Med2006*, when a subsynoptic vortex embedded into a larger cyclone intensified after the interaction with an upper-level PV streamer (Chaboureau *et al.*, 2012; Miglietta *et al.*, 2017; Miglietta and Rotunno, 2019). Interestingly, Moscatello *et al.* (2008b) highlighted the importance of sensible- and latent-heat fluxes during DC before the maximum intensity of *Med2006*, while Chaboureau *et al.* (2012) suggested a more important contribution to the intensification of the cyclone by the interaction with the jet stream aloft. In this category, we may also include

the small subsynoptic cyclones with a shallow warm core that form after an occlusion and exhibit tropical-like characteristics for a short period of time. *ILONA* was also embedded into a much larger low-pressure system, under a maximum of upper-level PV anomaly, and its evolution was closely tied to the precursor upper-level disturbance (Cioni *et al.*, 2016). Our study shows that DC was shallow with no MWDC/COV detections and confined to a small fraction of the cyclone periphery. Additional observational and numerical studies are needed to investigate the actual contribution of DC to their evolution.

5 | SUMMARY AND FUTURE WORK

In this study, infrared and microwave satellite diagnostics were used to study the evolution of DC in MTLCs which developed between 2005 and 2018. ERA5 reanalysis data complemented the analysis in order to explain the multiple effects of DLS on the organization of DC and the symmetry of the cyclones. Despite the sparse *in situ* observations and uncertainties in numerical reanalysis, we believe that the presented results elucidate the effects of DC on the structure and evolution of the MTLCs. As a last step to this contribution, a classification of MTLCs was proposed according to the DC contribution to their development and intensification.

The main findings can be summarised as follows:

- 1 Long-lasting and organized DC activity close to the centre of the MTLCs precedes the cyclone maximum intensity of *ROLF*, *TRIXIE*, *NUMA* and *ZORBAS*. For these cases, persistent DC is detected in the upshear quadrants during the cyclone intensification periods.
- 2 DC activity located solely downshear was not linked to intensification periods and was more frequent during moderate and strong DLS.
- 3 DLS affects cyclone structure and organization of DC in most of the MTLCs. Upshear DC activity was detected often during an upshear vortex tilt.
- 4 Decreasing DLS was observed during very weak and sporadic DC activity during *Med2005*, *Med2007* and *QENDRESA* which are amalgamated into a group based on a hypothesis that DC did not play a dominant role in their intensification.

Due to the much drier environment of the Mediterranean basin compared to the Tropics, additional studies are needed to explain the interactions between the downdraughts of storms, the ventilation of low-entropy air in the low/mid-levels but also the response of MTLCs' structure to different depths of DLS (e.g. Finocchio *et al.*, 2016). The

weakening of DLS during intense DC activity (Davis and Bosart, 2004) was not observed in this study, and since the VWS is directly related to mid/upper-tropospheric trough pathways, an additional study could incorporate methods to explain MTLCs and trough interactions (e.g. Fischer *et al.*, 2017). Moreover, very few studies have explored the mechanisms leading to the “cyclone-eyes” formation in MTLCs, either from subsidence linked to DC activity (Moscatello *et al.*, 2008b) or from dry air advection (Fita and Flaounas, 2018). Additional observational and numerical studies are needed to research and provide a complete understanding of the inner core of MTLCs. Previous studies have shown that DC is weaker or shallower during and after the maximum intensity of some MTLCs (e.g. Claud *et al.*, 2010; Miglietta *et al.*, 2013; Cioni *et al.*, 2016; Marra *et al.*, 2019) but this statement was not confirmed for the majority of the selected MTLCs presented in this study. In addition, the DC during *NUMA* followed the diurnal solar cycle, probably due to the radiative cooling of the cloud tops, a process that increases instability in the troposphere (Wu and Ruan, 2016), but additional analysis has to be conducted to investigate this feature. Finally, a numerical study of the DC contribution to the MTLCs’ evolution following this observational study should be carried out, with a special focus on the growth rates of the cyclones depending on the proposed classification.

ACKNOWLEDGEMENTS

This study was sponsored by the Direction générale de l’armement - Ministère des Armées (DGA) and a National Observatory of Athens internal grant. Meteosat data were retrieved from the Earth Observational Portal of EUMETSAT. MHS and AMSU-B data were obtained through the French Mixed Service Unit project ICARE/-Climserv/Aeris. The manual cyclone-track data for the MTLCs and all the scripts used for this study can be provided upon request. We would like to thank the three anonymous reviewers for their careful corrections and constructive suggestions during the review process.

ORCID

Stavros Dafis  <https://orcid.org/0000-0002-1513-1930>

REFERENCES

- Alhammoud, B., Claud, C., Funatsu, B.M., Béranger, K. and Chaboureaud, J.P. (2014) Patterns of precipitation and convection occurrence over the Mediterranean Basin derived from a decade of microwave satellite observations. *Atmosphere*, 5, 370–398. <https://doi.org/10.3390/atmos5020370>.
- Alvey, G.R., III, Zawislak, J. and Zipser, E. (2015) Precipitation properties observed during tropical cyclone intensity change. *Monthly Weather Review*, 143, 4476–4492. <https://doi.org/10.1175/MWR-D-15-0065.1>.
- Bedka, K., Brunner, J., Dworak, R., Feltz, W., Otkin, J. and Greenwald, T. (2010) Objective satellite-based detection of overshooting tops using infrared window channel brightness temperature gradients. *Journal of Applied Meteorology and Climatology*, 49, 181–202. <https://doi.org/10.1175/2009JAMC2286.1>.
- Bentley, A.M., Bosart, L.F. and Keyser, D. (2017) Upper-tropospheric precursors to the formation of subtropical cyclones that undergo tropical transition in the North Atlantic Basin. *Monthly Weather Review*, 145, 503–520. <https://doi.org/10.1175/MWR-D-16-0263.1>.
- Bentley, A.M., Keyser, D. and Bosart, L.F. (2016) A dynamically based climatology of subtropical cyclones that undergo tropical transition in the North Atlantic Basin. *Monthly Weather Review*, 144, 2049–2068. <https://doi.org/10.1175/MWR-D-15-0251.1>.
- Bracken, E. and Bosart, L.F. (2000) The role of synoptic-scale flow during tropical cyclogenesis over the North Atlantic Ocean. *Monthly Weather Review*, 128, 353–376. [https://doi.org/10.1175/1520-0493\(2000\)128<0353:TROSSF>2.0.CO;2](https://doi.org/10.1175/1520-0493(2000)128<0353:TROSSF>2.0.CO;2).
- Čampa, J. and Wernli, H. (2012) A PV perspective on the vertical structure of mature midlatitude cyclones in the Northern Hemisphere. *Journal of Atmospheric Sciences*, 69, 725–740. <https://doi.org/10.1175/JAS-D-11-050.1>.
- Carrió, D.S., Homar, V., Jansa, A., Romero, R. and Picornell, M.A. (2017) Tropicalization process of the 7 November 2014 Mediterranean cyclone: numerical sensitivity study. *Atmospheric Research*, 197, 300–312. <https://doi.org/10.1016/j.atmosres.2017.07.018>.
- Cavicchia, L. and von Storch, H. (2012) Simulation of medicanes in a high resolution regional climate model. *Climate Dynamics*, 39, 2273–2290. <https://doi.org/10.1007/s00382-011-1220-0>.
- Cavicchia, L., von Storch, H. and Gualdi, S. (2014) A long-term climatology of medicanes. *Climate Dynamics*, 43, 1183–1195. <https://doi.org/10.1007/s00382-013-1893-7>.
- Chaboureaud, J.P., Pantillon, F., Lambert, D., Richard, E. and Claud, C. (2012) Tropical transition of a Mediterranean storm by jet crossing. *Quarterly Journal of the Royal Meteorological Society*, 138(664), 596–611. <https://doi.org/10.1002/qj.960>.
- Chen, S. and Houze Jr, R.A. (1997) Diurnal variation and life-cycle of deep convective systems over the tropical Pacific warm pool. *Quarterly Journal of the Royal Meteorological Society*, 123(538), 357–388. <https://doi.org/10.1002/qj.49712353806>.
- Chung, E.S., Sohn, B.J. and Schmetz, J. (2008) CloudSat shedding new light on high-reaching tropical deep convection observed with Meteosat. *Geophysical Research Letters*, 35, L02814. <https://doi.org/10.1029/2007GL032516>.
- Cioni, G., Cerrai, D. and Klocke, D. (2018) Investigating the predictability of a Mediterranean tropical-like cyclone using a storm-resolving model. *Quarterly Journal of the Royal Meteorological Society*, 144(714), 1598–1610. <https://doi.org/10.1002/qj.3322>.
- Cioni, G., Malguzzi, P. and Buzzi, A. (2016) Thermal structure and dynamical precursor of a Mediterranean tropical-like cyclone. *Quarterly Journal of the Royal Meteorological Society*, 142(697), 1757–1766. <https://doi.org/10.1002/qj.2773>.
- Claud, C., Alhammoud, B., Funatsu, B.M. and Chaboureaud, J.P. (2010) Mediterranean hurricanes: largescale environment and convective and precipitating areas from satellite microwave observations. *Natural Hazards and Earth System Sciences*, 10, 2199–2213. <https://doi.org/10.5194/nhess-10-2199-2010>.

- Corbosiero, K.L. and Molinari, J. (2002) The effects of vertical wind shear on the distribution of convection in tropical cyclones. *Monthly Weather Review*, 130, 2110–2123. [https://doi.org/10.1175/1520-0493\(2002\)130<2110:TEOVWS>2.0.CO;2](https://doi.org/10.1175/1520-0493(2002)130<2110:TEOVWS>2.0.CO;2).
- Corbosiero, K.L. and Molinari, J. (2003) The relationship between storm motion, vertical wind shear, and convective asymmetries in tropical cyclones. *Journal of Atmospheric Sciences*, 60, 366–376. [https://doi.org/10.1175/1520-0469\(2003\)060<0366:TRBSMV>2.0.CO;2](https://doi.org/10.1175/1520-0469(2003)060<0366:TRBSMV>2.0.CO;2).
- Dafis, S., Rysman, J.F., Claud, C. and Flaounas, E. (2018) Remote sensing of deep convection within a tropical-like cyclone over the Mediterranean Sea. *Atmospheric Science Letters*, 19(6), e823. <https://doi.org/10.1002/asl.823>.
- Davis, C.A. and Bosart, L.F. (2004) The TT problem. *Bulletin of the American Meteorological Society*, 85, 1657–1662. <https://doi.org/10.1175/BAMS-85-11-1657>.
- Davis, C.A. and Bosart, L.F. (2003) Baroclinically induced tropical cyclogenesis. *Monthly Weather Review*, 131, 2730–2747. [https://doi.org/10.1175/1520-0493\(2003\)131<2730:BITC>2.0.CO;2](https://doi.org/10.1175/1520-0493(2003)131<2730:BITC>2.0.CO;2).
- Davolio, S., Miglietta, M.M., Moscatello, A., Pacifico, F., Buzzi, A. and Rotunno, R. (2009) Numerical forecast and analysis of a tropical-like cyclone in the Ionian Sea. *Natural Hazards and Earth System Sciences*, 9, 551–562. <https://doi.org/10.5194/nhess-9-551-2009>.
- DeMaria, M. (1996) The effect of vertical shear on tropical cyclone intensity change. *Journal of Atmospheric Sciences*, 53, 2076–2087. [https://doi.org/10.1175/1520-0469\(1996\)053<2076:TEOVSO>2.0.CO;2](https://doi.org/10.1175/1520-0469(1996)053<2076:TEOVSO>2.0.CO;2).
- DeMaria, M., Knaff, J.A. and Conell, B.H. (2001) A tropical cyclone genesis parameter for the tropical Atlantic. *Weather and Forecasting*, 16, 219–233. [https://doi.org/10.1175/1520-0434\(2001\)016<0219:ATCGPF>2.0.CO;2](https://doi.org/10.1175/1520-0434(2001)016<0219:ATCGPF>2.0.CO;2).
- Di Muzio, E., Riemer, M., Fink, A.H. and Maier-Gerber, M. (2019) Assessing the predictability of Medicanes in ECMWF ensemble forecasts using an object-based approach. *Quarterly Journal of the Royal Meteorological Society*, 145(720), 1202–1217. <https://doi.org/10.1002/qj.3489>.
- Dowdy, A.J., Pepler, A., Di Luca, A., Cavicchia, L., Mills, G., Evans, J.P., Louis, S., McInnes, K.L. and Walsh, K. (2019) Review of Australian east coast low pressure systems and associated extremes. *Climate Dynamics*, 53, 4887–4910. <https://doi.org/10.1007/s00382-019-04836-8>.
- Emanuel, K.A. (2005) Genesis and maintenance of “Mediterranean hurricanes”. *Advances in Geosciences*, 2, 217–220. <https://doi.org/10.5194/adgeo-2-217-2005>.
- Ernst, J.A. and Matson, M. (1983) A Mediterranean tropical storm. *Weather*, 38(11), 332–337. <https://doi.org/10.1002/j.1477-8696.1983.tb04818.x>.
- Evans, J.L. and Braun, A. (2012) A climatology of subtropical cyclones in the South Atlantic. *Journal of Climate*, 25, 7328–7340. <https://doi.org/10.1175/JCLI-D-11-00212.1>.
- Evans, J.L. and Guishard, M.P. (2009) Atlantic subtropical storms. Part I: Diagnostic criteria and composite analysis. *Monthly Weather Review*, 137, 2065–2080. <https://doi.org/10.1175/2009MWR2468.1>.
- Finocchio, P.M., Majumdar, S.J., Nolan, D.S. and Iskandarani, M. (2016) Idealized tropical cyclone responses to the height and depth of environmental vertical wind shear. *Monthly Weather Review*, 144, 2155–2175. <https://doi.org/10.1175/MWR-D-15-0320.1>.
- Fischer, M.S., Tang, B.H. and Corbosiero, K.L. (2017) Assessing the influence of upper-tropospheric troughs on tropical cyclone intensification rates after genesis. *Monthly Weather Review*, 145, 1295–1313. <https://doi.org/10.1175/MWR-D-16-0275.1>.
- Fischer, M.S., Tang, B.H., Corbosiero, K.L. and Rozoff, C.M. (2018) Normalized convective characteristics of tropical cyclone rapid intensification events in the North Atlantic and eastern North Pacific. *Monthly Weather Review*, 146, 1133–1155. <https://doi.org/10.1175/MWR-D-17-0239.1>.
- Fita, L. and Flaounas, E. (2018) Medicanes as subtropical cyclones: the December 2005 case from the perspective of surface pressure tendency diagnostics and atmospheric water budget. *Quarterly Journal of the Royal Meteorological Society*, 144(713), 1028–1044. <https://doi.org/10.1002/qj.3273>.
- Flaounas, E., Raveh-Rubin, S., Wernli, H., Drobinski, P. and Bastin, S. (2015) The dynamical structure of intense Mediterranean cyclones. *Climate Dynamics*, 44, 2411–2427. <https://doi.org/10.1007/s00382-014-2330-2>.
- Frank, W.M. and Ritchie, E.A. (2001) Effects of vertical wind shear on the intensity and structure of numerically simulated hurricanes. *Monthly Weather Review*, 129, 2249–2269. [https://doi.org/10.1175/1520-0493\(2001\)129<2249:EOVWSO>2.0.CO;2](https://doi.org/10.1175/1520-0493(2001)129<2249:EOVWSO>2.0.CO;2).
- Funatsu, B.M., Claud, C. and Chaboureaud, J.P. (2007) Potential of advanced microwave sounding unit to identify precipitating systems and associated upper-level features in the Mediterranean region: case studies. *Journal of Geophysical Research*, 112, D17113. <https://doi.org/10.1029/2006JD008297>.
- Funatsu, B.M., Rysman, J.F., Claud, C. and Chaboureaud, J.P. (2018) Deep convective clouds distribution over the Mediterranean region from AMSU-B/MHS observations. *Atmospheric Research*, 207, 122–135. <https://doi.org/10.1016/j.atmosres.2018.03.003>.
- Galanaki, E., Flaounas, E., Kotroni, V., Lagouvardos, K. and Argiriou, A. (2016) Lightning activity in the Mediterranean: quantification of cyclones contribution and relation to their intensity. *Atmospheric Science Letters*, 17, 510–516. <https://doi.org/10.1002/asl.685>.
- Gallina, G.M. and Velden, C.S. (2002) Environmental vertical wind shear and tropical cyclone intensity change utilizing enhanced satellite derived wind information. In: *25th Conference on Hurricanes and Tropical Meteorology*. San Diego, CA: American Meteorological Society, pp. 172–173.
- González-Alemán, J.J., Pascale, S., Gutierrez-Fernandez, J., Murakami, H., Gaertner, M.A. and Vecchi, G.A. (2019) Potential increase in hazard from Mediterranean hurricane activity with global warming. *Geophysical Research Letters*, 46, 1754–1764. <https://doi.org/10.1029/2018GL081253>.
- González-Alemán, J.J., Valero, F., Martín-León, F. and Evans, J.L. (2015) Classification and synoptic analysis of subtropical cyclones within the northeastern Atlantic Ocean. *Journal of Climate*, 28, 3331–3352. <https://doi.org/10.1175/JCLI-D-14-00276.1>.
- Gray, W.M. (1968) Global view of the origin of tropical disturbances and storms. *Monthly Weather Review*, 96, 669–700. [https://doi.org/10.1175/1520-0493\(1968\)096<0669:GVOTOO>2.0.CO;2](https://doi.org/10.1175/1520-0493(1968)096<0669:GVOTOO>2.0.CO;2).
- Hanley, D., Molinari, J. and Keyser, D. (2001) A composite study of the interactions between tropical cyclones and

- upper-tropospheric troughs. *Monthly Weather Review*, 129, 2570–2584. [https://doi.org/10.1175/1520-0493\(2001\)129<2570:ACSOTI>2.0.CO;2](https://doi.org/10.1175/1520-0493(2001)129<2570:ACSOTI>2.0.CO;2).
- Harnos, D.S. and Nesbitt, S.W. (2011) Convective structure in rapidly intensifying tropical cyclones as depicted by passive microwave measurements. *Geophysical Research Letters*, 38, L07805. <https://doi.org/10.1029/2011GL047010>.
- Harnos, D.S. and Nesbitt, S.W. (2016) Varied pathways for simulated tropical cyclone rapid intensification. Part I: Precipitation and environment. *Quarterly Journal of the Royal Meteorological Society*, 142(697), 1816–1831. <https://doi.org/10.1002/qj.2780>.
- Hong, G., Heygster, G., Miao, J. and Kunzi, K. (2005) Detection of tropical deep convective clouds from AMSU-B water vapor channels measurements. *Journal of Geophysical Research*, 110, D05205. <https://doi.org/10.1029/2004JD004949>.
- Hong, G., Heygster, G., Notholt, J. and Buehler, S.A. (2008) Interannual to diurnal variations in tropical and subtropical deep convective clouds and convective overshooting from seven years of AMSU-B measurements. *Journal of Climate*, 21, 4168–4189. <https://doi.org/10.1175/2008JCLI1911.1>.
- Hong, G., Heygster, G. and Rodriguez, C.A.M. (2006) Effect of cirrus clouds on the diurnal cycle of tropical deep convective clouds. *Journal of Geophysical Research*, 111, D06209. <https://doi.org/10.1029/2005JD006208>.
- Jones, S.C. (1995) The evolution of vortices in vertical shear. Part I: Initially barotropic vortices. *Quarterly Journal of the Royal Meteorological Society*, 121(524), 821–851. <https://doi.org/10.1002/qj.49712152406>.
- Kotta, D. and Kitsiou, D. (2019) Medicanes triggering chlorophyll increase. *Journal of Marine Science and Engineering*, 7(3), 75. <https://doi.org/10.3390/jmse7030075>.
- Kuo, Y., Shapiro, M.A. and Donall, E.G. (1991) The interaction between baroclinic and diabatic processes in a numerical simulation of a rapidly intensifying extratropical marine cyclone. *Monthly Weather Review*, 119, 368–384. [https://doi.org/10.1175/1520-0493\(1991\)119<0368:TIBBAD>2.0.CO;2](https://doi.org/10.1175/1520-0493(1991)119<0368:TIBBAD>2.0.CO;2).
- Lagouvardos, K., Kotroni, V., Nickovic, S., Jovic, D., Kallos, G. and Tremback, C.J. (1999) Observations and model simulations of a winter sub-synoptic vortex over the central Mediterranean. *Meteorological Applications*, 6, 371–383. <https://doi.org/10.1017/S1350482799001309>.
- Li, M., Ping, F., Chen, J. and Xu, L. (2016) A simulation study on the rapid intensification of typhoon *Megi* (2010) in vertical wind shear. *Atmospheric Science Letters*, 17, 630–638. <https://doi.org/10.1002/asl.713>.
- Lionello, P., Trigo, I.F., Gil, V., Liberato, M.L.R., Nissen, K.M., Pinto, J.G., Raible, C.C., Reale, M., Tanzarella, A., Trigo, R.M., Ulbrich, S. and Ulbrich, U. (2016) Objective climatology of cyclones in the Mediterranean region: a consensus view among methods with different system identification and tracking criteria. *Tellus A*, 68(1), 29391. <https://doi.org/10.3402/tellusa.v68.29391>.
- Machado, L.A.T., Laurent, H. and Lima, A.A. (2002) Diurnal march of the convection observed during TRMM-WETAMC/LBA. *Journal of Geophysical Research*, 107, 8064. <https://doi.org/10.1029/2001JD000338>.
- Marra, A.C., Federico, S., Montopoli, M., Avolio, E., Baldini, L., Casella, D., D'Adderio, L.P., Dietrich, S., Sanò, P., Torcasio, R.C. and Panegrossi, G. (2019) The precipitation structure of the Mediterranean tropical-like cyclone *Numa*: analysis of GPM observations and numerical weather prediction model simulations. *Remote Sensing*, 11(14), 1690. <https://doi.org/10.3390/rs11141690>.
- Mazza, E., Ulbrich, U. and Klein, R. (2017) The tropical transition of the October 1996 medicane in the western Mediterranean Sea: a warm seclusion event. *Monthly Weather Review*, 145(7), 2575–2595. <https://doi.org/10.1175/MWR-D-16-0474.1>.
- McTaggart-Cowan, R., Galarneau Jr, T.J., Bosart, L.F. and Milbrandt, J.A. (2010) Development and tropical transition of an Alpine lee cyclone. Part I: Case analysis and evaluation of numerical guidance. *Monthly Weather Review*, 138, 2281–2307. <https://doi.org/10.1175/2009MWR3147.1>.
- Miglietta, M.M., Cerrai, D., Laviola, S., Cattani, E. and Levizzani, V. (2017) Potential vorticity patterns in Mediterranean “hurricanes”. *Geophysical Research Letters*, 44, 2537–2545. <https://doi.org/10.1002/2017GL072670>.
- Miglietta, M.M., Laviola, S., Malvaldi, A., Conte, D., Levizzani, V. and Price, C. (2013) Analysis of tropical-like cyclones over the Mediterranean Sea through a combined modeling and satellite approach. *Geophysical Research Letters*, 40(10), 2400–2405. <https://doi.org/10.1002/grl.50432>.
- Miglietta, M.M. and Rotunno, R. (2019) Development mechanisms for Mediterranean tropical-like cyclones (medicanes). *Quarterly Journal of the Royal Meteorological Society*, 145(721), 1444–1460. <https://doi.org/10.1002/qj.3503>.
- Montgomery, M.T. and Farrell, B.F. (1992) Polar low dynamics. *Journal of Atmospheric Sciences*, 49, 2484–2505. [https://doi.org/10.1175/1520-0469\(1992\)049<2484:PLD>2.0.CO;2](https://doi.org/10.1175/1520-0469(1992)049<2484:PLD>2.0.CO;2).
- Moscattello, A., Miglietta, M.M. and Rotunno, R. (2008b) Numerical analysis of a Mediterranean “hurricane” over south-eastern Italy. *Monthly Weather Review*, 136, 4373–4397. <https://doi.org/10.1175/2008MWR2512.1>.
- Moscattello, A., Miglietta, M.M. and Rotunno, R. (2008a) Observational analysis of a Mediterranean ‘hurricane’ over south-eastern Italy. *Weather*, 63(10), 306–311. <https://doi.org/10.1002/wea.231>.
- Nolan, D.S. and Grasso, L.D. (2003) Three-dimensional, nonhydrostatic perturbations to balanced, hurricane-like vortices. Part II: Symmetric response and nonlinear simulations. *Journal of Atmospheric Sciences*, 60, 2717–2745. [https://doi.org/10.1175/1520-0469\(2003\)060<2717:NTPTBH>2.0.CO;2](https://doi.org/10.1175/1520-0469(2003)060<2717:NTPTBH>2.0.CO;2).
- Nolan, D.S., Moon, Y. and Stern, D.P. (2007) Tropical cyclone intensification from asymmetric convection: energetics and efficiency. *Journal of Atmospheric Sciences*, 64, 3377–3405. <https://doi.org/10.1175/JAS3988.1>.
- Noyelle, R., Ulbrich, U., Becker, N. and Meredith, E.P. (2019) Assessing the impact of sea surface temperatures on a simulated medicane using ensemble simulations. *Natural Hazards and Earth System Sciences*, 19, 941–955. <https://doi.org/10.5194/nhess-19-941-2019>.
- Olander, T.L. and Velden, C. (2009) Tropical cyclone convection and intensity analysis using differenced infrared and water vapor imagery. *Weather and Forecasting*, 24, 1558–1572. <https://doi.org/10.1175/2009WAF2222284.1>.
- Petterssen, S. (1956) *Weather Analysis and Forecasting*. In: *Weather and weather systems*, Vol. II, 2nd edition. New York, NY: McGraw-Hill. <https://doi.org/10.1002/qj.49708435918>.
- Posselt, D.J. and Martin, J.E. (2004) The effect of latent heat release on the evolution of a warm occluded thermal structure. *Monthly Weather Review*, 132, 578–599. [https://doi.org/10.1175/1520-0493\(2004\)132<0578:TEOLHR>2.0.CO;2](https://doi.org/10.1175/1520-0493(2004)132<0578:TEOLHR>2.0.CO;2).

- Pytharoulis, I. (2018) Analysis of a Mediterranean tropical-like cyclone and its sensitivity to the sea surface temperatures. *Atmospheric Research*, 208, 167–179. <https://doi.org/10.1016/j.atmosres.2017.08.009>.
- Pytharoulis, I., Craig, G.C. and Ballard, S.P. (2000) The hurricane-like Mediterranean cyclone of January 1995. *Meteorological Applications*, 7, 261–279. [https://doi.org/10.1016/S1464-1909\(99\)00056-8](https://doi.org/10.1016/S1464-1909(99)00056-8).
- Pytharoulis, I., Matsangouras, I.T., Tegoulas, I., Kotsopoulos, S., Karacostas, T.S. and Nastos, P.T. (2017) *Numerical study of the medicane of November 2014. In Perspectives on Atmospheric Sciences*. Berlin, Germany: Springer, pp. 115–121.
- Ragone, F., Mariotti, M., Parodi, A., von Hardenberg, J. and Pasquero, C. (2018) A climatological study of western Mediterranean medicanes in numerical simulations with explicit and parameterized convection. *Atmosphere*, 9(10), 397.
- Rasmussen, E. and Zick, C. (1987) A subsynoptic vortex over the Mediterranean with some resemblance to polar lows. *Tellus A*, 39, 408–425. <https://doi.org/10.3402/tellusa.v39i4.11770>.
- Raveh-Rubin, S. and Flaounas, E. (2017) A dynamical link between deep Atlantic extratropical cyclones and intense Mediterranean cyclones. *Atmospheric Science Letters*, 18, 215–221. <https://doi.org/10.1002/asl.745>.
- Reasor, P.D., Montgomery, M.T. and Grasso, L.D. (2004) A new look at the problem of tropical cyclones in vertical shear flow: vortex resiliency. *Journal of Atmospheric Sciences*, 61, 3–22. [https://doi.org/10.1175/1520-0469\(2004\)061<0003:ANLATP>2.0.CO;2](https://doi.org/10.1175/1520-0469(2004)061<0003:ANLATP>2.0.CO;2).
- Riemer, M., Montgomery, M.T. and Nicholls, M.E. (2010) A new paradigm for intensity modification of tropical cyclones: thermodynamic impact of vertical wind shear on the inflow layer. *Atmospheric Chemistry and Physics*, 10, 3163–3188. <https://doi.org/10.5194/acp-10-3163-2010>.
- Romera, R., Gaertner, M.Á., Sánchez, E., Domínguez, M., González-Alemán, J.J. and Miglietta, M.M. (2017) Climate change projections of medicanes with a large multi-model ensemble of regional climate models. *Global and Planetary Change*, 151, 134–143. <https://doi.org/10.1016/j.gloplacha.2016.10.008>.
- Romero, R. and Emanuel, K. (2017) Climate change and hurricane-like extratropical cyclones: projections for North Atlantic polar lows and medicanes based on CMIP5 models. *Journal of Climate*, 30(1), 279–299. <https://doi.org/10.1175/JCLI-D-16-0255.1>.
- Rysman, J.-F., Claud, C., Chaboureaud, J.-P., Delanoë, J. and Funatsu, B.M. (2016) Severe convection in the Mediterranean from microwave observations and a convection-permitting model. *Quarterly Journal of the Royal Meteorological Society*, 142(S1), 43–55. <https://doi.org/10.1002/qj.2611>.
- Rysman, J.-F., Claud, C. and Delanoë, J. (2017) Monitoring deep convection and convective overshooting from 60°S to 60°N using MHS: a Cloudsat/CALIPSO-based assessment. *IEEE Geoscience and Remote Sensing Letters*, 14, 159–163. <https://doi.org/10.1109/LGRS.2016.2631725>.
- Schmetz, J., Tjemkes, S.A., Gube, M. and van de Berg, L. (1997) Monitoring deep convection and convective overshooting with Meteosat. *Advances in Space Research*, 19(3), 433–441. [https://doi.org/10.1016/S0273-1177\(97\)00051-3](https://doi.org/10.1016/S0273-1177(97)00051-3).
- Setvak, M., Rabin, R.M. and Wang, P.K. (2007) Contribution of the MODIS instrument to observations of deep convective storms and stratospheric moisture detection in GOES and MSG imagery. *Atmospheric Research*, 83, 505–518. <https://doi.org/10.1016/j.atmosres.2005.09.015>.
- Shapiro, M.A. and Keyser, D. (1990) Fronts, jet streams and the tropopause. In: Newton, C.W. and Holopainen, E.O. (Eds.) *In Extratropical Cyclones, the Erik Palmén Memorial*. Boston, MA: American Meteorological Society, pp. 167–191. <https://doi.org/10.1007/978-1-944970-33-8>.
- Stevenson, S.N., Corbosiero, K.L. and Molinari, J. (2014) The convective evolution and rapid intensification of hurricane Earl (2010). *Monthly Weather Review*, 142, 4364–4380. <https://doi.org/10.1175/MWR-D-14-00078.1>.
- Stoelinga, M.T. (1996) A potential vorticity-based study of the role of diabatic heating and friction in a numerically simulated baroclinic cyclone. *Monthly Weather Review*, 124, 849–874. [https://doi.org/10.1175/1520-0493\(1996\)124<0849:APVBSO>2.0.CO;2](https://doi.org/10.1175/1520-0493(1996)124<0849:APVBSO>2.0.CO;2).
- Tang, B. and Emanuel, K. (2010) Midlevel ventilation's constraint on tropical cyclone intensity. *Journal of Atmospheric Sciences*, 67, 1817–1830. <https://doi.org/10.1175/2010JAS3318.1>.
- Tian, B., Soden, B.J. and Wu, X. (2004) Diurnal cycle of convection, clouds, and water vapor in the tropical upper troposphere: satellites versus a general circulation model. *Journal of Geophysical Research*, 109, D10101. <https://doi.org/10.1029/2003JD004117>.
- Tourville, N., Stephens, G., DeMaria, M. and Vane, D. (2015) Remote sensing of tropical cyclones: observations from CloudSat and A-Train profilers. *Bulletin of the American Meteorological Society*, 96(4), 609–622. <https://doi.org/10.1175/BAMS-D-13-00282.1>.
- Tous, M. and Romero, R. (2013) Meteorological environments associated with medicane development. *International Journal of Climatology*, 33, 1–14. <https://doi.org/10.1002/joc.3428>.
- Tous, M., Romero, R. and Ramis, C. (2012) Surface heat fluxes influence on medicane trajectories and intensification. *Atmospheric Research*, 123, 400–411. <https://doi.org/10.1016/j.atmosres.2012.05.022>.
- Trigo, I.F., Davies, T.D. and Bigg, G.R. (1999) Objective climatology of cyclones in the Mediterranean region. *Journal of Climate*, 12, 1685–1696. [https://doi.org/10.1175/1520-0442\(1999\)012%3C1685:OCOCIT%3E2.0.CO;2](https://doi.org/10.1175/1520-0442(1999)012%3C1685:OCOCIT%3E2.0.CO;2).
- Ulbrich, U., Lionello, P., Belušić, D., Jacobeit, J., Knippertz, P., Kuglitsch, F.G., Leckebusch, G.C., Luterbacher, J., Maugeri, M., Maheras, P., Nissen, K.M., Pavan, V., Pinto, J.G., Saaroni, H., Seubert, S., Toreti, A., Xoplaki, E. and Ziv, B. (2012) Climate of the Mediterranean: synoptic patterns, temperature, precipitation, winds, and their extremes. In: *The Climate of the Mediterranean Region*. Elsevier, pp. 301–346. <https://doi.org/10.1016/C2011-0-06210-5>.
- Wakimoto, R.M. and Black, P.G. (1994) Damage survey of hurricane Andrew and its relationship to the eyewall. *Bulletin of the American Meteorological Society*, 75, 189–200. [https://doi.org/10.1175/1520-0477\(1994\)075%3C0189:DSOHA%3E2.0.CO;2](https://doi.org/10.1175/1520-0477(1994)075%3C0189:DSOHA%3E2.0.CO;2).
- Walsh, K., Giorgi, F. and Coppola, E. (2014) Mediterranean warm-core cyclones in a warmer world. *Climate Dynamics*, 42, 1053–1066. <https://doi.org/10.1007/s00382-013-1723-y>.
- Wilcox, E.M. (2003) Spatial and temporal scales of precipitating tropical cloud systems in satellite imagery and the NCAR CCM3. *Journal of Climate*, 16(22), 3545–3559. [https://doi.org/10.1175/1520-0442\(2003\)016%3C3545:SATSOP%3E2.0.CO;2](https://doi.org/10.1175/1520-0442(2003)016%3C3545:SATSOP%3E2.0.CO;2).

- Winstanley, D. (1970) The North African flood disaster, September 1969. *Weather*, 25 (9), 390–403. <https://doi.org/10.1002/j.1477-8696.1970.tb04128.x>.
- Wu, Q. and Ruan, Z. (2016) Diurnal variations of the areas and temperatures in tropical cyclone clouds. *Quarterly Journal of the Royal Meteorological Society*, 142 (700), 2788–2796. <https://doi.org/10.1002/qj.2868>.
- Yang, G.Y. and Slingo, J. (2001) The diurnal cycle in the Tropics. *Monthly Weather Review*, 129, 784–801. [https://doi.org/10.1175/1520-0493\(2001\)129<0784:TDCITT>2.0.CO;2](https://doi.org/10.1175/1520-0493(2001)129<0784:TDCITT>2.0.CO;2).
- Zeng, Z., Wang, Y. and Chen, L. (2010) A statistical analysis of vertical shear effect on tropical cyclone intensity change in the North Atlantic. *Geophysical Research Letters*, 37, L02802. <https://doi.org/10.1029/2009GL041788>.
- Zhang, W., Villarini, G., Scoccimarro, E. and Napolitano, F. (2020) Examining the precipitation associated with medicanes in the

high-resolution ERA-5 reanalysis data. *International Journal of Climatology*. 1–7. <https://doi.org/10.1002/joc.6669>.

SUPPORTING INFORMATION

Additional supporting information may be found online in the Supporting Information section at the end of this article.

How to cite this article: Dafis S, Claud C, Kotroni V, Lagouvardos K, Rysman J-F. Insights into the convective evolution of Mediterranean tropical-like cyclones. *Q J R Meteorol Soc.* 2020;1–23. <https://doi.org/10.1002/qj.3896>

2.4 Summary and Discussion

In this chapter, the first detailed analysis of DC evolution, vertical wind shear and vortex tilt during MTLCs has been conducted. First, the MTLC ROLF was studied in detail using for the first time a combination of a ground-based lightning detection system and satellite diagnostics in the infrared and microwave spectrum from geostationary and polar-orbiting satellites to detect DC and OT/COV, as well as heavy rainfall. Several differences have been highlighted when it was compared with a climatology of extratropical cyclones in the Mediterranean, like the time of DC activity and rainfall peak relatively to the maximum intensity of the cyclone and the more than 24-hours' time-lag between the maximum lightning activity and the minimum SLP. One additional interesting finding was the large temporal lag between the peak of lightning activity and the occurrence of maximum DC activity. In fact, DC and OT/COV were detected even after the maximum intensity of ROLF, but lightning activity was scarce and weak, similar to tropical cyclones and hurricanes, raising questions on the dynamics of the clouds during MTLCs.

As a second step the satellite analysis was extended on 9 MTLCs (including ROLF) between 2005 and 2018, using again a combination of remote sensing techniques with infrared and microwave data. Results showed that symmetric DC around the centers of MTLCs is rare and short-lasting, and does not always result in intensification of the studied cases. In addition, the DC activity within 50 km from the MTLCs' centers was not connected with decrease of deep layer wind shear (DLS) and strong DC activity was observed during the turn of the vortex tilt upshear, resembling the vortex resiliency of TCs during strong DLS in order to reduce their vortex tilt (Reasor et al., 2004). By mentioning the strong DLS in TCs we usually refer to values of more than 10 m s^{-1} but in the Mediterranean, the DLS often exceeds this threshold and can reach extreme values above 20 m s^{-1} . Despite these high values of DLS that denote the presence of baroclinic zones in the close proximity of the MTLCs, the surface cyclones succeed to sustain their intensity and sometime to intensify, mostly under the influence of DC activity close to their center. The vortex tilt during strong DLS and the relative position of DC activity is illustrated in Fig. 2.7.

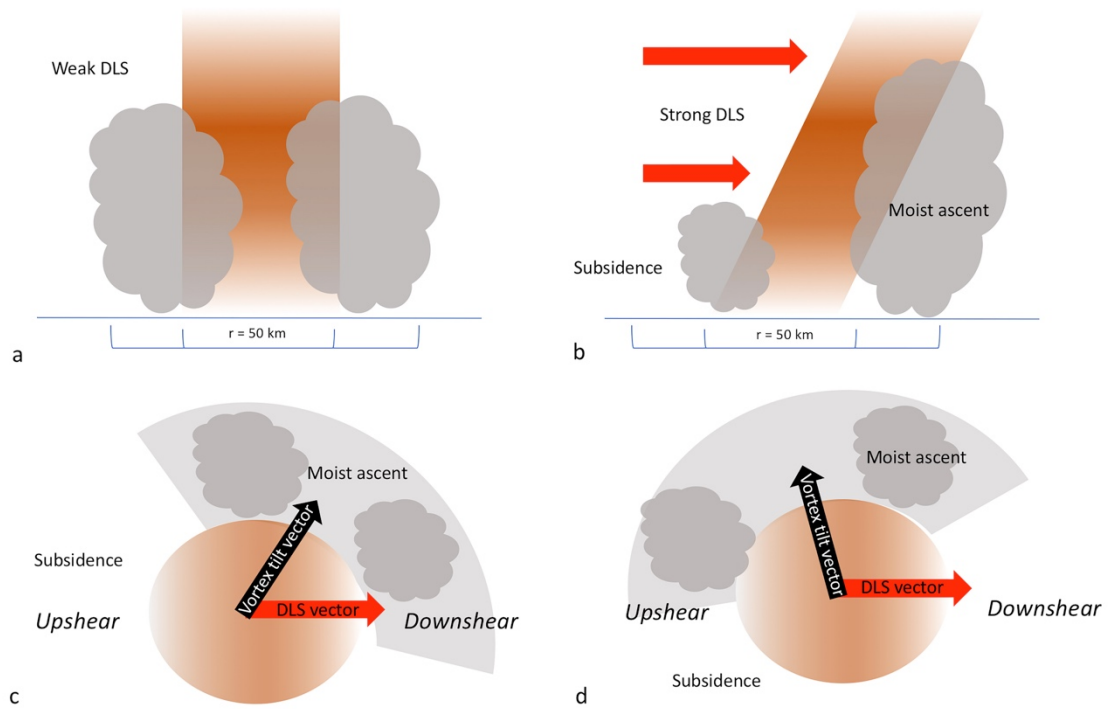


Fig. 2.7 Schematic illustration of the DC activity (grey shade) with respect to the DLS vector (red arrow) and vortex tilt (black arrow), close to the core of MTLCs (orange shade). During weak DLS the vortex tilt is small and DC activity can be found in all quadrants resulting in brief symmetric DC activity around the cyclone center (a), and during strong DLS the vortex tilt increases and DC activity is more asymmetric (b) mostly found in the downshear quadrants of the MTLCs. When DC is initiated downshear and is advected counter-clockwise, the vortex tilt is mostly found downshear left (c) (right in some exceptions). The DC activity is important in the upshear quadrants where usually subsidence is found, when the vortex tilt vector bends towards the upshear quadrants (d) and this period is connected with intensification of the MTLCs.

Moreover, the suggestion that MTLCs can be divided into different groups has also been discussed, similar to a previously proposed classification by Miglietta and Rotunno (2019). The proposed classification in this thesis is based on the position of DC activity relative to the DLS vector, the intensification periods based on DCPIXELS distribution, and the structure of the MTLCs. The first group of MTLCs is not connected with intense DC activity close to the cyclone centers and their intensification is not correlated well with the DC activity. The second group consists of some long-lasting MTLCs during which upshear DC activity is intense before and during their intensification periods during weak and moderate DLS. In the last group, some embedded MTLCs to larger cyclonic systems are included, and their DC activity cannot be clearly connected to their intensification periods which were limited in time compared to the MTLCs in Groups 1 & 2.

Chapter 3

Assessment of the contribution of diabatic processes in the intensification of Mediterranean tropical-like cyclones

3.1 Introduction

In the previous chapter a classification of the MTLCs into 3 categories was proposed, based on their DC evolution, and time of cyclone intensification. The MTLCs Med2005, Med2007 and QENDRESA, for which the maximum intensity of the cyclones is found at the early stages of their development and during weak DC activity, form the first group, the second group consists of the MTLCs ROLF, TRIXIE, NUMA and ZORBAS during which strong and long-lasting DC activity leads to intensification periods, and the last group is formed by Med2006 and ILONA which are short-lasting mesoscale cyclones embedded within larger cyclonic systems. One key feature in the DC activity is found in Group 2, where DC activity in the upshear quadrants of the cyclones is significant prior to their maximum intensity, something that is not observed in the other 2 groups. In order to investigate these features more in detail, we use state-of-the-art numerical modeling to help us explore the different intensification mechanisms involved in MTLCs.

The quantification of the relative roles of dry baroclinic vs moist diabatic processes on the development of the most intense cyclones is a long standing issue (Sanders, 1986; Wernli et al., 2002). While sensitivity studies using Numerical Weather Prediction (NWP) models can give helpful indications for single cases, a diagnostic framework is needed that can be applied to a wide range of modeling data in various spatial and temporal resolutions. To this end, we use a modified version of the classical pressure tendency equation (PTE) (Godson, 1948) and a PV budget technique based on online PV tracers in a NWP model. The purpose of this study is to improve the understanding of processes that set the vertical structure of PV and associated intensity changes of the studied cyclones during MTLCs, and quantify the relative contribution of the different physical processes involved. The main reasons to perform such an analysis are:

- Evaluate our hypothesis in Chapter 2 based on satellite observations that the MTLCs have distinct differences regarding the contribution of DC activity.
- Distinguish the periods during which MTLCs attain tropical-like characteristics.
- Quantify the contribution of diabatic processes in the intensification of MTLCs.

- Study the evolution of PV during MTLCs with special focus on the diabatically generated PV structures.

In Section 3.2.1 the configuration of the WRF model is presented, then there is a detailed description of the PV tracers in Section 3.2.2 and the pressure tendency diagnostics are shown in Section 3.2.3. The results of the numerical study and a summary with the final remarks are presented in Sections 3.3 and 3.4 respectively.

3.2 Data and methods

3.2.1 The numerical model (WRF)

A plethora of prognostic NWP models from the national weather agencies around the globe are currently used, considering different sources of weather observations. The numerical solutions are performed in a three-dimensional grid, by solving the governing partial differential equations derived from considering conservation of momentum and mass, the continuity equation, the equation of state and the first and second law of thermodynamics (Lynch, 2008; Jacob, 1999). According to the purpose of each research study or operational application, different spatial and temporal scales are used.

One of the most commonly used NWP models is the Weather Research and Forecasting model - Advanced Research WRF (WRF-ARW) (Skamarock et al., 2019). WRF has a large community of users and developers around the world, and was designed as the successor of the NWP Fifth-Generation Penn State/NCAR Mesoscale Model (MM5). WRF has two dynamic cores: the Advanced Research WRF (ARW) for research applications, and the Non-hydrostatic Mesoscale Model (NMM) for operational applications. WRF-ARW provides many advanced options in physics, numerics, and data assimilation, while WRF-NMM is less flexible in terms of options, but is computationally more efficient than WRF-ARW, more suitable for operational forecasting. For the purpose of our study, we use the WRF-ARW v.4.0 model and in the following paragraphs we describe the choice of physics and numeric options. From now on we will refer to WRF-ARW by the acronym WRF. The WRF physics options fall into several categories, each containing several choices. The physics categories are (1) microphysics, (2) cumulus parameterization, (3) planetary boundary layer (PBL), (4) land-surface model, and (5) radiation. In the following paragraphs, some explanations are provided to justify our choices and are summarized in Table 3.1.

WRF includes several options and the word “scheme” is often used when referring to a specific option for describing physics in the modelled domain. The physics categories are not independent of each other and their interactions are schematically shown in Fig. 3.1. The surface physics scheme describes the physics interactions between the surface layer and the land surface model which are often grouped together, but all the physics categories have interactions with the surface schemes (Skamarock et al., 2008; Jiménez and Dudhia, 2013). The physics packages are solved by the physics model drivers, separated from the dynamical solver, and they compute tendencies for the velocity components, potential temperature, and moisture fields. The initialization of the physics is called prior to the first model step and may include reading in data files for

physics tables or calculating look-up tables of functions and each physics module includes an initialization routine.

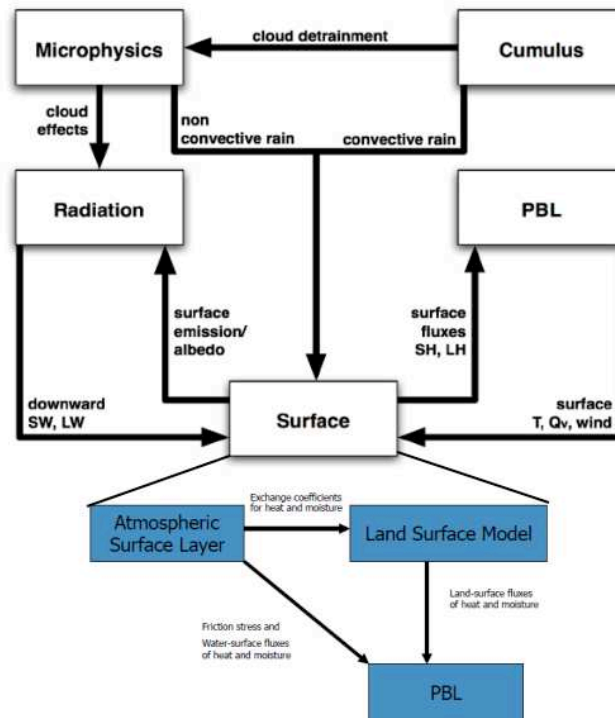


Fig. 3.1 Interactions of each physics category in the WRF model. Surface physics include atmospheric surface layer and land surface model (blue boxes) (source: Dudhia, 2012).

- WRF Grid and Nesting techniques

Grids in WRF are logically rectilinear¹ and the spatial discretization in the WRF solver uses a C grid staggering for the wind velocity variables. The normal velocities are staggered one-half grid length from the thermodynamic variables. The variable indices, (i, j, k) , indicate variable locations with $(x, y, \eta) = (i\Delta x, j\Delta y, k\Delta \eta)$. Variables for a WRF cell indexed (i, j, k) can be located at one of 4 possible points:

- at the center of the cell - theta points (mass points), not staggered
- at the center of the left face - U point, staggered in X
- at the center of the front face - V point, staggered in Y
- at the center of the bottom face - W point, staggered in Z

where U , V , and W are the components of the wind velocity vector at the geometrically horizontal and vertical directions. Scalar variables (geopotential, temperature) are defined at theta-points (θ) and the moisture variables, pressure and inverse density are computed at the mass points on the discrete grid. The grid lengths

¹A rectilinear grid is a logically rectangular grid in which the coordinates in physical space can be fully specified by the spacing of grid points along each grid axis. The gridpoints are located where the coordinate values intersect. The spacing along each axis may vary. (source: American Meteorological Glossary).

Δx and Δy are constants in the model formulation and changes in the physical grid lengths associated with the projections to the sphere are defined by the user. The coordinate definition for the nonhydrostatic equations is the sigma coordinate system and the vertical grid length $\Delta\eta$ is not a fixed constant but it is specified in the initialization. The η values vary from a value of 1 at the surface to 0 at the model top, decreasing monotonically (Fig. 3.2a).

The WRF equations follow a terrain-following hydrostatic-pressure vertical coordinate denoted by η , which is also referred to a mass vertical coordinate. In previous versions of the WRF model (prior to v.4.0), η was defined as:

$$\eta = \frac{p_d - p_t}{p_s - p_t} \quad (\text{Eq. 3.1})$$

where p_d is the hydrostatic component of the pressure of dry air, and p_s and p_t refer to values of p_d along the surface and top boundaries, respectively. In the WRF version 4.0, the vertical coordinate is slightly different than in Eq. 3.1 and allows the influence of the terrain on the coordinate surfaces to be removed more rapidly with increasing height above the surface, as illustrated in Fig. 3.2b. For this modified vertical coordinate, an hybrid sigma-pressure vertical coordinate is employed as described by Park et al. (2013), which is similar to that used in the National Center for Atmospheric Research (NCAR) Community Atmospheric Model (CAM).

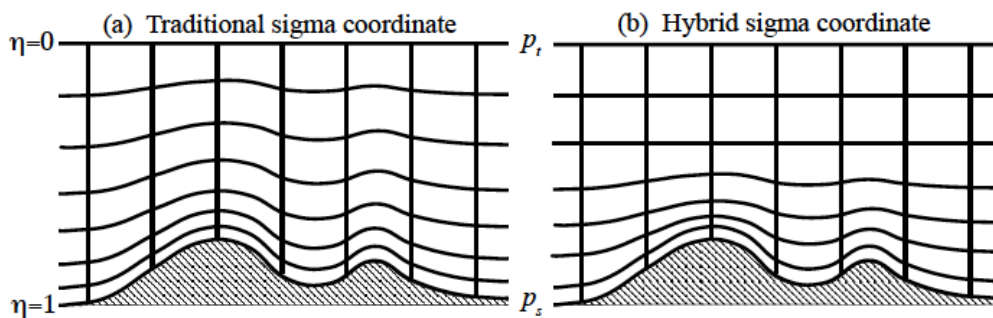


Fig. 3.2 The η coordinate system used for the old WRF versions, up to version 3.9 (a) and in WRF version 4.0 (b).

In order to simulate mesoscale phenomena, such as the MTLCS in this study, a dynamical downscaling technique must be applied to the coarse reanalysis data, which is achieved by nested-grid model runs. Grid nesting is defined as a finer-grid-resolution run, made as a subsequent run after a coarser-grid-resolution run. This is needed due to the fact that forcing/reanalysis data are too coarse to simulate precisely localized convection, topography and other phenomena. The nested boundary conditions also provide higher temporal resolution, specified by the user. A simulation involves one outer grid and may contain multiple inner nested grids which are referred to as “child grids”. Nested grid simulations can be produced using either the 1-way nesting or the 2-way nesting technique. The 1-way and 2-way nesting options refer to the way in which the coarse and fine grids interact. In both 1-way and 2-way simulation modes, the fine-grid boundary conditions (i.e., the lateral boundaries) are interpolated from the parent grid. For the needs of our study, an 1-way

technique was chosen with a 3:1 grid size ratio (Fig. 3.3). In this nesting technique, the only information exchange is from the parent grid to the child grid; hence, the name “1-way nesting”.

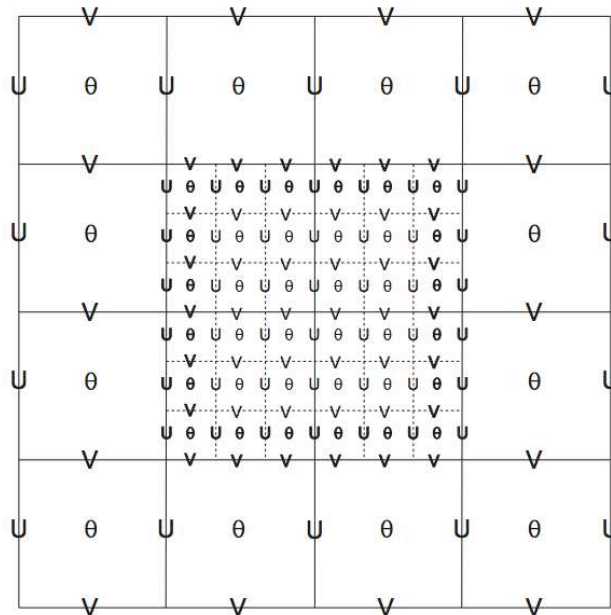


Fig. 3.3 Schematic representation of the nesting technique used in this study. An Arakawa-C grid staggering for a portion of a parent domain, with an imbedded nested domain using a 3:1 grid size ratio (i.e., 9 and 3 km grid increment in this study). Solid lines show the coarse grid cell boundaries, and the dashed lines are the boundaries for each fine grid cell of the nested domain. The horizontal components of velocity (U and V) are defined along the normal cell face, and the thermodynamic variables (θ) are defined at the center of each grid cell (source: Skamarock et al., 2019).

- WRF Planetary Boundary Layer schemes

The planetary boundary layer (PBL) is directly influenced by the surface processes in terms of heat exchange and mass fluxes. The purpose of the PBL schemes is to distribute the surface fluxes with boundary layer eddy fluxes (heat, moisture, momentum) and allow for PBL growth by entrainment (from the layers aloft the PBL top height). They are one-dimensional and determine the flux profiles within the well-mixed PBL and the more stable layer aloft, and thus provide the tendencies of temperature, moisture (including clouds), and horizontal momentum in the entire atmospheric column. Above PBL top, the PBL schemes also do vertical diffusion due to turbulence by solving the Turbulent Kinetic Energy (TKE) prediction equations in each column: for buoyancy and shear production, dissipation and vertical mixing. Diffusion in WRF is categorized under two parameters: the diffusion option and the K option. In our study, the Yonsei University (YSU) (Hong et al., 2006) PBL scheme is activated, so the vertical diffusion comes from the PBL scheme, and not by the diffusion scheme. The K option (horizontal diffusion) is diagnosed from just the horizontal deformation (2-D deformation). The YSU scheme treats explicitly the entrainment layer at the PBL top, which is defined by a critical bulk Richardson number equal to zero, thus the buoyancy profile determines the layer with maximum

entrainment or in other words, the layer at which diffusivity becomes zero. The YSU scheme is a first-order non-local scheme which means that it attempts to simulate the effects of large eddies in the convective PBL using model fields at many vertical levels in the lower troposphere. Several studies have shown the superiority of the YSU scheme over other options in the WRF model, as it more accurately simulates deep vertical mixing in buoyancy-driven PBLs with shallower mixing in strong-wind regimes and especially in environments with high liquid water content (e.g., Hu et al., 2010; Steeneveld et al., 2015), like deep convection over the sea which is the main focus of this thesis.

- **WRF Radiation and Land-Surface schemes**

The radiation schemes provide the atmospheric temperature tendencies through several processes which include absorption, reflection and scattering in the atmosphere and at the surface. The only source of radiation is the Sun and the schemes treat shortwave radiation for the visible and all other wavelengths of the solar spectrum. The upward flux of shortwave radiation is calculated from the reflection due to surface albedo. For the longer wavelengths, the longwave radiation includes infrared and thermal radiation absorbed and emitted by gases and the surface. The upward radiative longwave flux from the ground and the skin temperature are determined by the surface emissivity and the land-use type. In the presented simulations of this study, the Rapid Radiative Transfer Model (RRTM) scheme treats the longwave radiation and the Dudhia (MM5) scheme treats the shortwave radiation.

The Land-Surface schemes are one-dimensional models which provide the lower boundary conditions for the vertical fluxes treated by the PBL schemes and use variables calculated by the radiation, microphysics and convective schemes. They provide heat and moisture fluxes in multiple layers of the soil and include information about vegetation, root, canopy effects and snow/ice cover. The Noah 4-layer for soil temperature and moisture model is used for this study and provides sensible and latent heat fluxes to the PBL scheme. In addition, the “Revised MM5 similarity theory” surface layer scheme (Jiménez et al., 2012) is used to calculate friction velocities and exchange coefficients to be used by the Land-Surface scheme for the calculation of surface heat and moisture fluxes. This scheme is responsible for all the surface diagnostic fields over water surfaces. The Monin-Obukhov similarity theory (Monin and Obukhov, 1954) is used to compute the roughness lengths at the lowest model levels. Variables at 2 m and 10 m (e.g., temperature at 2 m and wind speed at 10 m heights) are computed through approximately log profiles that relate the lowest model level with the surface via a stability dependent profile of wind and scalars.

- **WRF Microphysics schemes**

The Microphysics scheme (MP) provides the atmospheric heat and moisture tendencies, averaged in grid-scale, resulting from radiative, dynamical or convective processes. These tendencies are solved using prediction equations for latent heat release from condensation, evaporation, deposition, sublimation, freezing and melting, for particle types (cloud water, rain drops, ice crystals, snow, graupel and hail) and their associated processes (e.g., aggregation, accretion, growth, fall-out). The MP schemes are divided into 2 main categories: Single-moment (SM) and Double-moment (DM). The SM schemes have one prediction equation for mass per

species (Q_r for rain, Q_s for snow, etc., where Q refers to mixing ratio) with particle size distribution being derived from fixed parameters (tables). The DM schemes add a prediction equation for number concentration per DM species (N_r for rain, N_s for snow, etc., where N refers to number concentration). The DM schemes are more computationally costly but they allow additional processes to SM schemes, such as size-sorting during particles fall-out and cloud condensation nuclei (CCN) effects. The fall-out terms of MP schemes handle the fall of particles (except cloud water) with lagrangian numerical methods which keep the schemes numerically stable.

The MP options have differing numbers of moisture variables, depending on the ice-phase and mixed-phase processes included. For example, graupel and hail are produced through riming between ice and water particles, which is one of the mixed-phase processes resolved by the MP schemes. For grid sizes less than 10 km, where updrafts may be resolved, mixed-phase schemes are recommended to be used, particularly in convective or icing situations (Skamarock et al., 2019). For coarser grids, the resolved weak vertical motions do not result in riming and these schemes can be avoided since they are more computationally expensive than less sophisticated MP schemes and would provide the same results.

In this study, the NSSL DM scheme is used since it realistically simulates the deep convection occurrence during the studied MTLCS (see more details in Section 3-Results). It is a DM scheme for cloud droplets, rain drops, ice crystals, snow, graupel, and hail. It also predicts the average graupel particle density, which allows graupel to span the range from frozen drops to low-density graupel. The NSSL MP scheme is suitable for cloud resolving simulations for research applications, especially on deep moist convection (Mansell et al., 2010).

- **WRF Convective parameterizations**

Because DC occurs on scales too small to be adequately resolved at coarse resolutions (e.g., 10 km grid increment), convective parameterization or cumulus schemes (CU hereafter) are used. The lack of capability of the NWP models to explicitly resolve convection at coarse domains is compensated by the use of CU parameterizations which calculate the rate of sub-grid-scale convective precipitation, the latent heat release and the redistribution of heat, moisture and momentum in the vertical. The first CU schemes in mid '70s parameterized convection by either relating the convective heating to moisture convergence in a column (Kuo, 1974; Anthes, 1977) or assuming the existence of a quasi-equilibrium state between the rate at which the large-scale processes destabilize the atmosphere and the rate of stabilization by an ensemble of convective clouds (Arakawa and Schubert, 1974). The modern and more sophisticated CU schemes are divided into 2 categories: a) adjustment type (e.g., Betts-Miller-Janjic) and b) mass-flux type (e.g., Kain-Fritsch, Grell-Freitas, Grell). The first type adjusts the column model sounding (vertical profile) towards a pre-determined, post-convective reference profile derived from climatology without the use of a plume model, while the latter type (and more complex) is based on an one-dimensional entraining plume model where convective available potential energy (hereafter CAPE) is consumed by the rearrangement of the air mass in a column (Fritsch and Chappell, 1980; Kain and Fritsch, 1990). The CAPE is used to diagnose the variability of conditional instability and is given by the following equation (Eq. 3.2):

Institut Polytechnique de Paris

91120 Palaiseau, France



$$CAPE = g \int_{LFC}^{EL} \left(\frac{T_p(z) - T_e(z)}{T_e(z)} \right) dz \quad (\text{Eq. 3.2})$$

where $T(z)$ is the temperature at height z , the subscripts p and e refer to the parcel and environmental values respectively, g is the acceleration of gravity, LFC is the level of free convection and EL is the equilibrium level (the level of neutral buoyancy).

The aim of CU schemes is to re-distribute the air in a column to account for vertical convective fluxes during deep convection. They transport (near-)surface air to top of a convective cloud (updrafts), and include subsidence within downdrafts that take mid-level air close or at the surface. Thus, they formulate the entrainment and detrainment of an atmospheric column and simulate the vertical structure of convection in individual columns (Fig. 3.4). It would be very inefficient in terms of computational time to perform these plume calculations for every individual grid point, so there are numeric “switches” to trigger or close the CU schemes. The triggers activate the scheme only in columns that meet certain criteria, such as presence of CAPE, weak convective inhibition (CIN) and a minimum cloud depth from parcel ascent between the lifted condensation level (LCL) and EL. The CIN diagnoses the negative buoyancy of the environment and it is calculated as:

$$CIN = -g \int_{Z_1}^{LFC} \left(\frac{T_p(z) - T_e(z)}{T_e(z)} \right) dz \quad (\text{Eq. 3.3})$$

where Z_1 is the originating level of the atmospheric parcel (usually averaged from the first 100 hPa from the surface). The closure switches determine the cloud mass-flux and remove CAPE by draining the atmospheric column. In addition, shallow convection needs to be parameterized by CU schemes. Shallow sub-grid clouds with nearly neutral buoyancy can form as shallow-convective updrafts detraining mass to their environment. They can be either remnants of previous updrafts or the cloud mass dispelled from currently active updraft cores. They can dissipate through lateral and vertical mixing, light precipitation, ice-crystal settling, and cloud-top entrainment instability, but they can also evolve into deep convection if the aforementioned criteria for CU triggering are met.

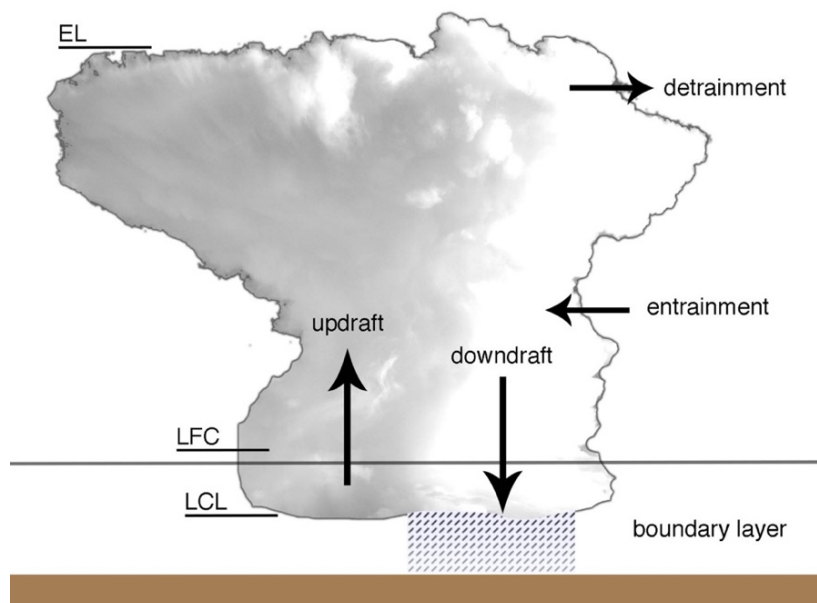


Fig. 3.4 Illustration of the main cumulus processes resolved by the CU schemes and the critical levels LCL (Lifted Condensation Level), LFC (Level of Free Convection) and EL (Equilibrium Level). The horizontal black line shows the level of the 0°C isotherm.

Numerous studies have shown the significant role of CU schemes in the performance of NWP models and the choice of CU scheme is linked to the appropriate representation of atmospheric conditions. For example, Mahoney and Lackman (2006) examined the sensitivity of forecasts of coastal cyclogenesis to the choice of the CU scheme and found significant differences among the various schemes, with the Kain–Fritsch (KF) scheme providing more accurate forecasts. Also, Manikin (2004) found great differences in ETA model forecasts using the KF and the Betts–Miller–Janjic (BMJ) (Betts and Miller, 1986; Janjic, 1994) schemes for two winter and summer cases. In addition, Gochis et al. (2002) studied the sensitivity of the evolution of the North American Monsoon system to the convective parameterization using the schemes of BMJ, KF and Grell (Grell, 1993; Grell et al., 1994). Among the three CPSs, KF generally gave significantly superior surface and upper-level verification error statistics. Moreover, Mazarakis et al. (2009) performed a sensitivity study of numerical forecasts to CU schemes for warm-period convective activity in Greece and results showed the superiority of the KF scheme among others. The high skill of the KF scheme in parameterizing DC was the main reason for using it in the simulations of this study.

The KF scheme is categorized by Stensrud (2007) as a low-level control convective scheme and is a mass-flux type scheme. Initiation of convection is governed by a trigger function which follows the concept of parcel theory in that, a parcel must be lifted to its level of free convection for deep convection to develop. In the original scheme version, the environmental CAPE is calculated based upon an undiluted ascent of the cloud base parcel, whereas in the latest version the environmental CAPE is calculated for an entraining parcel (Kain, 2004). The KF scheme has also the ability of detraining both snow and rain which is not the case for most of the available CU schemes in WRF. Sub-grid cloud fraction due to both deep and shallow convection is estimated and passed to the radiation schemes.

A summary of the WRF physics options used in this study is provided in Table 3.1.

Physics category	Definition	Scheme options used
Microphysics	Explicitly resolved water vapor, cloud, and precipitation processes	NSSL-2moment (Mansell et al., 2010)
Cumulus parameterization	Sub-grid-scale effects of convective and/or shallow clouds (activated only in parent domain)	Kain-Fritsch (Kain, 2004)
Surface layer	Calculation of friction velocities and exchange coefficients that enable the calculation of surface heat and moisture fluxes by the land-surface models and surface stress in the planetary boundary layer scheme	Revised MM5 Monin-Obukhov scheme (Jiménez et al., 2012)
Land Surface Model	Provides heat and moisture fluxes over land points and sea-ice points with atmospheric information from the surface layer scheme, radiative forcing from the radiation scheme, and precipitation forcing from the microphysics and convective schemes, together with internal information on the land's state variables and land-surface properties	Noah Land Surface Model: Unified NCEP/NCAR/AFWA scheme with soil temperature and moisture in four layers (<i>option = 2</i>)
Planetary Boundary Layer (PBL)	Vertical sub-grid-scale fluxes due to eddy transports in the whole atmospheric column	Yonsei University scheme: Non-local-K scheme with explicit entrainment layer and parabolic K profile in unstable mixed layer (<i>option = 1</i>)
Atmospheric Radiation	Atmospheric heating due to radiative flux divergence and surface downward longwave and shortwave radiation for the ground heat budget	For longwave radiation: RRTM scheme: Rapid Radiative Transfer Model (<i>option = 1</i>) For shortwave radiation: Dudhia scheme (<i>option = 1</i>)

Table 3.1 Summary of the WRF physics options used and their description based on Skamarock et al. (2019).

- Choice of the WRF Resolution

A numerical model domain is defined as the grid cells that are overlaid over a geographical area of interest for numerical modeling. Since the WRF domain has 3-D components, the concept of resolution includes the horizontal direction, the individual grid cell size (increment), the vertical direction and the number of vertical levels. Regarding the vertical resolution, there is no optimal number of pressure levels selection in WRF. For example, Aligo et al. (2009) tested several configurations of vertical resolution to investigate its impact on summer precipitation simulations, and found that a refined vertical grid resolution did not result in an improved simulation skill. But the simulation skill was improved when they increased the vertical resolution above the melting level (height when temperature becomes higher than 0 °C).

Regarding the horizontal resolution of the selected domains, several studies have shown that high-resolution simulations for precipitation (e.g., with a smaller than 10 km grid increment) are superior to coarse domains (e.g., Dafis et al., 2018; Cioni et al., 2016). As these horizontal resolutions close to 10 km are comparable with the depth of the atmosphere, they allow the numerically resolved vertical-turnover behavior: simulations first start to resolve deep convective clouds where explicit microphysics remove some of the CAPE from the troposphere at the expense of the CU scheme. At these resolutions in the range of 1 to 10 km the convective clouds and mass transport are only partially explicitly simulated as the intercloud separation scale is not adequately resolved (Arakawa and Wu, 2013). This range is also called the “Grey Zone” (Fig. 3.5), and it is recommended to switch off the CU scheme and let the MP scheme resolve explicitly the convective activity in the domain (Dudhia, 2012), but there is not a clear consensus about when the CU scheme should be used below 10 km grid increment. Sometimes these schemes have been found to be helpful in triggering convection in 5-10 km grid applications. Generally, they should not be used when the MP scheme can resolve the deep convective updrafts itself (e.g., < 4 km grid) (Skamarock et al., 2019).

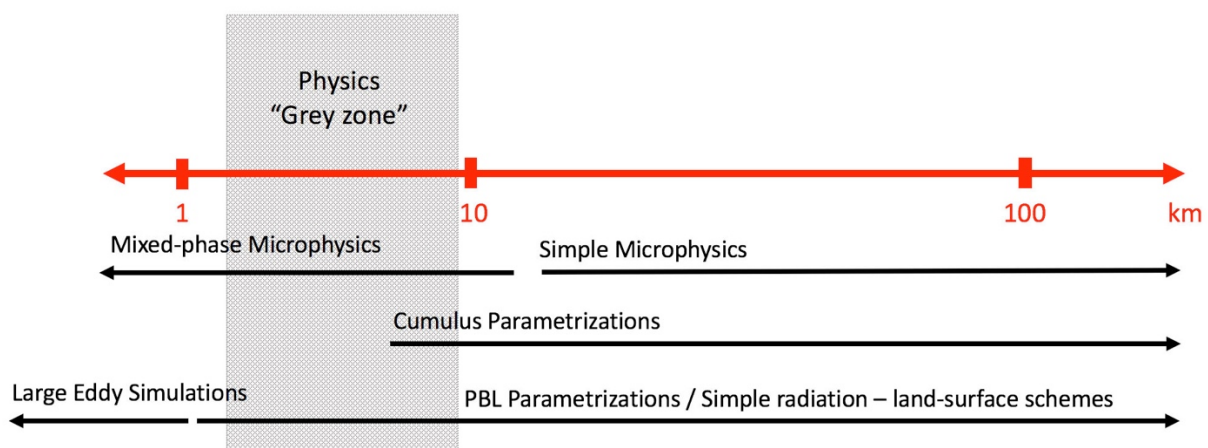


Fig. 3.5 Illustration of the horizontal resolution of a numerical model domain (red line) and the “Grey zone” (grey shading) discussed in the text. The black arrows indicate the range of the model horizontal resolution for which schemes should be used during numerical integrations.

- Analysis Nudging

In order to keep simulations close to the analyses and forcing (reanalysis) data during a numerical integration, extra forcing terms can be applied to the model equations. This technique is called “nudging” and can be implemented in a four-dimensional framework in three ways: a) analysis or grid nudging by forcing the simulation towards the forcing analysis grid-point by grid-point, b) observational nudging by forcing locally the simulation towards an observational dataset and c) spectral nudging which forces the simulation towards a spectra of waves in the analysis. The three techniques can be used in combination. The variables nudged in the model are the two horizontal wind components, the temperature and specific humidity.

An analysis nudging method is used for the simulations of this study in order to keep the coarse parent domain nudged close to the forcing analyses, while the inner domain is running un-nudged. By doing that, the boundary conditions for the inner (nested) domain have a better temporal resolution than if they were provided as linearly interpolated analyses. An extra tendency term is added to the variables’ equations as:

$$\frac{\partial \theta}{\partial t} = F(\theta) + G_{\theta} W_{\theta} (\hat{\theta}_o - \theta) \quad (\text{Eq. 3.4})$$

where $F(\theta)$ is the normal tendency terms due to physics, advection, etc., G_{θ} is a timescale controlling the nudging strength, and W_{θ} is an additional weight in time or space to limit the nudging, while $\hat{\theta}_o$ is the time- and space-interpolated analysis field value towards which the nudging relaxes the solution. Given that the nudging is an artificial forcing applied in the model, strong nudging may reduce or filter out extremes since it pushed the model toward a relatively smooth, large-scale state. For this reason in our study, the analysis nudging technique is only activated in the coarse parent domain every 3 hours and only for the temperature and wind fields.

3.2.2 Online potential vorticity tracers in WRF

The idea behind diabatic tracers of PV consists of the separation of the variable of interest φ into the sum of a materially conserved component φ_o , a diabatically generated component φ_d , and the resulted residual r_{φ} :

$$\varphi(x, t) = \varphi_o(x, t) + \varphi_d(x, t) + r_{\varphi}(x, t) \quad (\text{Eq. 3.5})$$

where x represents the location and t is time (Flaounas et al., 2020). The materially conserved and the diabatically generated parts are governed by the following equations:

$$\frac{D\varphi_o}{Dt} = 0 \quad (\text{Eq. 3.6})$$

$$\frac{D\varphi_d}{Dt} = S_{\varphi} \quad (\text{Eq. 3.7})$$

where S_φ is a source due to diabatic processes and the material derivative is described in Eq. 3.8:

$$\frac{D}{Dt} = \frac{\partial}{\partial t} + \mathbf{u} \cdot \nabla \quad (\text{Eq. 3.8})$$

and \mathbf{u} is the three-dimensional velocity field (u, v, w). In other words, φ_0 is unaffected by diabatic processes and therefore conserved following an air parcel, while φ_d is affected by diabatic processes. Since φ_0 is only affected by advection, this tracer is also called an *advection-only* tracer (e.g., Chagnon et al., 2013; Chagnon and Gray, 2015; Saffin et al., 2015). The sum of Eq. 3.5 and Eq. 3.6 yields the full evolution equation for φ and a small residual. The equations of motions in WRF have been specifically designed for the prognostic variables on the staggered Arakawa C grid, and this implies that there are differences in the advection of PV that is computed from the prognostic variables and that as a tracer (Whitehead et al., 2014), and this leads to the residual. At initialization time t_0 , $\varphi_0(x, t_0) = \varphi(x, t_0)$ and $\varphi_d(x, t_0) = 0$. The boundary conditions for φ_0 are the boundary conditions for φ while the values of φ_d are set to zero in the boundary.

The diabatic term φ_d can be further separated into a series of tracers of diabatic processes as follows:

$$\frac{D\varphi_d}{Dt} = \sum_{p \in \{proc\}} \varphi_p \quad (\text{Eq. 3.9})$$

where $\{proc\}$ is the set of parameterized diabatic processes p in the model. In this study, contributions from four parameterized processes are considered: (i) the PBL and turbulent mixing processes, (ii) convection, (iii) cloud microphysics, and (iv) radiation. Each tracer is selectively affected by the p th parameterized process and governed by the Eq. 3.10:

$$\frac{D\varphi_p}{Dt} = S_{\varphi,p} \quad (\text{Eq. 3.10})$$

where $S_{\varphi,p}$ represents the source due to the p th parameterized process so that:

$$S_\varphi = \sum_{p \in \{proc\}} S_{\varphi,p} \quad (\text{Eq. 3.11})$$

A module has been developed by Flaounas et al. (2020) and is implemented into WRF that calculates PV at every model time-step using the same numerical methods implemented to solve the evolution equations of the prognostic variables (velocity components, θ , and moisture variables – see paragraph 3.2.1) according to the following equations:

$$Q = -\frac{g}{\mu} (fk + \nabla \times \mathbf{V}_h) \cdot \nabla \theta \quad (\text{Eq. 3.12})$$

$$\frac{dQ}{dt} = -\frac{g}{\mu} [(fk + \nabla \times \mathbf{V}_h) \cdot \nabla \dot{\theta} + \nabla \times \mathbf{F} \cdot \nabla \theta] \quad (\text{Eq. 3.13})$$

where Q is the PV, g is the gravitational acceleration, f is the Coriolis coefficient, μ is the atmospheric column dry air mass, \mathbf{V}_h is the horizontal wind, \mathbf{F} is a mixing wind acceleration term that includes surface friction, turbulent and diffusive processes, θ is potential temperature and $\dot{\theta}$ is its time derivative. The term $(fk + \nabla \times \mathbf{V}_h)$ describes the 3-D field of absolute vorticity ξ_a , so Eq. 3.13 can be written in a more simple form as:

$$\frac{dQ}{dt} = -\frac{g}{\mu} [\xi_a \cdot \nabla \dot{\theta} + \nabla \times \mathbf{F} \cdot \nabla \theta] \quad (\text{Eq. 3.14})$$

The numerical solutions of PV tracers suffer from implicit diffusion associated with the implemented semi-Lagrangian advection technique and estimates of the PV sources suffer from inaccuracies related to interpolations associated with the estimation of relative vorticity and the potential temperature gradients. These problems result in the non-exact solutions in the PV tracer calculations and the numerical residual. The residual grows over time but it does not attain large values and its domain average is negligible when compared to the other tracers. The reader is encouraged to read more about the details for the residual growth in PV tracers in a numerical model in the study of Saffin et al. (2016).

The PV is calculated in the WRF model levels that range from 0 to 1 (see more details in Section 3.2.1) in order to avoid wind and temperature interpolations in pressure levels (Cao and Xu, 2011). First, the total PV is calculated and then a PV-budget diagnostic is actuated at every time step of the model integration to decompose the total PV into scalars which are several non-conserved partitions and one conserved partition (Lamarque and Hess, 1994; Stoeligna, 1996; Gray, 2006), the PV tracers. Every parameterized process can act as a source or a sink of PV and attain a non-conserved PV tracer. In total, six non-conserved PV tracers are computed, derived from latent heat release by microphysics (q_{mp}) and convection (q_{cu}) parameterisations, from turbulent fluxes of temperature (q_{bt}) by the PBL parameterisation, from atmospheric warming/cooling by shortwave (q_{sw}) and longwave radiation (q_{lw}) and finally from a mixed term of air-mass momentum acceleration (q_{mo}) which is partly provided by the boundary layer parameterisation. The conserved PV tracer (q_{co}) represents the contribution of the large-scale flow to PV and therefore, it is only subject to advection. The non-conserved PV tracers are in addition to advection, also subject to accumulations of net gains and losses of PV. These gains and losses of PV represent the right hand side terms of Eq. 3.14 and are derived from the net temperature and momentum forcing of the model physical parameterisations to the primitive equations. By following Stoeligna (1996), each PV tracer is calculated at every grid point as follows:

$$q_x(\tau) = q_x(0) + \int_1^\tau (-\mathbf{u} \cdot \nabla q_x + G_x) dt \quad (\text{Eq. 3.15})$$

where

$$G_x = -\frac{g}{\mu} \xi_a \cdot \nabla T_x$$

$$G_{x=mo} = -\frac{g}{\mu} (\nabla \times \mathbf{F}) \cdot \nabla \theta \quad (\text{Eq. 3.16})$$

where q_x is any PV tracer at a given time step τ , computed by the process x (*mp, cu, bl, sw, lw, mo or co*). The term $q_x(0)$ represents the value of each PV tracer in the initial conditions, while G_x is related to the PV sources and sinks and is calculated by Eq. 3.16, using the full model wind velocity and the temperature tendencies from the model parametrisations (T_x). Finally, the G_{mo} is calculated using the full model θ and F from the boundary layer parametrisation.

The total PV at the initial and boundary conditions in Eq. 3.15 is entirely attributed to the large-scale flow ($q_{co}(0)$) and G_x is initially set to zero, so as it is introduced into the domain by prescribing the total PV of the large-scale flow (regardless the process responsible for the production of PV) and it is interpreted as the conserved PV partition. Because q_{co} describes the total PV at the initial and boundary conditions, this means that the non-conserved PV tracers are all set to zero and start to be computed after the introduction of the initial conditions to the simulation. Setting a 12-hours spin-up period for the simulations of this study, guarantees that the PV tracers have already been started to be computed inside the domain. One special advantage of the PV-tracers diagnostic tool is that it accumulates the PV from the non-conserved PV tracers and makes it possible to attribute the intensification of the MTLCs to certain diabatic processes. At any model time step, the total PV equals to the sum of all PV tracers:

$$Q = q_{co} + q_{mp} + q_{cu} + q_{bl} + q_{sw} + q_{lw} + q_{mo} + q_r \quad (\text{Eq. 3.17})$$

where q_r is the residual which is attributed to the dynamical core of the model and to adjustments made by the model to the prognostic variables in the primitive equations.

When considering the storm-scale PV, friction can be neglected during the early stages of the cyclone spin-up (e.g., Schubert and Alworth, 1987) mostly because of the weak surface winds. Murthy and Boos (2019) found that the frictional spin-down tendency could be neglected in an approximate scaling for the intensification rate of TCs in an idealized model. In our study we will focus on those PV tracers that attain large magnitudes over the simulations (>0.5 PVU), so we neglect PV tendencies due to friction in this study. It was found that the PV tracer related to the air-mass momentum acceleration (q_{mo} or PVMO hereafter) attained very small values compared to the rest of the parameters in Eq. 3.17, most of the time less than 0.5 PVU, so it is not used for the detailed analysis of the PV evolution during the studied MTLCs, but it is used to compute the total atmospheric PV.

Moreover, the derived PV from the diabatic heating tendencies due to radiation, cloud microphysics, shallow convection, and deep convection during MTLCs (tendencies from turbulent diffusion and convection from microphysics) are summed and termed PVDIAB. On the other hand, we will hereafter refer to the conserved PV tracer with the name PVCO, so the total atmospheric PV is the sum of PVCO, PVDIAB and PVMO.

3.2.3 Pressure tendency equation

The diagnostic approach of the classical pressure tendency equation (PTE) used in this study is based on the study of Knippertz and Fink (2008), Knippertz et al. (2009) and Fink et al. (2012), which considers a

vertical column from the surface to an upper boundary at pressure p_2 , here chosen to be 50 hPa. The first step to derive the PTE is based upon the hydrostatic and the continuity equations (Pohle, 2010, her Chapters 4.1-4.3):

$$\frac{\partial}{\partial z} \left(\frac{1}{\rho} \frac{\partial p}{\partial t} \right) = -\frac{g}{\rho} \left(\frac{\partial \rho}{\partial t} \right) = \frac{g}{\rho} \left(\vec{v} \vec{\nabla}_p \rho + \omega \frac{\partial \rho}{\partial p} - \frac{d\rho}{dt} \right) \quad (\text{Eq. 3.18})$$

with the density ρ , the acceleration of gravity g , pressure p , and the horizontal and vertical wind components \vec{v} and ω . From the first law of thermodynamics and $p = \rho R_d T_v$, with the gas constant R_d , the terms on the right-hand side can be written as functions of the virtual temperature T_v :

$$g \frac{1}{\rho} \vec{v} \vec{\nabla}_p \rho = -g \frac{\vec{v}}{T_v} \vec{\nabla}_p T_v \quad (\text{Eq. 3.19})$$

$$g \frac{1}{\rho} \omega \frac{\partial \rho}{\partial p} = -g \frac{\omega}{p} \left(1 + \frac{R_d}{g} \cdot \frac{\partial T_v}{\partial z} \right) \quad (\text{Eq. 3.20})$$

$$g \frac{1}{\rho} \frac{d\rho}{dt} = g \left(\left(1 - \frac{R_d}{C_p} \right) \cdot \frac{\omega}{p} - \frac{\dot{Q}}{C_p T} - \frac{T}{T_v} \cdot 0.608 \cdot \frac{dq}{dt} \right) \quad (\text{Eq. 3.21})$$

where T is the dry temperature, C_p the specific heat capacity at constant pressure ($1004 \text{ J kg}^{-1} \text{ K}^{-1}$), and \dot{Q} represents the diabatic heating rate, q is the water vapor content and T_v is the virtual temperature. The following steps are: a) the replacement of the three terms in Eq. 3.19, 3.20, and 3.21 into the Eq. 3.18, the exchange of $g \cdot dz$ by $\frac{1}{\rho} dp$ and the integration between the surface (sfc) and the upper-level boundary p_2 , b) the replacement of the pressure tendency at the upper boundary which is in height coordinates, by the geopotential tendency in pressure coordinates, and c) the consideration of the influences of precipitation and evaporation to the surface pressure. The result is shown in Eq. 3.22:

$$\begin{aligned} \frac{\partial p_{sfc}}{\partial t} &= & (\text{Dp}) \\ \rho_{sfc} \frac{\partial \phi_{p_2}}{\partial t} & & (\text{D}\phi) \\ + \rho_{sfc} R_d \int_{sfc}^{p_2} -\vec{v} \vec{\nabla}_p T_v \, d \ln p & & (\text{TADV}) \\ + \rho_{sfc} R_d \int_{sfc}^{p_2} \left(\frac{R_d T_v}{C_p p} - \frac{\partial T_v}{\partial p} \right) \omega \, d \ln p & & (\text{VMT}) \\ + \rho_{sfc} R_d \int_{sfc}^{p_2} 0.608 \cdot T \frac{dq}{dt} \, d \ln p & & (\text{HUM}) \\ + \rho_{sfc} R_d \int_{sfc}^{p_2} \frac{T_v \dot{Q}}{C_p T} \, d \ln p & & (\text{DIAB}) \\ + g(E - P) & & (\text{EP}) \quad (\text{Eq.3.22}) \end{aligned}$$

where p_{sfc} is the surface pressure, ρ_{sfc} is the surface air density, ϕ_{p_2} is the geopotential at p_2 (50 hPa), R_d the gas constant for dry air ($287.058 \text{ J kg}^{-1} \text{ K}^{-1}$). The term Dp is the pressure tendency at the surface, $D\phi$ is the geopotential tendency at 50 hPa, $TADV$ is the net temperature advection, VMT is the vertical motion multiplied by the static stability, HUM is the net total change of the water vapor content (q), and $DIAB$ represents the diabatic processes that cause virtual temperature (T_v) changes in the air column. The EP term contains the effects of mass loss on the pressure fall due to precipitation (P) and the surface evaporation (E). The HUM term was calculated by using the mixing ratio of all available solid hydrometeors (rain, snow, graupel, ice, hail) and water vapor provided by the MP scheme but the results are always one magnitude lower than the rest of the pressure tendency terms, so HUM is omitted from the following calculations. The changes of q cause density changes, so they can be expressed in terms of temperature changes. Thus, the PTE can be written as:

$$\frac{\partial p_{sfc}}{\partial t} = \rho_{sfc} \frac{\partial \phi_{p_2}}{\partial t} + \rho_{sfc} R_d \int_{sfc}^{p_2} \frac{\partial T_v}{\partial t} d \ln p + g(E - P) + RES_{PTE} \quad (\text{Eq. 3.23})$$

$$\begin{array}{cccc} Dp & D\phi & ITT & EP \end{array}$$

From left to right, the terms denote the surface pressure tendency (Dp), the change in geopotential at the upper boundary ($D\phi$), the vertically integrated T_v tendency (ITT), the mass loss (increase) by precipitation P (evaporation E ; EP), and a residuum due to discretization (RES_{PTE}). Keeping all other terms zero, a lowering of the upper-level geopotential ($D\phi$) will cause surface pressure fall, since it must be associated with mass evacuation by divergent winds. If the column height remains constant, warming results in horizontal expansion and therefore in a loss of mass (i.e., surface pressure fall). In reality a combination of the two processes is typically found.

ITT consists of the terms in Eq. 3.24:

$$ITT = TADV + VMT + DIAB + RES_{ITT} \quad (\text{Eq. 3.24})$$

$TADV$ describes the effects of horizontal temperature advection and VMT the vertical motions on the column-integrated temperature tendency. $DIAB$ contains the influence of diabatic processes such as radiative warming/cooling, latent heat release due to phase changes of water, diffusion, and dissipation. Inside deep convective clouds the latent heat release related to microphysics and convective processes is the most important contribution to $DIAB$, resulting in an atmospheric warming and pressure fall. The $DIAB$ term can also be decomposed into the explicitly resolved diabatic processes by WRF:

$$DIAB = THD + TBL + TLW + TSW \quad (\text{Eq. 3.25})$$

where the THD term represents the diabatic processes due to microphysics, TBL the boundary-layer processes, TLW and TSW the longwave and shortwave radiation processes respectively. The term RES_{ITT} represents errors due to discretization in time and space, similar to RES_{PTE} .

A schematic example of an application of the equations (3.22) and (3.23) using the 30-minute WRF output data for a 100 km (or $\sim 1^\circ \times 1^\circ$) radius from the MTLCs center is illustrated in Fig. 3.6. The terms with time tendencies (Dp , $D\phi$, and ITT) are calculated for the box area or the volume-averaged changes between t_0 and $t_{-30\text{min}}$. The two instantaneous terms ($TADV$, VMT) are computed by performing an integration over the box volume. At the end, a time-series is constructed by moving the box along the MTLC tracks.

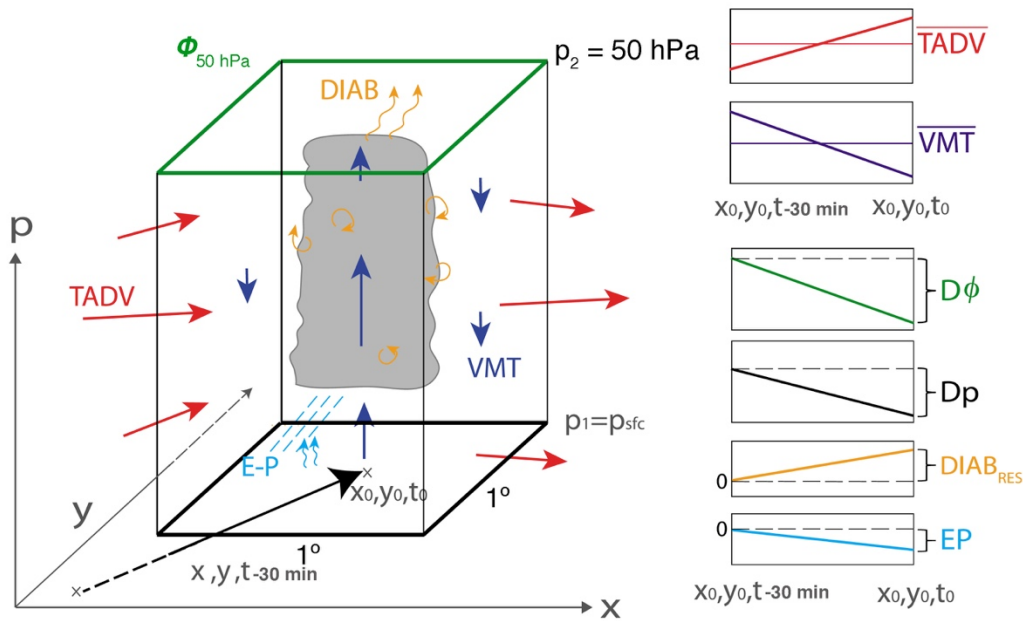


Fig. 3.6 Schematic illustration of the PTE methodology. The bold arrow in the x-y plane indicates the motion of the center of a surface cyclone between two analysis times t_0 and $t_{-30\text{min}}$ (arrow length not true to the scale). The surface pressure tendency equation is evaluated for the $1^\circ \times 1^\circ$ latitude-longitude box extending from the surface to 50 hPa centered on the position of the storm at t_0 . The terms of Eq. 3.23, $TADV$ (horizontal advection; red arrows) and VMT (vertical advection; dark blue vectors), are computed by integrating over the box volume and then averaging over t_0 and $t_{-30\text{min}}$ as schematically indicated in the two graphs in the top right corner. The computation of the terms $D\phi$, Dp , $DIAB$ (diabatic processes; curled orange vectors), and EP (evaporation minus precipitation; curled blue vectors and dashed blue lines) is illustrated in the lower four graphs on the right-hand side. Note that while $D\phi$ and Dp are simple differences between instantaneous values at t_0 and $t_{-30\text{min}}$, EP is the difference between two parameters accumulated between t_0 and $t_{-30\text{min}}$. $DIAB_{RES}$ is the residuum of Eq. 3.24 (adapted from Fink et al., 2012).

3.3 Results

3.3.1 Model set-up and case studies

In order to simulate the dynamics of the MTLCs with the WRF model, we use two-domain simulations as described in Section 3.2.1. A telescopic 1-way nesting technique is employed for each simulation, with the parent domain covering most of the Mediterranean basin, Central Europe and North Africa, with a horizontal resolution of 9 km (380 x 350 grid points). The inner domains have a 3 km grid increment with a varying size, as shown in Table 3.2 because every MTLC has a varying trajectory length. Each simulation is performed with 40 unevenly-spaced vertical levels, with a time step of 30 s and 10 s for the parent and the nested domains respectively. The start date and time, including a 12-hour spin-up period, as well as the duration of the model integration which is different for each MTLC, are also presented in Table 3.2. The outputs are saved every 1 hour for the parent domains and every 30 minutes for the nested domains. The ERA5 lateral and boundary conditions of the parent domain are forced into the model every 1 hour and analysis nudging is performed every 3 hours, relaxing the lateral boundary conditions of wind and temperature that are forced into the nested domain in a second step, towards the ERA5 reanalysis. For the MTLCs Med2005 and Med2007, no nudging is performed since the analysis nudging results in larger track biases when compared with the observed tracks. In addition, for all the simulations in the nested domains, the lateral and boundary conditions are forced by the parent domain in every model time step.

MTCL case	Nb of grid points in d02	Start date and time in UTC	Simulation duration (hours)
Med 2005	703 x 376	13 December 2005 1200	54
Med2006	391 x 361	25 September 2006 0600	41
Med2007	349 x 325	15 November 2007 0600	54
ILONA	301 x 271	19 January 2014 1800	66
QENDRESA	286 x 268	7 November 2014 0000	36
ROLF	286 x 268	6 November 2011 0000	84
TRIXIE	451 x 283	29 October 2016 0600	60
NUMA	301 x 253	16 November 2017 0600	72
ZORBAS	451 x 442	27 September 2018 1200	54

Table 3.2 The number of grid points (west-east x south-north) of the inner domains , the start date and time of each simulation including the 12 hours spin-up period, and the duration of the simulations in hours. The red font is used for the MTLC simulations that are discarded from the analysis.

The tracking of the simulated cyclone centers is achieved by following the minimum sea-level pressure (SLP) and the resulted MTLC trajectories are compared with the observed tracks discussed in Chapter 2. Table 3.3 shows the mean and max track bias and Fig. 3.7 shows the simulated and observed MTLCs trajectories for the 8 out of 9 MTLCs discussed so far, except for ILONA. For this cyclone, WRF does not simulate a cyclone with closed SLP contours or distinct centers of low-level vorticity, and thus, it is dismissed from further analysis. One interesting aspect of this case is that ERA5 does simulate the cyclone but the higher the resolution in WRF, the higher is the bias versus ERA5 reanalysis.

DC activity in the simulations is defined similar to Tao and Jiang (2015), by setting a threshold for the simulated reflectivity at two heights, but in addition, a threshold for the ice-water content (IWC) at 5 km altitude is used, representative for the presence of DC in the Mediterranean according to Rysman et al. (2017) and Funatsu et al. (2018). In this study, a WRF grid point is flagged with DC when the 20 dBZ contour of reflectivity reaches 5 km altitude with ice-water content (IWC) higher than 0.4 g m^{-3} and simultaneously the surface reflectivity is equal or greater than 20 dBZ. In the following paragraphs, we will refer to the grid points meeting the criteria for DC as “DCGRIDS”.

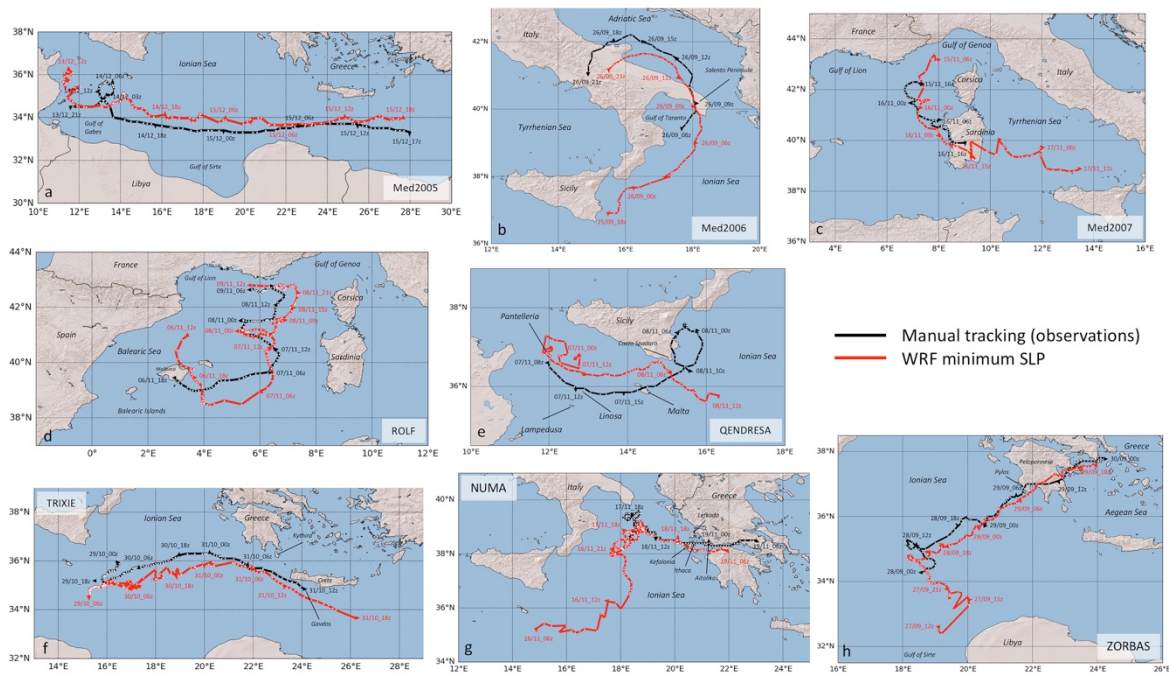


Fig. 3.7 The observed cyclone tracks (black) (position with white dots) and the tracks based on the position of minimum SLP from WRF plotted every 30 minutes (red) (a) for Med2005, (b) for Med2006, (c) for Med2007, (d) for ROLF, (e) QENDRESA, (f) TRIXIE, (g) NUMA and (h) ZORBAS. The main geographical features mentioned in the text are annotated.

For most of the cases, the mean track bias in WRF is less than 70 km (Table 3.3), except for QENDRESA and ROLF when the model is not able to accurately reproduce the cyclone track and for some instances, the distance bias is even more than 150 km. Despite the fact that the ERA5 reanalysis is able to reproduce the loop of QENDRESA south-east from Sicily (discussed in Chapter 2, also see Appendix 1 for details), the high-resolution simulation has a poor performance in realistically simulating the MTLC's trajectory, even after

trying several different model configurations (e.g., simulation start dates, spin-up periods, different microphysics, turning off the analysis nudging). On 7 November 2014 1200 UTC, the track bias with the observed track is more than 100 km and becomes more important the following hours, missing the landfall in Malta (crucial for the observed burst of DC activity as discussed in Chapter 2) and shows an almost landfall to the south-east coasts of Sicily at 0300 UTC on 8 November 2014, without translating northeast after 1800 UTC on 7 November 2014 (Fig. 3.7). Worth mentioning is that the cyclone trajectory in the parent domain of this simulation is much closer to the observed one, most probably due to the ERA5 analysis nudging. The poor model performance during QENDRESA has substantial consequences to the evolution of the simulated DC and an unrealistic evolution of the SLP and wind fields, and eventually it will not be discussed further in this study.

MTCL case	Mean track bias (km)	Max track bias (km) on date, time (UTC)
Med 2005	67	113 on 14 December 2005, 0830
Med2006	65	96 on 26 September 2006, 1930
Med2007	53	98 on 16 November 2007, 1500
QENDRESA	105	146 on 7 November 2014, 2300
ROLF	85	158 on 7 November 2011, 0330
TRIXIE	69	140 on 30 October 2016, 0600
NUMA	56	130 on 19 November 2017, 0600
ZORBAS	43	100 on 28 September 2018, 1900

Table 3.3 Mean and max MTCL track bias when comparing the distance between the observed and model tracks. Note that the comparison is performed only for the periods that the model outputs match the observations. The red font is used for the MTCL simulations that are discarded from the analysis.

Moreover, regarding the WRF simulation for ROLF, two main problems with the outputs lead us to ignore a detailed analysis of this MTCL with the common used model configuration. First, between 2100 UTC and 0800 UTC on 6 and 7 November 2011 respectively, the simulated MTCL follows a trajectory way more south than the observed one and with significantly larger propagating speed to the east after 0400 UTC on 7 November 2011. This behavior results in significant differences in DC activity compared to observations, with a constant model underestimation of the DC activity, especially during this period (Fig. 3.8d). Furthermore,

during the gradual intensification of the cyclone between 1200 UTC 7 November 2011 and 0300 UTC 8 November 2011, the simulated trajectory follows the observed one, much closer than the ERA5 reanalysis, but DC activity is again significantly underestimated by WRF and the minimum SLP does not fall below 1001.6 hPa at 0300 UTC on 8 November 2011, much higher than previous studies (e.g., Miglietta et al., 2013), and only 0.5 hPa lower than ERA5. Finally, after 1500 UTC 8 November 2011, the track bias increases again above 100 km by the early morning on 9 November 2011 (Fig. 3.7d), with simulated 10-m wind speeds up to only 10 m s^{-1} within 50 km from the cyclone center, when an ASCAT scan shows values higher than 20 m s^{-1} in the Gulf of Lion (see Fig. S1.2 in Appendix 1).

When comparing the DCGRIDS with DCPIXELS from Chapter 2 (compare Fig. 8 in QJRMS article with Fig. 3.8), we can see that for most of the MTLCs, the WRF performs well in realistically simulating the evolution of DC close to the cyclone centers, at least for the periods when such a comparison is possible. For Med2005, the model correctly simulates very limited or no DC activity within 50 km from the cyclone center between 0000 and 1200 UTC on 14 December 2005 and later the two distinct peaks in DC activity observed by DCPIXELS are also shown in the model output, even though there is a temporal lag of about 3 hours in peak activity (Fig. 3.8a). Similarly for Med2006, the model simulates the intense DC activity close to the cyclone center between 0600 and 1200 UTC on 26 September 2006, even though later there is a considerable difference between DCGRIDS and DCPIXELS when the cyclone moves over the Adriatic Sea until it makes landfall to Italy just before 2100 UTC (Fig. 3.8b). This model overestimation of DC activity can be explained by the cyclone track bias shown in Fig. 3.7, when the simulated Med2006 follows a trajectory closer to the Italian coast, resulting in strong low-level frictional convergence and unrealistic DC activity. Also the environment in the southern trajectory is more warm and moist, thus more unstable favoring DC activity (see Appendix 2, Fig. A2.4).

For Med2007, a comparison between DCPIXELS and DCGRIDS can only be performed after 1600 UTC 15 November 2007, when WRF correctly simulates intense DC activity close to the cyclone center during the deepening phase, before 1800 UTC 15 November 2007 (Fig. 3.8c). Then, a few hours before Med2007 makes landfall in Sardinia, both DCGRIDS and DCPIXELS start to increase in number, while the SLP is constantly rising. While the cyclone is over Sardinia, between 1200 and 1600 UTC 16 November 2007, the model simulates a weaker-than-observed DC activity, and when it propagates east over the Tyrrhenian Sea, a new round of DC activity starts and lasts until the end of the simulation.

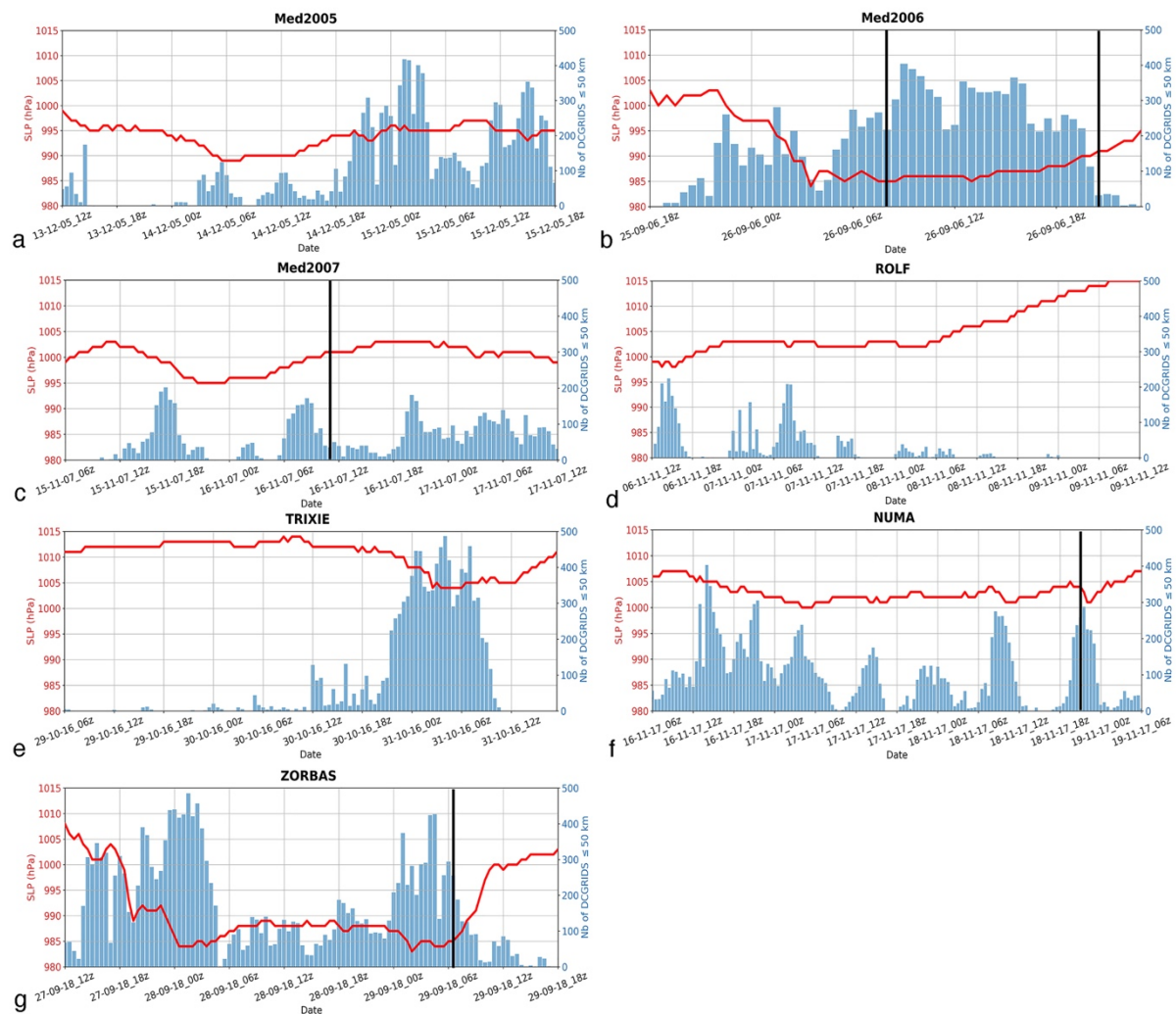


Fig. 3.8 Number DCGRIDS within 50 km from the cyclone centers (blue bars) and the minimum SLP (hPa) red line. The thick black lines indicate the time when the MTLCs make landfall.

During the first 24 hours of TRIKIE's simulation, DC activity is very limited close to the cyclone center, and only a few scattered DCGRIDS are simulated (Fig. 3.8e), while there are plenty of observed DCPIXELS. Nevertheless, the SLP does not change much during this period, until the late afternoon on 30 October 2016 when a burst of DC activity is observed and correctly simulated. The peak number of DCGRIDS is found about 6 hours after the DCPIXELS, during a deepening phase of TRIKIE. After reaching the lowest values, SLP remains rather constant below 1005 hPa between 0300 and 1300 UTC 31 October 2016, even after the significant decrease in the number of DCGRIDS after 0900 UTC. No DC is simulated or observed after 1100 UTC 31 October 2016.

Intense DC activity is simulated in the early stages of NUMA in South Ionian Sea between 0600 UTC 16 November 2017 and 0600 UTC 17 November 2017 (Fig. 3.8f). A comparison with the DCPIXELS shows that WRF overestimates the DC activity between 0000 and 0600 UTC. Later, the model and the observations show an increase of DC activity after 1200 UTC 17 November 2017, but in the model DCGRIDS are not simulated for several time steps, while more than 200 DCPIXELS are constantly observed until 0300 UTC 18 November

2017 (Fig. 8 in QJRMS article). The model simulates two more rounds of intense DC activity before NUMA makes landfall in Western Greece at 2100 UTC on 18 November 2017, and there is a very good agreement between DCPIXELS and DCGRIDS for the latter round between 1800 UTC 18 November 2017 and 0200 UTC 19 November 2017 during which a short-lasting but important amplification of the surface cyclone is simulated. The minimum SLP in the simulation differs only about 1 hPa when compared with surface station observations (see Appendix 1).

At the early stages of the explosive cyclogenesis of ZORBAS on 27 September 2018, intense DC activity is simulated by WRF very close to the cyclone center (Fig. 3.8g). The comparison with DCPIXELS starts at 0000 UTC on 28 September 2018, when the observations show a much weaker DC activity. For the following 24 hours, DC activity remains important in the simulation, confirmed by more than 100 DCPIXELS detected constantly, with a steady SLP below 990 hPa until the early morning on 29 September 2018. Then, a burst of DC activity is both simulated and observed, and ZORBAS reaches again 984 hPa a few hours before making landfall in Peloponnese, SW Greece (Fig. 3.7h). After crossing Peloponnese, ZORBAS starts weakening fast and so does the DC activity. The simulated minimum SLP during the landfall in Peloponnese is very close to the observed values by surface weather stations (989 hPa, see Appendix 1 for details).

3.3.2 Definition of tropical-like phase

In order to define the tropical-like periods of the studied MTLCs, two parameters describing their thermal structure and intensity are used. First, a 50-km average negative value of the lower-tropospheric thermal vorticity (Bentley and Metz, 2016) is computed for every time step defined as:

$$\zeta_T = \zeta_{g500} - \zeta_{g925} \quad (\text{Eq. 3.26})$$

where ζ_{g500} is the 500-hPa geostrophic relative vorticity and ζ_{g925} is the 925 hPa geostrophic relative vorticity. A negative value of ζ_T collocated with the MTLC centers indicates a warm core in the lower troposphere. The second parameter is the maximum SLP gradient (G) within 100 km from the MTLC centers, similar to Ragone et al. (2018). In the current study, a maximum $G = 0.5 \cdot 10^{-2} \text{ hPa km}^{-1}$ within the meridional and zonal directions from the cyclone centers is considered to be satisfied at every time step, regardless the topographic features. For both parameters to be computed, the curvilinear WRF grid had to be interpolated to a regular 3-km grid. When the criteria for both ζ_T and G are met, then we consider a “tropical-like” phase (Fig. 3.9). A detailed description of the evolution of the simulated MTLCs in the parent and inner domains is provided in Appendix 2 and the following 2 figures (Figs. 3.9-3.10) provide an overview of the intensity of the studied MTLCs.

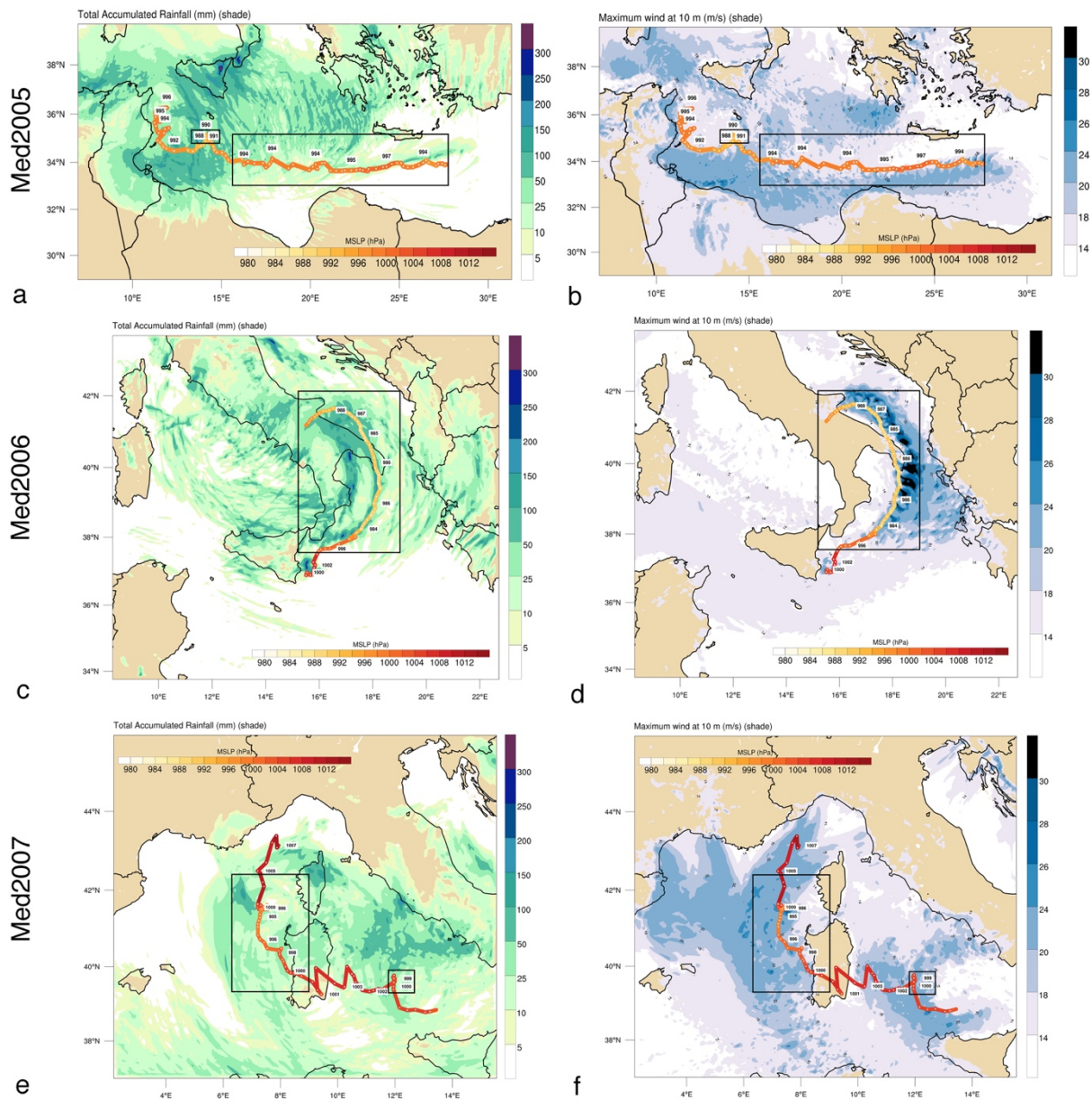


Fig. 3.9 The evolution of the SLP (hPa) (yellow-orange line) along the simulated cyclone trajectories, the total accumulated precipitation (mm) (green-blue shade) and the maximum 10-m wind speed (m s^{-1}) (blue-black shade) calculated at each time step (30 minutes) in the inner domain throughout the lifetime of the MTLCs. The black rectangles enclose the time instances when the cyclones have tropical-like characteristics. Plots are valid for Med2005 (a-b), Med2006 (c-d) and Med2007 (e-f).

The simulated Med2005 produces more precipitation in the pre-tropical-like stage, when situated between Sicily and Tunisia (Fig. 3.9a), and 10-m wind speeds are stronger in the southern part of the cyclone during most of the tropical-like period (Fig. 3.9b). Similar results were found in Fita and Flaounas (2018). On the other hand, Med2006 produces most of the precipitation during the tropical-like phase and within 100 km from the cyclone center (Fig. 3.9c) and more the 30 m s^{-1} 10-m wind speeds are simulated for several instances in the Ionian and Adriatic Seas (Fig. 3.9d). Med2007 barely reaches values up to 25 m s^{-1} within 100 km from the cyclone center and the total accumulated precipitation in the close vicinity of the cyclone does not exceed

150 mm. The latter can be partly explained by the much less available precipitable water in the Mediterranean in November and December, when compared with the other MTLCs occurring earlier in autumn. Though, when comparing NUMA and Med2007 which both developed in mid-November, the characteristics of the air masses discussed in Appendix 2, play an important role to the amount of the available precipitable water.

The simulated total accumulated precipitation in TRIXIE and ZORBAS locally exceeds 300 mm during their tropical-like phases (Fig. 3.10a-b and 3.10e-f), producing very strong 10-m wind speeds close to their centers, exceeding 30 m s^{-1} . The wind speeds of these cyclones can only be compared with Med2006. NUMA on the other hand, shows a weaker 10-m wind field (Fig. 3.10d) but very high accumulated precipitation, exceeding 200 mm within 24 hours very close to the cyclone center in North Ionian Sea (Fig. 3.10c), but there is also a peak of more than 300 mm in the Aegean Sea which may be attributed to NUMA.

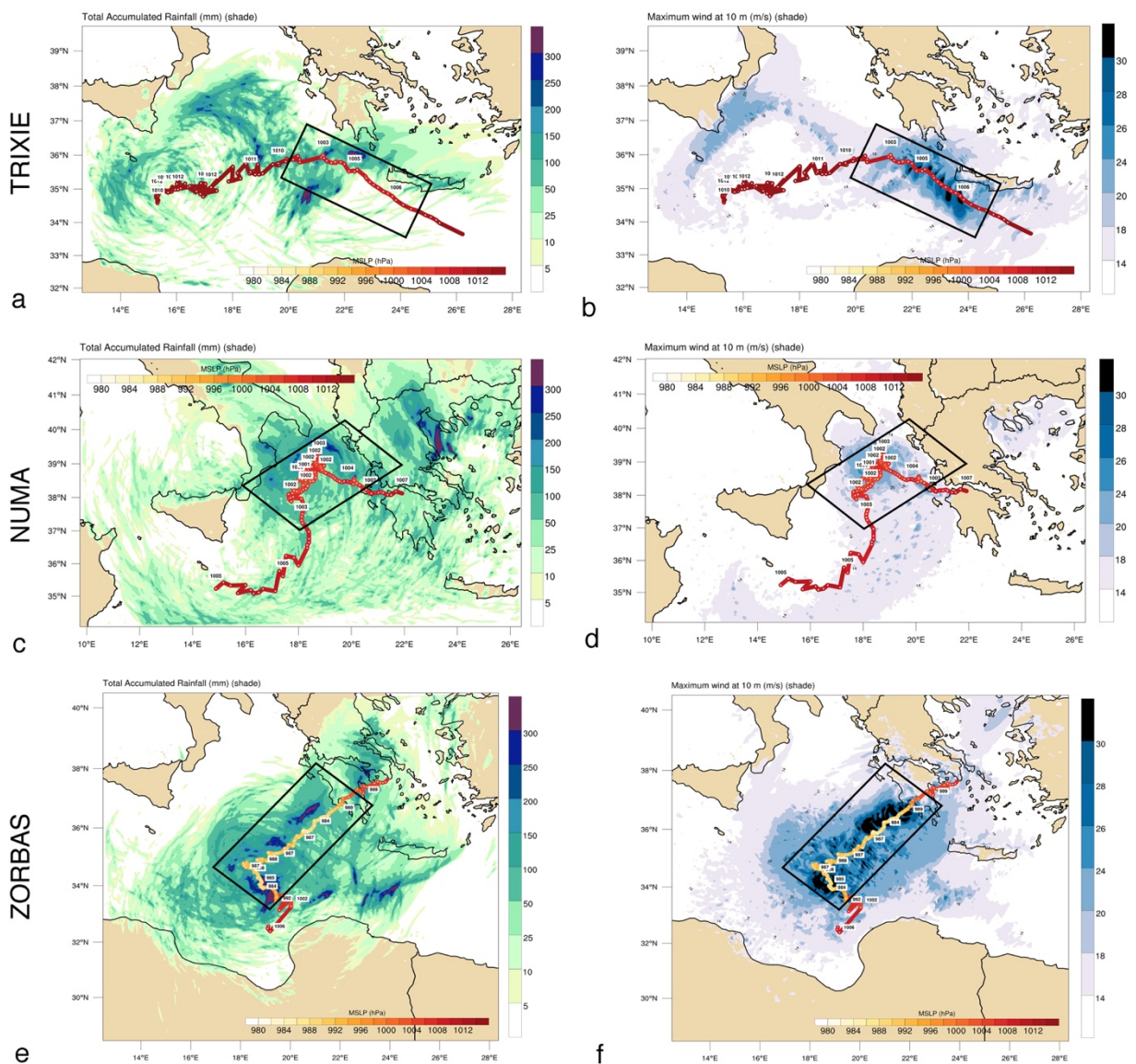


Fig. 3.10 As in Fig. 3.9 but for TRIXIE (a-b), NUMA (c-d) and ZORBAS (e-f).

3.3.3 MTLC pressure tendencies

To provide a deeper insight into the MTLCs' intensification periods and quantify the contribution of diabatic processes, Figs. 3.11 and 3.12 provide the surface pressure tendency rate (Dp) for the 6 studied MTLCs, decomposed in different terms as described in Section 3.2.3. The budget equation PTE is calculated for two radii around the MTLCs' centers and for 30-minute time steps. The changes of geopotential at the top of the atmospheric column, the effect of net evaporation minus precipitation on the mass of column and mass changes due to the vertical changes in water vapor are summarized by the PTE analysis shown in this paragraph. According to Eq. 3.23, Dp equals the sum of $D\phi$, ITT , EP and RES_{PTE} and it is shown in the left column of Figs. 3.11 and 3.12, while the right columns show the decomposed components of ITT (Eq. 3.24). Note that Dp and $D\phi$ are tendencies at a single level whereas ITT denotes an integral, and the integration is performed over $d(\ln p)$ and not dp . This means that an upper-tropospheric heating has a larger impact on Dp than heating in the lower troposphere.

All the cases are put into one graph in order to easily compare the evolution of Dp , and the stages during intensification periods are marked with the Latin numbers. In order to quantify the relative contribution of the diabatic processes resulting from latent heat release during DC ($DIAB_{cont}$) to the deepening of the MTLCs, an approach similar to Fink et al. (2012) is followed to calculate the contribution of THD to the total pressure tendency, but here we need to account also for the contributions of $D\phi$ and EP which often attain similar values to ITT :

$$DIAB_{cont} = \begin{cases} \frac{|THD|}{|THD| + |VMT| + |TADV| + |EP| + |D\phi| + |\Sigma TRES|} * 100, & \text{sgn}(THD) = \text{sgn}(TAVD) = \text{sgn}(VMT) = \text{sgn}(D\phi) \\ \frac{|THD|}{|THD| + |TADV| + |EP| + |D\phi| + |\Sigma TRES|} * 100, & \text{sgn}(THD) = \text{sgn}(TAVD) = \text{sgn}(D\phi) \wedge \text{sgn}(THD) \neq \text{sgn}(VMT) \\ \frac{|THD|}{|THD| + |VMT| + |EP| + |D\phi| + |\Sigma TRES|} * 100, & \text{sgn}(THD) = \text{sgn}(VMT) = \text{sgn}(D\phi) \wedge \text{sgn}(THD) \neq \text{sgn}(TADV) \end{cases}$$

(Eq. 3.27)

where $\Sigma TRES$ is the sum of the diabatic processes TSW , TLW , TBL and the residuals (RES_{PTE} and RES_{ITT}).

For Med2006, TRIKIE, NUMA and ZORBAS diabatic processes contribute more to the surface pressure fall (up to 95%) than horizontal temperature advection, while for Med2005 and Med2007, there seems to be a much more important contribution from the baroclinicity during their lifetime with short periods of important $DIAB_{cont}$ (Eq.3.27) which do not lead to significant cyclone deepening. It must be pointed out that even for the periods when diabatic processes dominate the intensification of the cyclones, the baroclinicity is also acting either in opposing or in further contribution of cyclone deepening through horizontal temperature advection ($TADV$) or changes of the geopotentials ($D\phi$). Moreover, the $TADV$ term is closely connected with the vertical wind shear, since high values of $TADV$ correspond to a strong upper-level wind field and thus, strong DLS.

In the following paragraphs, the findings of the PTE analyses for each case are discussed in detail, and from now on we will refer to the PTE analysis for the 100 km radius as “PTE100” and for the 250 km radius as “PTE250”.

- Med2005

During the deepening stage I of Med2005 on 13 and 14 December 2005 (Fig. 3.11a), the deepening rate is attributed to the lowering geopotentials ($D\phi$) close to the PV streamer (Fig. A2.1b-d), the warm air advection mainly in the upper troposphere ($TADV < 0$, Fig. 3.11b) and the loss of water mass due to rainfall (EP). Interestingly, by comparing the PTE100 and PTE250 analyses (Fig. 3.11 vs 3.12), we see an important difference in $DIAB_{cont}$ between 1200 UTC 13 December and 0000 UTC 14 December 2005, especially during the maximum deepening rate. For the latter analysis, the 30-40 % $DIAB_{cont}$ can be explained by the widespread distribution of DCGRIDS further than 100 km away from the cyclone center (not shown), while closer to the center, only a few scattered DCGRIDS are simulated by WRF (Fig. A2.2b and Fig. 3.8a). At the same time, the horizontal warm-air temperature advection ($TADV$) has about the same contribution in cyclone deepening in both cases, and together with the upper-level lowering geopotentials, their baroclinic contribution in the deepening of Med2005 is higher than 50%. After 0000 UTC on 14 December 2005, dry and cold upper-tropospheric air mass intrusion started influencing the Med2005, opposing the deepening ($ITT > 0$), and this is in accordance with the vertical alignment between the 500 hPa cut-off low, the position of the 500-hPa jet-stream and the surface cyclone (Fig. A2.1a). In addition, as the deepening rate is decreasing close to the end of stage I, the $D\phi$ has values closer to 0, especially for PTE250, as the PV streamer wraps around Med2005.

After 1200 UTC on 14 December, Med2005 acquires a warm-core structure as shown in the theta-e fields in Fig. A2.2c, DC activity in the model is limited and mostly close to the cyclone center, but the upper-tropospheric cold and dry air intrusion within progressively increasing wind shear (Fig. 8a in QJRMS article) becomes more important as denoted by the increasing $TADV$ values both in PTE100 and PTE250. Moreover, the core of the 500 hPa cut-off low is now found more than 300 km north from Med2005 (Fig. A2.1c), resulting in strong baroclinicity and mostly negative $D\phi$, which tends to deepen the cyclone, opposing the positive ITT . This is also the case in the cyclone deepening stage II, when lowering geopotentials, weak DC activity and the PV streamer amplify the cyclone with a maximum rate of 1 hPa 30 min⁻¹, but only in PTE100. The small size of Med2005 smooths the Dp deepening rate close to 0 and diabatic processes contribute only a small fraction to the total decreasing pressure tendency in PTE100 and PTE250, but around 0300 UTC on 15 December 2005 increasing DC activity close to the center, briefly increases the $DIAB_{cont}$ up to 80%. This simulated convective burst is also observed by a sudden increase of DCPIXELS, discussed in Chapter 2 (Figs. 7-8a in QJRMS article).

During the last deepening stage of Med2005 (stage III), there is an overestimation of the simulated DC activity when DCGRIDS are compared with the observations (see Fig. 3.8a and Fig. 8a in QJRMS article), but again there is a big difference in the $DIAB_{cont}$ between PTE100 (60-75%) and PTE250 (15-30%). Also the relative position of the 500 hPa cut-off low (found over Greece on 15 December 2005) results in negative $D\phi$,

and rainfall in PTE100 shows mass evacuation, both resulting in negative Dp but it only lasts for less than 3 hours between 0900 and 1200 UTC on 15 December 2005 (Fig. 3.11a). At the same time, an opposing effect on Dp is found by the cold-air advection in the upper-levels and diabatic cooling ($TADV > 0$) during very strong DLS, and the diabatic cooling due to longwave radiation ($TLW > 0$). By the end of stage III the filling of Med2005 started again, resulting in fast weakening of the surface cyclone which in reality started a few hours before based on the satellite analysis in Chapter 2.

- Med2006

The MTLC that developed in the Ionian Sea on 25 September 2006 has 2 main deepening stages in the WRF simulation (Fig. 3.11c-3.12c). The first (stage I) starts at the beginning of the simulation at 1200 UTC on 25 September and lasts until the landfall of the cyclone in South Italy (Fig. 3.7b), just before 0800 UTC on 26 September 2006. At the early stages of this period, the cyclone quickly attained tropical-like characteristics (Fig. 3.9c-d) and the negative ITT close to $-1 \text{ hPa } 30 \text{ min}^{-1}$ until 2300 UTC on 25 September 2006 was mostly attributed to diabatic heating during DC and loss of water mass due to rainfall ($EP < 0$), especially in PTE100 (Fig. 3.11c). The PTE100 shows mid/upper-level diabatic cooling during horizontal air advection ($TADV > 0$) (Fig. 3.11d) but this is not the case in PTE250 (Fig. 3.12d). After 0000 UTC on 26 September 2006, the $DIAB_{cont}$ becomes more important, reaching values up to 90% and at the same time the geopotentials become lower ($D\phi < 0$) as the PV streamer approaches the Med2006 from west-northwest (Fig. A2.3b), but also the RES_{ITT} attains absolute values larger than $1 \text{ hPa } 30 \text{ min}^{-1}$. During this stage, many DCGRIDS close to the cyclone center show an intense DC activity, dominating the cyclone deepening rate and apart from the high $DIAB_{cont}$ values, strong adiabatic cooling is also simulated ($VMT > 0$), opposing to the cyclone deepening, which results in slight positive ITT (Fig. 3.11c and 3.12c).

After the landfall of Med2006 in South Italy between 0800 and 1000 UTC on 26 September 2006 and the slight increasing of the SLP (Fig. 3.8b and 3.11c-3.12c), the cyclone is again over the sea, propagating north in the Adriatic Sea. Med2006 is now under the left exit of a mid-level jet stream (Fig. A2.3c-e) and WRF simulates a second short-lasting deepening period (stage II). $D\phi$ values are now fluctuating close to 0, and again diabatic heating during DC activity seems to play the main role in the deepening rate with $DIAB_{cont} > 60\%$ in PTE100 (Fig. 3.11d) and in PTE250 (Fig. 3.12d). After 1200 UTC on 26 September 2006, Med2006 is in a much drier and colder environment than before, with positive ITT values and decreasing THD , along with a slight increase of diabatic cooling ($TADV > 0$) which result in positive Dp and gradual cyclone weakening until the second landfall in the Italian coasts after 2100 UTC (Fig. 3.7b and 3.8b).

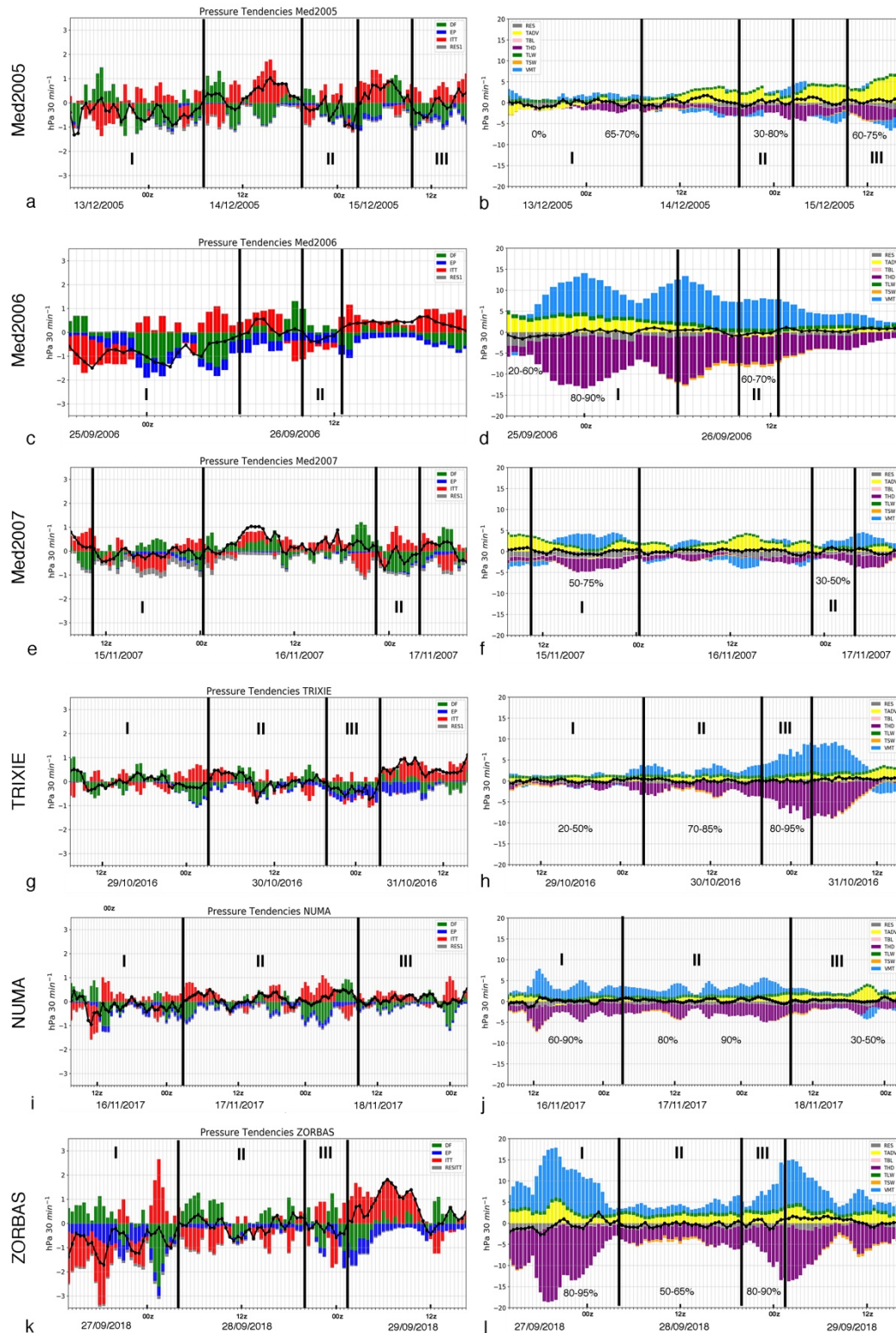


Fig. 3.11 Results for the PTE analysis for a 100 km radius from the MTLCs' center (PTE100): (left column) surface pressure tendency (Dp) (black line), decomposed into contributions by geopotential at 50 hPa ($D\phi$), integrated column temperature (ITT) and water loss or gains due to evaporation and rainfall (EP). (Right column) integrated temperature term (ITT) (black line), decomposed into contributions by vertical movements (VMT), horizontal temperature advection (TADV) and different diabatic heating processes due to the planetary boundary layer (TBL), due to short-wave radiation (TSW), long-wave radiation (TLW) and microphysics (THD). The residuals due to temporal and spatial discretization are shown in grey. The relative contribution of THD to the total negative pressure tendency is shown in percent in the right column. Note the different scale for pressure on the left axis of both columns.

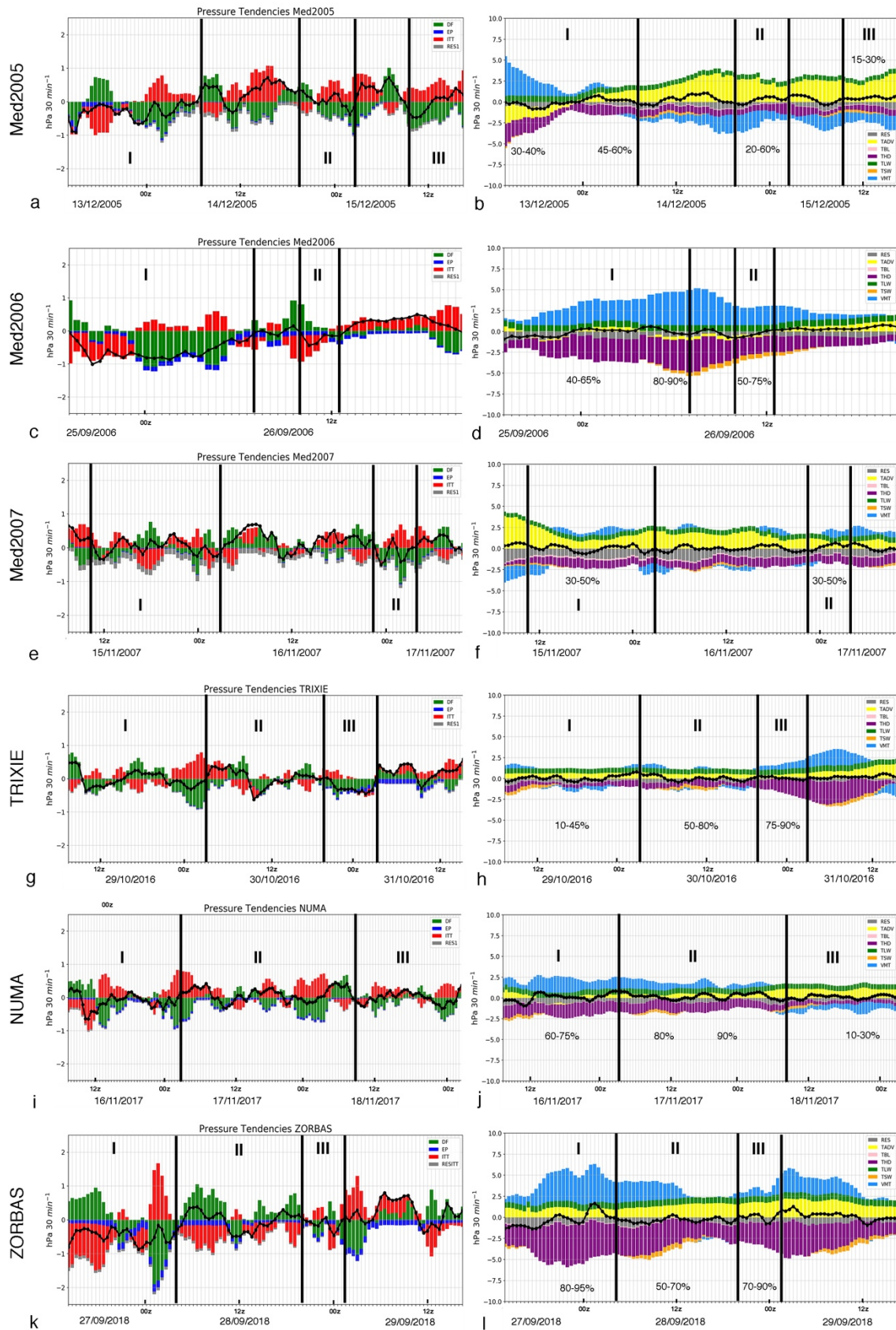


Fig. 3.12 As in Fig. 3.11 but for a 250 km radius (PTE250).

- Med2007

The surface pressure during Med2007 did not change much during the tropical-like phase of the cyclone before reaching Sardinia on 16 November 2007 (Fig. 3.7c and 3.9e-f). In PTE100 (Fig. 3.11e) a cyclone amplification stage is simulated between 1000 UTC on 15 November 2007 and 0000 UTC on 16 November 2007, but in PTE250 (Fig. 3.12e) brief negative Dp values are followed by equally positive values, showing a rather stable stage. Nevertheless, this difference highlights the small size of the MTLC, and the need to account for the different radii in PTE analysis in similar cases.

After a strong diabatic cooling and cold horizontal temperature advection that results in an increase to the surface pressure before 1000 UTC on 16 November 2007 during the deepening stage I, pulsating DC activity marked by scattered and short-lasting DCGRIDS, tends to contribute to the cyclone deepening, mostly in PTE100. In both PTE analyses, RES_{ITT} is significant and comparable to THD making it difficult to assess the $DIAB_{cont}$ which is estimated to range between 30 and 75% during stage I. To complicate things further, the presence of a strong PV streamer aloft (Fig. A2.5d) results in very small changes of the upper-tropospheric geopotentials but the negative $D\phi$ values follow the maximum deepening rates (down to -0.6 hPa 30 min^{-1}), whereas the $DIAB_{cont}$ has the highest values when Dp attains values close to -0.1 and -0.3 hPa 30 min^{-1} in PTE100 (Fig. 3.11e). In PTE250, a constant horizontal temperature advection results in diabatic cooling and opposes the cyclone deepening rates during the whole lifetime of Med2007. The evacuation of warm air from the core of the cyclone during 15 m s^{-1} DLS (Fig. 8c in QJRMS article) occurs during weak DC activity that cannot contribute to the mid/upper-level tropospheric heating.

During the second deepening stage (II), when Med2007 is found over the Tyrrhenian Sea (Fig. 3.9e-f), the cyclone has tropical-like characteristics for brief periods, now mostly having a cold core structure and a strong vertical tilt. In addition, the precedent DC activity has eroded the PV streamer to a great extent (not shown) and the cyclone seems to have only brief deepening phases during the decreasing cold-air advection ($TADV$ close to 0, especially in PTE100) and DC activity. The $DIAB_{cont}$ is estimated to contribute about 30-50% in the short-lasting deepening phases of the cyclone.

- TRIXIE

During the MTLC TRIXIE, the surface pressure close to the cyclone center was quite steady during the first 36 hours, between 0600 UTC 29 and 1800 UTC 30 October 2016, and minimum SLP was fluctuating between 1010 and 1014 hPa (Fig. 3.8e). DC activity according to WRF was very sporadic and short-lasting, mostly far away from the cyclone center, with $DIAB_{cont}$ accounting only about 10-50% to the short-lasting deepening phases in stage I (Fig. 3.11g-3.12g). In addition, the weak 500 hPa cut-off low (Fig. A2.7a) and the absence of a strong PV streamer aloft (Fig. A2.7b) result in small fluctuations in $D\phi$ values (Fig. 3.11g - 3.12g). A constant diabatic cooling due to longwave radiation and horizontal temperature advection is also found in this stage, balancing any positive contribution of diabatic heating to the deepening rates. Only near the end of this stage $D\phi$ attains values close to -1 hPa 30 min^{-1} (Fig. 3.11g - 3.12g), with slightly higher values of THD during DC activity (Fig. 3.11h - 3.12h).

In stage II, DCGRIDS are simulated closer to the cyclone center but they are still sporadic and short-lasting. Only between 0900 and 1200 UTC on 30 October 2016 Dp reaches values down to $-0.7 \text{ hPa } 30 \text{ min}^{-1}$, mostly attributed to DC activity ($DIAB_{cont} \sim 70\text{-}85\%$). Near the end of Stage II, the progressively further increase of DC activity is balanced by increasing geopotentials, so the pressure tendency rate remains close to zero for both PTE100 and PTE250. It is after 1800 UTC on 30 October 2016 when widespread and intense simulated DC activity (Fig. 3.8e) (in accordance with observations) marks the beginning of the third deepening stage (III) when both decreasing geopotentials and diabatic heating during DC activity result in an 9 hPa SLP drop in the center of TRIXIE in 12 hours. During the whole Stage III the $D\phi$ has negative values close to $-0.5 \text{ hPa } 30 \text{ min}^{-1}$, followed by smaller negative values of EP during intense rainfall. It is estimated that $DIAB_{cont}$ reaches values up to 95% during this period, with THD reaching values down to $-9 \text{ hPa } 30 \text{ min}^{-1}$ in PTE100 (Fig. 3.11g) and $-2.5 \text{ hPa } 30 \text{ min}^{-1}$ in PTE250 (Fig. 3.12g). Despite the high contribution of diabatic processes during DC activity in amplifying TRIXIE, the synoptic-scale processes are also important during this stage as the lowering geopotentials due to the approach of a trough in northeast, over Greece (Fig. A2.7c-e), results in further deepening of the cyclone. The intense DC activity continued after Stage III when TRIXIE started propagating south/southeast in the early morning on 31 October 2016, but the cyclone weakened significantly due to an increasing horizontal temperature advection of drier and colder air masses ($TADV > 0$) during increasing DLS (Fig. 8g in QJRMS article and also see A2.8e), the diabatic cooling of longwave radiation ($TLW > 0$), increasing geopotentials ($D\phi > 0$) as the cyclone was moving away from the approaching trough and the adiabatic cooling due to vertical motions ($VMT > 0$) which are almost equal and positive to THD (Fig. 3.11h - 3.12h).

- NUMA

During the first deepening stage (I) of NUMA between 1800 UTC on 16 November 2017 and 0300 UTC on 17 November 2017 (Fig. 3.11i – 3.12i), widespread simulated DCGRIDS close to the cyclone center result in minimum ITT values when the Dp also reaches a minimum, down to $-1 \text{ hPa } 30 \text{ min}^{-1}$ in PTE250 and $-1.6 \text{ hPa } 30 \text{ min}^{-1}$ in PTE100. Between 1000 and 1300 UTC on 16 November 2017 it is calculated that $DIAB_{cont}$ reaches values up to 90%, while baroclinic processes have a negative effect in the deepening rate. During the rest of Stage I, DC activity is first developing close to the cyclone center and then is expanding outwards, resulting in fluctuations of THD and VMT values in PTE100, significantly smoothed in PTE250 (Fig. 3.12j). In addition, the 500 hPa cut-off low becomes vertically aligned with the surface cyclone only after 0000 UTC 17 November 2017 (Fig. A2.9a-c) and until then, their relative displacement helped the surface cyclone to further deepen during negative $D\phi$ (strong baroclinicity).

In the morning on 17 November 2017, NUMA has a well-defined warm core structure and DC activity is very active close to the cyclone center (Fig. 3.8f). Despite that, no significant deepening rates are simulated, even though THD often reaches values down to $-3 \text{ hPa } 30 \text{ min}^{-1}$ in PTE100 (Fig. 3.11j) and $-2 \text{ hPa } 30 \text{ min}^{-1}$ in PTE250 (Fig. 3.12j). This is mostly due to the balanced increasing surface pressure by adiabatic cooling during vertical motions ($VMT > 0$) which has equal and opposite values with THD . Also during negative values of $D\phi$ and THD , the deepening rate is balanced by the diabatic cooling during horizontal air advection ($TADV > 0$)

and diabatic cooling due to longwave radiation ($TLW > 0$). During the short-lasting negative Dp values, $DIAB_{cont}$ is calculated between 80-90%. Finally, the third deepening stage (III) (although characterized by comparable periods of cyclone filling), starts when NUMA propagates southeast, towards Greece on 18 November 2017. During this period, the PV streamer is far away, southeast from NUMA (Fig. A2.9f) and geopotentials start to fall as a trough is approaching from the north (Fig. A2.9e). The deepening rates are more important in PTE250 than in PTE100, highlighting the synoptic changes in the environment of NUMA, under the influence of baroclinic processes. $DIAB_{cont}$ was calculated only up to 50% for a short period of time during this period. The sudden increase of $TADV$ coincides with the landfall of NUMA in West Greece (Fig. 3.7g and 3.8f) when the warm-core of the cyclone starts to suffer from increasing DLS. A combination of diabatic heating and decreasing geopotentials limit the filling of NUMA and result even in a brief surface cyclone amplification between 2100 UTC 18 November 2017 and 0000 UTC 19 November 2017.

- ZORBAS

The MTLC ZORBAS is marked by 2 distinct intensification periods: the first one when the cyclone is not yet tropical-like cyclone, having fronts and a cold core structure (Stage I in Fig. 3.11k - 3.12k), and the second one before making landfall to Greece (Stage III in Fig. 3.11k - 3.12k), when diabatic processes seem to play a dominant role to the cyclone intensification. In-between, ZORBAS seems to experience a rather steady phase, remaining a cyclone with high intensity, with brief intensification periods (e.g., around 1200 UTC 28 September 2018) which are not clearly mirrored to the minimum SLP at the center of the cyclone (Fig. 3.8g). During this period, DC activity is important within 100-200 km from the cyclone center, resulting in $DIAB_{cont}$ up to 70%.

In Stage I ZORBAS develops under a strongly baroclinic environment north from the Libyan coasts on 27 September 2018 and intense DC activity close to its center results in lower than $-3 \text{ hPa } 30 \text{ min}^{-1}$ ITT with a $DIAB_{cont}$ up to 95% (Fig. 3.11i - 3.12l). At the same time, the 500 hPa cut-off low is not in phase with the surface cyclone until 0900 UTC on 28 September 2018 (Fig. A2.11a-c). For that reason, the $D\phi$ fluctuates a lot, between -1.9 and $+1 \text{ hPa } 30 \text{ min}^{-1}$ in PTE250 (Fig. 3.12k). Also, the intense rainfall associated with the DC activity results in large negative EP values, especially in PTE100 (Fig. 3.11k) but the RES_{ITT} attains comparable or even larger values, making it difficult to calculate with high confidence the diabatic contribution to the cyclone amplification. Worth mentioning is that there is a constant advection of cool and dry mid/upper-level air towards the core of ZORBAS as the $TADV$ reaches values up $+5 \text{ hPa } 30 \text{ min}^{-1}$ in PTE100.

Between 0600 and 2100 UTC on 28 September 2018, ZORBAS has a full warm-core structure and its minimum SLP is rather steady, fluctuating between 987-989 hPa according to WRF. DC is active and intense in all cyclone quadrants, but due to the increasing diabatic cooling ($TADV > 0$), no significant deepening is simulated. The high values of $TADV$ can explain the spiral-cloud form of ZORBAS, as dry air is wrapped around the cyclone (Fig. 9j in QJRMS article). The PV streamer aloft is significantly eroded by the preceded DC activity (Fig. A2.11d) and only when the $D\phi$ term attains negative values after 1000 UTC on 28 September

2018, a short-lasting cyclone deepening is simulated. The $DIAB_{cont}$ is about 50-70% between 1000 and 1500 UTC 28 September 2018.

During the late night on 28 September 2018 and until 0200 UTC on 29 September 2018, a third deepening stage is simulated, resulting in a 4 hPa SLP drop in ZORBAS' center, after a burst of DC activity (Fig. 3.8g). The eroded PV streamer remains in the vicinity of the cyclone, resulting in erratic changes of $D\phi$, and a jet-stream is wrapped around ZORBAS, explaining the high values of $TADV$ (Fig. A2.11e-f). Around 0000 UTC 29 September 2018, ITT reaches again very low values, down to $-1.8 \text{ hPa } 30 \text{ min}^{-1}$ in PTE100 and $-0.8 \text{ hPa } 30 \text{ min}^{-1}$ in PTE250. During this period, the $DIAB_{cont}$ is calculated up to 90%, explaining the fast deepening of ZORBAS before making landfall in SW Greece a few hours later. Despite the lowering geopotentials ($D\phi < 0$) in the early morning on 29 September 2018 due to the north displacement of the mid-tropospheric low-pressure system as shown in Fig. A2.11e, the ITT term reaches values up to $+1.5 \text{ hPa } 30 \text{ min}^{-1}$, mostly attributed to the intrusion of drier and colder air masses in the mid/upper-troposphere ($TADV > +3.0 \text{ hPa } 30 \text{ min}^{-1}$ in PTE100). Again, RES_{ITT} reaches absolute values larger than $1 \text{ hPa } 30 \text{ min}^{-1}$, which are equal or larger than $D\phi$ and EP complicating the calculation of the contribution of these variables in the cyclone deepening in Stage III.

3.3.4 The evolution of vertical PV structures

After examining the periods during which DC has an important contribution to the intensification of the MTLCs, the evolution of their PV structures with the help of PV tracers will provide a new insight to the vertical structures. The evolution of the upper-level PV structures near the dynamic tropopause which separates the well-mixed troposphere from the stratified stratosphere and is defined by a discontinuity in the isentropic PV field (Reed, 1955), is better examined in isentropic surfaces because in the absence of frictional and diabatic effects, air parcels flow along constant isentropes and their PV is conserved. During diabatic heating through latent heat release, PV values increase below the heat source maximum and are reduced just above it (Raymond and Jiang, 1990). Climatological studies have shown that stratosphere-troposphere exchange can result in significant downward mass fluxes associated with PV streamers (Wernli and Bourqui, 2002; Sprenger et al., 2007) and the isentropic surfaces between 290 and 350 K are associated with the intrusion of stratospheric PV in the Northern Hemisphere. In order to study the changes of the large-scale upper-level PV structures in this thesis, the PVCO on different isentropic surfaces is computed and the special interest is on its interaction with DC activity in the low/mid-troposphere, producing low-level PV (PVDIAB) during the MTLCs. Among the 6 studied MTLCs several differences on the evolution of the PV streamers are identified due to the erosion of PVCO by upper-level divergence and cooling effects above DC, but the influence on the PV streamers and their interaction with PVDIAB varies among the MTLCs. In this paragraph we will discuss these differences between the MTLCs ZORBAS, NUMA, TRIXIE and Med2006 for which the diabatic contribution to their deepening rate is very important, as it was previously discussed in the PTE analysis.

The divergent (irrotational) zonal and meridional wind components are calculated by first computing the divergence using the average wind components in the isobaric levels between 200 and 300 hPa as follows:

$$\nabla \cdot \vec{v} > 0 \quad (\text{Eq. 3.28})$$

where $\vec{v} = (u, v)$ is the horizontal wind vector and the derivatives are computed via centered finite differences.

During the developing stage of ZORBAS, the PV streamer defined by the PVCO variable at the 330 K isentropic surface is significantly modified by the intense DC activity (Fig. 3.13). This PV streamer of stratospheric origin seems to have a direct influence on the initial low-level disturbance just north the coasts of Libya on 27 September 2018 where synoptic ascent has a maximum ahead (east) of the long-wave trough (see Appendix 2, Fig. A2.11a). Figures 3.13a-b show the modification of the PV streamer above the simulated DCGRIDS. During the DC activity, WRF simulates strong convergence at the low levels (not shown) and strong divergence aloft, near the tropopause (e.g., see the irrotational winds in Fig. 3.13c). The satellite imagery is consistent with these patterns of divergence, as a large outflow of cirrus clouds is visible during the rapid development of ZORBAS, and they are reduced as the cyclone reaches its maximum intensity just after 0300 UTC 28 September 2018.

More specifically, the initially concentrated low-level PV anomaly on 27 September shown in Fig. 3.13a, comes quickly in phase with the PV streamer while there is a constant increase of the low-level tangent wind along the isentropic surfaces (3.15a), bringing warm and moist air close to the cyclone center. After 1800 UTC 27 September 2018, widespread DC activity close to ZORBAS' center (Figs. 3.14b-c) creates high values of PVDIAB, resulting in a vertical PV-tower structure (Fig.3.14c) during the rapid deepening of the cyclone, reaching the maximum intensity after 0000 UTC 28 September 2018. The PV-tower extends until 300 hPa and it is coupled with the PV streamer while the DC activity continues to reduce the upper-level PVCO (Fig.3.13c). For the following 18 hours DC activity is slightly reduced close to the cyclone center, the PV-tower is intensifying as the PVDIAB is accumulated within ZORBAS' core (Fig. 3.15a) but the PVCO values still exceed 2 PVU below 300 hPa. The PV-tower is connected with reservoir of high stratospheric PV until the afternoon on 28 September 2018 (Fig. 3.13e and 3.15b). During the late night on 28 September 2018, after a significant erosion of the PV streamer, ZORBAS now enters the second deepening phase when PVDIAB alone sustains the PV-tower structure that extends up to 300 hPa (Fig.3.15c) and the cyclone reaches again its maximum intensity at 0300 UTC on 29 September 2018. By the early morning on 29 September 2018, PVCO at the 330 K isentropic surface has values close to 1 PVU above ZORBAS (3.13f), and the 2 PVU isoline is now found near 200 hPa (Fig. 3.15c) and there is a discontinuity with the high PVDIAB values below. As the cyclone makes landfall in Greece, the PVDIAB is also eroded due to friction and the core of the cyclone is filled with drier continental air masses during increasing vertical wind shear, evident by the increasing tangent wind values up to 400 hPa, resulting in cyclone filling. By the end of the simulation, larger than 2 PVU PVDIAB values are found only below 700-800 hPa (not shown).

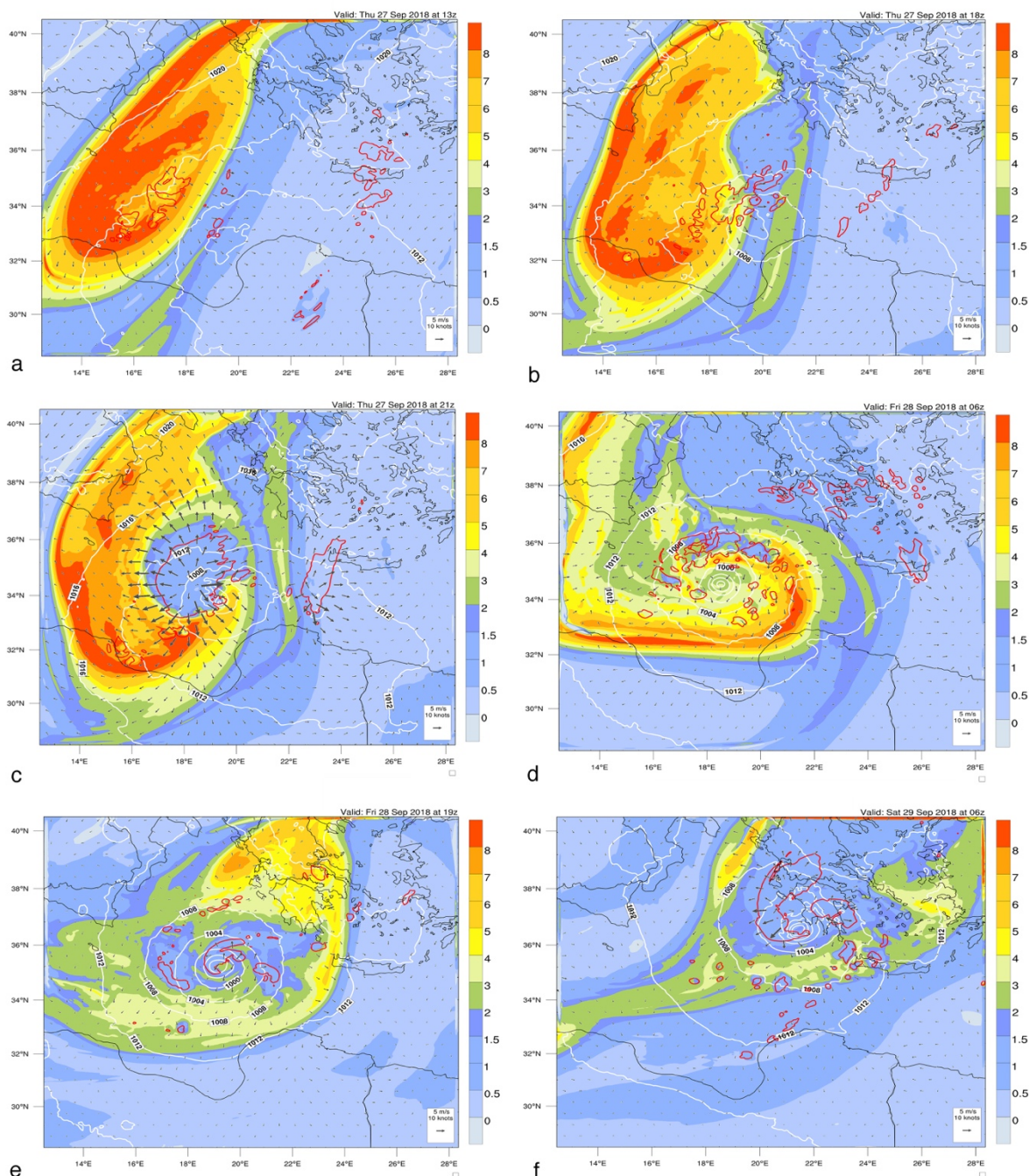


Fig. 3.13 The potential vorticity attributed to the large-scale flow (the conserved PV, PVCO) at the isentropic surface 330 K (shade), mean 300-200 hPa irrotational winds (arrows), DCGRIDS (red contours), and sea-level pressure (hPa) (white contours) during ZORBAS, valid for 27 September 2018 at 1300 UTC(a), at 1800 UTC (b) and at 2100 UTC (c), for 28 September 2018 at 0600 UTC (d) and 1900 UTC (e), for 29 September 2018 at 0600 UTC (f).

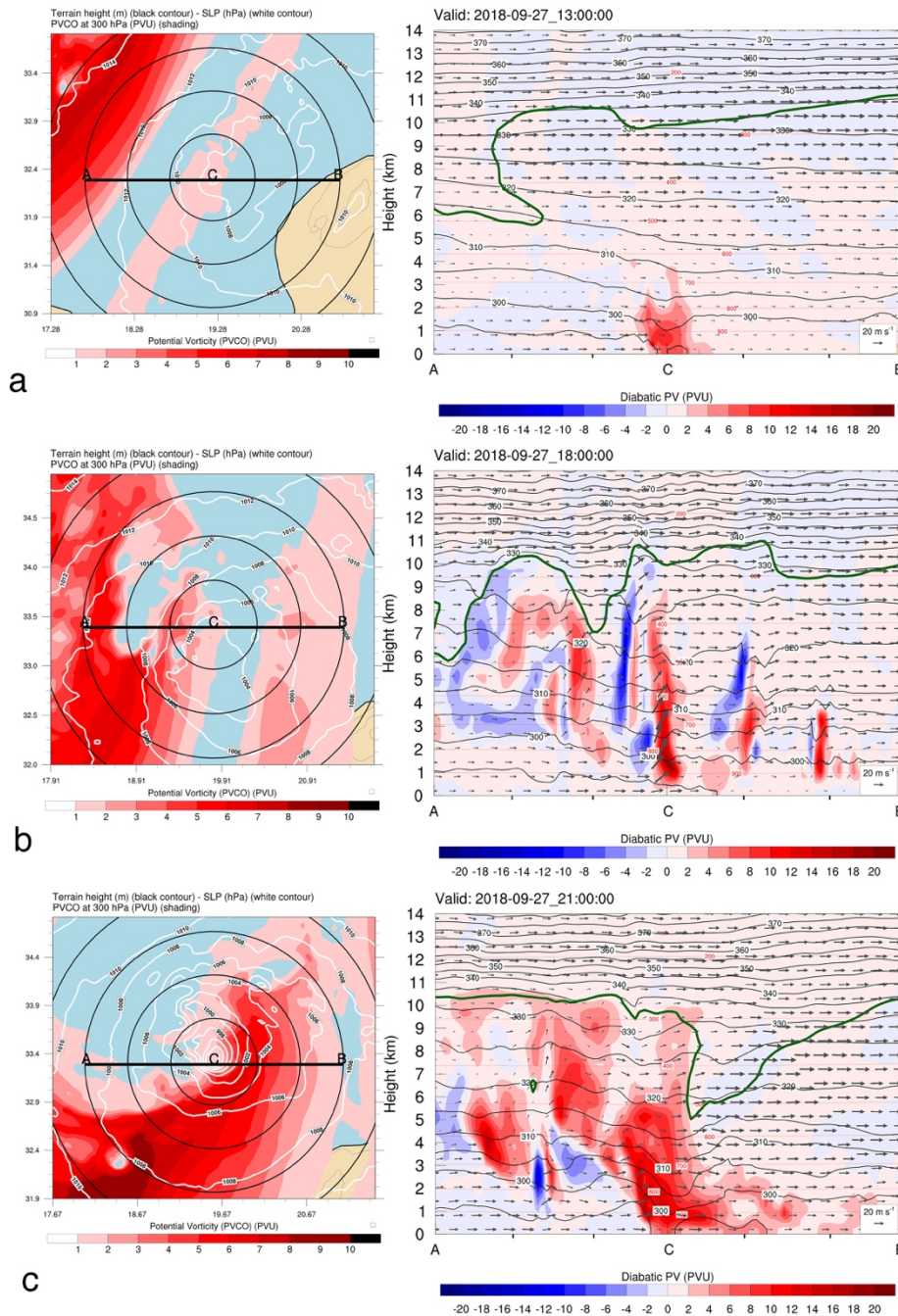


Fig. 3.14 Left (maps): horizontal cross-section of the conserved potential vorticity (PVCO) at 300 hPa (shade, PVU), SLP (white contours, hPa) and topography (land is shown in beige and the sea in light blue). The center of the cyclone which is also the center of the vertical cross-section is marked with the letter “C” and the two edges of the cross section by the letters “A” and “B”. The circles are drawn every 50 km from “C”. Right: vertical cross-section of potential vorticity produced by diabatic processes (PVDIAB) (shade, PVU) and tangent wind (arrows, with vertical component multiplied by a factor of 10). The 2 PVU PVCO is shown with a thick green line, isentropic surfaces (Kelvin) are shown with thin black lines and isobaric surfaces (hPa) with thin red lines. The graphs are valid for ZORBAS, for 27 September 2018 at 1300 UTC (a), at 1800 UTC (b) and at 2100 UTC (c).

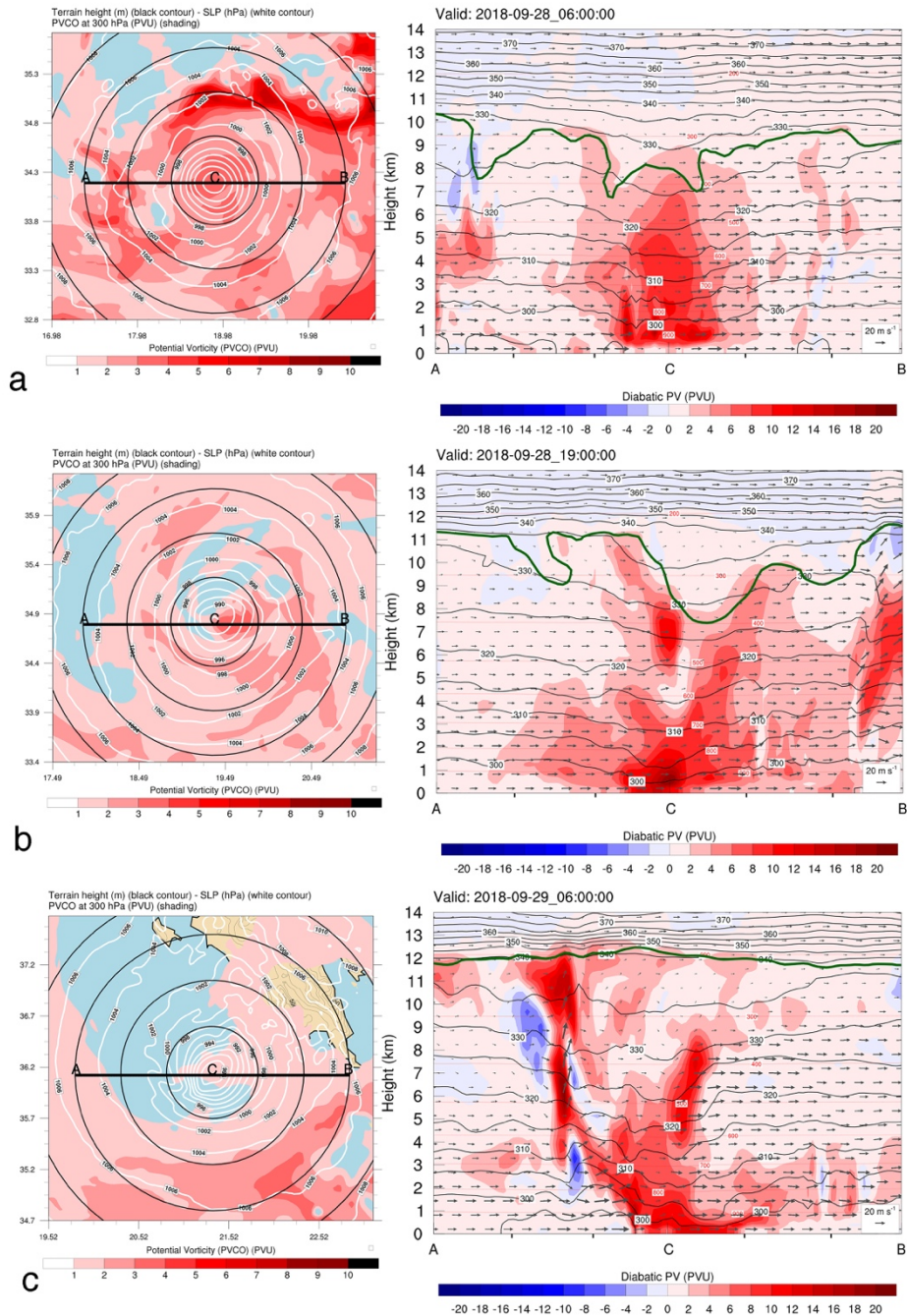


Fig. 3.15 As in Fig. 3.14 for ZORBAS, but valid for 28 September 2018 at 0600 UTC (a), at 1900 UTC (b), and for 29 September 2018 at 0600 UTC (c).

A similar analysis for NUMA, but for the 315 K isentropic surface, since the dynamic tropopause was found in a lower altitude than ZORBAS, reveals that the PV streamer is also significantly eroded by DC activity, but a PV-tower structure also develops during this case. First, when the PV streamer starts to wrap around NUMA from the south (Fig.3.16a) on 16 and 17 November 2017, the surface cyclone reaches its maximum intensity, but PVDIAB values larger than 2 PVU are only found below 600 hPa and high PVCO values penetrate down to the 500 hPa isobaric surface just above the cyclone center, as a high-PVCO blob gets detached from the streamer (Fig.3.17a). In the following hours, the isentropic influx of warm and moist air masses and the DC activity close to NUMA's center (Fig. 3.16b) results in a more concentrated low-level PV

anomaly (Fig.3.17b), and a “tilted” PV-tower forms by the night on 17 November and lasts until the morning on 18 November 2017, extending up to 300-400 hPa (Fig. 3.16c and 3.17c). By the afternoon on 18 November 2017, WRF simulates the complete erosion of the PVCO above NUMA, now found above 10 km height or the 320 K isentropic surface in the stratified stratosphere (Fig.3.16d and 3.18a). During this period there is a significant absence of DCPIXELS in the observations, confirming the absence of DCGRIDS in the simulation. The upper-level eastern advection of PVCO and preceded DC activity together led to this PVCO weakening above NUMA. After 2000 UTC on 18 November 2017 a burst of DC activity results in the production of high PVDIAB over NUMA (Fig. 16e), creating again a PV-tower that extends up to 400 hPa and the surface cyclone deepens about 4 hPa in 4 hours before making a landfall in Western Greece (Fig. 3.16f and 3.18b). At the same time, the tangent wind near the surface also intensifies but only in the western parts of the cyclone.

Even though it seems that the DC activity follows the solar diurnal cycle on 18 November 2017 as it was discussed in Chapter 2 and it is partly simulated by WRF (Fig. 3.8f), there is no evidence in the numerical results, either by the PTE or the PV analyses that this oscillation of the DC activity is attributed to radiation effects, as it has been proven in TCs, but the vertical distribution of PV appears to be a more important factor. After the erosion of PVCO in the afternoon on 18 November, the warm-core structure of NUMA is distorted and is limited below 600 hPa as it can be seen by the perturbation of isentropic surfaces in Fig. 3.18a. It is assumed that the weakening tangent winds result in the lack of low-level convergence to promote convection, until the cyclone moves close to the coasts of Greece where frictional convergence and increasing wind shear promotes the burst of DC activity. After crossing Kefalonia, NUMA has a very shallow warm-core structure with high PVDIAB below 600 hPa (Fig. 3.18c).

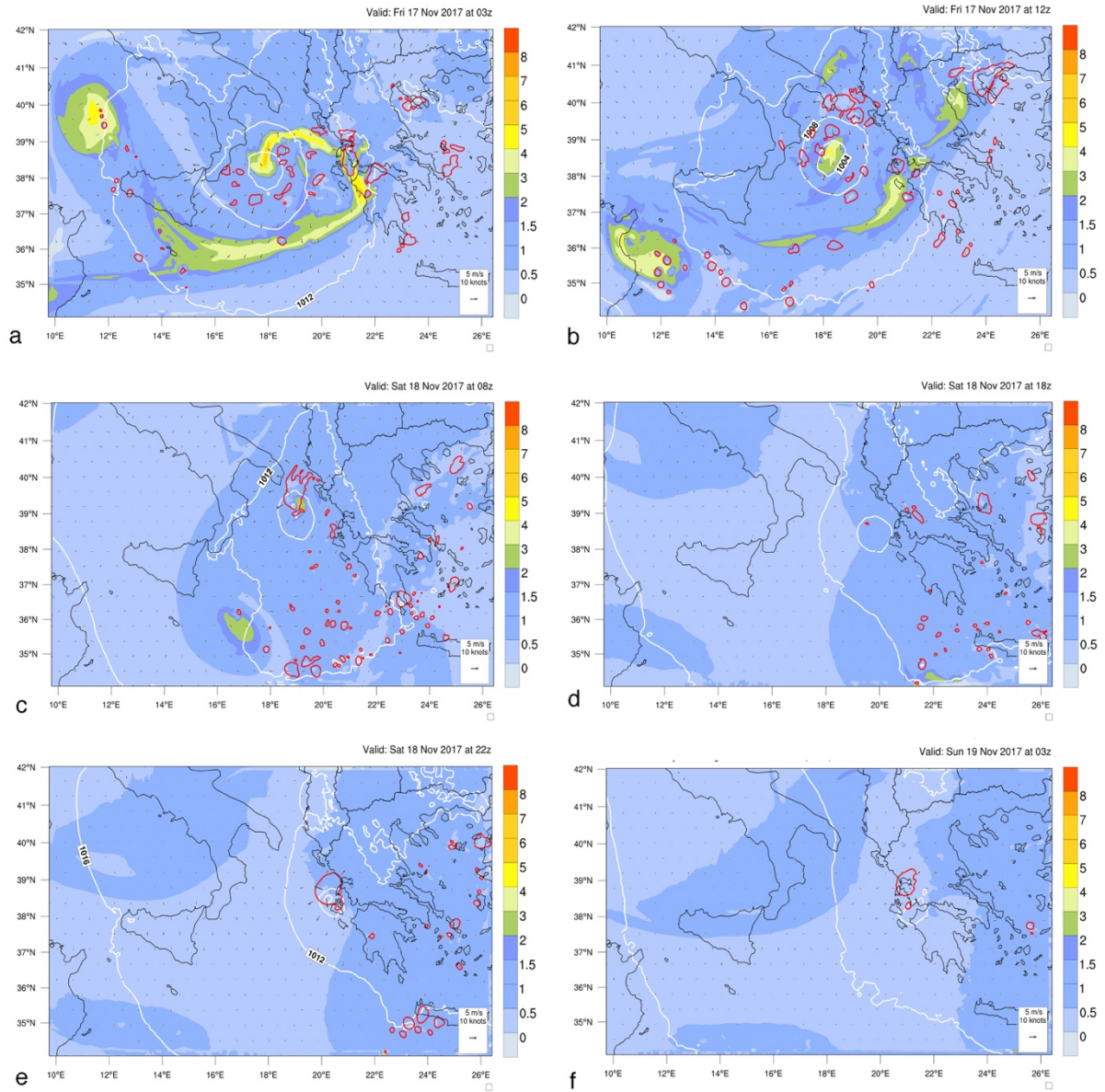


Fig. 3.16 As in Fig. 3.13 but for NUMA and the PVCO at the 315 K isentropic surface, valid for 17 November 2017 at 0300 UTC (a) and 1200 UTC (b), for 18 November 2017 at 0800 UTC (c), 1800 UTC (d) and 2200 UTC (e), and for 19 November 2017 at 0300 UTC (f).

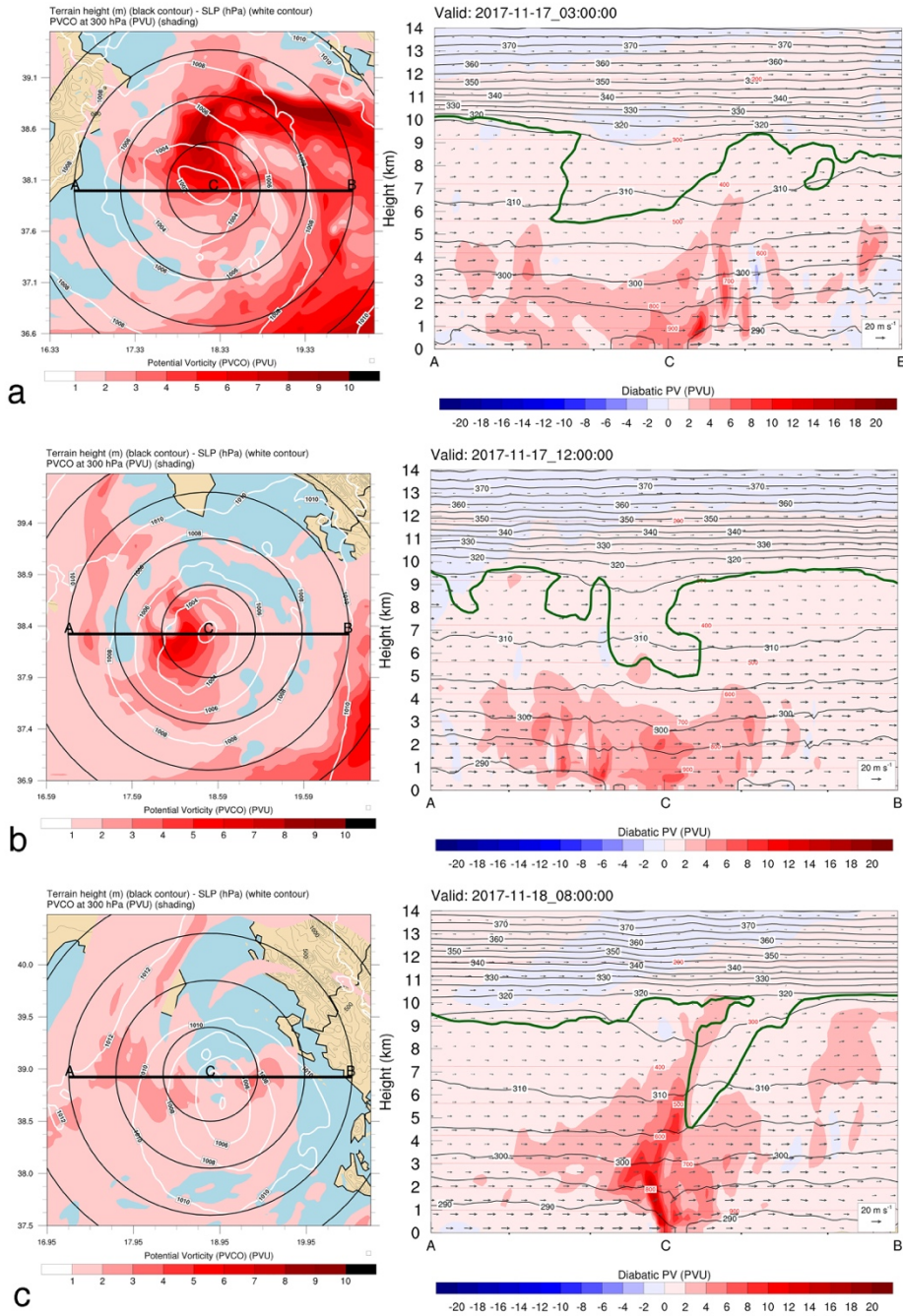


Fig. 3.17 As in Fig. 3.14 but for NUMA, valid for 17 November 2017 at 0300 UTC (a) and 1200 UTC (b), and for 18 November 2017 at 0800 UTC (c).

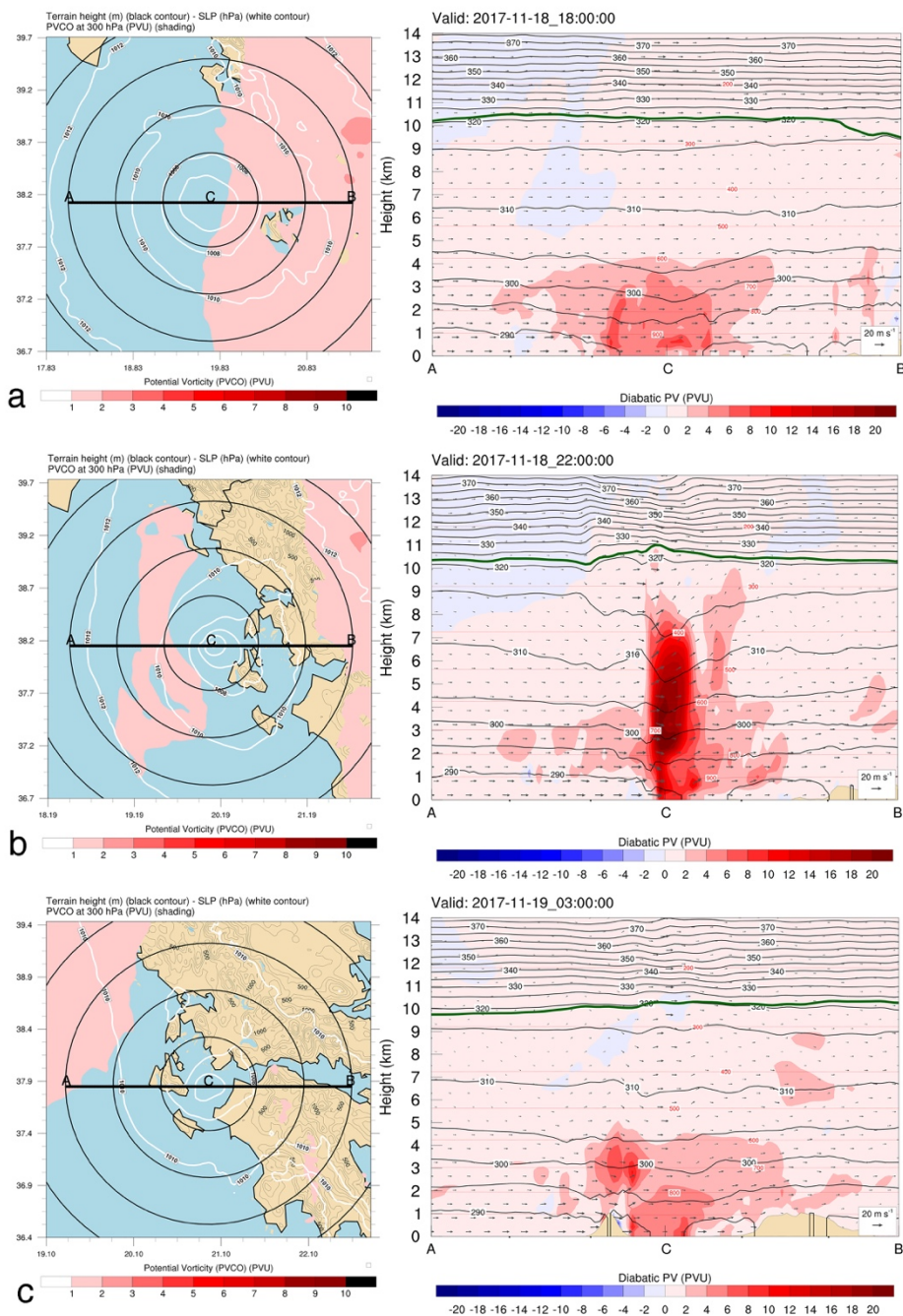


Fig. 3.18 As in Fig. 3.14 but NUMA, valid for 1800 UTC (d) and 2200 UTC (e), and for 19 November 2017 at 0300 UTC (f).

A different evolution of the vertical PV structure is found in the simulation of Med2006. For this case, a PV streamer and strong DC activity on 25 September 2006 (Fig. 19a) results in the development of a low-level PV anomaly (Fig. 3.20a-b) under the left exit of a jet streak (Fig. A2.3a-c) evident by the strong tangent winds in the upper-troposphere (Fig. 3.20b). The 330 K isentropic analysis of PVCO shows a limited structural erosion of the PV streamer by DC activity during the early stages of Med2006, and the absence of a PV-tower during the explosive deepening phase (Fig. 3.19b and 3.20b). This mostly has to do with the north-eastern advection of the PV streamer rather than the intensity of the DC activity, as the convective cells extend through the whole troposphere, creating PV dipoles and bringing low PV values above 300 hPa (Fig. 3.20a). As it is

also shown in the PTE100 analysis, the strong mid/upper-level wind flow removes the high theta-e air masses from the core of Med2006, bringing low-entropic air, resulting in a vortex tilt and a shallow concentration of high PVDIAB (Fig. 3.20b). Despite this, the cyclone is deepening with a high rate until the time of landfall in the morning on 26 September 2006, when the high PVCO and PVDIAB values become vertically aligned, creating a PV-tower (3.19c and 3.21a). This vertical structure of PV remains the same until the second landfall of Med2006 in Central Italy, without resulting in further deepening but rather helps the surface cyclone to sustain its high intensity (Fig.3.19d and 3.21b).

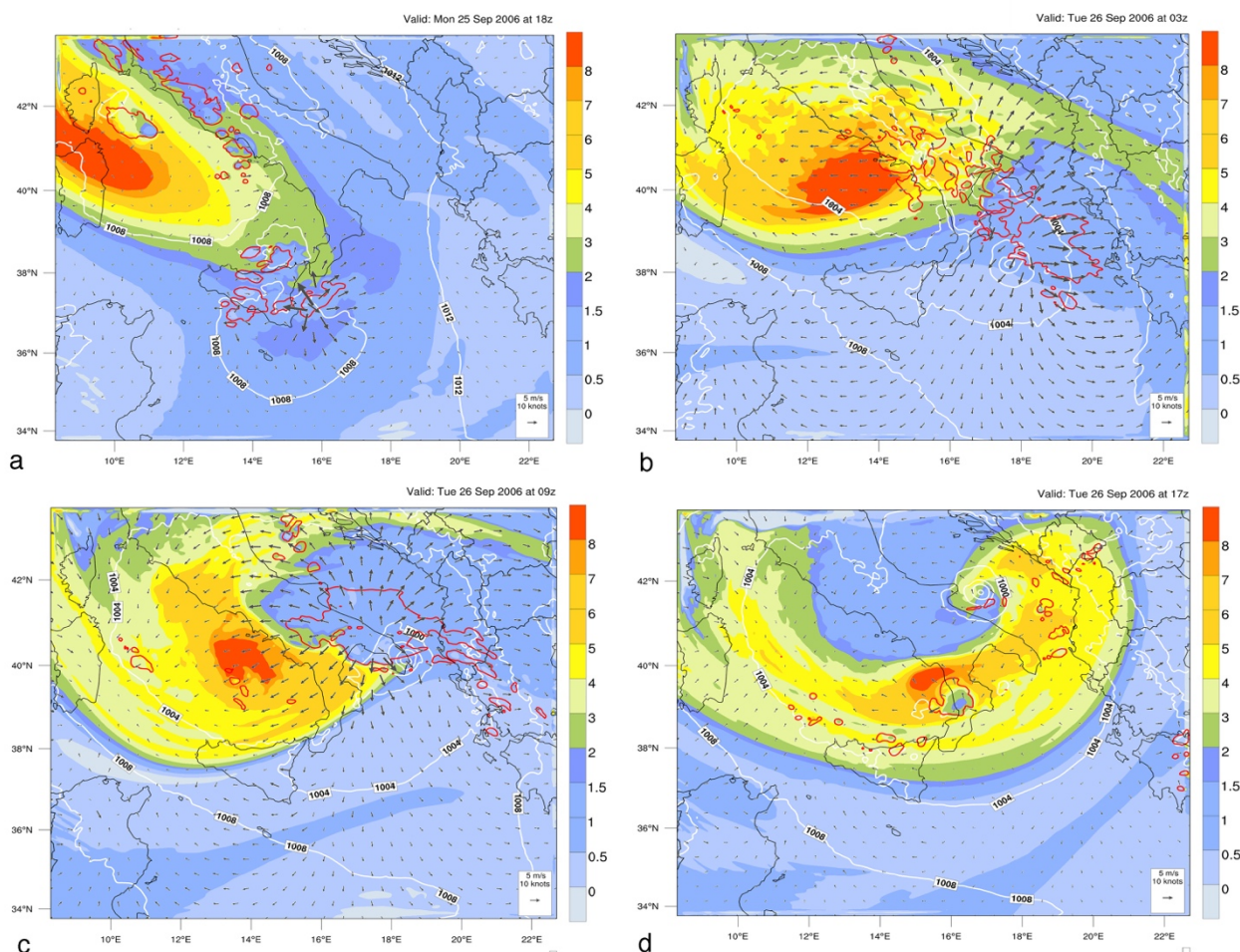


Fig. 3.19 As in Fig. 3.13 but for Med2006, valid for 25 September 2006 at 1800 UTC (a), 26 September 2006 at 0300 UTC (b), at 0900 UTC (c) and at 1800 UTC (d).

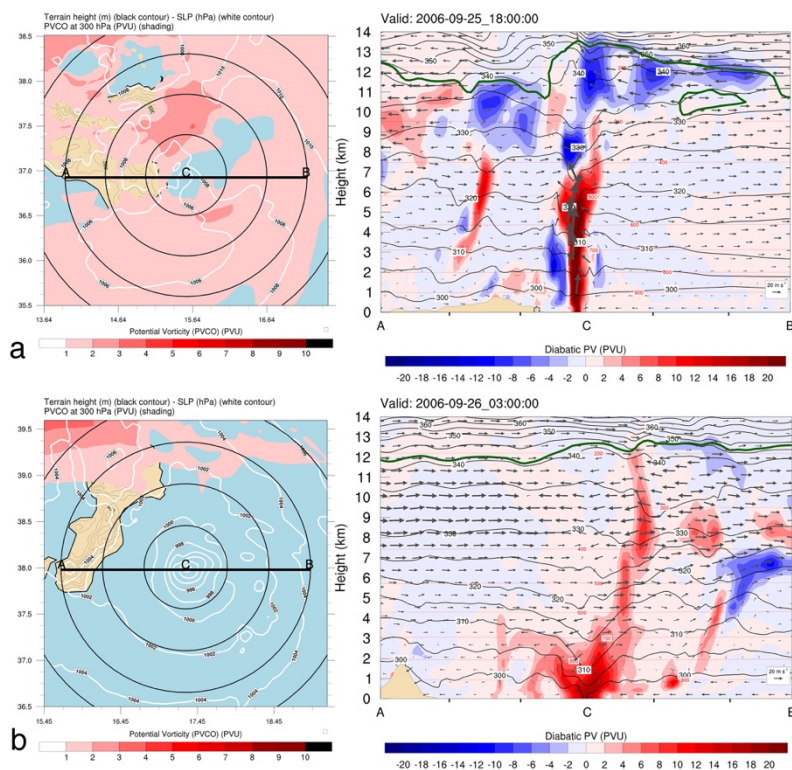


Fig. 3.20 As in Fig. 3.14 but for Med2006, valid for 25 September 2006 at 1800 UTC (a), 26 September 2006 at 0300 UTC (b).

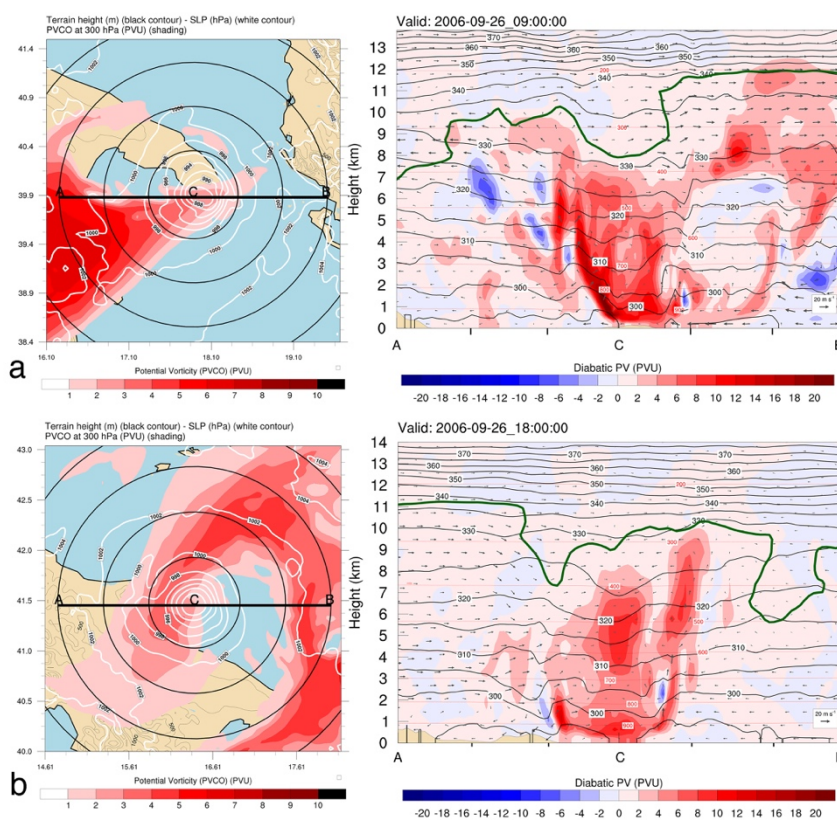


Fig. 3.21 As in Fig. 3.13 but for Med2006, valid for 26 September 2006 at 0900 UTC (a) and at 1800 UTC (b).

In contrast with ZORBAS, NUMA and Med2006, TRIXIE is associated with a very weak PV streamer that has values more than 2 PVU at the 330 K isentropic surface during the non-tropical-like phase on 29 and 30 October 2016 (Fig. 3.22a-b and 3.23a-b). The initial low-level PV anomaly attributed to PVDIAB stays below 700 hPa until the late afternoon on 30 October 2016 when DC activity close the cyclone center starts producing high PVDIAB values up to the tropopause (Fig. 3.22c and Fig. 3.23c). The constant DC activity close to the cyclone center results in a strong deepening of TRIXIE until the early morning on 31 October 2016 (Fig. 3.22d-e and Fig. 3.23a-b) when a PV-tower attributed only to PVDIAB, develops and extends up to 300 hPa. At the same time, the 2 PVU PVCO is limited higher, close to 200 hPa in the lower stratosphere. Finally, when DC activity stops after 0900 UTC 31 October 2016, the low-level PV anomaly shown in Fig. 3.24c continues to have values higher than 2 PVU below 700 hPa, just as it did in the initial non-tropical-like stage. This period is characterized by fair weather conditions, even the absence of clouds around TRIXIE in the simulations and the observations.

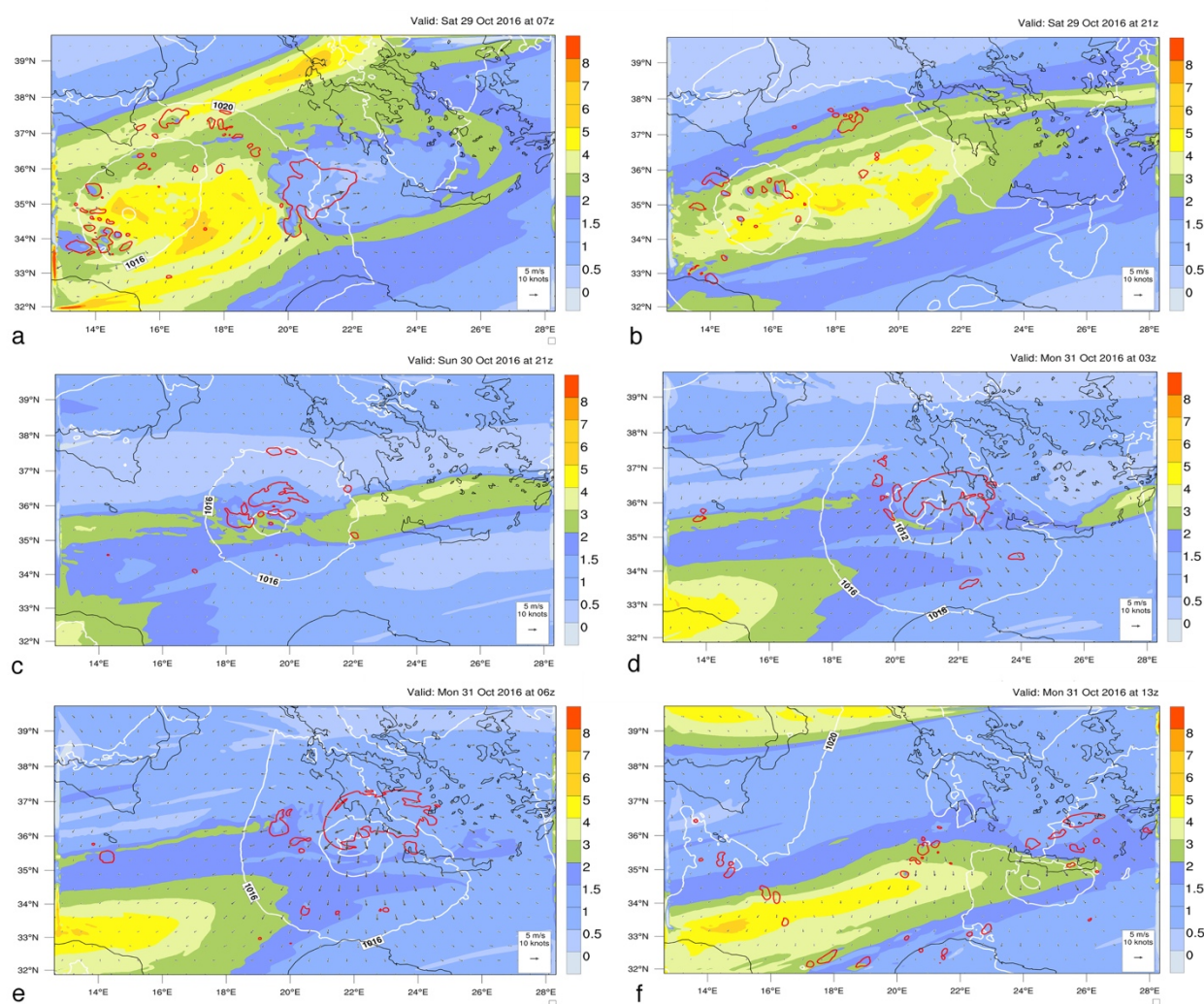


Fig. 3.22 As in Fig. 3.13 but for TRIXIE, valid for 29 October 2016 at 0700 UTC (a), at 2100 UTC (b), for 30 October 2016 at 2100 UTC (c), for 31 October 2016 at 0300 UTC (d), at 0600 UTC (e) and at 1500 UTC (f).

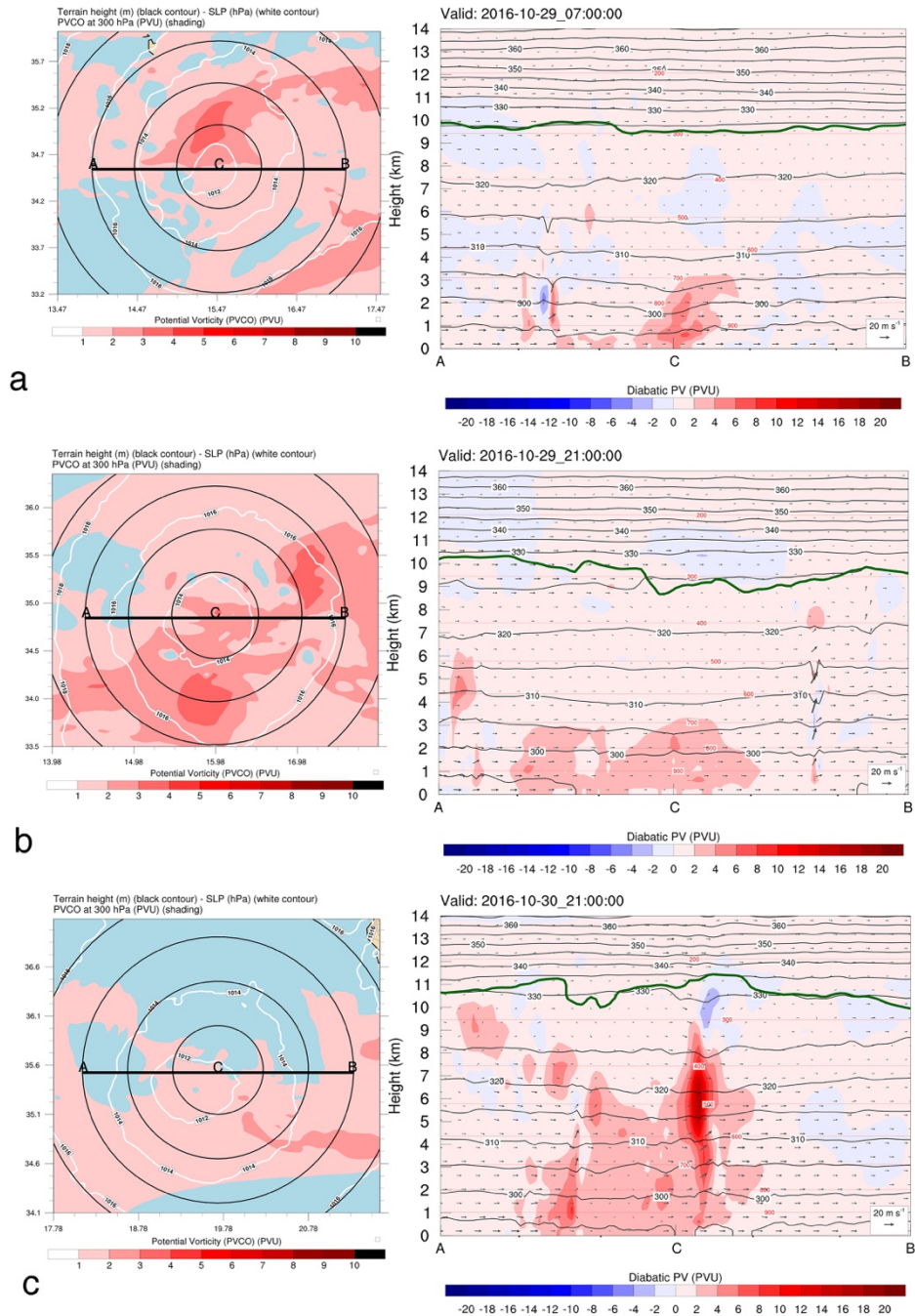


Fig. 3.23 As in Fig. 3.14 but for TRIXIE, valid for 29 October 2016 at 0700 UTC (a), at 2100 UTC (b), for 30 October 2016 at 2100 UTC (c).

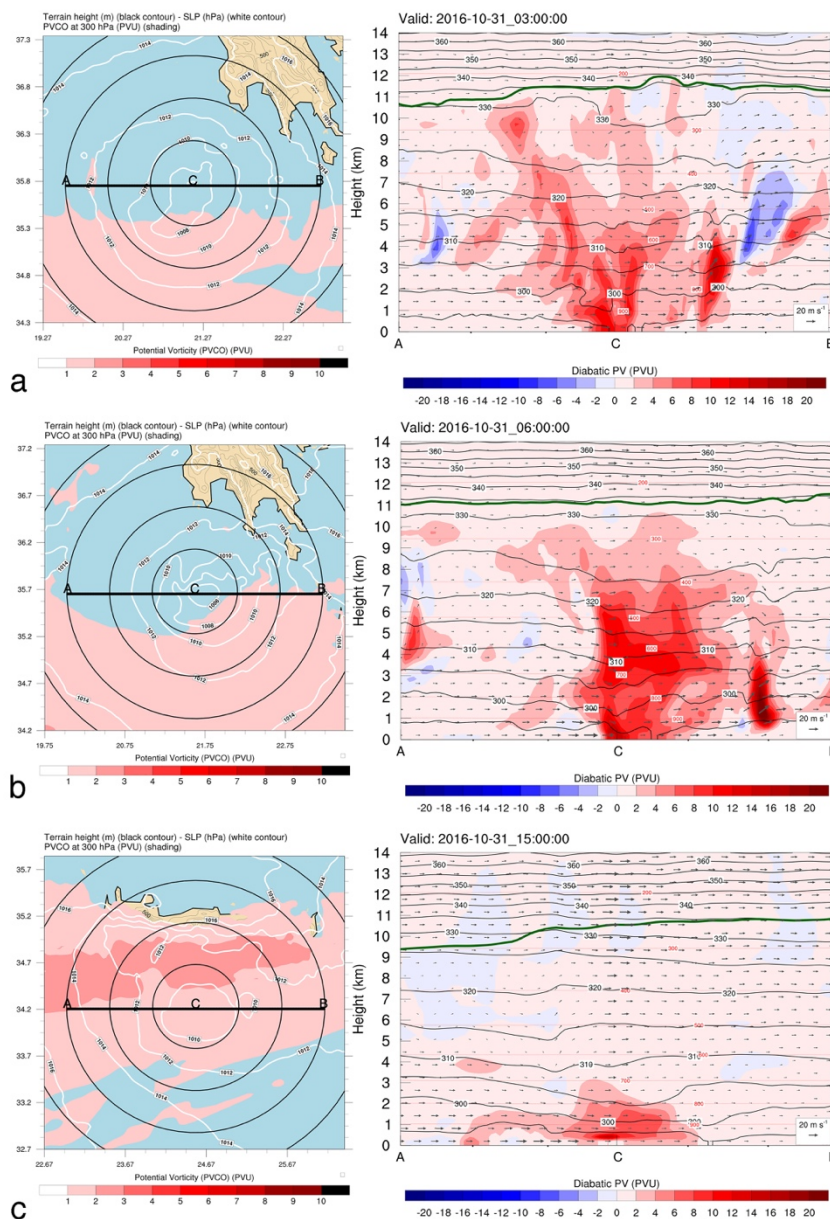


Fig. 3.24 As in Fig. 3.14 but for TRIXIE, valid for 31 October 2016 at 0300 UTC (a), at 0600 UTC (b) and at 1500 UTC (c).

3.3.5 Connecting the PV evolution with cyclone intensity

After examining the 3 different evolution-types of vertical PV structures and attributing the contribution of diabatic processes to the deepening rates via the PTE analyses, we can now review the proposed classification of the MTLCs in Chapter 2. According to this classification and the results in this chapter, MTLCs in Group 1 experience limited DC activity that does not contribute much to their intensification. By computing the mean PVDIAB, the mean PVCO and within 100 km from the centers of Med2005 and Med2007, we can interpret the presence of high large-scale and of stratospheric/upper-tropospheric origin PV (PVCO) during their whole lifetime, and low values of PVDIAB in the lower troposphere (Fig. 3.25a-c).

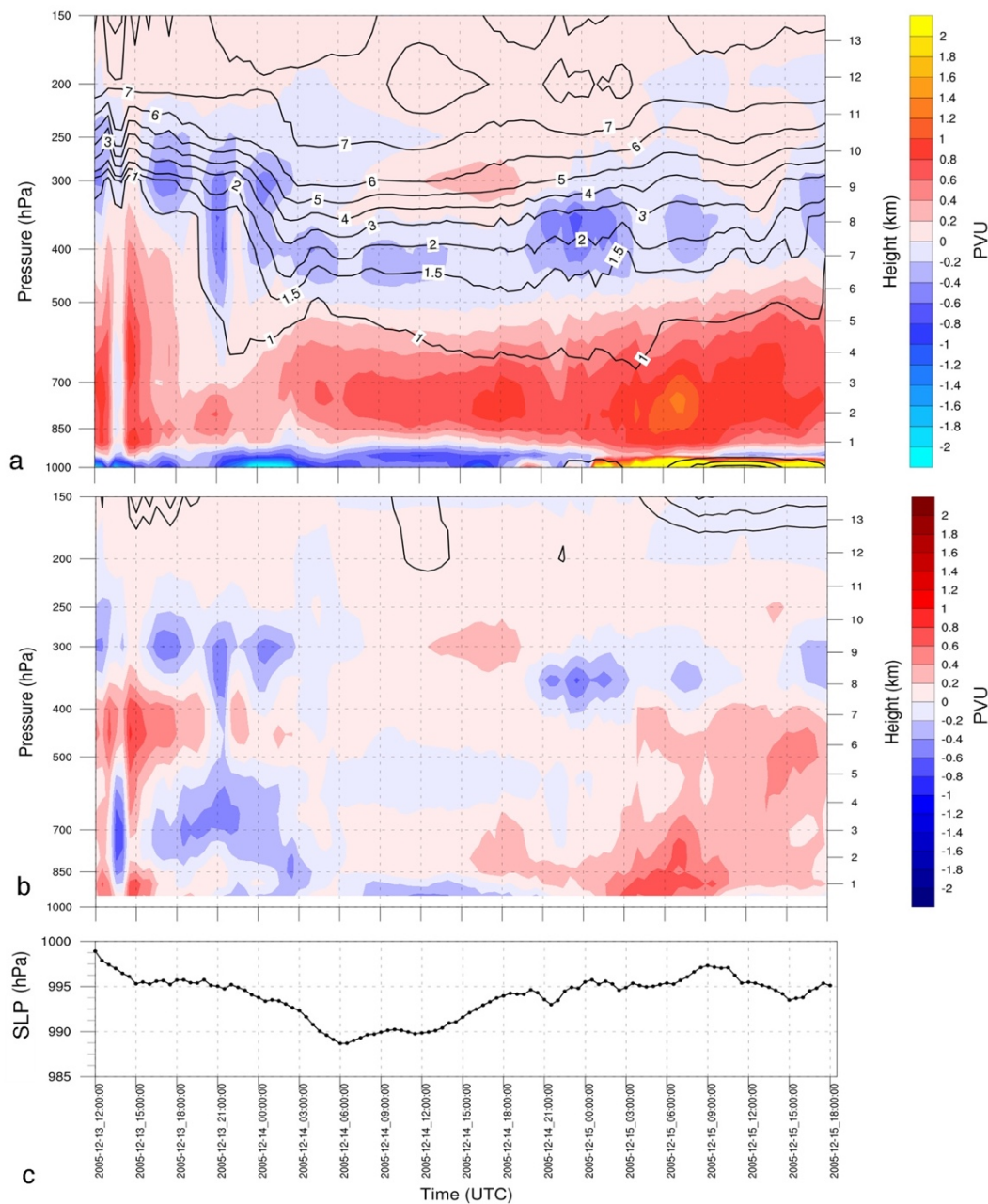


Fig. 3.25 Time-pressure diagrams for average values within 100 km from the cyclone center of Med2005 for (a) PVDIAB (shaded, PVU) and PVCOC (black contours, PVU), and (b) the anomalies of PVDIAB (shaded, PVU) and PVCOC (black contours-only positive, PVU) with respect to the time of maximum cyclone intensity (minimum SLP shown below in hPa in (c)).

In addition, there is no PV-tower development, a clear distinction from the other 2 groups. When computing the anomalies of PVCOC and PVDIAB with respect to the times of maximum cyclone intensity, we see that during the intensification periods, PVDIAB in the lower troposphere is weaker or has the same values than later time instances (Fig. 3.25b). Also high PVCOC values are found deep in the troposphere, down to 500 hPa for a prolonged period of time (Figs. 3.25a-3.26a), showing the constant influence of the PV streamers that do not significantly weaken by the weak and scattered DC activity. Especially for Med2007, PVDIAB is mostly negative after the landfall of the cyclone in Sardinia after 1000 UTC 16 November 2007 (Fig. 3.26a) and has a maximum during the maximum intensity of the cyclone at 2100 UTC on 15 November 2007. During

the maximum intensity of Med2007 the DC activity contributes about 50-85 % to the deepening rate of surface pressure according to the PTE analyses.

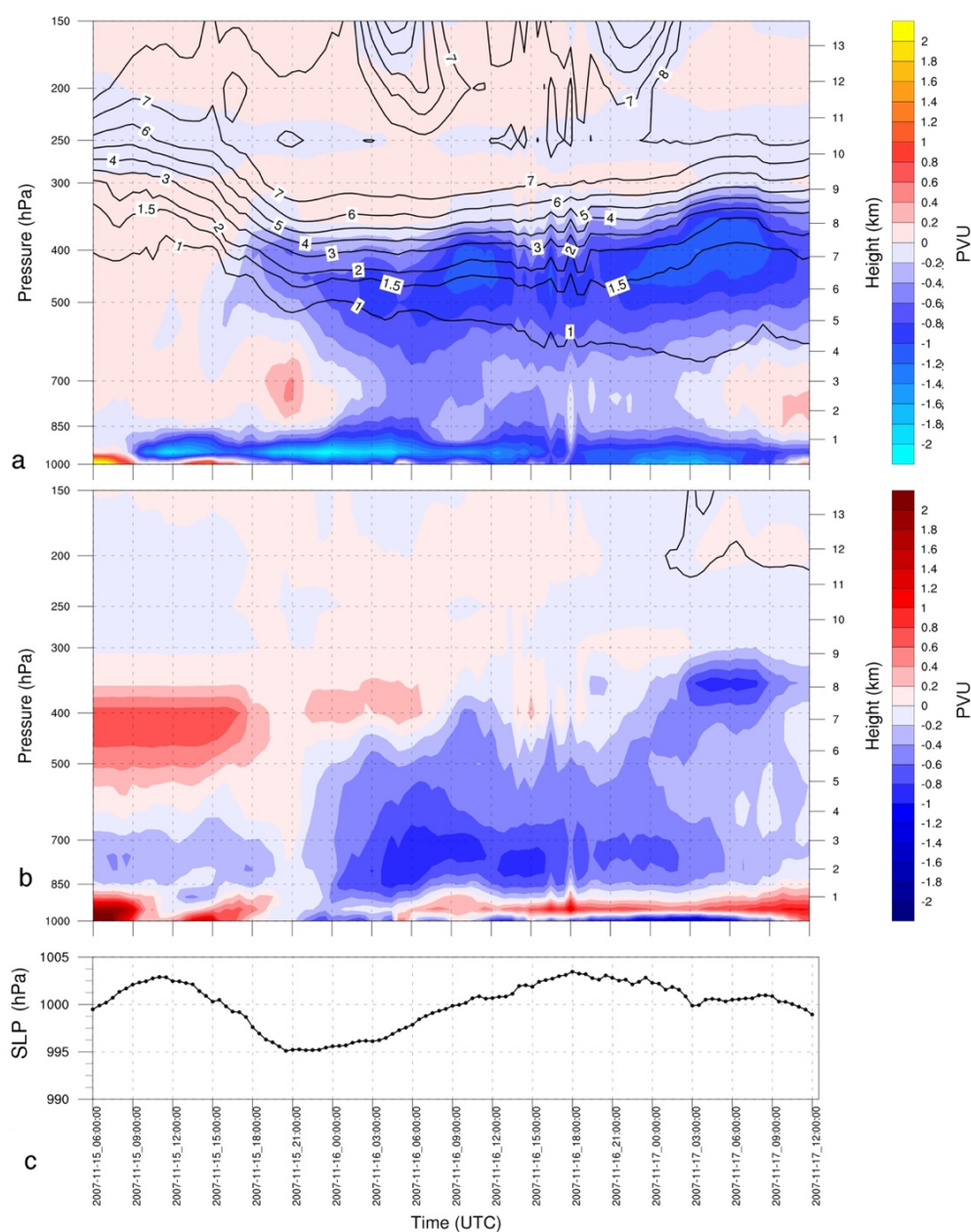


Fig. 3.26 As in Fig. 3.25 but for Med2007.

The unrealistically high PVDIAB values in the first model levels and the negative values above in the PBL between 0600 and 1800 UTC on 15 November 2007 can be attributed to the strong turbulent diffusion from the PBL parameterization scheme. Indeed, there is a sharp vertical gradient of temperature fluxes within the PBL throughout the simulation (not shown), slightly reduced when the cyclone is over Sardinia.

Regarding the Group 2 which includes TRIXIE, NUMA and ZORBAS, we see the development of PV-towers during their intensification periods, some of them extending higher than 400 hPa. Moreover, the PVCO in the mid/upper troposphere is reduced about 18-24 hours prior to the time of maximum intensity of TRIXIE (Fig. 3.27) and NUMA (Fig. 3.28), while for ZORBAS only the second and shorter intensification period occurs after the weakening of the PV streamer (Fig. 3.29a-b).

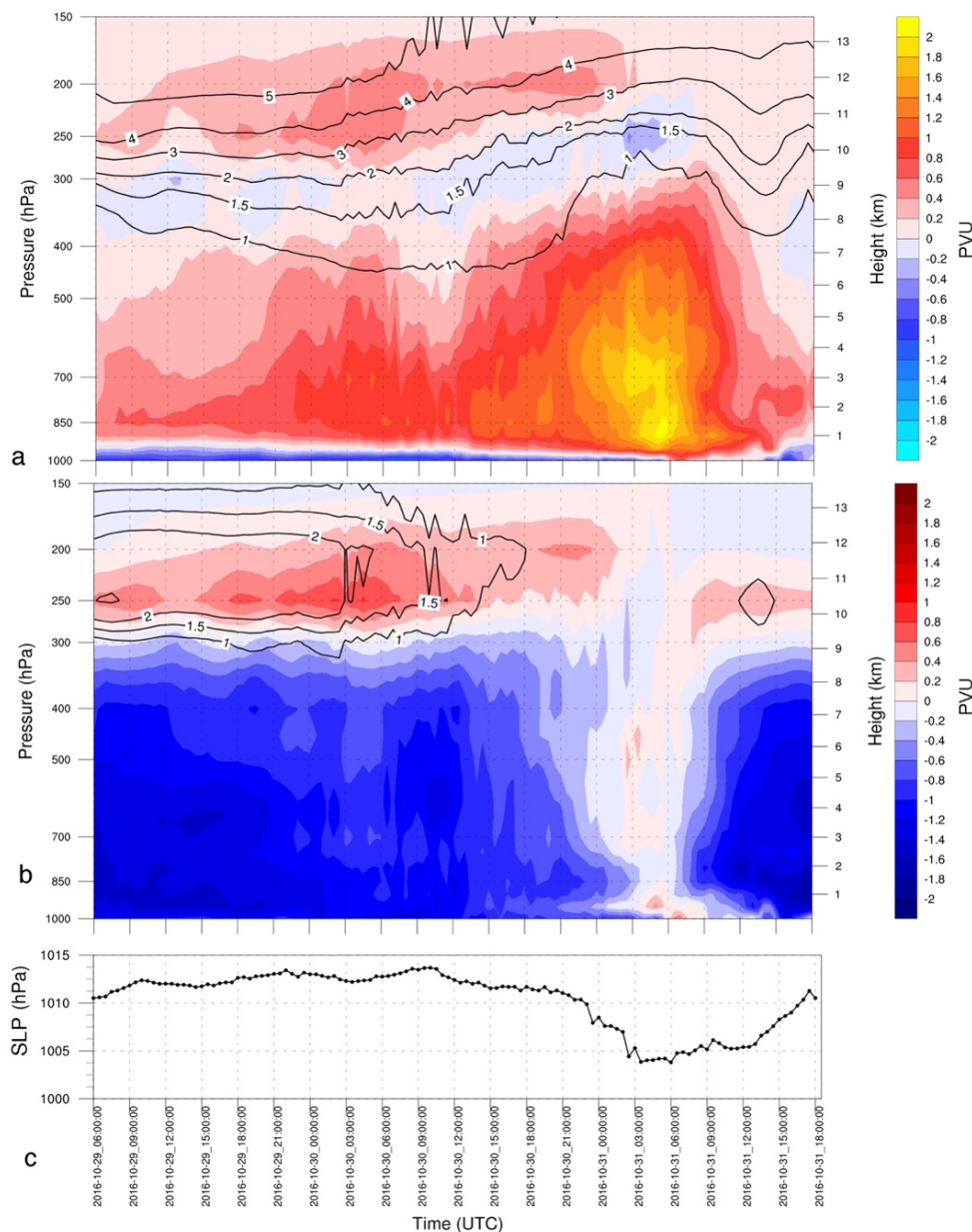


Fig. 3.27 As in Fig. 3.25 but for TRIXIE

For NUMA and ZORBAS, prolonged periods of high PVDIAB production are connected with the sustained high intensity of the surface vortices or short-lasting intensification periods during local increases of PVDIAB between 850 and 600 hPa (e.g., between 1200-1700 UTC 17 November 2017 for NUMA in Fig. 3.28). Also for these 2 MTLCs, the PVDIAB-towers are connected with the reservoir of high PVCO in the upper-troposphere and stratosphere during most of their evolution, but both amplify a few hours before their lysis in an environment where the upper-level forcing is not crucial to the low-level cyclone amplification, same as in TRIXIE (Fig. 3.27).

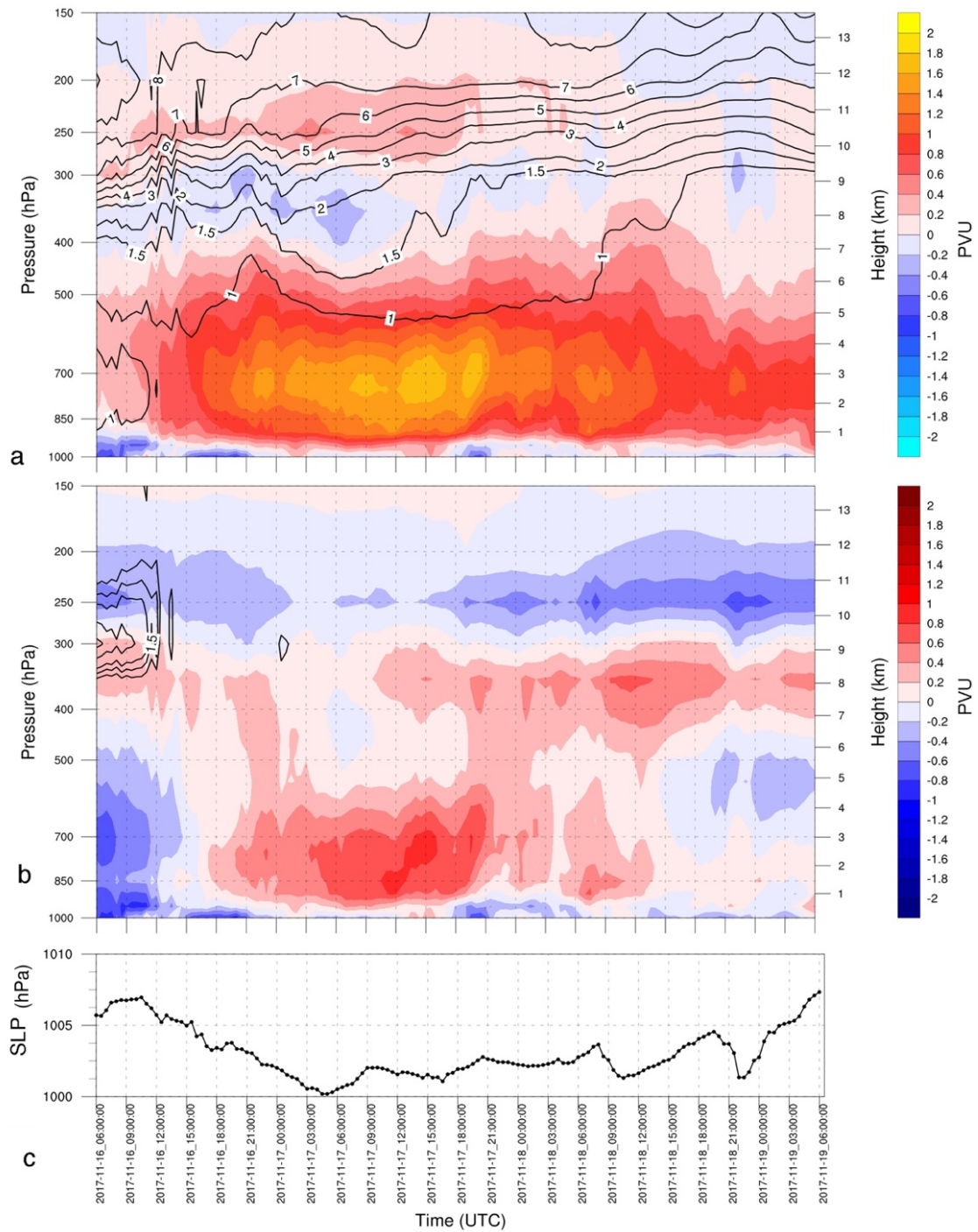


Fig. 3.28 As in Fig. 3.25 but for NUMA

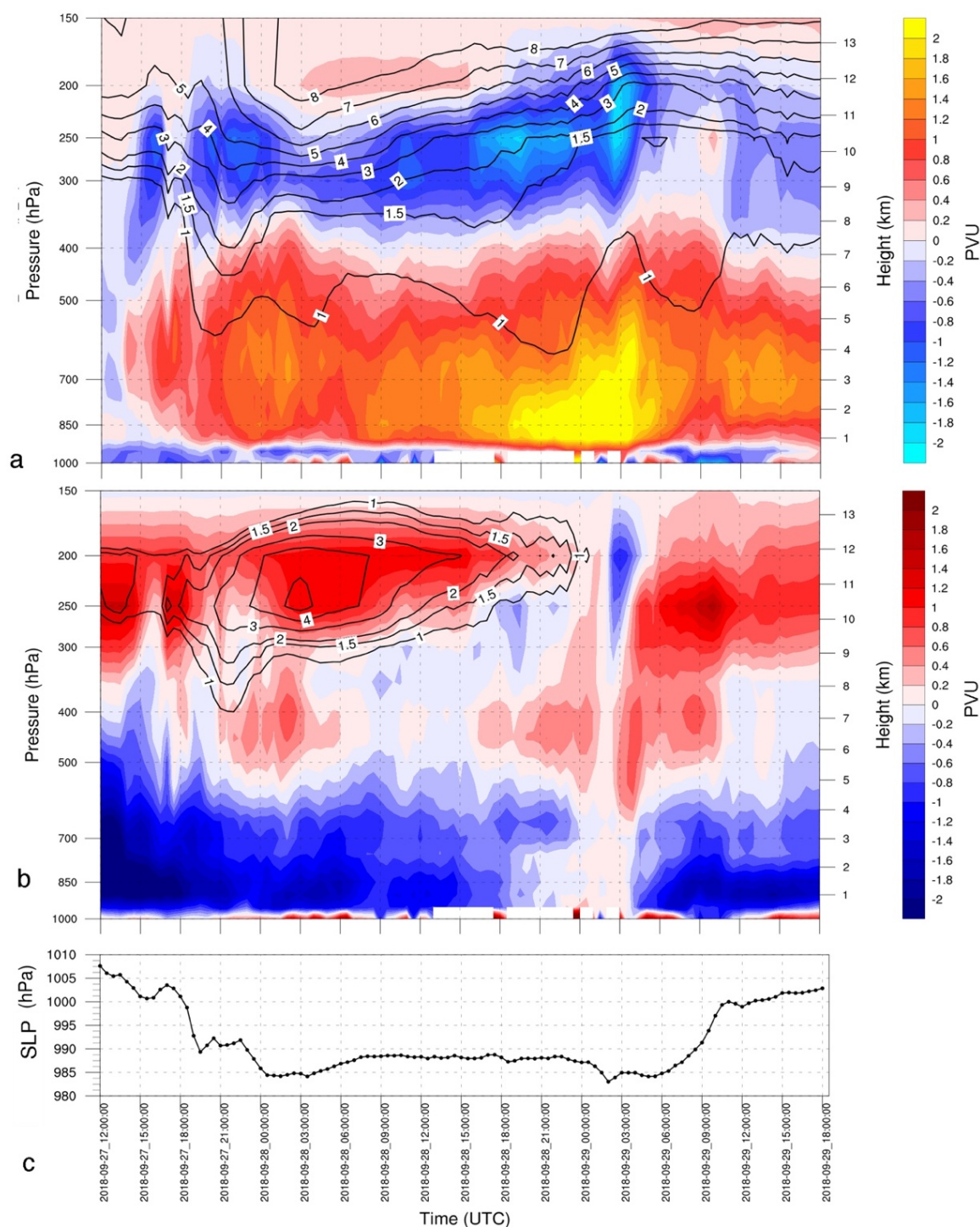


Fig. 3.29 As in Fig. 3.25 but for ZORBAS

The PVDIAB for TRIXIE and ZORBAS is much higher during their maximum intensity than the precedent periods, but mostly during ZORBAS, very low PVDIAB values are simulated in the upper-troposphere and lower stratosphere, forming a PVDIAB dipole (Fig. 3.29a). Only during these periods these 2 cyclones exhibit structures similar to tropical cyclones but with a much smaller size, with the maximum tangent wind intensity about 30-50 km away from their center just below the maximum tropospheric diabatic heating, with an almost windless atmospheric column in their cores (Fig. 3.30). Near the surface, WRF simulates the influx of air masses towards the cyclone centers and a flow of opposite direction near 400 hPa (Fig. 3.30a-c).

Moreover, in the cyclone “eye” there is subsidence, most pronounced during the maximum intensity of ZORBAS (Fig. 3.30c). Regarding the total PV that is computed by adding the PVCO, PVMO and PVDIAB, we see the development of a PV tower extending from the surface up to 300 hPa, with low (negative) values between 300 and 200 hPa just above the cyclone center of TRIXIE and ZORBAS (Fig. 3.30b-d).

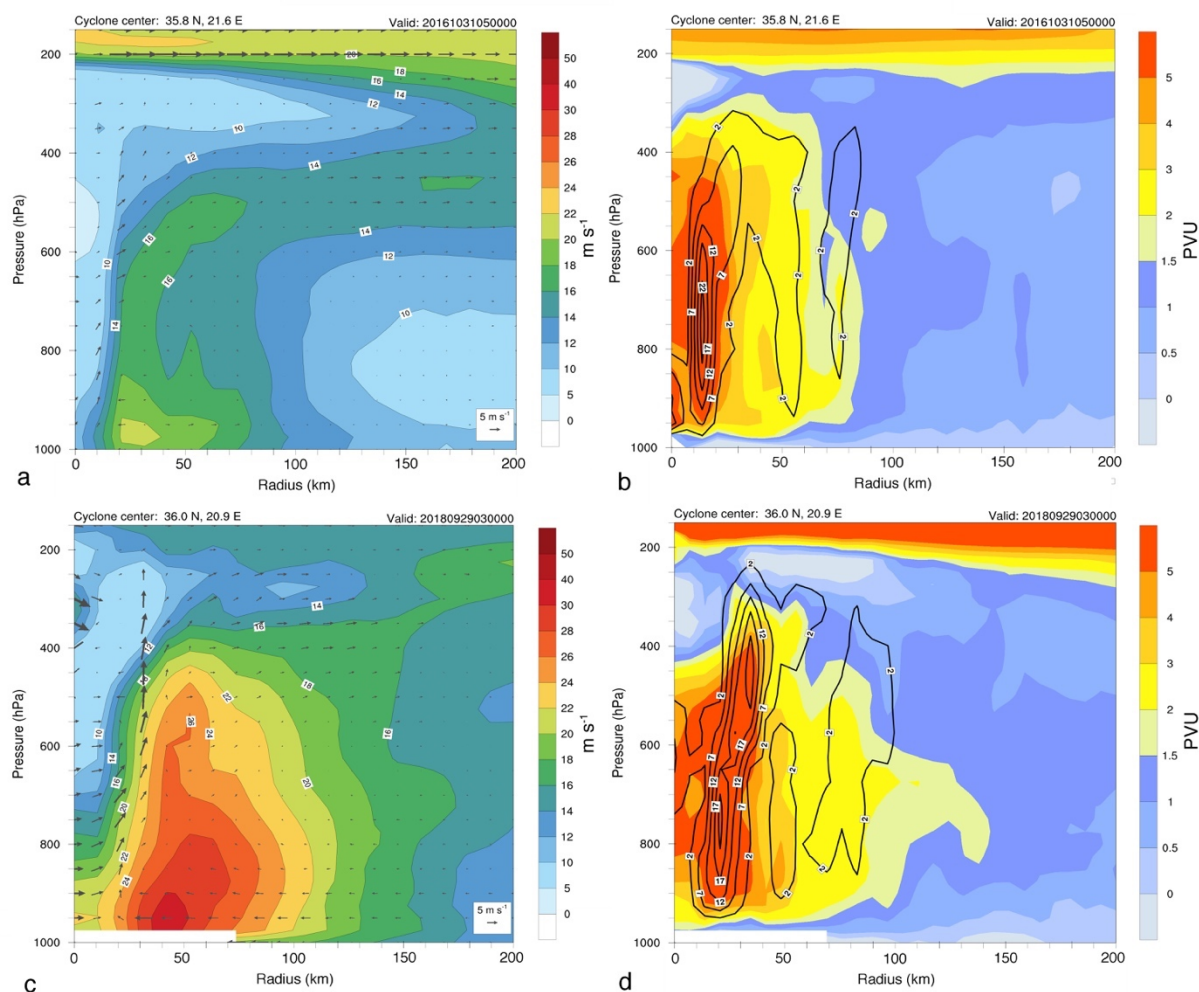


Fig. 3.30 Radius-pressure diagrams for the azimuthal-mean tangential wind (m s^{-1}) (shade) and the radial wind multiplied by the vertical velocity (m s^{-1}) (vectors) (left), total potential vorticity (PVU) (shade) and diabatic heating (K h^{-1}) (right) valid for (a-b) TRIXIE and (c-d) ZORBAS.

In addition, it is interesting to compare the spatial extent of the PV-towers among the 3 MTLCs, by computing the total PV and comparing it with PVDIAB for the isobaric levels between 900 and 400 hPa (Fig. 3.31). For this layer the most important contribution to the total PV is expected by PVDIAB, but PVCO and PVMO also contribute to a comparable extent. For TRIXIE, as discussed earlier, the total PV within 100 km from the cyclone center can be mostly attributed to PVDIAB, with the 2 PVU isoline extending up to 50 km from TRIXIE’s center during the maximum cyclone intensity (Fig. 3.31a). The higher PVDIAB values than total PV in after 1300 UTC 31 October 2016 can be attributed to the negative PVMO values between 900 and 400 hPa. NUMA also experiences more than 2 PVU of total PV within the first 50 km from the cyclone center, but it is only partly attributed to PVDIAB (Fig. 3.31b). On the other hand, ZORBAS has two different periods

during which PVDIAB contributes the most to the total PV, first between 1500 UTC 27 September 2018 and 0300 UTC 28 September 2018 and then again after 1800 UTC on 28 September 2018 during the second intensification period (Fig. 3.31c). In-between these periods, more than 2 PVU of total PV is calculated between 900 and 400 hPa and it extends up to 100 km around ZORBAS, but PVDIAB reaches 2 PVU values only within the first 20 km from the cyclone center.

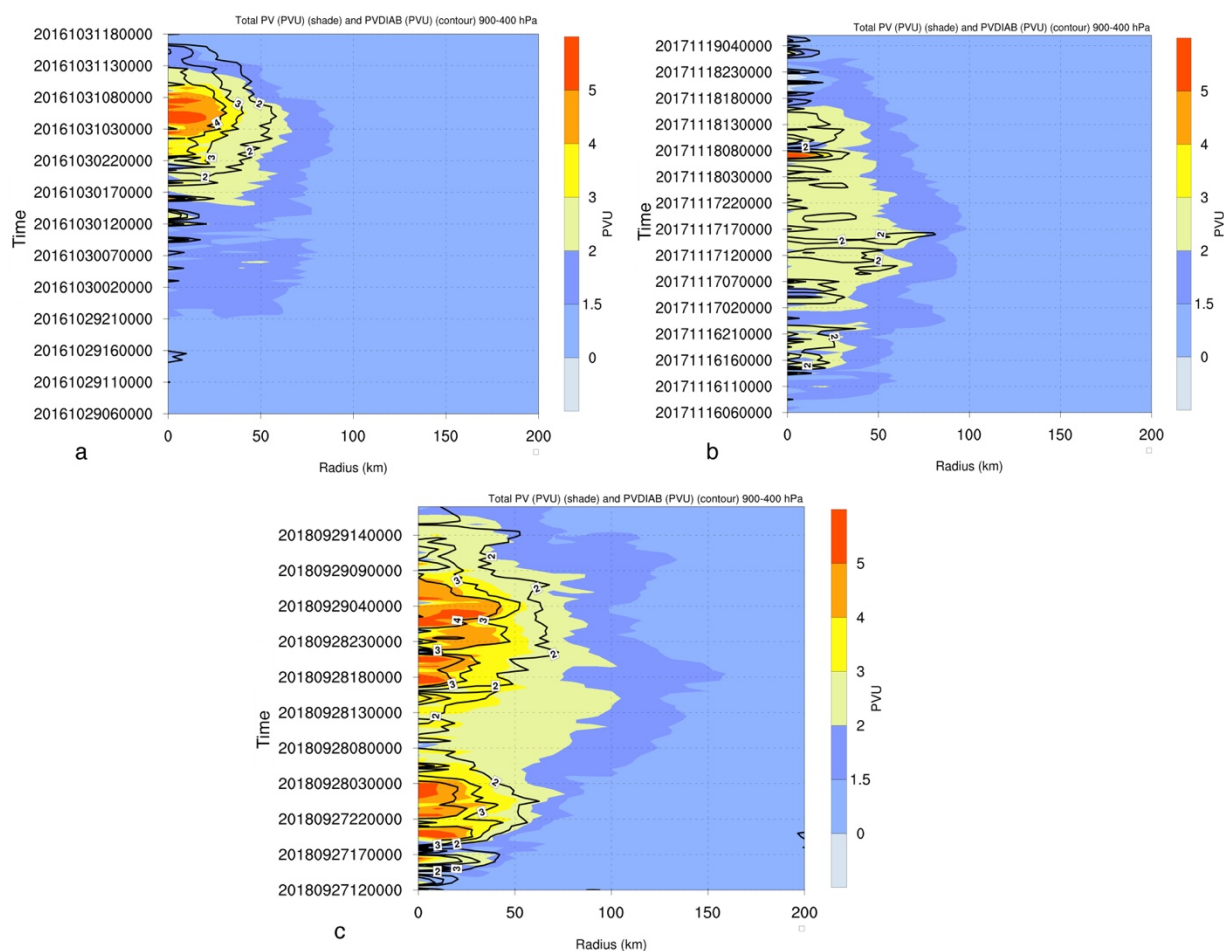


Fig. 3.31 Radius-time diagrams for the total potential vorticity calculated by the sum of PVCO, PVDIAB and PVMO (PVU) (shade) and PVDIAB (PVU) (contour) for (a) TRIXIE, (b) NUMA and (c) ZORBAS.

In the 3rd proposed group of MTLCs, Med2006 shows a different evolution of the vertical PV structures. During its explosive deepening between 2200 UTC 25 September 2006 and 0330 UTC 26 September 2006, a PV-tower develops by strong tropospheric diabatic heating that becomes in phase with the strong upper-tropospheric PVCO during its first landfall (Fig. 3.32a). PVDIAB reaches a maximum between 850 and 700 hPa just after the landfall and before Med2006 reaches the Adriatic Sea (Fig. 3.7b-3.8b). The high intensity of the cyclone is sustained for several hours under the presence of high PVDIAB and high PVCO in the troposphere (Fig. 3.32a-b).

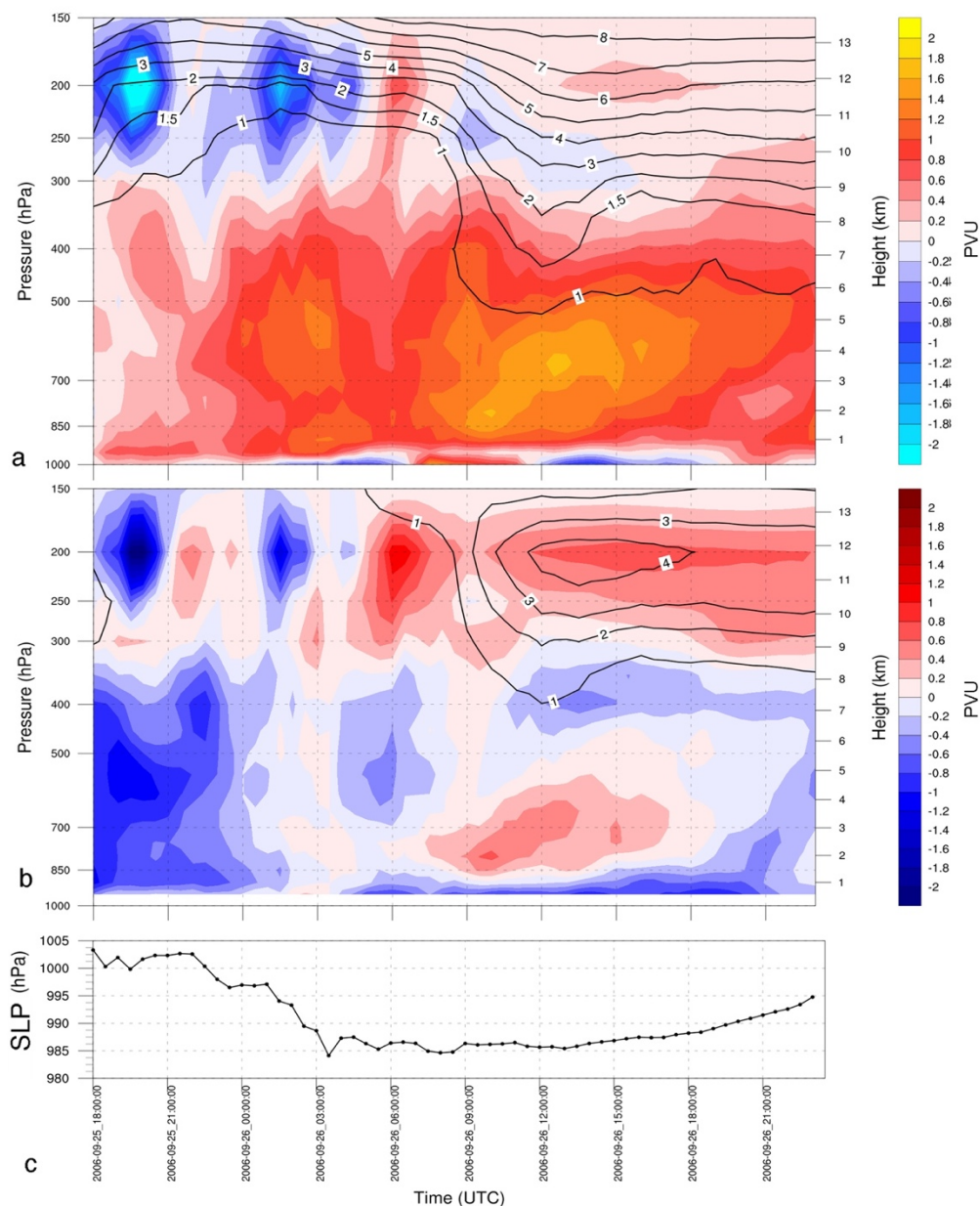


Fig. 3.32 As in Fig. 3.25 but for Med2006 (a-b)

The strong negative PVDIAB values above 250 hPa during the deepening phase of Med2006 between 1800 UTC 25 September 2006 and 0300 UTC 26 September 2006 resemble similar periods of the vertical PVDIAB dipoles in TRIXIE and ZORBAS but they are not in phase with the maximum PVDIAB in the mid/low-troposphere. These negative values are attributed to DC activity that produce strong divergence aloft, but the cyclone is strongly tilted during this period, and the lowest PVDIAB values near the tropopause are calculated within 50-100 km away from the cyclone center and not above the core of Med2006, as in TRIXIE and ZORBAS. Nevertheless, PVDIAB also has the highest contribution to the total PV according to Fig. 3.33, but it is concentrated very close to the cyclone center, mostly within less than 40 km from Med2006 center.

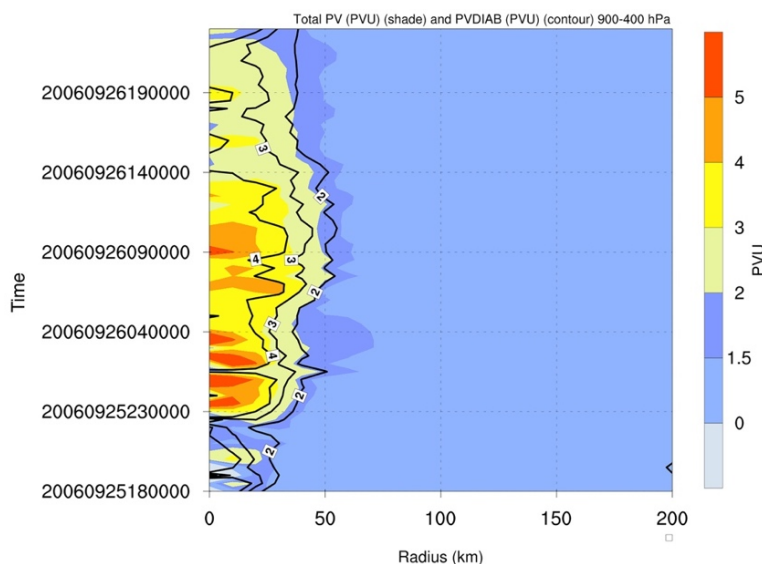


Fig. 3.33 As in Fig. 3.32 but for Med2006.

3.3 Summary and discussion

In this chapter, a numerical study on the contribution of DC in the intensification of MTLCs has been conducted. The main motivation for conducting such a study was the proposed classification of the MTLCs in Chapter 2, after examining the evolution of DC activity during 9 MTLCs between 2005 and 2018. The numerical study was performed on the 6 out of the 9 cases and at least one of them is included in each of the 3 proposed MTLC groups.

First, a PTE analysis was employed and it was the first time to account for the different MTLC radius on computing the relative contribution of the thermodynamic processes in the deepening rate of the cyclones. The choice of the storm radius seems to be very important when considering mesoscale cyclones in high-resolution simulations. The surface-pressure deepening rate can be different depending on the storm radius when average values are used. Results confirmed the hypothesis in Chapter 2 about the small contribution of DC activity in the intensification of the MTLCs in Group 1 and the important contribution of diabatic processes in the intensification of the MTLCs in Groups 2 and 3. The PTE analysis is proven to be a useful tool in quantifying the contribution of DC activity in the deepening of the examined MTLCs, but our study also highlights the limitations of this approach in very high-resolution numerical experiments. The most significant drawback of the PTE calculations is the large numerical residuals due to discretization. By taking into account these residuals and comparing the deepening rate contributions of the different PTE parameters, it was found that TRIXIE, NUMA and ZORBAS amplified under the presence of strong DC activity when opposing baroclinic factors were acting in suppressing the cyclone deepening. Also Med2006 experienced strong deepening during intense DC activity, but baroclinicity was comparably strong, either promoting or suppressing the cyclone amplification. The limited DC activity close to the cyclone centers of Med 2005 and Med2007 was mirrored in the PTE analyses, even though Med2007 experienced short periods of high DC activity during its amplification according to the PTE100.

As a second step, PV tracers were used to study the evolution of the vertical PV structures and most importantly to quantify the diabatic contribution in the total PV production and the relative interactions between the different PV features during the studied MTLCs. Results show that even though the Group 2 and 3 cyclones experienced the highest tropospheric diabatic PV (PVDIAB), the low-level PV anomalies interacted with the large-scale and upper-tropospheric/stratospheric PV (PVCO) in different ways.

The PV tracers can be used to explain the convective evolution of the MTLCs. For example, TRIXIE is not associated with a strong synoptic upper-level feature but it succeeds in amplifying to a great extent during DC activity. One possible explanation for the convective development of TRIXIE is provided by the Diabatic Rossby Waves (or Vortex) theory (Raymond and Jiang, 1990; Snyder and Lindzen, 1991; Moore and Montgomery, 2004). According to this theory, a wave can grow in the absence of upper-level forcing if there is a positive thermal advection to the east of a low-level PV anomaly that leads to upward motions and latent-heat release. The isentropic lifting of air parcels that travel northward results in a constant production of PVDIAB to the east of the initial low-level PV anomaly. Indeed, during TRIXIE, the strong southerly flow of warm and moist air downshear (east) from the center of the cyclone between the late afternoon on 30 October 2016 and early morning on 31 October 2016 (Fig. 3.34), results in a steady increase of low-level PVDIAB that is accumulated over time as the cyclone is moving east, where there is a positive PVDIAB tendency. The maximum southerly wind is simulated between 900 and 800 hPa about 60 km east from the cyclone center with a pronounced low-level PVDIAB anomaly during the rapid intensification of TRIXIE (Fig. 3.34d). The positive PVDIAB tendency stops when TRIXIE is found in South Greece (Fig. A2.8c-e) where moisture and eventually CAPE (not shown) are reduced due to the advection of colder and drier air masses from the Aegean Sea.

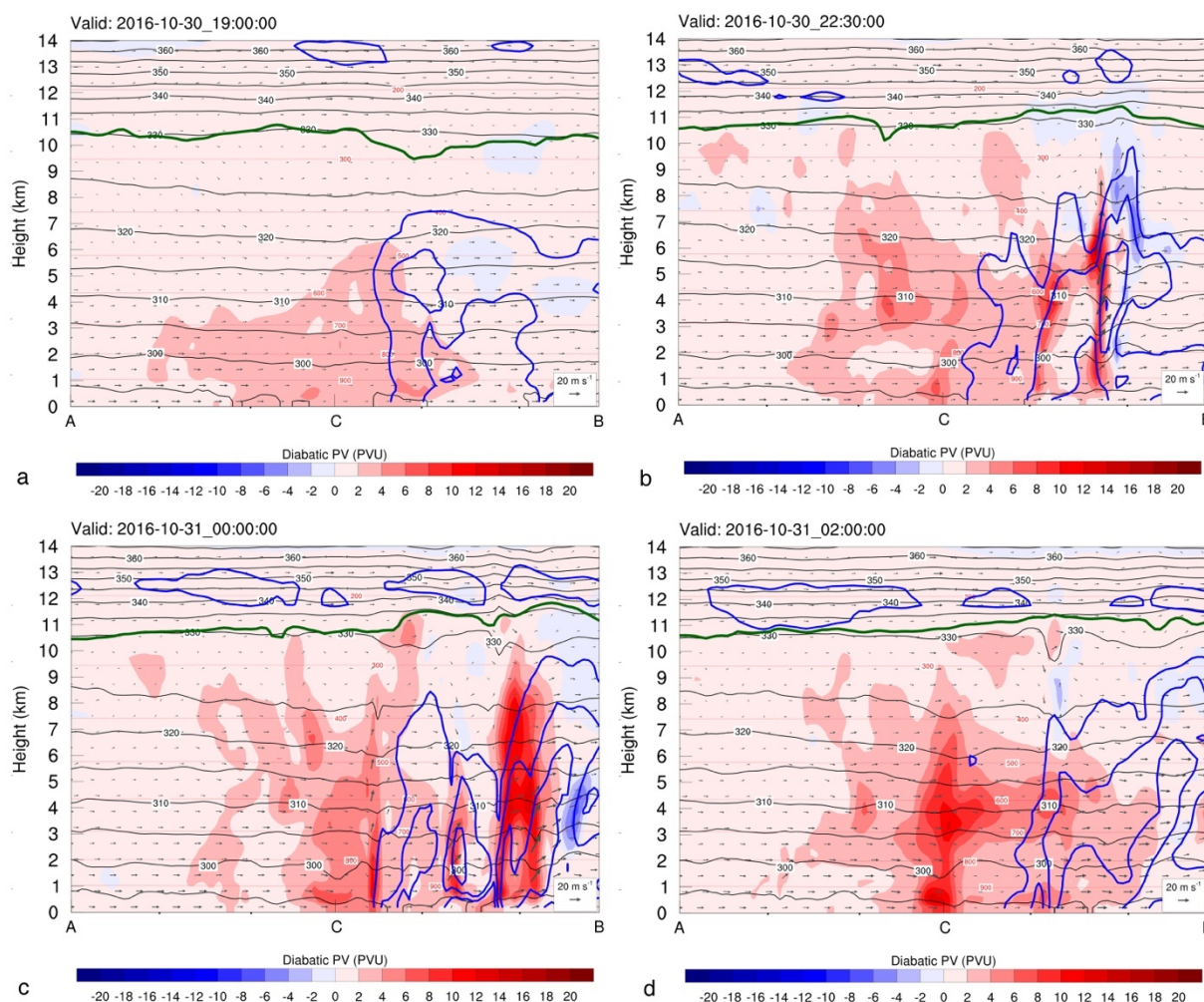


Fig. 3.34 As in Fig. 3.14 but for TRIXIE for an west-to-east cross-section. The blue contours show the meridional wind component (southerly wind) between 5 and 30 m s^{-1} with a 5 m s^{-1} step. Plots are valid for 1900 UTC 30 October 2016 (a), 2230 UTC 30 October 2016 (b), 0000 UTC 31 October 2016 and 0200 UTC 31 October 2016 (c).

The main interactions between the different PV anomalies at each stage for the examined MTLCs are shown schematically in Fig. 3.35 and discussed below:

Stage 1

The surface cyclone is initiated by an upper-level PV anomaly, a process that is seen in the majority of MTLCs (Miglietta et al., 2017), but it is not always of the same magnitude or has the same vertical penetration in the troposphere. For example, the PV streamers at Stage 1 of NUMA, ZORBAS (Fig. 3.35a) and Med2006 (Fig. 3.35b) are much stronger than during Stage 1 of TRIXIE (Fig. 3.35c). The period of Stage 1 varies between 6 hours (ZORBAS) and 36 hours (TRIXIE) until the low-level PVDIAB becomes important. This period is discussed in Hoskins et al. (1985) and describes the “action at a distance” of the upper-level anomaly on the surface baroclinicity. In this case, the low diabatic PV in the mid/upper-troposphere has a negligible effect on the modification of PVCO, which mostly modified by the large-scale flow by advection. The surface

cyclone is either sustained to its initial intensity or gradually amplifies, but the latter is strongly dependant on the PVDIAB production tendency, for example, the previously discussed Diabatic Rossby Vortex mechanism for TRIXIE.

Stage 2

This stage is common for ZORBAS, NUMA and Med2006, as the PVDIAB anomaly becomes dominant in the low/mid troposphere and becomes vertically aligned with the upper-level PVCO. Also the low-level warm anomaly becomes a seclusion and forms a warm-core cyclone (e.g., Fig. A2.12c), while the constant latent heat release in moist ascent acts as source of PVDIAB which is accumulated near the core of the cyclone and reaches the upper-troposphere forming a PV-tower (Rossa et al., 2000; Čampa and Wernli, 2012; Chaboureau et al., 2012; Miglietta et al., 2017). The advection of PVDIAB out of the cyclone core most probably is strongly affected by the mean wind flow and shear, but further investigations will be necessary to fully understand this process. The relative importance of the PVCO over the PVDIAB is also difficult to be quantified due to the highly non-linear processes involved.

A different evolution in Stage 2 is marked during TRIXIE (Fig. 3.35c) as a PV-tower never forms, but high values of PV throughout the troposphere are solely attributed to PVDIAB. The upper-level PVCO anomaly seems to have a little effect on the cyclone during this stage, since it only provides some vertical motion above the collocated PVDIAB anomaly, but it should be much weaker than the vertical motions due to DC activity. This is a period of strong intensification and it is described as a “seclusion intensification” by Grønås (1995) and Grønås and Kvamsto (1995) in polar-low cases. In these two studies, the authors suggest that the diabatic intensification of Montgomery and Farrell (1992) plays a key-role during the seclusion process. The “dome of PVDIAB” in the troposphere (Fig. 3.35c – Stage2) can be attributed to the development of a Diabatic Rossby Vortex. Similar PV structures have been identified in other extratropical cyclones, for example during the winter storm Lothar (Wernli et al., 2002), the February 2005 East Coast snowstorm (Moore et al. 2008), and the December 2005 North Atlantic cyclone (Boettcher and Wernli, 2011).

Stage 3

During the last stage at which the MTLCs can intensify or sustain their intensity before their lysis, the upper-level PVCO anomaly is significantly modified and eroded due to the effects of long-lasting DC activity (upper-level divergence and cooling). The strong PVDIAB anomaly can either intensify the cyclone without the help of upper-level PVCO (for e.g., during NUMA and ZORBAS) or the two separate PV anomalies will continue to interact similar to Stage 1 (for e.g., during Med2006) but without further amplification of the surface cyclone. It is worth mentioning also that only during this stage ZORBAS exhibited characteristics similar to a tropical cyclone or hurricane (see Fig. 3.30a-b). Moreover, during this stage in ZORBAS, NUMA and TRIXIE, DC activity is initiated in the downshear quadrants and is cyclonically wrapped to the upshear quadrants, but it never totally wraps the cyclone centers, suggesting strong subsidence in the upshear quadrants, as discussed in Chapter 2 and Appendix 1. This evolution of DC activity around the cyclones is well simulated by the WRF model.

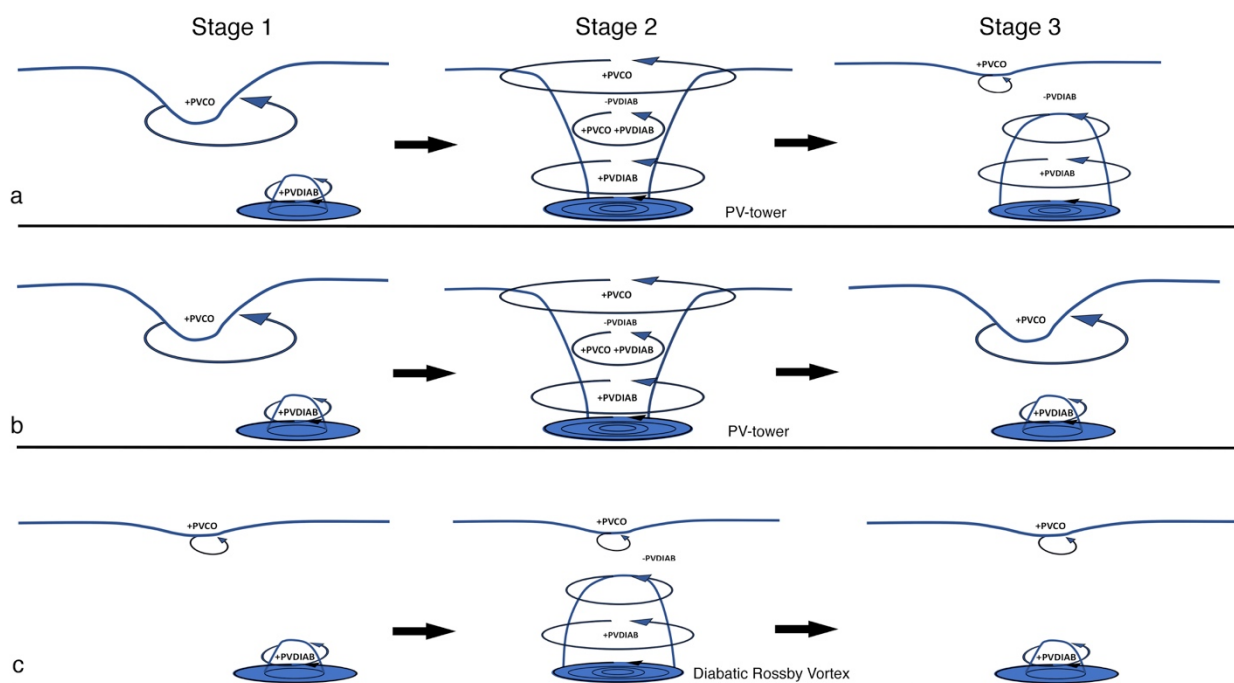


Fig. 3.35 A schematic diagram of the different stages of the MTLCs ZORBAS and NUMA (a), Med2006 (b) and TRIXIE (c) (see text for details). The 2 PVU isoline of the upper-level PV (PVCO) anomaly and the low-level diabolic PV (PVDIAB) anomaly are shown with blue contours. The “+” and “-” symbols indicate the sources and sinks of each PV anomaly. Each PV anomaly and its effects are indicated by the size of curved arrows. The induced surface circulation and its relative strength is indicated by the number of enclosed blue circles. The PV-tower and Diabolic Rossby Vortex stages are also indicated and the black arrows show the evolution of each stage.

Chapter 4

Conclusions and future work

4.1 Questions addressed in this thesis

The Mediterranean tropical-like cyclones (MTLCs) have always been challenging in forecasting due to their rapid development and small size. Recent advances in computational power and in the physics of numerical models have increased our understanding on the contribution of deep moist convection to their development. However, still many questions about the relative contribution of baroclinic versus diabatic processes remain and this thesis tried to address some of them.

Until now, there has not been a systematic investigation of the baroclinic and non-baroclinic environments in which MTLCs develop and problems associated with the lack of observations and the parameterizations of diabatic processes in numerical models create challenges and limitations to any attempt. In order to optimize the numerical models and suggest the development and the location of observational platforms, we first need to understand the different mechanisms involved in the intensification and evolution of MTLCs. Previous studies with diagnostic methods have been applied to tropical cyclones (TCs) and polar lows (PLs), and have shown how crucial is the release of latent heat during their intensification. For the MTLCs, only recent studies started implementing similar diagnostics and tried to compare their findings with their tropical and polar counterparts (e.g., Fita and Flaounas, 2018; Miglietta et al., 2017; 2019). In the current study, novel diagnostics for both observations and numerical results have been applied to address the following questions:

- **How does deep convection evolve during the MTLCs?**

First, an observational case study on MTLC ROLF was performed which showed that the evolution of DC activity and lightning resembled more the TCs rather than the Mediterranean extratropical cyclones. Maximum DC activity was detected by both infrared and microwave satellite observations about a day before the maximum intensity of the cyclone. In order to investigate the evolution of DC activity during other MTLCs and explore the similarities in DC evolution with ROLF, a prototype objective infrared satellite diagnostic was used along with microwave diagnostics and numerical reanalysis in a larger sample of MTLCs that developed between 2005 and 2018. It was found that long-lasting DC activity close to the centers of MTLCs does not always result in intensification periods but it rather contributes to sustain their intensity. For ROLF, TRIXIE, NUMA and ZORBAS long-lasting DC activity in their upshear quadrants was connected with cyclone intensification periods, while downshear DC activity alone did not lead to a further surface cyclone

amplification. On the other hand, Med2005, Med2007 and QENDRESA experienced intensification periods mostly during very weak and sporadic DC activity. In addition, the vertical wind shear was found to affect the location of DC activity and vortex tilt, resulting in significant vortex structure changes, especially during periods with strong wind shear. One limitation of this study was the lack of observations during earlier stages of development of these MTLCs and the limited number of the studied MTLC cases due to the manual tracking of their centers through satellite imagery. Unfortunately, today there is no reliable and objective tool to automatically track the MTLCs centers in satellite imagery. One implication of this is that our findings may not fully represent the long-term climatological distributions and that the early stages of some MTLCs are not totally covered by this observational study (e.g., Med2006 and ZORBAS), but the very different DC evolution among the cases suggest that these MTLCs may be representative cases. Nevertheless, the MTLCs were classified into three groups regarding their convective evolution and structure. For the first group of MTLCs, DC activity does not seem to play a dominant role to their intensification, like it does for the rest two proposed groups.

- **What is the relative contribution of diabatic processes in the intensification of MTLCs?**

To answer this question, numerical modeling was employed and the numerical results were evaluated against observations to verify their validity. The simulated DC activity and cyclone tracks were compared with satellite observations, and simulations that incorporated significant biases with observations, were discarded from further analysis. The remaining cases of simulated MTLCs were used to apply a modified version of the classical PTE analysis to quantitatively assess the contribution of diabatic processes in the surface pressure tendency rates. For the first time, the budget equation of PTE was applied for two storm radii and results showed the differences in the contribution of the thermodynamic parameters in the amplification of the MTLCs, and especially for the diabatic processes. Results from the two PTE analyses show that diabatic processes indeed play an important role during the MTLCs in the proposed Groups 2 and 3, while for Group 1 diabatic processes have similar or less important contribution to the cyclone intensification with baroclinic processes.

- **How does the vertical distribution of potential vorticity change during convective activity in MTLCs?**

A novel tool for calculating the PV tendencies of different parameterized and explicitly resolved physical processes in a high-resolution numerical model was utilized, with a special focus on the diabatic production of PV during the studied MTLCs. Most of the MTLCs have a low-level PV maximum between 850 and 700 hPa which is attributed to a diabatic source of PV (PVDIAB) in the maximum melting level. One important interpretation of the PV tracer analysis is the interaction between the PVDIAB and the large-scale upper-tropospheric PV (PVCO) during the lifetime of MTLCs. The evolution of the vertical PV structures was different among the cases, both at the developing and the mature stages, with a partial erosion of the upper-level PV streamers under bottom-heavy PVDIAB production. The highest production of PVDIAB coincided with the highest contribution of diabatic processes in the negative surface pressure tendencies discussed in the

PTE analyses. During certain periods of the MTLC Groups 2 and 3, a PV-tower structure is simulated, and some other instances the high values of total PV throughout the troposphere are solely attributed to PVDIAB. The latter cases are simulated only for the Group 2 MTLCs, for which the diabatic processes play a dominant role to their amplification and show brief cyclone structures similar to hurricanes. More specifically for TRIXIE, since this cyclone was not amplified under the influence of an upper-level synoptic weather system, we studied the interaction of the initial low-level PVDIAB anomaly with the downshear warm-air advection which seems to have aided the development of a Diabatic Rossby Vortex. Both baroclinicity and diabatic processes have played an important role to the intensification of this cyclone which is placed in Group 2, but further investigation is needed to quantify the actual contribution of baroclinicity in this case.

To summarize, despite the limitations in both the observational and numerical analyses presented in this thesis, advances in the understanding of the contribution of diabatic processes in the intensification of MTLCs have been made. Despite the high contribution of DC activity in the intensification of the MTLCs in Groups 2 and 3, results from the current study show similarities with intense extratropical cyclones forming as in the Shapiro-Keyser model that have been discussed in Godske et al. (1957) for the Atlantic extratropical cyclones, and in Montgomery and Farrell (1992) for the polar low dynamics. These secluded cyclones experience thermodynamic (diabatic) intensification similar to the presented MTLCs. The PV-tower development is also a common feature in explosive extratropical cyclogenesis, but the strong low-level PVDIAB anomalies that were simulated in TRIXIE, NUMA and ZORBAS have also similarities with TCs and polar lows. The latter PV structures though, develop for very short periods of time relative to the MTLCs' lifetime and only during these stages the cyclones exhibit tropical-like characteristics in the satellite imagery, like a cloud-free "eye" that forms through subsidence in the core of the MTLCs (e.g., in TRIXIE and ZORBAS, Figs. 3.30a-c), a frontless structure and hurricane-force winds very close to their center. The diagnostics and methodology presented in this study must be extended in a larger MTLC dataset in both observational and numerical reanalyses in order to better understand the dynamics of MTLCs and propose improvements in their detection and forecasting.

4.2 Future work

In this thesis a first assessment of the role of deep convection in the intensification of MTLCs has been conducted. In addition to the questions posed in Chapter 1, the results have also raised further questions for future studies which are discussed below.

There is a number of possibilities for future work that relate to the observational study in Chapter 2. Since there is no objective and automatic way to detect MTLCs in the satellite imagery, more research is needed towards a robust tracking procedure to discriminate MTLCs from other extratropical cyclones. A tracking algorithm would provide additional archive MTLC cases to be investigated, by applying the diagnostics proposed in this study. New infrared and microwave diagnostics can be developed for the existing satellite platforms, but also explore the capabilities of upcoming ones, such as the Third-Generation METEOSAT

satellite and the Advanced Technology Microwave Sounder (ATMS). Moreover, the ESA-Satellite constellation (Sentinels) which consists of polar orbiting satellites carrying multispectral instruments can provide new information on the structure of MTLCs in the near future.

The intensity of DC activity also needs to be better addressed in the satellite observations, for example with the aid of the integrated ice-water content calculated by passive microwave observations (Rysman et al., 2021). Including more information in the existing diagnostics rather than thresholds in the brightness temperatures, will provide a better definition for the presence of stratiform and deep convection. One additional and indirect application of this development would be the study of lightning activity during MTLCs which exhibits a peculiar evolution when compared with other mid-latitude extratropical cyclones. The absence of lightning activity in DC close to the center of MTLCs raises questions about the thermodynamic structure of convective clouds before and after the tropical-like phases. Another question that can be addressed by an improved definition of DC is the diurnal changes of DC activity during MTLCs and the convective pulses that can be connected with surface pressure tendencies. If these cyclones exhibit tropical characteristics, why does the DC activity not follow the diurnal solar cycle as it does during TCs (e.g., Wu and Ruan, 2016; Ditchek et al., 2018)?

In addition to the proposition of observational future studies, several questions have been raised in this thesis during the interpretation of the numerical results. For instance, in very high-resolution mode the tracking of the cyclones becomes challenging and the minimum SLP or vorticity maxima are not always representative of the cyclone centers, especially during the development stages of the cyclones and strong DC activity. Furthermore, the existing diagnostics for the thermal structure of MTLCs and warm-core cyclones in general, have been developed for coarse-resolution (spatially and temporally) datasets, raising concerns about their applications in high-resolution numerical simulations. For example, the cyclone phase diagrams (Hart, 2003) must be calculated for a large number of cyclones in high-resolution experiments and a special study dedicated on the structure and intensity of MTLCs must be conducted to replace the subjective thresholds that have been used so far in the literature (e.g., storm radius, upper-tropospheric boundaries, etc.).

This thesis leaves another open question about the robustness of the numerical results by using only one parameterization for the microphysics (MP). More numerical experiments need to be performed and most probably with an ensemble of numerical experiments in order to study the differences of diabatic heating among the available MPs and what is the impact on the production of PVDIAB and evolution of vertical PV structures in general. Such an approach must be performed after validating the numerical simulations with observations and apart from a simple comparison between the simulated and observed DC activity, a model-to-satellite approach may provide more objective validation results. One problem that these future studies will most certainly face is the large spread of the simulated outputs and their weak correlation. One possible solution to tackle this problem could be the assimilation of satellite and radar observations (e.g., Duffourg et al., 2010; Lavanant et al., 2011; Martinet et al., 2013) or more sophisticated numerical nudging techniques (e.g., spectral nudging) in order to constrain the simulations to numerical analysis or to the observations. These procedures could possibly provide better simulations for the 3 omitted case-studies in this thesis (ROLF,

ILONA and QENDRESA) even if the same numerical forcing is used (e.g., ERA5), that will allow to apply the presented methodology also to these MTLCs.

Understanding the vertical distribution of PV in MTLCs is crucial because the low/mid-level PV maximum has implications to the vortex motion and intensification. Without a clear definition of the simulated DC activity it is difficult to assess the contribution of stratiform versus the deep convective diabatic processes to the production of PVDIAB. Both modes of convection have been proven to contribute in the spin-up of TCs and TDs (e.g., Murthy and Boos, 2019) and it will be worth studying their evolution during MTLCs and possibly connect their contribution to the net vorticity changes in a future study. Furthermore, the bottom-heavy PVDIAB anomalies may contribute to the changes of the steering flow during MTLCs, a feature that is known to be important in other types of diabatically-driven cyclones (Hoskins et al., 1985; Boos et al., 2015). This feature may explain the erratic loops of some MTLCs when they attain their tropical-like characteristics (e.g., QENDRESA).

In Chapter 2, the intense upshear DC activity is connected with intensification periods which are then related to the development of PV-towers and structures similar to a Diabatic Rossby Vortex in Chapter 3. A more detailed future study can explore the possible connection between the production of high low-level PVDIAB in the upshear quadrants of MTLCs, its radial and adiabatic advection and quantify the role of WISHE on the evolution of energy fluxes during these periods. The vertical and horizontal PVDIAB dipoles shown in Chapter 3 (e.g., Figs. 3.15c-3.20a) suggest the presence of very intense vortical towers (Hendricks et al., 2004) during the intensification of the MTLCs in Groups 2 and 3. So far, no study has investigated the storm dynamics in the vicinity of the MTLCs' cores and what is the reason for the sudden burst of DC activity in relation with the environment of the cyclones or if there is another self-aggregation mechanism of DC (Muller and Romps, 2018) (for e.g., during TRIXIE).

As mentioned at the beginning of this final chapter, there is a high concern in the scientific community about the forecasting challenges during the MTLCs. There is still no answer to the question why many Mediterranean cyclones fail to experience a tropical transition and become MTLCs, despite many false alarms in the NWP forecasts. Without a clear definition for the so-called “medicanes”, it is hard to make any strict discrimination between intense extratropical cyclones and MTLCs, even though the lack of frontal activity is one of the main features of the latter type of cyclones. A future study can answer the question when do MTLCs stop having fronts, or if they are attended by fronts for some periods of time, similar to the study of Schemm et al. (2018) who studied the periods when extratropical cyclones start having frontal activity. A Lagrangian approach could also provide answers for both the origin of air masses that contribute to MTLCs structural and intensity changes (similar to Fita and Flaounas, 2018), but also provide new insights to the evolution of PVDIAB during intense DC activity. The observed and simulated upper-level divergent flow during the MTLCs has not been studied so far, and whether if MTLCs are associated with WCBs and CCBs and how they interact with DC and the downstream development of the cyclones (e.g., Schemm and Wernli, 2013; Binder et al., 2016; Oertel et al., 2020), remains unknown. Finally, when most of the aforementioned questions get answers in the near future, probably a more clear definition of the MTLCs will be possible.

Many more cases of MTLCs are needed to be studied in order to provide a more specific definition to this type of cyclones. So far, for the studied MTLCs, but also those discussed in Miglietta and Rotunno (2019), there have not been cases with purely diabatic intensification and self-sustaining mechanisms, but rather baroclinicity and diabatic processes co-exist during the development of the MTLCs. Taking into account the findings of this study and by altering the initial definition of the MTLCs in paragraph 1.1, we can propose the following definition of a MTLC or a “medicane”:

“A medicane is an intense mesoscale maritime secluded cyclone which experiences tropospheric heating by convective activity and exhibits a front-less structure with gale-force wind speeds close to the centre of the depression. The synergy of baroclinic instability and diabatic processes contributes to the formation and intensification of a medicane and according to their relative contribution, these cyclones can be classified into 2 categories:

- *Type 1: medicanes with a shallow warm-core mostly driven by baroclinicity and weak diabatic processes.*
- *Type 2: medicanes with a deep warm-core mostly driven by strong diabatic processes under the influence of baroclinicity”*

According to our initial 3-fold classification, the MTLCs in Group 1 (Med2005, Med2007 and QENDRESA) can be defined by the *Type 1 medicanes* and MTLCs in Groups 2 (ROLF, TRIXIE, NUMA and ZORBAS) form the *Type 2 medicanes*. There is not an exhaustive study of the MTLCs in Group 3 (Med2006 and ILONA), but Med2006 can be defined by the *Type 2 medicanes*, since it experienced significant diabatic heating under the presence of strong baroclinicity. These 2 types of medicanes can share common characteristics at their early stages of development, for e.g., the formation of a seclusion under the influence of an upper-tropospheric PV streamer, but during the mature/tropical-like stage there are distinct differences, such as the formation of a PV-tower and the essential contribution of diabatic heating in the intensification or maintenance of the surface cyclone intensity in the *Type 2 medicanes*.

Appendix 1

Supporting Information for

Insights into the convective evolution of Mediterranean tropical-like cyclones

The Manual Tracking procedure

The following figures show examples of manually tracking the tropical-like cyclones QENDRESA (Fig. S1.1) and ROLF (Fig. S1.2). For the former case, the well-defined cyclonic curvature in infrared brightness temperature of cloud tops is evident in all 4 time-steps, while for the 2 out of 4 time steps, deep-convection diagnostics complement the analysis. For the latter case, we show a time-step when the successive satellite images used did not show a clear cyclonic pattern for subjectively defining the cyclone centre, but scatterometer data provided better insight into the cyclone structure and centre position. For similar time-steps with not clear cyclone centres and in the absence of microwave imagery or scatterometers, a step-by-step animation of SEVIRI imagery (e.g., IR10.8 channel or HRV channel during the day) provided a first guess on the cyclone centre, and then we repeated the same procedure for additional infrared channels in order to correct the position of the cyclone centre.

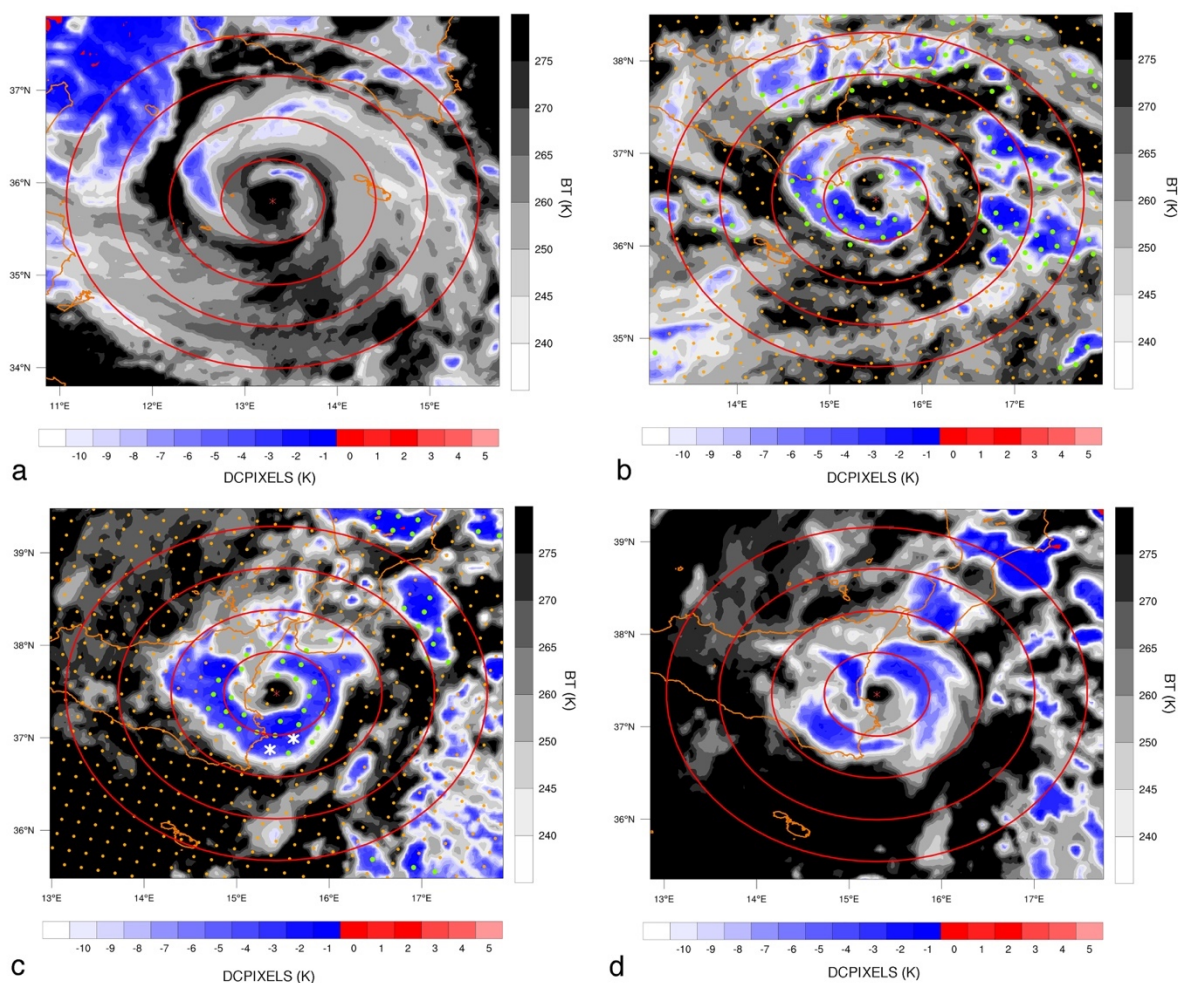


Fig. S1.1 Infrared brightness temperature (BT) from channel IR10.8 (K) (grey) and DCPIXELS (K) (blue and red) derived from SEVIRI Meteosat-9 satellite during QENDRESA. Overlapped dots: diagnostics from microwave sounders for deep convection (MWDC) (green), convective overshooting (COV) (white asterisks) and the scanning footprint (orange) within 15 minutes from SEVIRI scans. The red circles enclose disks within 200 km from the centre of the cyclone, plotted every 50 km, the red asterisk shows the cyclone centre and the coastline is shown with an orange solid line. Top: on 7 November 2014 at 1330 UTC (a), at 2000 UTC (MWDC by MHS Metop-B) (b), and on 8 November 2014 at 0400 UTC (MWDC by MHS NOAA-18) (c) and at 0530 UTC (d)

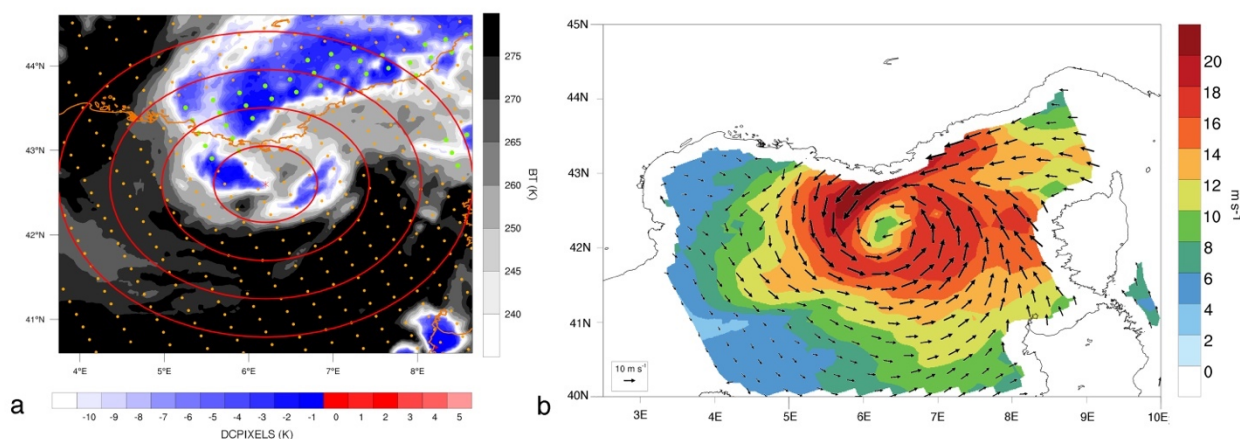


Fig. S1.2 (a) As in Fig. S1.1 but for ROLF on 8 November 2011 at 2000 UTC (MWDC by MHS Metop-A) and (b) Near-surface wind speed (shading) and direction (arrows) (m s^{-1}) by ASCAT on-board MetOp-A at 2000 UTC.

The convective evolution of MTLCs and ERA-5 performance

(The mentions for figures in this paragraph refer to the QJRMS article)

An analysis of DCPIXELS for Med2005 showed a decreasing DC activity close to the centre of the cyclone at the early stages of the manual tracking (Fig. 7a and 8a). Before, the cyclone was embedded in an area of strongly sheared convection under a cut-off low in the Gulf of Gabes (Fita and Flaounas, 2018, their Figs. 3 & 4). Between 2100 UTC 13 December and 1200 UTC 14 December the weak DC activity coincided with the minimum SLP of 989.5 hPa according to ERA5 at 0400 UTC 13 December (Fig. 8a) and remained steady until 1200 UTC 14 December. The Lampedusa station (LICD) reported 991 hPa minimum SLP at 0600 UTC 14 December with a $+0.8 \text{ hPa } 3\text{-hr}^{-1}$ pressure tendency and 3 m s^{-1} wind speed from NW, while Pantelleria station reported 993.6 hPa and 19 m s^{-1} about 180 km NW from the cyclone centre indicating a weak pressure gradient within the first 200 km from the cyclone centre. At the same time, ERA5 minimum SLP was 990.2 hPa about 80 km east from LICD (Fig. 1) at 0600 UTC and 990.8 hPa for the nearest grid point to LICD (996 hPa for Pantelleria) capturing well the weak pressure gradient of the cyclone core. The DLS was decreasing rapidly, with a minimum of 6.2 m s^{-1} at 0900 UTC 14 December 2005, and the mean DLS vector was turning from 270° (western direction) towards 180° (southern direction), with a minimum of the vortex tilt at 0700 UTC 14 December 2005 (Fig. 8b) and a wide cloud-free area (Fig. 7a). During this period the cyclone was not experiencing any intensity change, despite the lack of DC, suggesting that other dynamical processes than DC were responsible for the steady-state of the cyclone. After 1200 UTC 14 December 2005 an approaching trough from NW resulted in a rapid increase of DLS speed from 7 to 25 m s^{-1} and a vortex tilt, which coincided with a sudden convective initiation at the downshear left quadrant of the cyclone with detections of COV from SEVIRI and MWDC from AMSU-B, suggesting intense DC activity (Fig. 7b). Moreover, a small “eye-like” cloud-free area started to be visible and an analysis of the cyclone structure in Fig. 7b shows the northern vortex tilt about 90° left of the DLS vector and DC activity in the upshear left part of the cyclone. The convective activity was sustained until 0200 UTC 15 December 2005 (Fig. 8a) when the vortex tilt reached

another minimum despite the strong DLS of about 25 m s^{-1} . After 0200 UTC, another burst of convective activity started when a strong eastern vortex tilt was initiated, this time in parallel with the DLS vector (Fig. 8b) when DC was organized at the downshear right and left quadrants. Between 0700 UTC and 1000 UTC 15 December 2005 it was the only period when DC was wrapped around the cyclone centre resulting in a small “eye” with a radius smaller than 25 km when DC was present even at the upshear left and right quadrants (Fig. 7c). Med2005 experienced very strong VWS with DLS exceeding 20 m s^{-1} for more than 20 hours (Fig. 8a), but the vortex tilt could be characterized as limited compared to the rest of the case studies (Fig. 8b).

The evolution of convection during MTLC Med2007 was similar to Med2005, even though the two cyclones developed in different areas of the Mediterranean Sea and within different environments, so the precursor extratropical cyclones may have significant differences. The SLP analysis from ERA5 showed a wide low-pressure system extending from Corsica and Sardinia towards the Balkans where surface stations reported minimum SLP between 995-1000 hPa in Italy, Croatia and Serbia on 15 November 2007. The Med2007 developed in the western parts of this low-pressure system and it is discussed in detail in McTaggart-Cowan et al. (2010). The manual tracking of the cyclone centre was possible after 15 November 2007 1600 UTC, after the emergence of the cyclone south of a strongly sheared line of widespread DC (Fig. 7d). According to reanalysis data, the mid-level low was not in phase with the surface cyclone, with a strong vortex tilt during the period of decreasing DLS (Fig. 8c). At the same time, only sporadic and disorganized DC was detected close to the cyclone centre within 50 – 100 km (Fig. 7d-e & 8d). The cyclone reached the maximum intensity in the early morning of 16 November 2007 at 0000 UTC according to the numerical study of McTaggart-Cowan et al. (2010), just before the cyclone reaches the west coasts of Sardinia (Fig. 1b & Fig. 7f), while ERA5 analysis shows the minimum SLP about 3 hours earlier, at 2100 UTC on 15 November (Fig. 3c). The SLP at the cyclone centre was not significantly changing during this period of weak DC activity, suggesting a steady state of the cyclone between 15 November 2100 UTC and 16 November 2007 0600 UTC. The minimum SLP at Capo Caccia weather station in NW Sardinia was 999.5 hPa at 0500 UTC about 20 km east from the cyclone centre with a $-3.8 \text{ hPa } 3\text{-hr}^{-1}$ pressure tendency. ERA5 slightly underestimated the cyclone intensity placing the centre of the cyclone about 30 km more to the west from the observed track, with 1002.8 hPa minimum SLP and 1004.7 hPa for the closest grid point to Capo Caccia station at 0500 UTC. The DLS decrease during the early morning of 16 November cannot be solely attributed to the weak and scattered DC activity. In Fig. 8c a closer look to the evolution of the vortex tilt shows a constant change of the mid-level relative vorticity max, while the DLS vector is constantly towards NE. When DC started again to be detected close to the centre after 0600 UTC (Fig. 8d) the vortex tilt reached a minimum with a 15 m s^{-1} mean DLS (Fig. 8c). DC was wrapped around a small cloud-free area of the cyclone centre only between 1200 and 1300 UTC on 16 November 2007 (Fig. 7f) but surface wind observations in Sardinia showed sustained winds of less than 10 m s^{-1} suggesting that the cyclone had already weakened to a great extent.

QENDRESA reached the peak of intensity on 7 November 2014 1700 UTC (according to ERA5, Cioni et al., 2018 and Carrió et al., 2017) but similarly to Med2005 during the preceded period, DC was not detected within 50 km from the cyclone centre (Fig. 7g & Fig. 8e), when a dry slot visible in the WV6.2 channel was entering the circulation (not shown). Between 0800 UTC when QENDRESA was over Pantelleria, and 1200

UTC on 7 November 2014 when it reached Linosa (Fig. 1f & Fig. 7g), an estimated 10.1 hPa deepening of the cyclone took place in the absence of DC activity (Cioni et al., 2018). During the same period, DLS was decreasing rapidly from 18 m s^{-1} at 0800 UTC to 8 m s^{-1} at 1200 UTC (Fig. 8e) with a small northern vortex tilt and to the right of the DLS vector (Fig. 8f). While the cyclone was passing close to the south-eastern part of Sicily within 50 km from the cyclone centre between 1800 and 2000 UTC on 7 November 2014, the Cozzo Spadaro station (LICO) reported maximum sustained winds only up to 11.4 m s^{-1} , significantly weaker than 7 hours before when LICD station within the same distance from the centre was reporting wind gusts up to 37.6 m s^{-1} at 1200 UTC. The DC continued to be active close to the centre of QENDRESA according to SEVIRI and MHS on 8 November 2014 when the cyclone reached the eastern coasts of Sicily (Fig. 7i), and a filling of the cyclone was observed by surface stations at 0800 UTC, with an increase of 17.6 hPa within 16 hours. The big loop of QENDRESA's trajectory shown in Fig. 1f may be attributed to the turn of the DLS vector (Fig. 8f). During the DC activity close to the centre between 1500 UTC and 2100 UTC on 7 November 2014, the DLS vector was turning from SW to NE directions and so did QENDRESA. At the same period, the vortex tilt was on the right of the DLS vector but turned downshear with the DC initiation over Malta, but in general, the vortex tilt was small (Fig. 8f). Then, after 2100 UTC the DLS vector suddenly changed direction towards the South-West and QENDRESA stopped propagating north, turning as well South-West, towards the coasts of Sicily in the early morning on 8 November 2014 (Fig. 1f & 8f).

The manual tracking of ROLF started on 6 November 2011 1800 UTC over the Balearic Islands (Fig. 1d) when DC was gradually starting to concentrate close to the cyclone centre. Only scattered convective cells were detected by 7 November 2011 0000 UTC when a MCS appeared in the downshear right quadrant and remained phase-locked, close to the centre for about 6 hours in the downshear left quadrant, producing COV (Fig. 9a). The DLS was ranging between $6\text{-}9 \text{ m s}^{-1}$ until the night of 7 November 2011, and changed direction when ROLF turned NE during the late afternoon and night. After 7 November 2011 2100 UTC, the increasing DLS coincided with a period of organized DC in all quadrants and especially in the upshear parts of the cyclone (Fig. 9b), resulting in the formation of a small symmetrical cloud-free area with a radius of fewer than 20 km. The maximum intensity of ROLF was estimated a while later, on 8 November 2011 0300 UTC when DC and COV were mostly found downshear. Despite the widespread DC activity in all quadrants and within 200 km radial distance from the centre, DLS was still increasing in speed, reaching values up to 16.6 m s^{-1} at 1000 UTC 8 November 2011. To this end, the strong eastern DLS and vortex tilt may be responsible for the burst of a large MCS with multiple COV detections in the downshear and upshear left quadrants, which was first detected around 0800 UTC and lasted for about 12 hours (Fig. 9c). At 1920 UTC 8 November 2011 satellite scatterometer data showed a symmetric cyclonic vortex with uncontaminated observations of 18 m s^{-1} sustained wind speeds (not shown), right after the dissipation of the MCS. The cyclone finally dissipated in the southern coasts of France after 0000 UTC 9 November 2011 and could not be tracked anymore after 0600 UTC.

TRIXIE was an MTLC which formed as a response to a mid-level cut-off low over the Ionian Sea on 27 October 2016 and lasted for about 4 days. According to ERA5, during the first two days, the cyclone experienced a warm-seclusion, but the mid/upper-level trough remained far away from the surface vortex

before the detection of the tropical-like characteristics. The manual tracking of TRIXIE was possible after 29 October 2016 0000 UTC, when the vortex tilt was fluctuating between 70 – 130 km to the S-SE from the surface cyclone centre and DC was detected towards the vortex tilt and in the downshear quadrants (Fig. 9d). During the 29 October and first half of 30 October 2016 even though DC was found in all quadrants, it was characterized by pulsating storms and not organized storm cells close to the cyclone centre. During this period DLS had speed values of about 10 m s^{-1} , but the vortex tilt was significantly large (more than 100 km), most of the time a few degrees to the left of DLS vector (Fig. 8g), and DC did not develop in the upshear quadrants. This pattern changed when DC started to be detected close to and over the cyclone centre after 12000 UTC 30 October 2016 when the DLS and vortex tilt started changing direction NE. This change resulted in vertical alignment of the surface and mid-level vortex and DC was detected in the upshear quadrants (Fig. 9e-f). Between 0000 – 0200 UTC 31 October 2016 a small cloud-free area was detected resembling an “eye” with a radius smaller than 20 km (Fig. 9f), which became bigger after 0200 UTC but still surrounded by DC and COV. The maximum intensity of the cyclone was estimated at 0400 UTC when an upper-level anticyclonic outflow was visible in the satellite imagery (not shown), before the cyclone reaches the western coasts of Greece. TRIXIE lost its structure after 0700 UTC, possibly due to the increasing wind shear close to 15 m s^{-1} and the effects of topography, but continued to produce excessive precipitation and sustained wind speeds up to 14 m s^{-1} and gusts up to 33.8 m s^{-1} in West Crete and the islands of Gavdos and Kythira (Fig. 1g). Excessive rainfall was recorded in Crete with up to $180 \text{ mm } 12 \text{ hour}^{-1}$. The last surface observation of the minimum SLP was 1003.4 hPa with a $-9 \text{ hPa } 3\text{-hr}^{-1}$ trend at 1135 UTC in Gavdos with a subsequent 8 hPa increase of the SLP within an hour and surprisingly, under a cloud-free sky.

NUMA was associated with a cut-off low with a centre over southern Italy on 16 November 2017. The manual tracking started on 17 November 2017 0000 UTC when weak 6-8 m s^{-1} DLS but a strong vortex tilt was estimated by ERA5. DC was detected away from the cyclone centre until the afternoon of 17 November 2017 but was organized in almost all quadrants with COV detections (Fig. 9g). During the late afternoon and night on 17 November 2017, DC started to organize close to the cyclone centre, while the vortex tilt was decreasing and became more aligned with the DLS vector (Fig. 9h). A storm cell that was first detected at 1400 UTC downshear was then wrapped around the cyclone and remained active in the upshear left quadrant for almost 12 hours producing COV for several hours (Fig. 9h) and possibly resulted in a minimum vortex tilt at 2000 UTC. The maximum intensity of the cyclone was estimated by ERA5 a few hours later, at 0300 UTC on 18 November 2017 or at 0000 UTC as in the simulations of Marra et al. (2019). During that period, DC was found in all quadrants within 50 – 100 km from the centre, and occasionally an “eye-like” feature with 20 km radius was observed in the satellite imagery. In the early morning of 18 November 2017 DC started to decrease rapidly everywhere in the cyclone periphery, when an increasing eastern vortex tilt and the DLS vector resulted in the propagation of NUMA east, towards Greece. The following widespread initiation of DC in parallel to the west coasts of Greece may have been a response to the eastern vortex tilt and the increase of DLS. During the late afternoon of 18 November 2017 an MCS, which was developed 10 hours earlier in the downshear left quadrant, was now locked in the upshear left quadrant, creating a quasi-symmetric DC structure around NUMA, with a cloud-free centre (Fig. 9i). Surface observations in West Greece suggest that NUMA was still

a very well structured and intense MTLC, even after landfall: the weather station of the Ionian-Puglia network (Kalimeris et al., 2016) in Kipouria-Palliki (38.1°N, 20.2°E) in Kefalonia reported maximum sustained 10-min wind speed 25 m s⁻¹ and wind gusts up to 30 m s⁻¹ at 2058 UTC. Another observation of SLP minimum 999.8 hPa was observed later in Ithaca (38.3°N, 20.7°E) at 2350 UTC with a -8.2 hPa 3-hr⁻¹ trend and SLP at NUMA's centre remained below 1000 hPa until 0220 UTC when the weather station in Aitoliko (38.4°N, 21.4°E) reported 999.6 hPa with a -7.8 hPa 3-hr⁻¹ trend and a sharp wind direction change according to the NOAA network (Lagouvardos et al., 2017). At that time, DC was weakening rapidly close to the cyclone centre, but a storm that was first detected over Lefkada on 18 November 2017 2300 UTC within 100-150 km far from the centre, was still active at 0600 UTC on 19 November 2017 over Greece producing excessive precipitation under COV detections by MHS.

ZORBAS was first an extratropical cyclone found in the north coasts of Libya on 27 September 2018. The evolution of DC in ZORBAS resembles TRIXIE's but the evolution of the vortex tilt was almost the opposite. When the manual detection started on 28 September 2018 0000 UTC, the DLS was decreasing below 10 m s⁻¹ with an almost perfect vertical alignment between the mid-level and the surface vortices. DC was most pronounced in the outer parts of the cyclone and organized in two bands until 1200 UTC (Fig. 9j). Later, DC started to organize close to the centre and the DLS was turning to a fixed NE direction with speed values close to 10 m s⁻¹. An MCS that was first detected downshear at 1400 UTC was then cyclonically wrapped around the centre and remained in the upshear quadrants for about 10 hours, when another MCS developed in the downshear right quadrant and resulted in symmetric DC structure with a cloud-free area in the centre during the late night of 28 September 2018 (Fig. 9k). At 0000 UTC when the cyclone was located at 35.9°N and 20.3°E, two observations from ships were available from the National Centres for Environmental Prediction/National Weather Service/NOAA/U.S. Department of Commerce (2004), reporting sustained wind speeds of 21 m s⁻¹ about 70 km E (id="DKZR2" at 35.0°N, 21.1°E) and 120 km NE (id="9HA3047" at 36.5°N, 21.5°E). The lowest SLP measured by the first ship was 1003.3 hPa and 1006.0 hPa from the latter, suggesting that the SLP at the centre of the cyclone was below 1000 hPa, in accordance with ERA5 value of 998.2 hPa. An impressive observation of 25.7 m s⁻¹ sustained wind speed and 1002 hPa SLP was reported at 0500 UTC by the ship "9HA3047" when it was located at 36.9°N and 19.6°E, about 140 km W-NW from the cyclone centre, outside the very deep convective clouds in the west/upshear left part of the cyclone (Fig. 9l). These observations show that ZORBAS was intensifying while propagating towards Peloponnese, in Greece, despite the opposite analysis by ERA5. The pass of MHS onboard NOAA-18 satellite on 29 September 2019 0810 UTC over ZORBAS provided information about the deep vertical extent of the MCS which was wrapped around the cyclone with many MWDC/COV detections, and a large area of positive DCPIXELS detected by SEVIRI (Fig. 9l). An increase of DLS up to 14 m s⁻¹ with a NE direction and a strong NW vortex tilt (Fig. 9l) between 0900 and 1100 UTC was estimated by ERA5 when the centre of the cyclone was making landfall in South-West Peloponnese. During this period a small "eye-like" structure with a radius of 10 km was detected about 10 km south from Pylos station (NOAAN network) which reported at 1000 UTC 988.7 hPa minimum SLP with a -9.3 hPa 3-hr⁻¹ trend, 22.2 m s⁻¹ maximum sustained 10-minute wind speed and wind gusts up to 33.3 m s⁻¹ at 1110 UTC. Widespread damage was reported in Southern Greece mainly due to severe wind

gusts, storm surge and floods (accumulated rainfall up to 261 mm in 24 hours and 506 mm in 48 hours) as ZORBAS was dissipating over land. DC was not anymore detected after 1900 UTC on 29 September 2018 over Greece. ZORBAS is probably the first documented MTLC that hit land with maximum intensity.

Appendix 2

Synoptic and mesoscale analysis during the MTLCs

The synoptic-scale flow that leads to the development of the studied MTLCs according to WRF, has several similarities among the cases, but also distinct differences, mostly related to the season of occurrence. For example, much lower geopotentials associated with lower temperatures in November (Med2007, NUMA) and December (Med2005) than in September (Med2006, ZORBAS) and October (TRIXIE) lead to differences in the large-scale flow, especially at the early stages of the studied MTLCs.

A first overview of the maps shows the advection of low geopotential heights over the Mediterranean during the south propagation of long-wave troughs with different size, extent, tilt and propagation speed. During the early stages of most of the studied MTLCs, the upper-level streamers have several different shapes, but almost all of them are initially connected with high-PV reservoirs over Northern Europe. The mid-level troughs eventually become cut-offs over the Mediterranean, but PV streamers do not always get totally detached from the nearby upper-level depressions (e.g., Med2006 and Med2007 in Figs. A2.3-A2.5) and for one case (TRIXIE) the upper-level PV was very weak compared to the rest of the cases (Fig. A2.7). In addition, the surface cyclones that develop into these strongly baroclinic environments with strong horizontal thermal gradients, are initially tilted in the vertical axis, with the mid-level vortex positioned a few hundred kilometers away. This stage describes the typical extratropical cyclone development, with cold-core or shallow warm-core systems that are surrounded by distinct fronts, and sometimes, nearby topographic features trigger low-level vorticity perturbations. For example, Med2006 emerged just offshore the coasts of Sicily during an approaching trough (Fig. A2.3) and Med2007 developed in the lee side of the Alps during a strong northerly flow (Fig. A2.5). In the following paragraphs, the WRF outputs from the parent and inner domains will be discussed in detail.

- **Med2005**

Starting the synoptic analysis with Med2005, a strongly vertically-tilted cyclone can be seen in Fig. A2.1a, where a cut-off low with a 500 hPa center over NW Libya is about 200 km south from a surface low-pressure system between Sicily and Tunisia. The cyclone is developing in a strong baroclinic environment, evident by the presence of a strong jet stream that was wrapped around the mid-level cold drop on 13 December 2005, responsible for the presence of strong vertical wind shear (not shown) and large-scale upward motions (high omega values at 400 hPa in Fig. A2.1a). At the same time, an elongated PV streamer is found in the upper troposphere, extending from Central Europe towards Central Mediterranean, curved over the Balearic Sea and Algeria (Fig. A2.1b), with comparable wind speeds at 300 hPa and 500 hPa. Near the surface, a well-defined cold front is visible at 950 hPa in Fig. A2.2a, traveling fast north-east with embedded DC and strong

adiabatic heating producing upper-level divergence. The cold front at 1800 UTC on 13 December 2005 extends for more than 1000 km from Sicily towards Libya and ahead of it, there is a plume of very moist air masses with more than 20 mm precipitable water (Fig. A2.2a) feeding with moisture several storms (Fig. A2.2b). The low-level vorticity field is still very messy with several maxima along the coast of North Africa (Fig. A2.2b). For the following 12 hours, constant deepening of the cyclone is simulated during a seclusion and Med2005 starts to attain tropical-like characteristics.

The maximum cyclone intensity (as of the minimum SLP) is simulated at 0600 UTC on 14 December 2005, during low DC activity (DCGRIDS) in accordance with the observations (see Chapter 2). At the same time, the low-level flow south of the Med2005 is very strong with more than 30 m s^{-1} at 950 hPa but only 10-15 m s^{-1} in the north side (Fig. A2.2c) and even less than 5 m s^{-1} at 850 hPa (Fig. A2.2d). The strong vertical and horizontal wind shear, and the limited DC activity create an unfavorable environment for further intensification of the cyclone. As the cut-off low moves fast north-east on 14 December 2005, it is merged with another trough over the Balkans (Fig. A2.1c-d) and the MTLC Med2005 is now traveling fast east, close to the coasts of Libya, under the mid/upper-level jet streak with a weak gradual filling of the surface cyclone. At the same time, the PV streamer at 300 hPa is also weakening with a slow rate, and it is advected by the mean flow over the Eastern Mediterranean (Fig. A2.1d-f). The simulated DC activity is limited and pulsating close to the center of Med2005 on 14 December 2005 (Fig. A2.2d-f) and results in low PVDIAB values near the tropopause, weakening the PVCO (not shown).

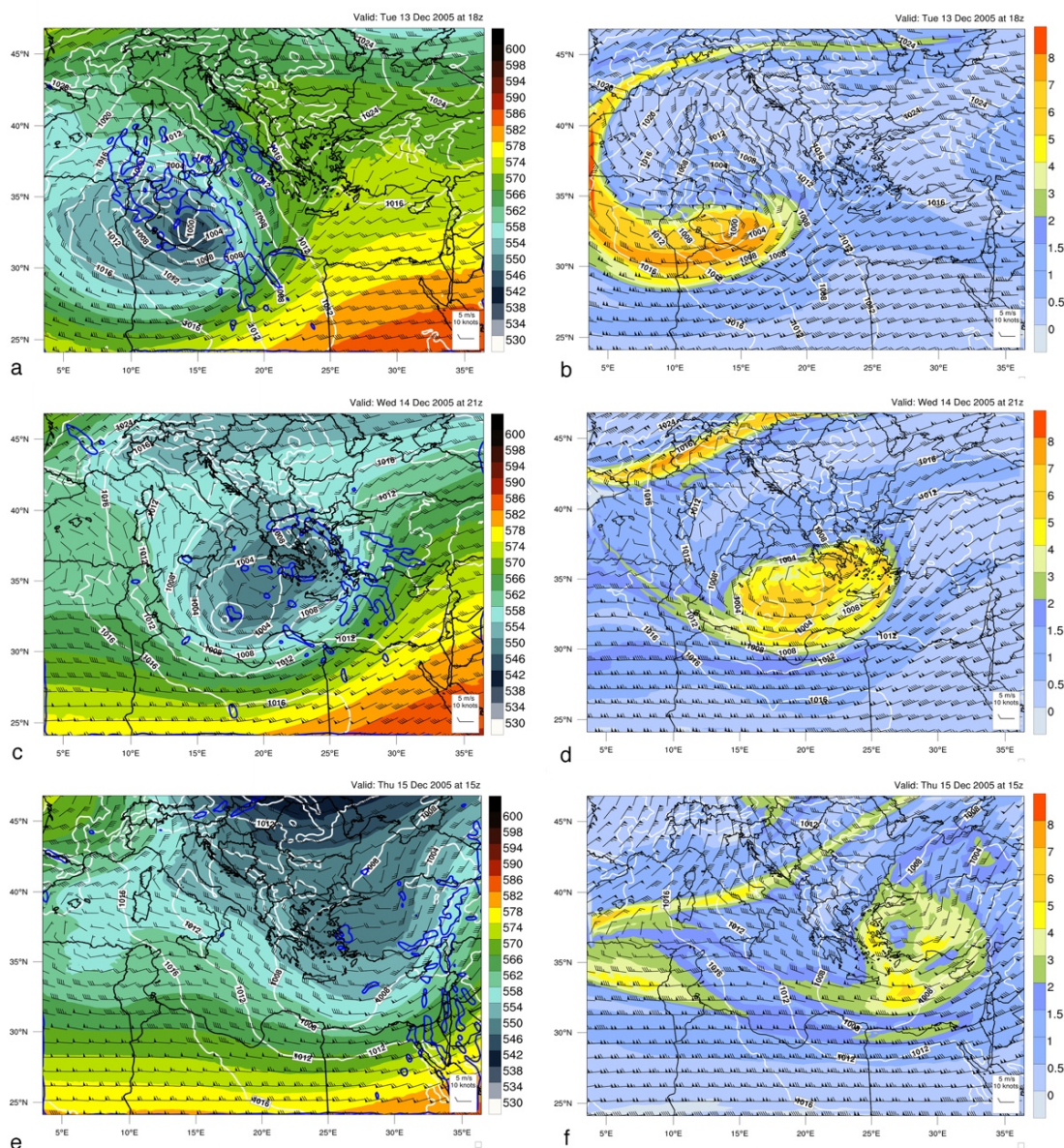


Fig. A2.1 Outputs from the parent domain valid for Med2005: (Left column) Geopotential height (gpm) (shade) and wind (barbs) at 500 hPa, and sea-level pressure (hPa) (white contours), and omega at 400 hPa less than -0.6 Pa s^{-1} (enclosed by blue contours). (Right column) potential vorticity (shade) and wind (barbs) at 300 hPa, and sea-level pressure (hPa) (white contours) for (a-b) 1800 UTC 13 December 2005, (c-d) 2100 UTC 14 December 2005 and (e-f) 1500 UTC 15 December 2005.

On 15 December 2005, Med2005 is found about 300 km south of Crete, having a more well-defined low-level warm core (Fig. A2.2e) and DC activity is mostly simulated in the north side of the cyclone, just like the observed DC activity, as discussed in Chapter 2. The low/mid-level jet stream in the southern parts of the cyclone is still strong and the relative vorticity at 850 hPa is higher than the previous days, concentrated very close to the cyclone center (Fig. A2.2f). The surface cyclone despite being in the left entrance of a mid-level jet stream (Fig. A2.1c-e), where downward synoptic motions are favored, and under the influence of strong vertical and horizontal shear, it survived more than 18 hours until its lysis during the night on 15 December 2005.

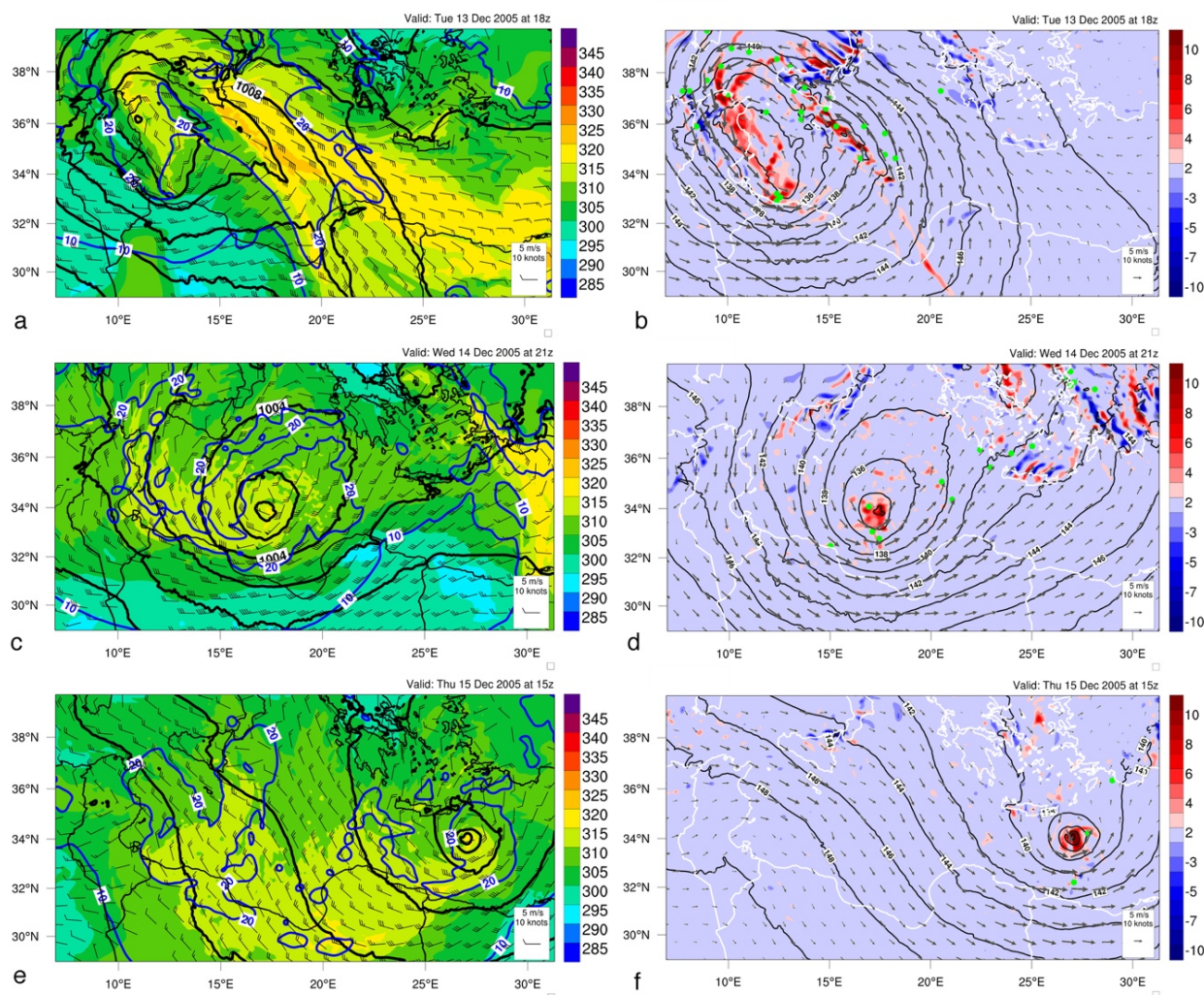


Fig. A2.2 Outputs from the inner domain for Med2005: (Left column) Sea-level pressure (hPa) (black contours), equivalent potential temperature (K) (shade) and wind (barbs) at 950 hPa, and precipitable water (mm) (blue contours). (Right column) geopotential height (gpm) (black contours), wind (vectors) and relative vorticity (10^{-4} s^{-1}) (shade) at 850 hPa, with green dots marking grid points with diabatic heating higher than 5 K h^{-1} between 900 and 500 hPa for (a-b) 13 December 2005 at 1800 UTC, (c-d) 14 December 2005 at 2100 UTC, and (e-f) 15 December 2005 at 1500 UTC.

- **Med2006**

The development of Med2006 is also associated with a mid-level cut-off low, but this time the surface cyclone is embedded into a much larger cyclonic system (Figs. A2.3a-c-e). First, a weak surface cyclone develops in the Sicily-Tunisia strait on 25 September 2006, while a secondary low-pressure center is found in the Tyrrhenian Sea, under the core of the mid-level cut-off low. Med2006 develops inside a very moist and warm air mass with more than 340 K theta-e values at 950 hPa and precipitable water locally exceeding 40 mm (Fig. A2.4a). This highly unstable environment creates favorable conditions for the simulated DC shown in Figs. A2.4b-d to grow upscale and downstream to the surface cyclone in the Ionian Sea, producing upper-level divergence and consequently, low-level convergence with extreme values of low-level vorticity (Fig. A2.4d).

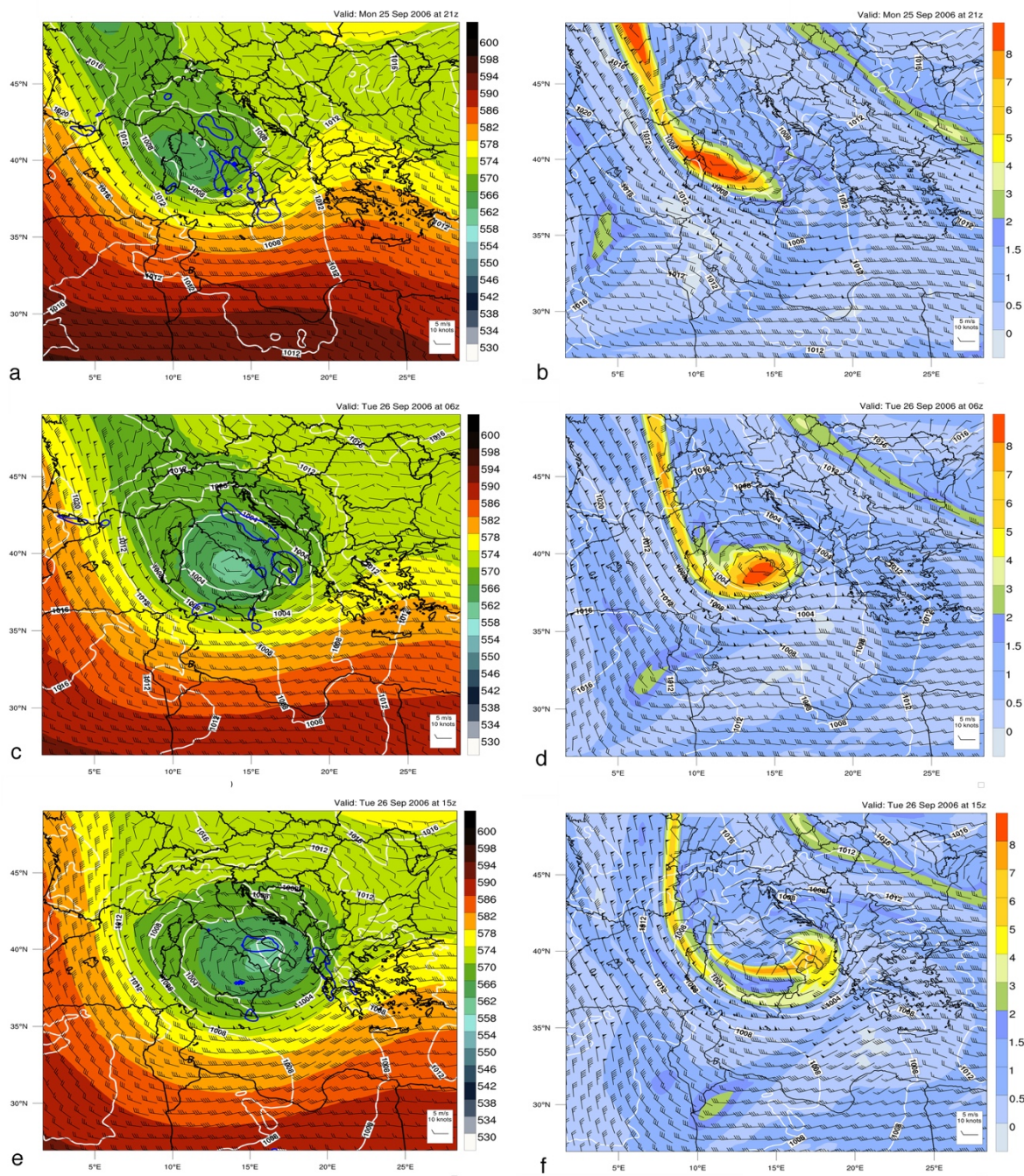


Fig. A2.3 As in Fig. A2.1 but for Med2006, valid for (a-b) 2100 UTC 25 September 2006, (c-d) 0600 UTC 26 September 2006 and (e-f) 1500 UTC 26 September 2006.

In the early morning on 26 September 2006 and at the west and south parts of Med2006, a jet stream is gradually intensifying (Fig. A2.3c) and a strong PV streamer with values exceeding 8 PVU at 300 hPa was simulated over the Tyrrhenian Sea (Fig. A2.3d). While the surface cyclone is intensifying rapidly in the Ionian Sea between 0300 and 0900 UTC on 26 September 2006, the PV streamer attains a “treble-clef” structure over Italy. Med2006 reaches its maximum intensity at the left exit of the mid-level jet stream at 0330 UTC according to WRF, where strong vertical motions are favored (Fig. A2.3c) and makes landfall in Apulia, South Italy after 0800 UTC 26 September 2006. Intense downshear DC activity is simulated constantly until the exit of the

cyclone over the Adriatic Sea after 1000 UTC. The generated low PV values near the tropopause above the strong mid-level diabatic heating lead to the PV streamer erosion (Fig. A2.3d-f). While over the Adriatic Sea, the SLP at the center of Med2006 is almost steady until 2000 UTC 26 September 2006 fluctuating between 986 and 990 hPa, while DC activity is decreasing (Fig. A2.4f) as the cyclone is moving into a drier and colder, thus less unstable environment (Fig. A2.4e). During the late night on 26 September 2006, Med2006 makes landfall again in Italy, this time in the Gargano Peninsula, after a substantial weakening.

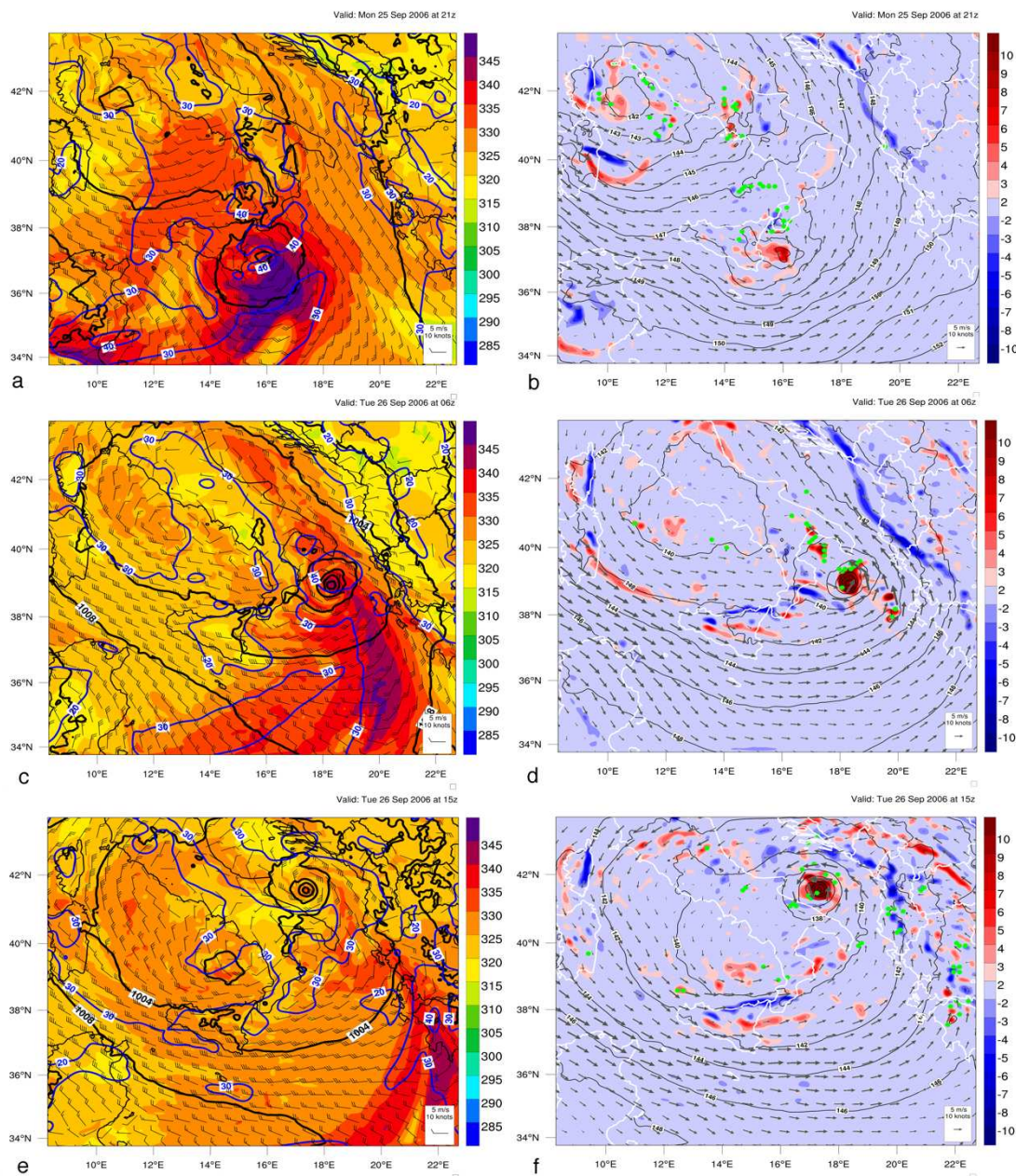


Fig. A2.4 As in Fig. A2.1 but for Med2006, valid for (a-b) 2100 UTC 25 September 2006, (c-d) 0600 UTC 26 September 2006 and (e-f) 1500 UTC 26 September 2006.

- **Med2007**

The main synoptic feature during Med2007 is a long-wave trough bringing unseasonably cold air masses over Western Mediterranean after crossing Central Europe. A strong embedded short-wave trough accompanies this trough, denoted by a 500-hPa cyclonic center over South-eastern France in Fig. A2.5a where

upward motions are simulated by WRF. High values of PV are also advected over Southern France and Gulf of Lion where the low-level cyclogenesis of Med2007 takes place in the afternoon on 15 November 2007 (Fig. A2.5b). The low-level flow on the Gulf of Lion is very strong, exceeding 25 m s^{-1} at 950 hPa (Fig. A2.6a) and strong low-level convergence zones develop, resulting in DC activity close to the cyclone center (Fig. A2.6b). By the late night on 15 November, a warm seclusion forms (Fig. A2.6a) with very high low-level vorticity (Fig. A2.6b), although with a quite asymmetric structure, but it starts showing tropical-like characteristics with the absence of frontal activity and DC close to the cyclone center.

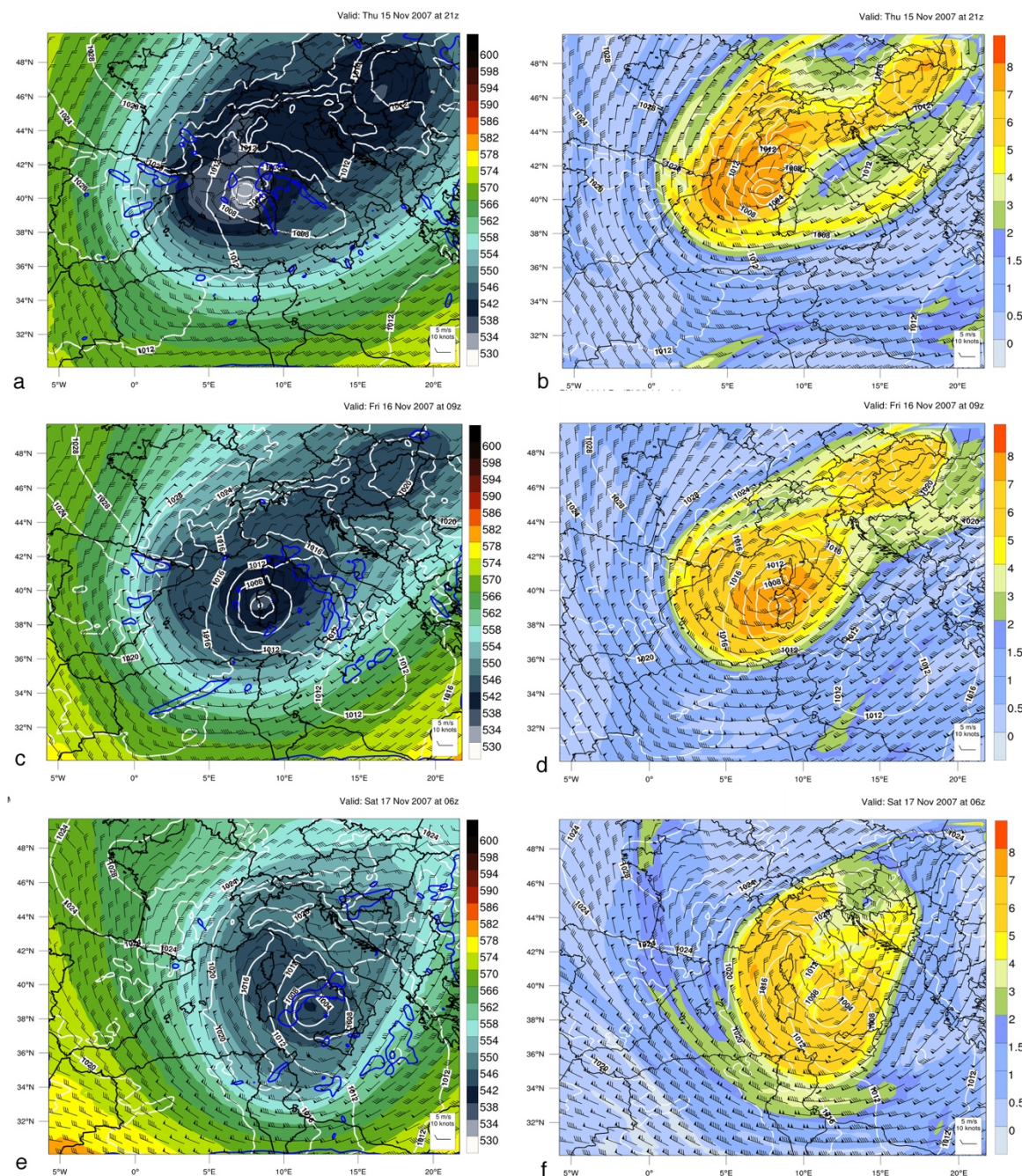


Fig. A2.5 As in Fig. A2.1 but for Med2007, valid for (a-b) 2100 UTC 15 November 2007, (c-d) 0900 UTC 16 November 2007 and (e-f) 0600 UTC 17 November 2007.

In the early morning on 16 November 2007, two distinct mid-level low-pressure systems are found in the simulation, the first over the North-west Balkans and the second (Med2007) under the core of the western mid-level cold drop, moving fast towards Sardinia (Fig. A2.5c). No significant modification of the PV anomaly is simulated aloft (e.g., at 300 hPa in Fig. A2.5d), while a jet stream is wrapped cyclonically around the core of the mid-level cut-off low, resulting in high vertical wind shear. Med2007 makes landfall in Sardinia at 1000 UTC on 16 November 2007 and is found over the Tyrrhenian Sea by 1800 UTC, having weakened about 4 hPa while crossing Sardinia and having lost its tropical-like structure. Finally, a second round of intensification started in the Tyrrhenian Sea where the low and mid-level vortices were vertically aligned (Fig. A2.5e) with some weak fronts forming to the southern and eastern parts of the cyclone (Fig. A2.6e), with important large-scale upward motions and slightly higher-than-before precipitable water. The PV streamer in the parent domain does not show any significant weakening at 300 hPa where PV values still exceed 5-6 PVU (Fig. A2.5f), while in the inner domain, at the isentropic surface of 300 K, the near-tropopause PV has been eroded after a prolonged period of DC activity (not shown). This difference can be attributed a) to the very low altitude of the dynamic tropopause, below 300 hPa and b) to the differences between the parameterized convection in the parent domain and the explicitly resolved convection in the inner domain that have an impact on the structure of the PV streamer. Med2007 is now over a much warmer and more moist environment but DC activity is mostly far away from the cyclone center and relative vorticity at 850 hPa has maxima on the developing fronts (Fig. A2.6f).

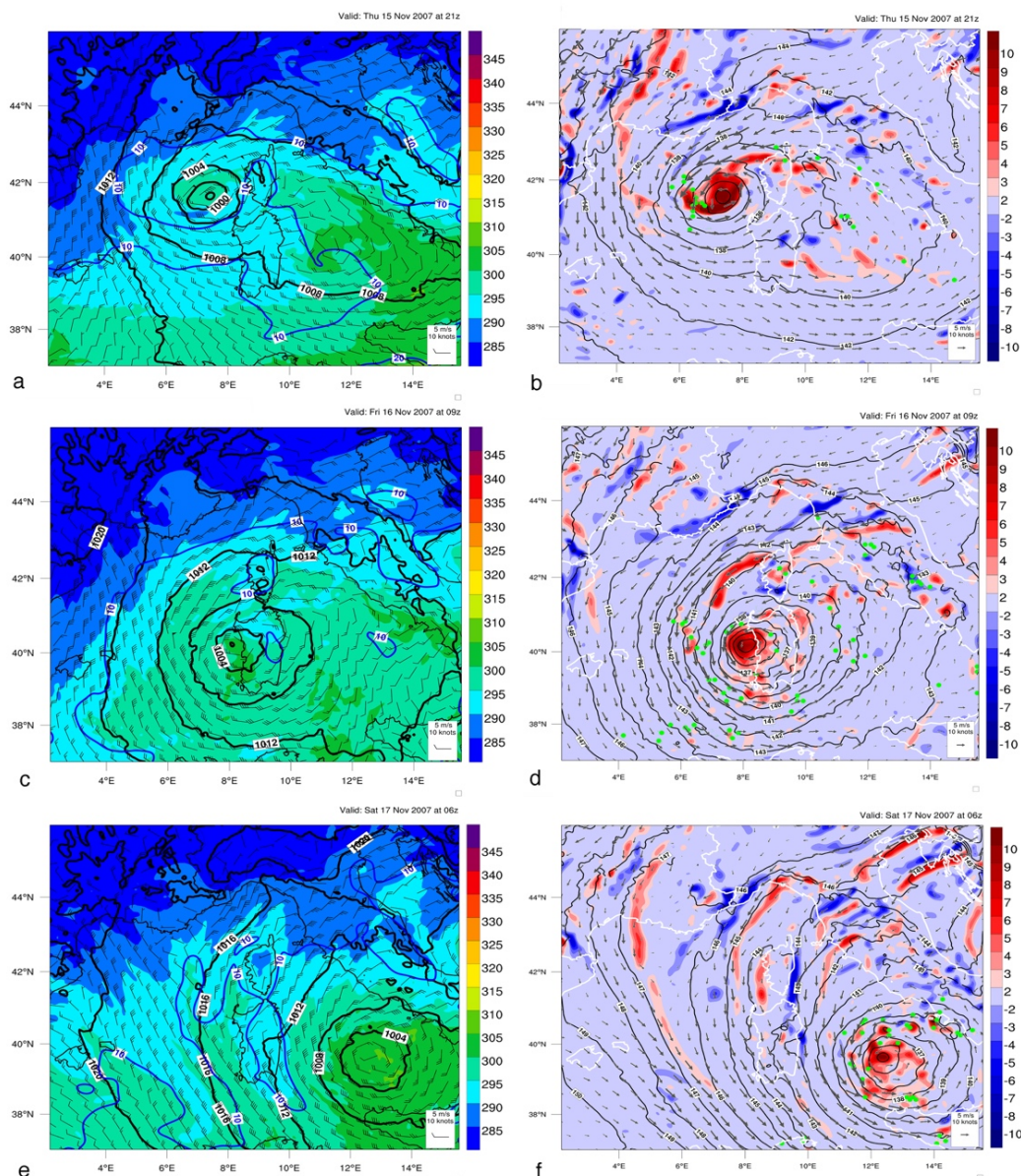


Fig. A2.6 As in Fig. A2.2 but for Med2007, valid for (a-b) 2100 UTC 15 November 2007, (c-d) 0900 UTC 16 November 2007 and (e-f) 0600 UTC 17 November 2007.

- **TRIXIE**

TRIXIE develops between the Gulf of Gabes and South Ionian Sea on 29 October 2016 as a response to a mid/upper-level trough with a positive tilt and an axis extending between the Black Sea and Tunisia (Fig. A2.7a). By the early morning on 29 October 2016, two main mid-level cyclonic features are found in the WRF simulation, but only the one with the highest 500 hPa geopotentials and the lowest 300 hPa PV values (Fig. A2.7b) is associated with a closed low-level cyclonic circulation (Figs. A2.8a-b). The low-level environment is characterized by high theta-e and precipitable water values (Fig. A2.8a) with several vorticity maxima (Fig. A2.8b), mostly related to the scattered DCGRIDS with intense mid-tropospheric diabatic heating. This is the genesis area of TRIXIE which starts traveling slowly east, with a slightly decreasing SLP until the afternoon on 30 October 2016 and a strong vertical tilt (not shown). In the meantime, the upper-level PV streamer has

already weakened a lot, with values less than 2 PVU at the 320 K isentropic surface (not shown), indicating that the dynamical tropopause was even higher than the 300 hPa.

During the late afternoon on 30 October 2016, a sudden increase of DC activity close to the center of TRIXIE marks the start of a strong deepening phase. Between 2100 UTC 30 October 2016 and 0600 UTC 31 October 2016 TRIXIE deepens about 7 hPa before reaching the west coasts of South Greece (Figs. A2.8c-d). In South Ionian Sea there is no synoptic forcing for large scale upward motions or upper-level divergence to easily explain this convective burst. The intense DC activity though, promoted strong upper-level divergence (not shown) which has also promoted the low-level convergence to sustain the DC activity until the early morning on 31 October 2016, when the maximum of 850 hPa vorticity, the minimum SLP and the maximum near-surface wind speed is simulated at 0600 UTC on 31 October 2016. Eventually, TRIXIE starts weakening fast south of Crete while it moves south-east, and the mid-level flow increases significantly as another trough approaches from north-east (Figs. A2.7e-f), reducing the geopotentials and increasing the mid-tropospheric flow (jet stream).

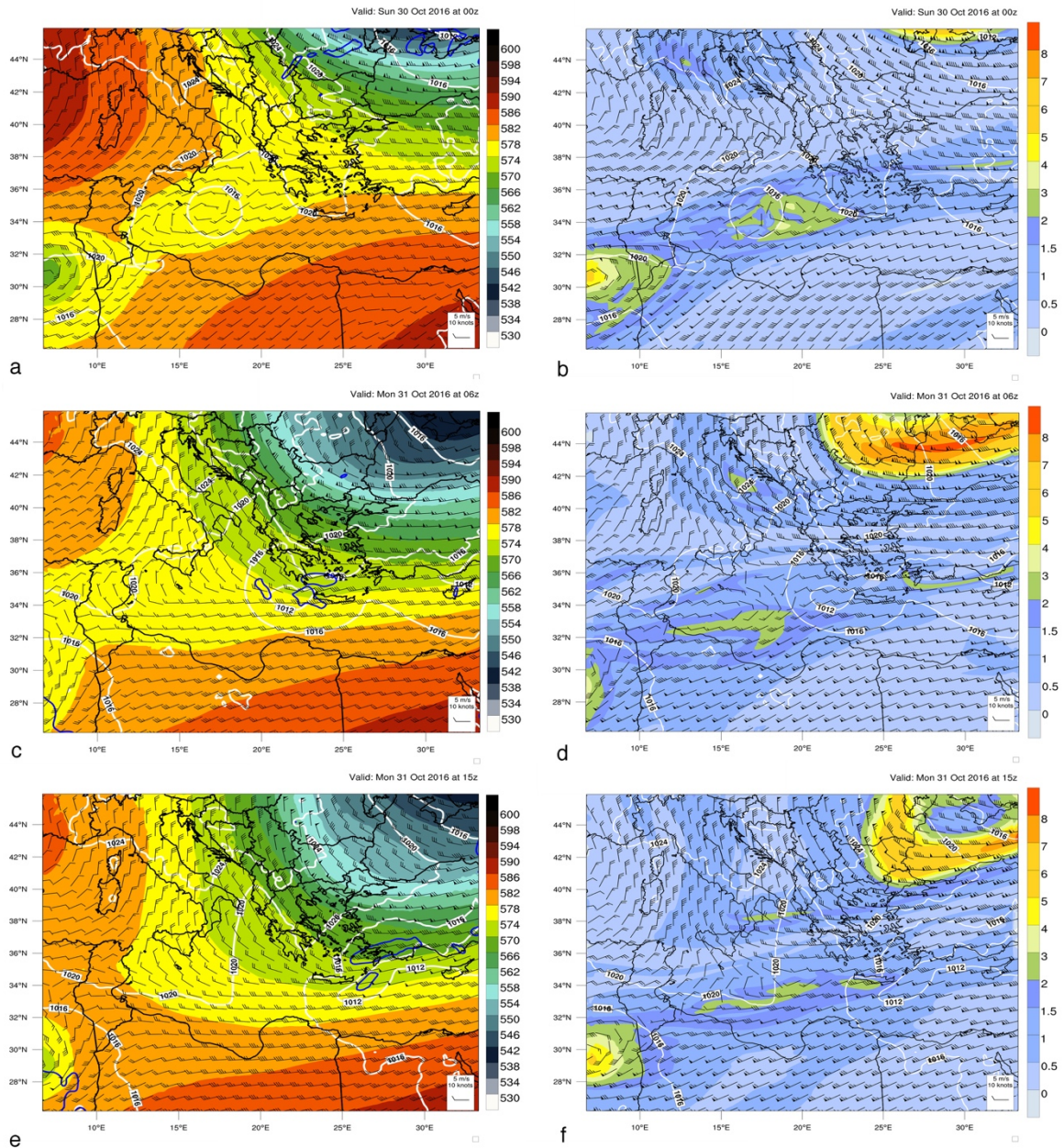


Fig. A2.7 As in Fig. A2.1 but for TRIXIE, valid for (a-b) 0000 UTC 30 October 2016, (c-d) 0600 UTC 31 October 2016 and (e-f) 1500 UTC 31 October 2016.

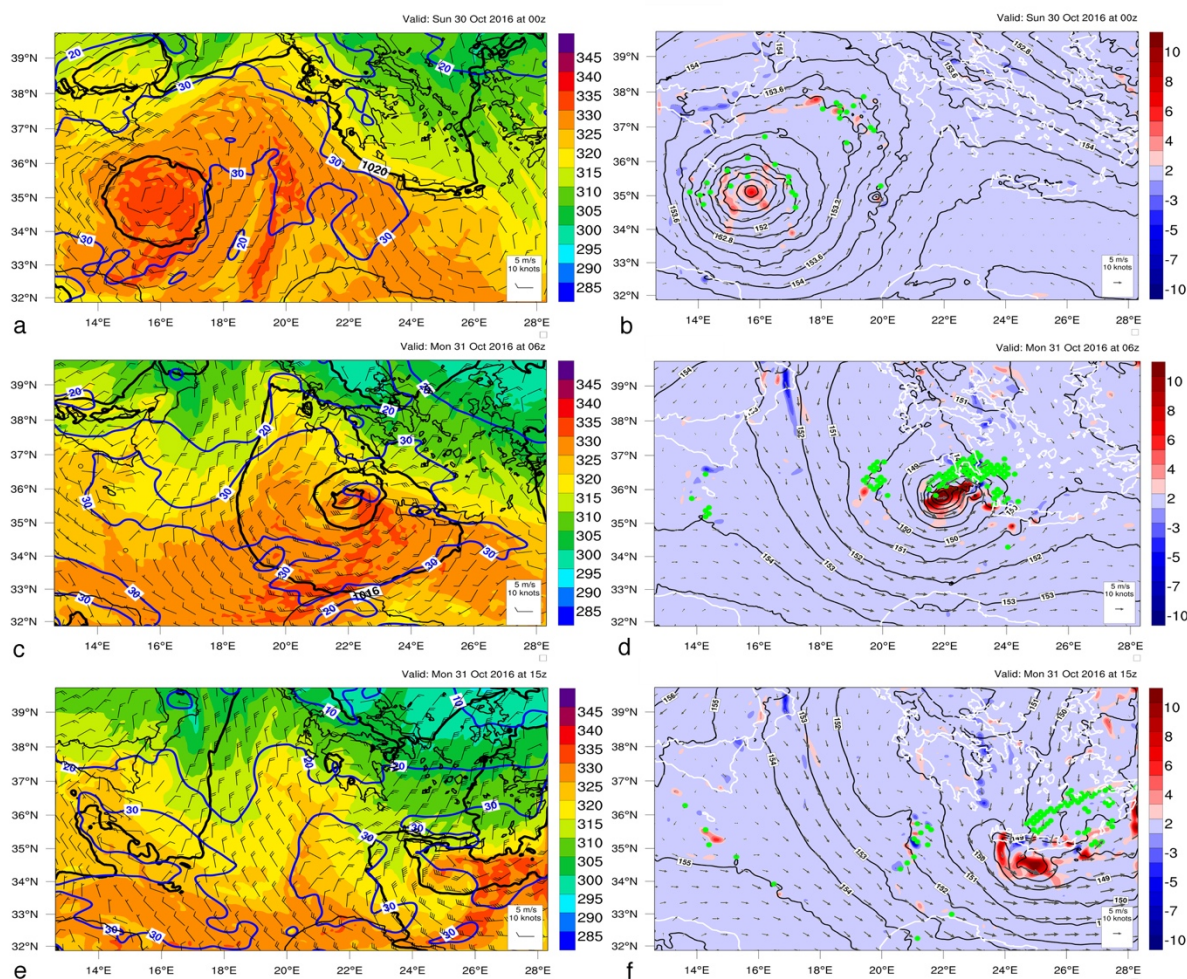


Fig. A2.8 As in Fig. A2.2 but for TRIXIE, valid for (a-b) 0000 UTC 30 October 2016, (c-d) 0600 UTC 31 October 2016 and (e-f) 1500 UTC 31 October 2016.

- NUMA

In the early morning on 16 November 2017, a large mid-level cut-off low is found over Italy and a surface cyclone starts to develop just south from Sicily where strong mid-level upward motions are favored in the left exit of a jet-stream over the Ionian Sea (Fig. A2.9a). The cyclone is vertically tilted with the 500 hPa cyclonic center more than 100 km northwest from the surface cyclone, over Sicily, but the mid and low-level vortices become vertically aligned just after 0000 UTC on 17 November 2017 as NUMA travels north-east over the North Ionian Sea. On 16 and 17 November 2017, NUMA has an asymmetric and swallow warm core, after a seclusion during the late night on 17 November 2017, fully formed by 0000 UTC on 18 November 2017 (Fig. A2.10c). DC activity is mostly disorganized and far away from the cyclone center (Fig. A2.10d) but it does have an impact on the structure of the PV streamer aloft. During the seclusion processes, the relative vorticity at 850 hPa increases substantially in the cyclone center (Fig. A2.7d).

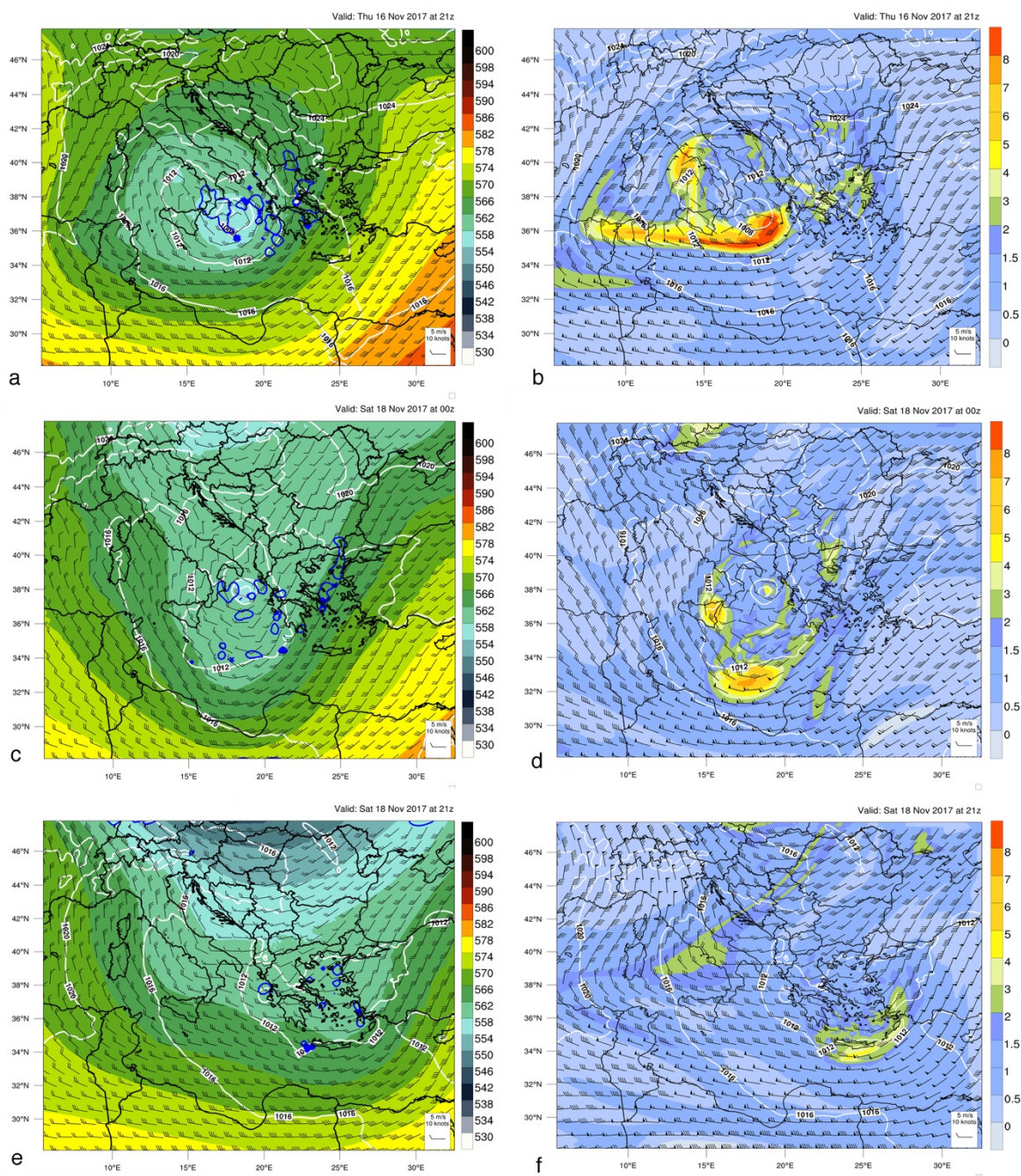


Fig. A2.9 As in Fig. A2.1 but for NUMA, valid for (a-b) 2100 UTC 16 November 2017, (c-d) 0000 UTC 18 November 2017 and (e-f) 2100 UTC 18 November 2017.

NUMA stays almost stationary in the North Ionian Sea for almost 36 hours with the minimum SLP values fluctuating between 1001 and 1003 hPa, without significant changes in the low-level vorticity values close to the cyclone center, despite the constant DC activity. The cyclone starts moving east after 1200 UTC on 18 November 2017 and reaches the coasts of West Greece by 0000 UTC on 19 November 2017. The movement of NUMA east most probably is triggered by the approaching trough from the north which is surrounded by several short-wave troughs, shown as perturbations of the 500 hPa geopotential heights in Fig. A2.9e and a blob of 300 hPa PV in Fig. A2.9f. NUMA's PV streamer is only partially eroded by DC activity as it is advected east from the large-scale flow with values higher than 4 PVU at the 320 K isentropic surface (not shown). During the late night on 18 and early morning on 19 November 2017, NUMA is a swallow warm-

core MTLC with high low-level vorticity, producing gale-force wind speeds near the surface (Fig. A2.10e) but with a significantly weakened wind flow at 850 hPa, with DC activity only to the north side of the cyclone (Fig. A2.10f).

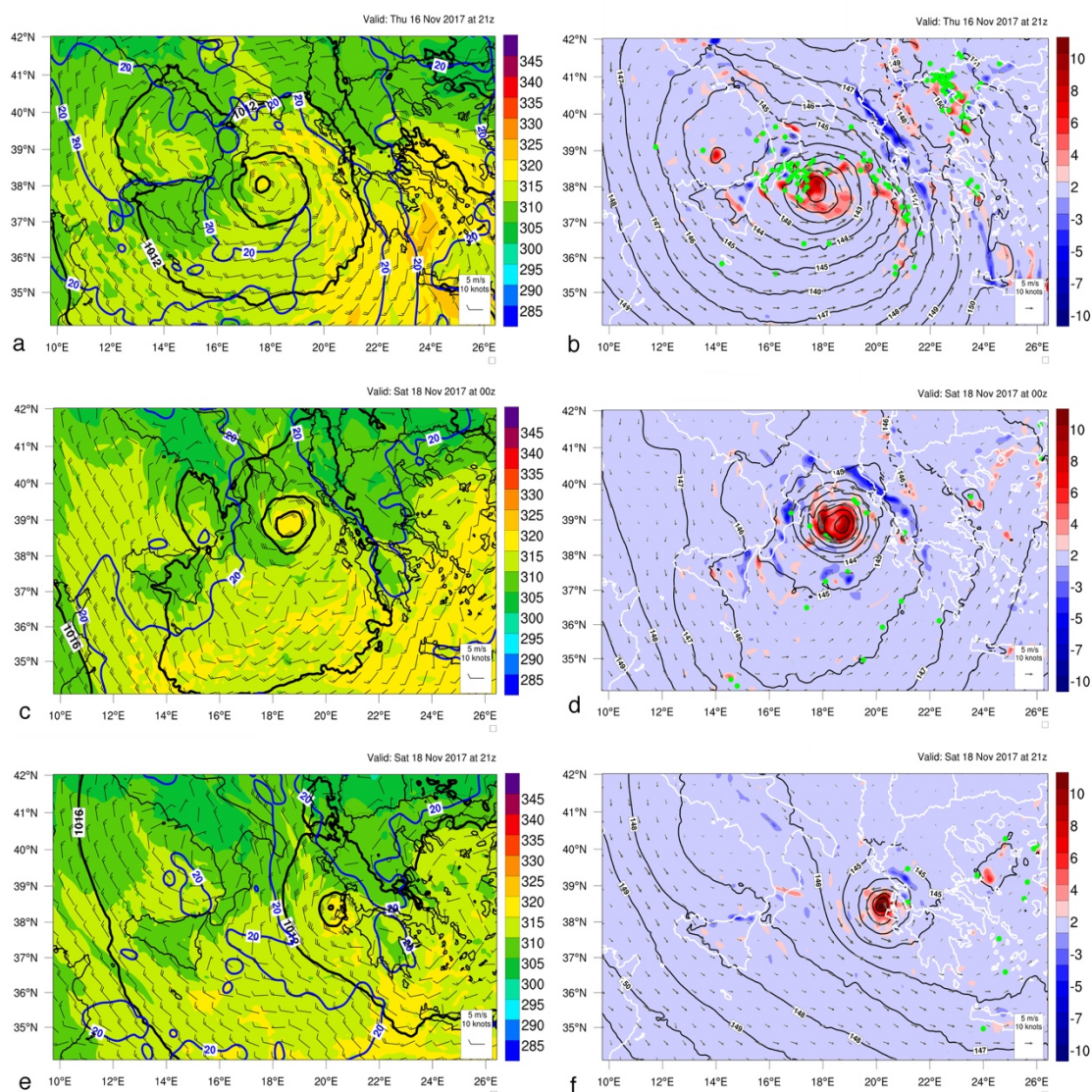


Fig. A2.10 As in Fig. A2.2 but for NUMA, valid for (a-b) 2100 UTC 16 November 2017, (c-d) 0000 UTC 18 November 2017 and (e-f) 2100 UTC 18 November 2017.

- **ZORBAS**

An unseasonably cold air-mass advection from North-east Europe towards Central Mediterranean takes place on 26 and 27 September 2018. Figure A2.11a shows the formation of a mid-level cut-off low after an anticyclonic Rossby wave breaking over the Balkans and the Black Sea, splitting the elongated upper-tropospheric PV streamer (>8 PVU at 300 hPa) extending from Russia towards Libya into two PV maxima: a) one over the South Ionian Sea and b) another one over the Black Sea. ZORBAS emerges as low-level vortex a few kilometers north from the coasts of Libya in the morning of 27 September 2018 during strong downshear and upshear activity, though not always close to the cyclone center (Figs. A2.12a-b). The cold air-mass over

the warm and moist Mediterranean Sea results in strong baroclinicity with strong upward motions and a 30-40 m s^{-1} 500-hPa jet-stream (Fig. A2.11a). In the afternoon on 27 September 2018, a warm and a cold front are found in the WRF simulation, east and south from ZORBAS' center respectively (Fig. A2.12a). DC activity is mostly activity in the occlusion over the north/north-west part of the cyclone (Fig. A2.12b) and the PV streamer is severely eroded (Fig. A2.10b).

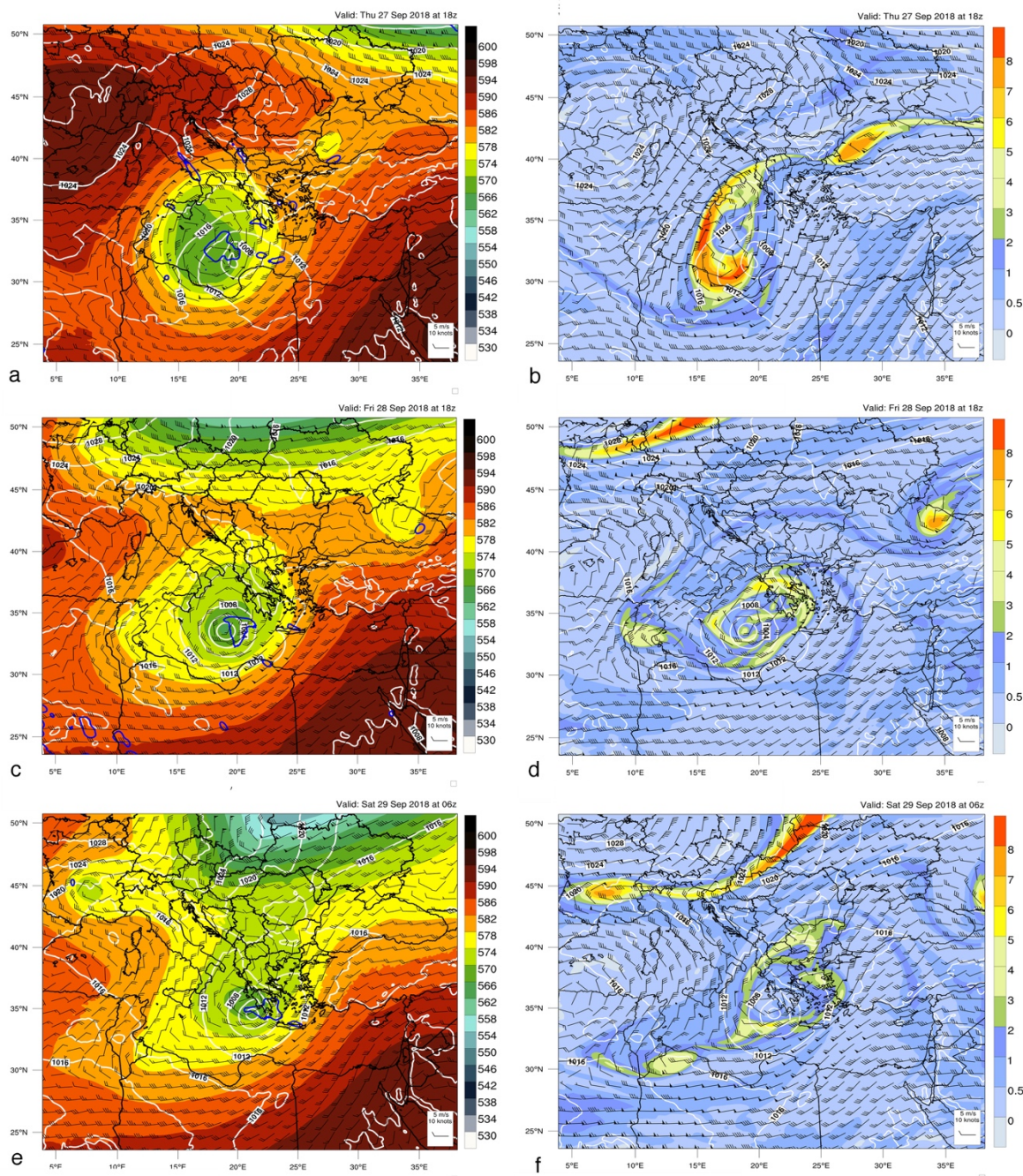


Fig. A2.11 As in Fig. A2.1 but for ZORBAS, valid for (a-b) 1800 UTC 27 September 2018, (c-d) 1800 UTC 28 September 2018 and (e-f) 0600 UTC 29 September 2018.

About 12 hours later, at 0600 UTC 28 September 2018, ZORBAS has a deep warm core and is vertically aligned with the 500-hPa cut-off low (Fig. A2.11c), after reaching its maximum intensity 0300 UTC

and the SLP stays rather steady for 24 hours, below 990 hPa. By 1800 UTC 28 September 2018, the PV streamer at 300 hPa has a “vortex rollup” structure (Hoskins et al., 1985), indicating a strong seclusion (Fig. A2.11d and Fig. A2.12c). In addition, the radius of near-surface maximum wind speed is found closer than 50 km from the cyclone center and DC activity starts to develop very close to the cyclone center, expanding outwards (Fig. A2.12d). A second round of cyclone deepening starts after 0000 UTC 29 September 2018, when ZORBAS deepens with a rate of -1 hPa hr^{-1} for about 4 hours during intense DC activity in all quadrants. Eventually, the cyclone reaches the coasts of South-west Greece after 0600 UTC 29 September 2018 as a very intense MTLC with a deep warm core (Fig. A2.12e) and gale-force winds with a maximum near the surface, but even at 850 hPa the simulated winds exceed 20 m s^{-1} (Fig. A2.12f). The strong upper-level flow is weakening while ZORBAS constantly moves north-east towards Greece, and the PV streamer is significantly eroded with values below 1 PVU at the 320 K isentropic surface in the vicinity of ZORBAS (not shown).

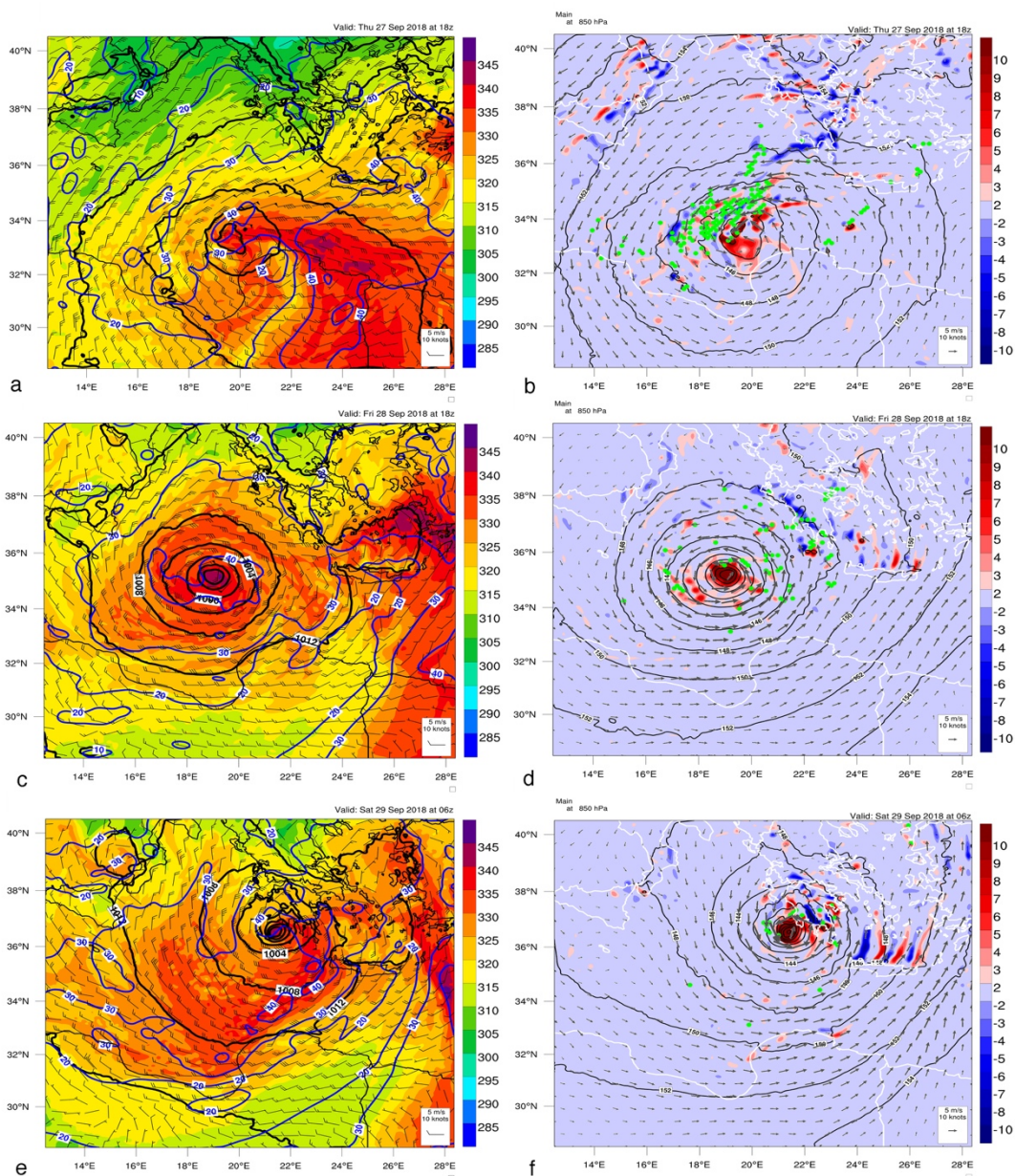


Fig. A2.12 As in Fig. A2.2 but for ZORBAS, valid for (a-b) 1800 UTC 27 September 2018, (c-d) 1800 UTC 28 September 2018 and (e-f) 0600 UTC 29 September 2018.

Abbreviations

CAPE = Convective Available Potential Energy

CCB = Cold Conveyor Belt

COV = Convective Overshooting detection by Microwave Sounders

DC = Deep Convection

DCGRIDS = WRF grid points with deep convection

DCPIXELS = METEOSAT satellite pixels with deep convection

DLS = Deep Layer wind Shear 300-850 hPa

DIAB = Diabatic processes that cause virtual temperature changes

Dp = Pressure tendency at the surface

D ϕ = Geopotential tendency at 50 hPa

ECMWF = European Center for Medium-Range Weather Forecasts

ERA5 = The fifth generation numerical reanalysis by ECMWF

IFS = Integrated Forecasting System

MCS = Mesoscale Convective System

MTLCs = Mediterranean tropical-like cyclones

MWDC = Micro-Wave Deep Convection

NOA = National Observatory of Athens

NOAAN = The National Observatory of Athens Automatic Network

NWP = Numerical Weather Prediction

PBL= Planetary Boundary Layer

PV = Potential Vorticity

PVU = Potential Vorticity Units ($10^{-6} \text{ m}^{-2} \text{ s}^{-1} \text{ K kg}^{-1}$)

PVCO= Conserved Potential Vorticity

PVDIAB = Diabatic Potential Vorticity

PVMO = Potential Vorticity attributed to momentum

PTE = Pressure Tendency Equation

TADV = Net temperature advection (vertically integrated)

TC = Tropical Cyclone

TD = Tropical Depression

TT = Tropical Transition

VWS = Vertical Wind Shear

WCB = Warm Conveyor Belt

WRF = Weather and Research Forecast

VMT = The vertical motion multiplied by the static stability

References

1. Adler, R.F., Markus, M.J., and Fenn, D.D. (1985) Detection of severe Midwest thunderstorms using geosynchronous satellite data. *Monthly Weather Review*, 51, 769-781.
2. Alhammoud, B., Claud, C., Funatsu, B.M., Béranger, K., and Chaboureau, J.-P. (2014) Patterns of Precipitation and Convection Occurrence over the Mediterranean Basin Derived from a Decade of Microwave Satellite Observations, *Atmosphere* 5, 370-398. <https://doi.org/10.3390/atmos5020370>
3. Aligo, E., Gallus, W., and Segal, M. (2009) On the Impact of WRF Model Vertical Grid Resolution on Midwest Summer Rainfall Forecasts. *Weather and Forecasting* 24 (2), 575–94.
4. Anthes, R.A. (1977) A cumulus parameterization scheme utilizing a one-dimensional cloud model. *Monthly Weather Review*, 105, 270-286.
5. Arakawa, A., and Wu, C.-M. (2013) A unified representation of deep moist convection in numerical modeling of the atmosphere. Part I, *Journal of the Atmospheric Sciences*, 70(7), 1977–1992. doi:10.1175/JAS-D-12-0330.1
6. Arakawa, A., and Schubert, W.H. (1974) Interaction of a Cumulus Cloud Ensemble with the Large-Scale Environment, Part I. *Journal of the Atmospheric Sciences*, 31, 674–701. [https://doi.org/10.1175/1520-0469\(1974\)031<0674:IOACCE>2.0.CO;2](https://doi.org/10.1175/1520-0469(1974)031<0674:IOACCE>2.0.CO;2)
7. Attinger, R., Spreitzer, E., Boettcher, M., Forbes, R., Wernli, H., Joos, H. (2019) Quantifying the role of individual diabatic processes for the formation of PV anomalies in a North Pacific cyclone. *Quarterly Journal of Royal Meteorological Society*, 145, 2454–2476. <https://doi.org/10.1002/qj.3573>
8. Balsamo, G., Viterbo, P., Beljaars, A., Van den Hurk, B., Hirschi, M., Betts, A.K, Scipal, K. (2009) A revised hydrology for the ECMWF model. *Journal of Hydrometeorology*. <https://doi.org/10.1175/2008JHM1068.1>
9. Bedka, K., J. Brunner, Dworak, R., Feltz, W., Otkin, J., and Greenwald, T. (2010) Objective Satellite-Based Detection of Overshooting Tops Using Infrared Window Channel Brightness Temperature Gradients. *Journal of Applied Meteorology and Climatology*, 49, 181–202. <https://doi.org/10.1175/2009JAMC2286.1>
10. Bentley, A.M., Bosart, L.F., and Keyser, D. 2017: Upper-Tropospheric Precursors to the Formation of Subtropical Cyclones that Undergo Tropical Transition in the North Atlantic Basin. *Monthly Weather Review*, 145, 503–520, <https://doi.org/10.1175/MWR-D-16-0263.1>
11. Bentley, A.M., Keyser, D., and Bosart, L.F. (2016) A Dynamically Based Climatology of Subtropical Cyclones that Undergo Tropical Transition in the North Atlantic Basin. *Monthly Weather Review*, 144, 2049–2068, <https://doi.org/10.1175/MWR-D-15-0251.1>

12. Bentley, A.M., and Metz, N.D. (2016) Tropical Transition of an Unnamed, High-Latitude, Tropical Cyclone over the Eastern North Pacific. *Monthly Weather Review*, 144, 713–736, <https://doi.org/10.1175/MWR-D-15-0213.1>
13. Bennartz, R., Bauer, P. (2003) Sensitivity of microwave radiances at 85–183 ghz to precipitating ice particles. *Radio Science*, 38(4). doi:10.1029/2002RS002626
14. Betts, A.K., and Miller, M.J. (1986) A new convective adjustment scheme. Part II: single column tests using GATE wave, BOMEX, ATEX and arctic air-mass data sets. *Quarterly Journal of Royal Meteorological Society*, 112, 693-709.
15. Bjerkness, J. and Solberg, H. (1922) Life cycles of cyclones and the polar front theory of atmospheric circulation. *Geophysisks Publikationer*, 3, 1–18. 13.
16. Binder, H., Boettcher, M., Joos, H., and Wernli, H. (2016) The role of warm conveyor belts for the intensification of extratropical cyclones in Northern Hemisphere winter. *Journal of the Atmospheric Sciences*, 73, 3997–4020.
17. Boettcher, M., and Wernli, H. (2011) Life Cycle Study of a Diabatic Rossby Wave as a Precursor to Rapid Cyclogenesis in the North Atlantic—Dynamics and Forecast Performance. *Monthly Weather Review*, 139, 1861–1878. <https://doi.org/10.1175/2011MWR3504.1>
18. Boos, W.R., Hurley, J.V., and Murthy, V.S. (2015) Adiabatic westward drift of Indian monsoon depressions. *Quarterly Journal of the Royal Meteorological Society*, 141, 1035–1048. <https://doi.org/10.1002/qj.2454>
19. Bormann, N., and Bonavita, M. (2013) Spread of the ensemble of data assimilations in radiance space. ECMWF Technical Memorandum 708.
20. Bonsignori, R. (2007) The Microwave Humidity Sounder (MHS): in-orbit performance assessment. In: Society of Photo-Optical Instrumentation Engineers (SPIE) Conference Series, Society of Photo-Optical Instrumentation Engineers (SPIE) Conference Series, vol 6744, p0, <https://doi.org/10.1117/12.737986>
21. Bouin, M.N., and Brossier, C.L. (2020) Impact of a medicane on the oceanic surface layer from a coupled, kilometer-scale simulation. *Ocean Science*, 16, 1125-1142. <https://doi.org/10.5194/os-16-1125-2020>
22. Bosart, L.F., and Bartlo, J.A. (1991) Tropical Storm Formation in a Baroclinic Environment. *Monthly Weather Review*, 119, 1979–2013. [https://doi.org/10.1175/1520-0493\(1991\)119<1979:TSFIAB>2.0.CO;2](https://doi.org/10.1175/1520-0493(1991)119<1979:TSFIAB>2.0.CO;2)
23. Brunner, J.C., Ackerman, S.A., Bachmeir, A.S., Rabin, R.M. (2007) A quantitative analysis of the enhanced-V feature in relation to severe weather. *Weather and Forecasting*, 22, 853-872, [10.1175/WAF1022.1](https://doi.org/10.1175/WAF1022.1)
24. Browning, K.A. (2004) The sting at the end of the tail: Damaging winds associated with extratropical cyclones. *Quarterly Journal of Royal Meteorological Society*, 130, 375–399.
25. Browning, K.A., and Roberts, N.M. (1994) Structure of a frontal cyclone. *Quarterly Journal of Royal Meteorological Society*, 120, 1535–1557.
26. Browning, K. A. (1986) Conceptual models of precipitation systems. *Weather Forecasting*, 1, 23–41.

27. Büeler, D., and Pfahl, S. (2017) Potential Vorticity Diagnostics to Quantify Effects of Latent Heating in Extratropical Cyclones. Part I: Methodology. *Journal of the Atmospheric Sciences*, 74, 3567–3590. <https://doi.org/10.1175/JAS-D-17-0041.1>
28. Čampa, J., and Wernli, H. (2012) A PV perspective on the vertical structure of mature midlatitude cyclones in the northern hemisphere. *Journal of the Atmospheric Sciences* 69, 725–740. <https://doi.org/10.1175/JAS-D-11-050.1>
29. Cao, J., and Xu, Q. (2011) Computing hydrostatic potential vorticity in terrain-following coordinates. *Monthly Weather Review*, 139, 2955–2961.
30. Carlson, T. N. (1980) Airflow through midlatitude cyclones and the comma cloud pattern. *Monthly Weather Review*, 108, 1498–1509.
31. Carrió, D.S., Homar, V., Jansa, A., Romero, R., Picornell, M.A. (2017) Tropicalization process of the 7 November 2014 Mediterranean cyclone: Numerical sensitivity study. *Atmospheric Research* 197, 300–312. <https://doi.org/10.1016/j.atmosres.2017.07.018>
32. Cavicchia, L., von Storch, H., and Gualdi, S. (2014a) A long-term climatology of medicanes. *Climate Dynamics* 43, 1183–1195. <https://doi.org/10.1007/s00382-013-1893-7>
33. Cavicchia, L., von Storch, H. and Gualdi, S. (2014b) Mediterranean tropical-like cyclones in present and future climate. *Journal of Climate*, 27(19), 7493–7501.
34. Cavicchia, L., and von Storch, H. (2012) Simulation of medicanes in a high resolution regional climate model. *Climate Dynamics* 39, 2273–2290. <https://doi.org/10.1007/s00382-011-1220-0>
35. Chaboureaud, J.P., Pantillon, F., Lambert, D., Richard, E. and Claud, C. (2012) Tropical transition of a Mediterranean storm by jet crossing. *Quarterly Journal of the Royal Meteorological Society*, 138, 596–611. <https://doi.org/10.1002/qj.960>
36. Chagnon, J. M., and Gray, S.L. (2015) A Diabatically Generated Potential Vorticity Structure near the Extratropical Tropopause in Three Simulated Extratropical Cyclones. *Monthly Weather Review*, 143, 2337–2347. <https://doi.org/10.1175/MWR-D-14-00092.1>
37. Chagnon, J.M., Gray, S.L. and Methven, J. (2013) Diabatic processes modifying potential vorticity in a North Atlantic cyclone. *Quarterly Journal of the Royal Meteorological Society*, 139, 1270–1282. [doi:10.1002/qj.2037](https://doi.org/10.1002/qj.2037)
38. Chan, J.C.L. (2005) The physics of tropical cyclone motion. *Annual Review of Fluid Mechanics*, 37(1), 99–128.
39. Chan, J.C.L. (2002) Ensemble forecasting of tropical cyclones. *WMO Bulletin*, 51, 247–252.
40. Chen, S., and Houze, R.A. Jr. (1997) Diurnal variation and life-cycle of deep convective systems over the tropical Pacific warm pool. *Quarterly Journal of the Royal Meteorological Society*, 123, 357–388. <https://doi.org/10.1002/qj.49712353806>
41. Chung, E.S., Sohn, B.J., and Schmetz, J. (2008) CloudSat shedding new light on high-reaching tropical deep convection observed with Meteosat, *Geophysical Research Letters*, 35, L02814, <https://doi.org/10.1029/2007GL032516>

42. Cioni, G., Malguzzi, P., and Buzzi, A. (2016) Thermal structure and dynamical precursor of a Mediterranean tropical-like cyclone. *Quarterly Journal of the Royal Meteorological Society* 142, 1757–1766. <https://doi.org/10.1002/qj.2773>
43. Cioni, G., Cerrai, D. and Klocke, D. (2018) Investigating the predictability of a Mediterranean tropical-like cyclone using a storm-resolving model. *Quarterly Journal of the Royal Meteorological Society*, 144, 1598–1610. <https://doi.org/10.1002/qj.3322>
44. Claud, C., Alhammoud, B., Funatsu, B.M., Chaboureau, J.P. (2010) Mediterranean hurricanes: largescale environment and convective and precipitating areas from satellite microwave observations. *Natural Hazards and Earth System Sciences* 10, 2199–2213. <https://doi.org/10.5194/nhess-10-2199-2010>
45. Cohen, N.Y., and Boos, W.R. (2016) Perspectives on Moist Baroclinic Instability: Implications for the Growth of Monsoon Depressions. *Journal of the Atmospheric Sciences*, 73, 1767–1788. <https://doi.org/10.1175/JAS-D-15-0254.1>
46. Dacre, H.F., and Gray, S.L. (2009) The Spatial Distribution and Evolution Characteristics of North Atlantic Cyclones. *Monthly Weather Review*, 137, 99–115. <https://doi.org/10.1175/2008MWR2491.1>
47. Dafis, S., Rysman, J.F., Claud, C., and Flaounas, E. (2018) Remote sensing of deep convection within a tropical-like cyclone over the Mediterranean Sea. *Atmospheric Science Letters*, 19. <https://doi.org/10.1002/asl.823>
48. Davis, C., and Bosart, L.F. (2004) The TT Problem. *Bulletin of American Meteorological Society* 85, 1657–1666. <https://doi.org/10.1175/BAMS-85-11-1657>
49. Davis, C.A., and Bosart, L.F. (2003) Baroclinically induced tropical cyclogenesis. *Monthly Weather Review* 131, 2730–2747. [https://doi.org/10.1175/1520-0493\(2003\)131<2730:BITC>2.0.CO;2](https://doi.org/10.1175/1520-0493(2003)131<2730:BITC>2.0.CO;2)
50. Delanoë, J., Protat, A., Jourdan, O., Pelon, J., Papazzoni, M., Dupuy, R., Gayet, J.-F., Jouan, C. (2013) Comparison of airborne in situ, airborne radar–lidar, and spaceborne radar–lidar retrievals of polar ice cloud properties sampled during the POLARCAT campaign. *Journal of Atmospheric and Oceanic Technology*, 30, 57–73, doi: 10.1175/JTECH-D-11-00200.1
51. Dee, D.P., Uppala, S.M., Simmons, A.J., Berrisford, P., and co-authors (2011) The ERA-Interim reanalysis: Configuration and performance of the data assimilation system. *Quarterly Journal of the Royal Meteorological Society*, 137, 553–597.
52. De Vries, Methven, H., Frame, J.,-T.H.A., and Hoskins, B.J. (2010) Baroclinic Waves with Parameterized Effects of Moisture Interpreted Using Rossby Wave Components. *Journal of the Atmospheric Sciences*, 67, 2766–2784. <https://doi.org/10.1175/2010JAS3410.1>
53. Ditchek, S.D., Molinari, J., Corbosiero, K.L., and Fovell, R.G. (2019) An Objective Climatology of Tropical Cyclone Diurnal Pulses in the Atlantic Basin. *Monthly Weather Review*, 147, 591–605. <https://doi.org/10.1175/MWR-D-18-0368.1>
54. Duffourg, F., Ducrocq, V., Fourrié N., Jaubert, G., and Guidard, V. (2010) Convective scale data assimilation of satellite infrared radiances over the Mediterranean : sensitivity to the observation operator. *Journal of Geophysical Research*, 115, D15107, 14 pp.. doi:10.1029/2009JD012936

55. Ducrocq, V., and co-authors (2014) HyMeX-SOP1: The field campaign dedicated to heavy precipitation and flash flooding in the northwestern Mediterranean. *Bulletin of the American Meteorological Society*, 95, 1083–1100.
56. Dowdy, A.J., Pepler, A., Di Luca, A., Cavicchia, L., Mills, G., Evans, J.P., Louis, S., McInnes, K.L., and Walsh, K. (2019) Review of Australian east coast low pressure systems and associated extremes. *Climate Dynamics* 53, 4887–4910. <https://doi.org/10.1007/s00382-019-04836-8>
57. Dudhia, J. (2012) “Overview of WRF Physics.” WRF Users’ Tutorial 2012, http://www2.mmm.ucar.edu/wrf/users/tutorial/201301/dudhia_physics.pdf
58. Dvorak, V. (1975) A technique for the analysis and forecasting of tropical cyclone intensities from satellite pictures. *Monthly Weather Review*, 103, 420–430, [https://doi.org/10.1175/1520-0493\(1975\)103<0420:TCIAAF>2.0.CO;2](https://doi.org/10.1175/1520-0493(1975)103<0420:TCIAAF>2.0.CO;2)
59. Eliassen, A. (1951) Slow thermally or frictionally controlled meridional circulation in isentropic coordinates. Ph.D. thesis, University of Wisconsin, Madison, 294 pp.
60. Emanuel, K.A. (2005) Genesis and maintenance of “Mediterranean hurricanes”. *Advances in Geosciences* 2, 217–220. <https://doi.org/10.5194/adgeo-2-217-2005>
61. Emanuel, K.A., and Rotunno, R. (1989) Polar lows as arctic hurricanes. *Tellus Series A: Dynamic Meteorology And Oceanography*, 41, 1-17. doi:10.1111/j.1600-0870.1989.tb00362.x
62. Emanuel, K.A. (1986) An Air-Sea Interaction Theory for Tropical Cyclones. Part I: Steady-State Maintenance. *Journal of the Atmospheric Sciences*, 43, 585–605. [https://doi.org/10.1175/1520-0469\(1986\)043<0585:AASITF>2.0.CO;2](https://doi.org/10.1175/1520-0469(1986)043<0585:AASITF>2.0.CO;2)
63. Ernst, J.A., Matson, M. (1983) A Mediterranean tropical storm. *Weather* 38, 332–337. <https://doi.org/10.1002/j.1477-8696.1983.tb04818.x>
64. Ertel, H. (1942) Ein neuer hydrodynamischer Wirbelsatz. *Meteorologische Zeitschrift*, 9, 271–281.
65. Evans, J.L. and Braun, A. (2012) A Climatology of Subtropical Cyclones in the South Atlantic. *Journal of Climate*, 25, 7328–7340. <https://doi.org/10.1175/JCLI-D-11-00212.1>
66. Evans, J. L., and Guishard, M.P. (2009) Atlantic subtropical storms. Part I: Diagnostic criteria and composite analysis. *Monthly Weather Review* 137, 2065–2080. <https://doi.org/10.1175/2009MWR2468.1>
67. Ferraro, R.R., Weng, F., Grody, N.C., Zhao, L. (2000) Precipitation characteristics over land from the NOAA-15 AMSU sensor. *Geophysical Research Letters*, 27(17), 2669–2672.
68. Flaounas, E., Gray, S.L., and Teubler, F. (2020) A process-based anatomy of Mediterranean cyclones: From baroclinic lows to tropical-like systems. *Weather and Climate Dynamics Discussion*, <https://doi.org/10.5194/wcd-2020-48>, in review.
69. Flaounas, E., Lagouvardos, K., Kotroni, V., Claud, C., Delanoë, J., Flamant, C., Madonna, E. and Wernli, H. (2016) Processes leading to heavy precipitation associated with two Mediterranean cyclones observed during the HyMeX SOP1. *Quarterly Journal of the Royal Meteorological Society*, 142, 275-286. doi:10.1002/qj.2618
70. Flaounas, E., Raveh-Rubin, S., Wernli, H., Drobinski, P., Bastin, S. (2015) The dynamical structure of intense Mediterranean cyclones. *Climate Dynamics* 44, 2411-2427. <https://doi.org/10.1007/s00382-014-2330-2>

71. Fink, A. H., Pohle, S., Pinto, J. G., and Knippertz, P. (2012) Diagnosing the influence of diabatic processes on the explosive deepening of extratropical cyclones, *Geophysical Research Letters*, 39, L07803. doi:10.1029/2012GL051025
72. Fita, L., and Flaounas, E. (2018) Medicanes as subtropical cyclones: the December 2005 case from the perspective of surface pressure tendency diagnostics and atmospheric water budget *Quarterly Journal of the Royal Meteorological Society* 144, 1028–1044. <https://doi.org/10.1002/qj.3273>
73. Fita, L., Romero, R., and Ramis, C. (2006) Intercomparison of intense cyclogenesis events over the Mediterranean basin based on baroclinic and diabatic influences. *Advances in Geosciences (Proceedings PLINIUS 2006)*, 7, 333–342.
74. Fritz, C., Wang, Z., Nesbitt, S. W., and Dunkerton, T. J. (2016) Vertical structure and contribution of different types of precipitation during Atlantic tropical cyclone formation as revealed by TRMM PR, *Geophysical Research Letters*, 43, 894–901, doi:10.1002/2015GL067122
75. Fritsch, J.M., and Chappell, C.F. (1980) Numerical prediction of convectively driven mesoscale pressure systems. Part I: convective parameterization. *Journal of the Atmospheric Sciences*, 37, 1722-1732.
76. Funatsu, B.M., Rysman, J.F., Claud, C., and Chaboureau, J.-P. (2018) Deep convective clouds distribution over the Mediterranean region from AMSU-B/MHS observations. *Atmospheric Research*, 207, 122–135. <https://doi.org/10.1016/j.atmosres.2018.03.003>
77. Funatsu, B. M., Claud, C., and Chaboureau, J.-P. (2007) Potential of Advanced Microwave Sounding Unit to identify precipitating systems and associated upper-level features in the Mediterranean region: Case studies. *Journal of Geophysical Research* 112, D17113. <https://doi.org/10.1029/2006JD008297>
78. Gaertner, M.Á., González-Alemán, J.J., Romera, R. and co-authors (2018) Simulation of medicanes over the Mediterranean Sea in a regional climate model ensemble: impact of ocean–atmosphere coupling and increased resolution. *Climate Dynamics*, 51, 1041–1057. <https://doi.org/10.1007/s00382-016-3456-1>
79. Galanaki, E., Flaounas, E., Kotroni, V., Lagouvardos, K., Argiriou, A. (2016) Lightning activity in the Mediterranean: quantification of cyclones contribution and relation to their intensity. *Atmospheric Science Letters* 17, 510–516. <https://doi.org/10.1002/asl.685>
80. Gelaro, R., and co-authors (2017) The Modern-Era Retrospective Analysis for Research and Applications, Version 2 (MERRA-2). *Journal of Climate*, 30, 5419–5454, <https://doi.org/10.1175/JCLI-D-16-0758.1>
81. Gloersen, P., Barath, F.T. (1977) A scanning multichannel microwave radiometer for nimbus-g and seasat-a. *Journal of Oceanic Engineering*, IEEE 2(2):172-178
82. Gochis D.J., Shuttleworth, W.J., and Yang, Z.L. (2002) Sensitivity of the modeled North American monsoon regional climate to convective parameterization. *Monthly Weather Review*, 130, 1282-1298.
83. Godson, W.L. (1948) A new tendency equation and its application to the analysis of surface pressure changes. *Journal of Meteorology*, 5, 227-235.
84. Godske, C.L., Bergeron, T., Bjerknes, J., and Bundgaard, R.C. (1957) Dynamic meteorology and weather forecasting. *American Meteorological Society*, Boston.
85. González-Alemán, J. J., Pascale, S., Gutierrez-Fernandez, J., Murakami, H., Gaertner, M. A., and Vecchi, G.A. (2019) Potential increase in hazard from Mediterranean hurricane activity with global warming. *Geophysical Research Letters* 46, 1754–1764. <https://doi.org/10.1029/2018GL081253>

86. González-Alemán, J.J., Valero, F., Martín-León, F., and Evans, J.L. (2015) Classification and Synoptic Analysis of Subtropical Cyclones within the Northeastern Atlantic Ocean. *Journal of Climate* 28, 3331-3352. <https://doi.org/10.1175/JCLI-D-14-00276.1>
87. Gray, S.L. (2006) Mechanisms of midlatitude cross-tropopause transport using a potential vorticity budget approach. *Journal of Geophysical Research*, 111, D17113, doi: 10.1029/2005JD006259
88. Grell, G.A., Dudhia, J., Stauffer, D.R.A (1994) A description of the fifth generation Penn State/NCAR Mesoscale Model (MM5) NCAR Tech. Note NCAR/TN-3801STR, 138 pp.
89. Grell, G.A. (1993) Prognostic evaluation of assumptions used by cumulus parameterizations. *Monthly Weather Review*, 121, 764-787.
90. Grønås, S. (1995) The seclusion intensification of the New Year's day storm 1992. *Tellus A*, 47: 733-746. doi:10.1034/j.1600-0870.1995.00116.x
91. Grønås, S. and Kvamstø, N.G. (1995) Numerical simulations of the synoptic conditions and development of Arctic outbreak polar lows. *Tellus A*, 47, 797-814. doi:10.1034/j.1600-0870.1995.00121.x
92. Harold, J.M., Bigg, G.R., and Turner, J. (1999) Mesocyclone activity over the North-East Atlantic. Part 1: vortex distribution and variability. *International Journal of Climatology*, 19, 1187-1204. [https://doi.org/10.1002/\(SICI\)1097-0088\(199909\)19:11<1187::AID-JOC419>3.0.CO;2-Q](https://doi.org/10.1002/(SICI)1097-0088(199909)19:11<1187::AID-JOC419>3.0.CO;2-Q)
93. Hart, R.E. (2003) A Cyclone Phase Space Derived from Thermal Wind and Thermal Asymmetry. *Monthly Weather Review*, 131, 585–616.
94. Hausman, S.A., Ooyama, K.V., and Schubert, W.H. (2006) Potential vorticity structure of simulated hurricanes. *Journal of the Atmospheric Sciences*, 63, 87–108. doi:10.1175/JAS3601.1
95. Hendricks, E.A., Montgomery, M.T., and Davis, C.A. (2004) The Role of “Vortical” Hot Towers in the Formation of Tropical Cyclone Diana (1984). *Journal of the Atmospheric Sciences*, 61, 1209–1232. [https://doi.org/10.1175/1520-0469\(2004\)061<1209:TROVHT>2.0.CO;2](https://doi.org/10.1175/1520-0469(2004)061<1209:TROVHT>2.0.CO;2)
96. Hersbach, H., Bell, B., Berrisford, P., and co-authors (2020) The ERA5 global reanalysis. *Quarterly Journal of the Royal Meteorological Society*, 146, 1999–2049. <https://doi.org/10.1002/qj.3803>
97. Holzer, A., and Groenenemeijer, P. (2014) Satellite Based Climatology of (Sub-) Tropical Cyclones in Europe. *14th European Meteorological Society Annual Meeting*, Prague. <https://meetingorganizer.copernicus.org/EMS2014/EMS2014-73.pdf>
98. Homar, V., Romero, R., Stensrud, D.J., Ramis, C., and Alonso, S. (2003) Numerical diagnosis of a small, quasi-tropical cyclone over the western Mediterranean: dynamical vs boundary factors. *Quarterly Journal of the Royal Meteorological Society*, 129, 1469-1490.
99. Hong, S.-Y., Y. Noh, and J. Dudhia, (2006b) A new vertical diffusion package with an explicit treatment of entrainment processes. *Monthly Weather Review*, 134, 2318-2341.
100. Hong, G., Heygster, G., and Rodriguez, C.A.M. (2006a) Effect of cirrus clouds on the diurnal cycle of tropical deep convective clouds. *Journal of Geophysical Research*, 111, D06209, <https://doi.org/10.1029/2005JD006208>
101. Hong, G., Heygster, G., Miao J., and Kunzi, K. (2005) Detection of tropical deep convective clouds from AMSU-B water vapor channels measurements. *Journal of Geophysical Research*, 110, D05205. <https://doi.org/10.1029/2004JD004949>

102. Hoskins, B.J., McIntyre, M., and Robertson, A.W. (1985) On the use and significance of isentropic potential vorticity maps. *Quarterly Journal of the Royal Meteorological Society*, 111, 877–946. <https://doi.org/10.1002/qj.49711147002>
103. Houze, R.A. (2014) *Cloud Dynamics*, 104, 1-432. ISBN: 9780123742667
104. Houze, R.A. (1997) Stratiform precipitation in regions of convection: A meteorological paradox? *Bulletin of the American Meteorological Society*, 78, 2179–2196.
105. Houze, R.A., Jr. (1989) Observed structure of mesoscale convective systems and implications for large-scale heating. *Quarterly Journal of the Royal Meteorological Society*, 115, 425-461. doi:10.1002/qj.49711548702
106. Hu, X.M., Nielsen-Gammon, J.W., and Zhang, F. (2010) Evaluation of three planetary boundary layer schemes in the WRF model, *Journal of Applied Meteorology and Climatology*, 49, 1831–1844, doi:10.1175/2010JAMC2432.1, 2010
107. Hurley, J.V. and Boos, W.R. (2015) A global climatology of monsoon low-pressure systems. *Quarterly Journal of the Royal Meteorological Society*, 141, 1049-1064. doi:10.1002/qj.2447
108. Jacob, D., Petersen, J., Eggert, B., and co-authors (2014) EURO-CORDEX: new high-resolution climate change projections for European impact research. *Regional Environmental Change*, 14:, 563–578.
109. Jacob, D.J. (1999) *Introduction to Atmospheric Chemistry*. Princeton University Press, 280 pp.
110. Janjic, Z.I. (1994) The step-mountain ETA coordinate model: further developments of the convection, viscous sublayer, and turbulence closure schemes. *Monthly Weather Review*, 122, 927-945.
111. Jiménez, P.A., and Dudhia J. (2013) On the Ability of the WRF Model to Reproduce the Surface Wind Direction over Complex Terrain. *Journal of Applied Meteorology and Climatology*, 52, 1610–1617. <https://doi.org/10.1175/JAMC-D-12-0266.1>
112. Jiménez, P., Dudhia, J., Gonzalez-Ruoco, J.F., Navarro, J., Montavez, J.P., and Garcia-Bustamente, E. (2012) A revised scheme for the WRF surface layer formulation. *Monthly Weather Review*, 140, 898-918.
113. Kain, J.S. (2004) The Kain–Fritsch convective parameterization: an update. *Journal of Applied Meteorology*, 43, 170-181.
114. Kain, J.S., and Fritsch, M.A (1990) The one-dimensional entraining/detraining plume model and its application in convective parameterization. *Journal of the Atmospheric Sciences*, 47, 2784-2802.
115. Kalimeris, A., Kolios, S., Halvatzaras, D., Posa, D., Delaco, S., Palma, M., Skordilis, C., and Myrsilides, M. (2016) The Ionian-Puglia network of meteorological-environmental stations. *Geophysical environment and technical description. Odysseus 7*, 1–45.
116. Kalnay, and co-authors (1996) The NCEP/NCAR 40-year reanalysis project, *Bulletin of American Meteorological Society*, 77, 437-470.
117. Karbou, F., Aires, F., Prigent, C., Eymard, L. (2005) Potential of advanced microwave sounding unit-A (AMSU-A) and AMSU-B measurements for atmospheric temperature and humidity profiling over land. *Journal of Geophysical Research: Atmospheres* (1984–2012) 110(D7). doi:10.1029/2004JD005318
118. Kepert, J.D. (2010) Slab- and height-resolving models of the tropical cyclone boundary layer. Part I: Comparing the simulations. *Quarterly Journal of the Royal Meteorological Society*, 136, 1686-1699. doi:10.1002/qj.667

119. Kidd, C., Matsui, T., Chern, J., Mohr, K., Kummerow, C., Randel, D. (2016) Global precipitation estimates from cross-track passive microwave observations using a physically based retrieval scheme. *Journal of Hydrometeorology*, 17(1), 383-400.
120. Knippertz, P., Fink, A.H., and Pohle, S. (2009) Reply. *Monthly Weather Review*, 137, 3151–3157.
121. Knippertz, P., and Fink, A.H. (2008) Dry-season precipitation in tropical West Africa and its relation to forcing from the extratropics, *Monthly Weather Review*, 136, 3579–3596. doi:10.1175/2008MWR2295.1
122. Kuo, Y., Shapiro, M.A., and Donall, E.G. (1991) The Interaction between Baroclinic and Diabatic Processes in a Numerical Simulation of a Rapidly Intensifying Extratropical Marine Cyclone. *Monthly Weather Review* 119, 368–384. [https://doi.org/10.1175/1520-0493\(1991\)119<0368:TIBBAD>2.0.CO;2](https://doi.org/10.1175/1520-0493(1991)119<0368:TIBBAD>2.0.CO;2)
123. Kuo, H.L. (1974) Further studies of the parameterization of the influence cumulus convection on large scale flow. *Journal of the Atmospheric Sciences*, 31, 1232-1240.
124. Lagouvardos, K., Kotroni, V., Bezes, A., Koletsis, I., Kopania, T., Lykoudis, S., Mazarakis, N., Papagiannaki, K., and Vougioukas, S. (2017) The automatic weather stations NOANN network of the National Observatory of Athens: operation and database. *Geoscience Data Journal* 4, 4-16. <https://doi.org/10.1002/gdj3.44>
125. Lagouvardos, K., Kotroni, V., and Defer, E. (2007) The 21–22 January 2004 explosive cyclogenesis over the Aegean Sea: observations and model analysis. *Quarterly Journal of the Royal Meteorological Society*, 133, 1519-1531.
126. Lagouvardos, K., Kotroni, V., Nickovic, S., Jovic, and D., Kallos, G. (1999) Observations and model simulations of a winter sub-synoptic vortex over the central Mediterranean. *Meteorological Applications* 6, 371–383. <https://doi.org/10.1017/S1350482799001309>
127. Lamarque, J.-F., and Hess, P. (1994) Cross-tropopause mass exchange and potential vorticity budget in a simulated tropopause folding. *Journal Of The Atmospheric Sciences*, 51, 2246-2269. doi:10.1175/1520-0469(1994)051<2246:CTMEAP>2.0.CO;2
128. Lavanant, L., Fourrié, N., Gambacorta, A., Grieco, G., Heilliette, S., Hilton, F., Kim, M.-J., McNally, A.P., Nishihata, H., Pavelin, E.G., and Rabier, F. (2011) Comparison of cloud products within IASI footprints for the assimilation of cloudy radiances. *Quarterly Journal of the Royal Meteorological Society*, 137,1988-2003. DOI:10.1002/qj.917
129. Laviola, S., and Levizzani, V. (2011) The 183-WSL fast rain rate retrieval algorithm: Part I: Retrieval design. *Atmospheric Research*, 99, 443-461. <https://doi.org/10.1016/j.atmosres.2010.11.013>
130. Lim, E., and Simmonds, I. (2009) Effect of tropospheric temperature change on the zonal mean circulation and SH winter extratropical cyclones. *Climate Dynamics*, 33, 19–32. <https://doi.org/10.1007/s00382-008-0444-0>
131. Lynch, P. (2008) The origins of computer weather prediction and climate modeling. *Journal of Computational Physics*, 227(7), 3431-3444. <https://doi.org/10.1016/j.jcp.2007.02.034>
132. Machado, L.A.T., Laurent, H., and Lima, A.A. (2002) Diurnal march of the convection observed during TRMM-WETAMC/LBA. *Journal of Geophysical Research* 107, 8064. <https://doi.org/10.1029/2001JD000338>

133. McIntyre, M. E. (1993) Isentropic distributions of potential vorticity and their relevance to tropical cyclone dynamics. *Tropical Cyclone Disasters*, J. Lighthill, G. Holland, Z. Zhemina, and K. Emanuel, Eds., Peking University Press, 143–156.
134. Mahoney, K.M., and Lackmann, G.M. (2006) The Sensitivity of Numerical Forecasts to Convective Parameterization: A Case Study of the 17 February 2004 East Coast Cyclone. *Weather and Forecasting*, 21, 465–488. <https://doi.org/10.1175/WAF937.1>
135. Manikin, G.S. (2004) The impact of choice of convective scheme on synoptic features in the NCEP ETA model. Preprints, *20th Conf. on Weather Analysis and Forecasting*, Seattle, Washington, American Meteorological Society, Paper 4.3.
136. Mansell, E.R. (2010) On Sedimentation and Advection in Multimoment Bulk Microphysics. *Journal of the Atmospheric Sciences*, 67, 3084–3094. <https://doi.org/10.1175/2010JAS3341.1>
137. Markowski, P.M., and Richardson, Y.P. (2010) *Mesoscale Meteorology in Midlatitudes*. Wiley Blackwell, 424 pp.
138. Marra, A.C., Federico, S., Montopoli, M., Avolio, E., Baldini, L., Casella, D., D’Adderio, L.P., Dietrich, S., Sanò, P., Torcasio, R.C., and Panegrossi, G. (2019) The Precipitation Structure of the Mediterranean Tropical-Like Cyclone Numa: Analysis of GPM Observations and Numerical Weather Prediction Model Simulations. *Remote Sensing*, 11, 1690. <https://doi.org/10.3390/rs11141690>
139. Martinet, P., Fourrié N., Guidard, V., Rabier, F., Montmerle, T., and Brunel, P. (2013) Towards the use of microphysical variables for the assimilation of cloud-affected infrared radiances. *Quarterly Journal of the Royal Meteorological Society*, 139, 1402–1416. DOI:10.1002/qj.2046
140. Martínez-Alvarado, O., Gray, S.L., and Methven, J. (2016) Diabatic processes and the evolution of two contrasting summer extratropical cyclones. *Monthly Weather Review*, 144, 3251–3276. doi:<https://doi.org/10.1175/MWR-D-15-0395.1>
141. Mazarakis, N., Kotroni, V., Lagouvardos, K., Argiriou, A.A. (2009) The sensitivity of numerical forecasts to convective parameterization during the warm period and the use of lightning data as an indicator for convective occurrence, *Atmospheric Research*, 94(4), 704-714, <https://doi.org/10.1016/j.atmosres.2009.03.002>
142. Mazza, E., Ulbrich, U., and Klein, R. (2017) The Tropical Transition of the October 1996 Medicane in the Western Mediterranean Sea: A Warm Seclusion Event. *Monthly Weather Review* 145, 7, 2575-2595. <https://doi.org/10.1175/MWR-D-16-0474.1>
143. McTaggart-Cowan, R., Davies, E.L., Fairman, J.G., Galarneau, T.J., and Schultz, D.M. (2015) Revisiting the 26.5°C Sea Surface Temperature Threshold for Tropical Cyclone Development. *Bulletin of the American Meteorological Society*, 96, 1929–1943. <https://doi.org/10.1175/BAMS-D-13-00254.1>
144. McTaggart-Cowan, R., Galarneau, T.J., Bosart, L.F., and Milbrandt, J.A. (2010) Development and Tropical Transition of an Alpine Lee Cyclone. Part I: Case Analysis and Evaluation of Numerical Guidance. *Monthly Weather Review*, 138, 2281–2307. <https://doi.org/10.1175/2009MWR3147.1>
145. Miglietta, M.M., and Rotunno, R. (2019) Development mechanisms for Mediterranean tropical-like cyclones (medicanes). *Quarterly Journal of the Royal Meteorological Society*, 145, 1444–1460. <https://doi.org/10.1002/qj.3503>

146. Miglietta, M. M., Cerrai, D., Laviola, S., Cattani, E., and Levizzani, V. (2017) Potential vorticity patterns in Mediterranean “hurricanes”. *Geophysical Research Letters* 44, 2537-2545. <https://doi.org/10.1002/2017GL072670>
147. Miglietta, M.M., Laviola, S., Malvaldi, A., Conte, D., Levizzani, V., and Price, C. (2013) Analysis of tropical-like cyclones over the Mediterranean Sea through a combined modeling and satellite approach, *Geophysical Research Letters* 40, 10, 2400-2405. <https://doi.org/10.1002/grl.50432>
148. Miglietta, M.M., Moscatello, A., Conte, D., Mannarini, G., Lacorata, G., and Rotunno, R. (2011) Numerical analysis of a Mediterranean ‘hurricane’ over south-eastern Italy: sensitivity experiments to sea surface temperature. *Atmospheric Research*, 101, 412-426. <http://dx.doi.org/10.1016/j.atmosres.2011.04.006>
149. Möller, J.D., and Smith, R.K. (1994) The development of potential vorticity in a hurricane-like vortex. *Quarterly Journal of the Royal Meteorological Society*, 120, 1255-1265. doi:10.1002/qj.49712051907
150. Molinari, J., Skubis, S., Vollaro, D., Alsheimer, F., and Willoughby, H.E. (1998) Potential Vorticity Analysis of Tropical Cyclone Intensification. *Journal of the Atmospheric Sciences*, 55, 2632–2644. [https://doi.org/10.1175/1520-0469\(1998\)055<2632:PVAOTC>2.0.CO;2](https://doi.org/10.1175/1520-0469(1998)055<2632:PVAOTC>2.0.CO;2)
151. Monin, A.S., and Obukhov, A.M. (1954). ‘Osnovnye zakonomernosti turbulentnogo peremeshivaniya v prizemnom sloe atmosfery (Basic Laws of Turbulent Mixing in the Atmosphere Near the Ground)’. *Trudy geofiz. inst. AN SSSR* 24(151): 163–187.
152. Montgomery, M.T., and Farrell, B.F. (1992) Polar Low Dynamics. *Journal of the Atmospheric Sciences* 49, 2484–2505. [https://doi.org/10.1175/1520-0469\(1992\)049<2484:PLD>2.0.CO;2](https://doi.org/10.1175/1520-0469(1992)049<2484:PLD>2.0.CO;2)
153. Moore, R.W., Montgomery, M.T., and Davies, H.C. (2008) The integral role of a diabatic Rossby vortex in a heavy snowfall event. *Monthly Weather Review*, 136, 1878–1897.
154. Moore, R. W., and Montgomery, M.T. (2004) Reexamining the Dynamics of Short-Scale, Diabatic Rossby Waves and Their Role in Midlatitude Moist Cyclogenesis. *Journal of the Atmospheric Sciences*, 61, 754–768. [https://doi.org/10.1175/1520-0469\(2004\)061<0754:RTDOSD>2.0.CO;2](https://doi.org/10.1175/1520-0469(2004)061<0754:RTDOSD>2.0.CO;2)
155. Moscatello, A., Miglietta, M.M., and Rotunno, R. (2008b) Numerical analysis of a Mediterranean “Hurricane” over South-eastern Italy. *Monthly Weather Review*, 136, 4373–4397. <https://doi.org/10.1175/2008MWR2512.1>
156. Moscatello, A., Miglietta, M.M., and Rotunno, R. (2008a) Observational analysis of a Mediterranean ‘Hurricane’ over South-eastern Italy. *Weather* 63, 306-311. <https://doi.org/10.1002/wea.231>
157. Muller, J.C., and Romps, D.M. (2018) Acceleration of tropical cyclogenesis by self-aggregation feedbacks. *Proceedings of the National Academy of Sciences*, 115 (12) 2930-2935; DOI: 10.1073/pnas.1719967115
158. Mugnai, A., Cooper, H.J., Smith, E.A., Tripoli, G.J. (1990) Simulation of microwave brightness temperatures of an evolving hailstorm at SSM/I frequencies. *Bulletin of the American Meteorological Society*, 71(1),2–13.
159. Mugnai, A., and Smith, E.A. (1988) Radiative transfer to space through a precipitating cloud at multiple microwave frequencies. Part I: model description. *Journal of Applied Meteorology* 27(9),1055–1073.

160. Murthy, V.S., Boos, W.R. (2019) Understanding the vertical structure of potential vorticity in tropical depressions. *Quarterly Journal of the Royal Meteorological Society*, 145, 1968–1991. <https://doi.org/10.1002/qj.3539>
161. Nastos, P.T., Karavana Papadimou, K., Matsangouras, I.T. (2018) Mediterranean tropical-like cyclones: Impacts and composite daily means and anomalies of synoptic patterns. *Atmospheric Research*, 208, 156-166. <https://doi.org/10.1016/j.atmosres.2017.10.023>
162. National Centers for Environmental Prediction/National Weather Service/NOAA/U.S. Department of Commerce (2004): NCEP ADP Global Surface Observational Weather Data, October 1999 - continuing. Research Data Archive at the National Center for Atmospheric Research, Computational and Information Systems Laboratory. <https://doi.org/10.5065/4F4P-E398>. Accessed† 20 Nov 2019.
163. Noyelle, R., Ulbrich, U., Becker, N., and Meredith, E. P. (2019) Assessing the impact of sea surface temperatures on a simulated medicane using ensemble simulations. *Natural Hazards and Earth System Sciences*, 19, 941-955. <https://doi.org/10.5194/nhess-19-941-2019>
164. Oertel, A., Boettcher, M., Joos, H., Sprenger, M., and Wernli, H. (2020) Potential vorticity structure of embedded convection in a warm conveyor belt and its relevance for large-scale dynamics. *Weather Climate and Dynamics*, 1, 127–153. <https://doi.org/10.5194/wcd-1-127-2020>
165. Olander, T.L., and Velden, C. (2009) Tropical Cyclone Convection and Intensity Analysis Using Differenced Infrared and Water Vapor Imagery. *Weather and Forecasting* 24, 1558–1572. <https://doi.org/10.1175/2009WAF2222284.1>
166. Onogi, K., and co-authors (2007) The JRA-25 reanalysis. *Journal of the Meteorological Society of Japan*. 85, 369–432. doi: 10.2151/jmsj.85.369
167. Panegrossi, G., Dietrich, S., Marzano, F.S., Mugnai, A., Smith, E.A., Xiang, X., Tripoli, G.J., Wang, P.K., and Poiaras Baptista, J.P.V. (1998) Use of cloud model microphysics for passive microwave-based precipitation retrieval: significance of consistency between model and measurement manifolds. *Journal of the Atmospheric Sciences*, 55, 1644–1673.
168. Park, S.-H., Skamarock, W., Klemp, J., Fowler, L., and Duda, M. (2013) Evaluation of global atmospheric solvers using extensions of the Jablonowski and Williamson baroclinic wave test case. *Monthly Weather Review*, 141, 3116-3129.
169. Parker, D. J., and Thorpe, A. J. (1995) Conditional Convective Heating in a Baroclinic Atmosphere: A Model of Convective Frontogenesis. *Journal of the Atmospheric Sciences*, 52, 1699–1711. [https://doi.org/10.1175/1520-0469\(1995\)052<1699:CCHIAB>2.0.CO;2](https://doi.org/10.1175/1520-0469(1995)052<1699:CCHIAB>2.0.CO;2)
170. Petty, G.W. (1995) The status of satellite-based rainfall estimation over land. *Remote Sensing of the Environment*, 51(1),125–137.
171. Pinto, J.G., Zacharias, S., Fink, A.H., Leckebusch, G.C., Ulbrich, U. (2009) Factors contributing to the development of extreme North Atlantic cyclones and their relationship with the NAO. *Climate Dynamics*, 32, 711–737. <https://doi.org/10.1007/s00382-008-0396-4>
172. Pohle, S. (2010), Synoptische und dynamische Aspekte tropisch-extratropischer Wechselwirkungen: Drei Fallstudien von Hitzetiefentwicklungen über Westafrika während des AMMA-Experiment 2006 (In

- German). Ph.D. thesis at the University of Cologne, Germany, online available at <https://core.ac.uk/download/pdf/12010683.pdf>
173. Posselt, D.J., and Martin, J.E. (2004) The Effect of Latent Heat Release on the Evolution of a Warm Occluded Thermal Structure. *Monthly Weather Review*, 132, 578–599. [https://doi.org/10.1175/1520-0493\(2004\)132<0578:TEOLHR>2.0.CO;2](https://doi.org/10.1175/1520-0493(2004)132<0578:TEOLHR>2.0.CO;2)
174. Prezerakos, N., Flocas, H. and Brikas, D. (2006) The role of the interaction between polar and subtropical jet in a case of depression rejuvenation over the Eastern Mediterranean. *Meteorology and Atmospheric Physics*, 92, 139–151. <https://doi.org/10.1007/s00703-005-0142-y>
175. Pytharoulis, I. (2018) Analysis of a Mediterranean tropical-like cyclone and its sensitivity to the sea surface temperatures. *Atmospheric Research* 208, 167-179. <https://doi.org/10.1016/j.atmosres.2017.08.009>
176. Pytharoulis, I., Craig, G.C., and Ballard, S.P. (2000) The hurricane-like Mediterranean cyclone of January 1995. *Meteorological Applications* 7, 261-279. [https://doi.org/10.1016/S1464-1909\(99\)00056-8](https://doi.org/10.1016/S1464-1909(99)00056-8)
177. Ragone, F., Mariotti, M., Parodi, A., von Hardenberg, J., and Pasquero, C. (2018) A climatological study of western Mediterranean medicanes in numerical simulations with explicit and parameterized convection. *Atmosphere*, 9(10), 397.
178. Rasmussen, E., Zick, C. (1987) A subsynoptic vortex over the Mediterranean with some resemblance to polar lows. *Tellus A* 39, 408–425. <https://doi.org/10.3402/tellusa.v39i4.11770>
179. Raymond, D.J. (2012) Balanced thermal structure of an intensifying tropical cyclone. *Tellus*, 64, 19181. doi.org/10.3402/tellusa.v64i0.19181
180. Raymond, D. J., and H.Jiang, 1990: A theory for long-lived mesoscale convective systems. *Journal of the Atmospheric Sciences*, 47, 3067–3077.
181. Reasor, P.D., Montgomery, M.T., and Grasso, L.D. (2004) A new look at the problem of tropical cyclones in vertical shear flow: Vortex resiliency. *Journal of the Atmospheric Sciences*, 61, 3–22. [https://doi.org/10.1175/1520-0469\(2004\)061<0003:ANLATP>2.0.CO;2](https://doi.org/10.1175/1520-0469(2004)061<0003:ANLATP>2.0.CO;2)
182. Reed, R.J., Kuo, Y.-H., Albright, M.D., Gao, K., Guo, Y.-R., and Huang, W. (2001) Analysis and modeling of a tropical-like cyclone in the Mediterranean Sea *Meteorology and Atmospheric Physics*, 76, 183-202.
183. Reed, R. J. (1955) A study of a characteristic type of upper-level frontogenesis, *Journal of Meteorology*, 12, 226–237.
184. Ritchie, E.A., and Holland, G.J. (1997) Scale Interactions during the Formation of Typhoon Irving. *Monthly Weather Review*, 125, 1377–1396. [https://doi.org/10.1175/1520-0493\(1997\)125<1377:SIDTFO>2.0.CO;2](https://doi.org/10.1175/1520-0493(1997)125<1377:SIDTFO>2.0.CO;2)
185. Romera, R., Gaertner, M.Á., Sánchez, E., Domínguez, M., González-Alemán, J.J., and Miglietta, M.M. (2017) Climate change projections of medicanes with a large multi-model ensemble of regional climate models. *Global and Planetary Change*, 151, 134–143. <https://doi.org/10.1016/j.gloplacha.2016.10.008>

186. Romero, R., and Emanuel, K. (2017) Climate Change and Hurricane-Like Extratropical Cyclones: Projections for North Atlantic Polar Lows and Medicanes Based on CMIP5 Models. *Journal of Climate*, 30 (1), 279-299. <https://doi.org/10.1175/JCLI-D-16-0255.1>
187. Rossa, A.M., Wernli, H. and Davies, H.C. (2000) Growth and decay of an extra-tropical cyclone's PV-tower. *Meteorology and Atmospheric Physics*, 73, 139–156. doi:<https://doi.org/10.1007/s007030050070>
188. Rossby, C-G. (1940) Planetary flow patterns in the atmosphere. *Quarterly Journal of the Royal Meteorological Society*, 66, 68-87.
189. Ruti, P.M., Somot, S., Giorgi, F., and co-authors (2015) MED-CORDEX initiative for Mediterranean climate studies. *Bulletin of American Meteorological Society*, 97,1187–1208.
190. Rysman, J.F., Claud, C., and Dafis, S. (2021) Global monitoring of deep convection using passive microwave observations, *Atmospheric Research*, 247, 105244, <https://doi.org/10.1016/j.atmosres.2020.105244>
191. Rysman, J.-F., Panegrossi, G., Sanò, P., Marra, A., Dietrich, S., Milani, L., and Kulie, M. (2018) SLALOM: An all-surface snow water path retrieval algorithm for the GPM Microwave Imager. *Remote Sensing*, 10(8), 1278. <https://doi.org/10.3390/rs10081278>
192. Rysman, J.F., Claud, C., and Delanoë, J. (2017) Monitoring Deep Convection and Convective Overshooting From 60° S to 60° N Using MHS: A Cloudsat/CALIPSO-Based Assessment. *IEEE Geoscience and Remote Sensing Letters* 14, 159–163. <https://doi.org/10.1109/LGRS.2016.2631725>
193. Rysman, J.F., Claud, C., Chaboureau, J.P., Delanoë, J., and Funatsu, B.M. (2016) Severe convection in the Mediterranean from microwave observations and a convection-permitting model. *Quarterly Journal of the Royal Meteorological Society* 142, 43–55. <https://doi.org/10.1002/qj.2611>
194. Saffin, L., Methven, J., and Gray, S.L. (2016) The non-conservation of potential vorticity by a dynamical core compared with the effects of parametrized physical processes. *Quarterly Journal of the Royal Meteorological Society*, 142, 1265-1275. doi:10.1002/qj.2729
195. Sanders, F., 1986: Explosive Cyclogenesis in the West-Central North Atlantic Ocean, 1981–84. Part I: Composite Structure and Mean Behavior. *Monthly Weather Review*, 114, 1781–1794, [https://doi.org/10.1175/1520-0493\(1986\)114<1781:ECITWC>2.0.CO;2](https://doi.org/10.1175/1520-0493(1986)114<1781:ECITWC>2.0.CO;2)
196. Schemm, S., Sprenger, M., and Wernli, H. (2018) When during Their Life Cycle Are Extratropical Cyclones Attended by Fronts?. *Bulletin of the American Meteorological Society*, 99, 149–165. <https://doi.org/10.1175/BAMS-D-16-0261.1>
197. Schemm, S., and Wernli, H. (2014) The Linkage between the Warm and the Cold Conveyor Belts in an Idealized Extratropical Cyclone. *Journal fo the Atmospheric Sciences*, 71, 1443–1459. <https://doi.org/10.1175/JAS-D-13-0177.1>
198. Schmetz, J., Tjemkes, S.A., Gube, M., and van de Berg, L. (1997) Monitoring deep convection and convective overshooting with METEOSAT. *Advances in Space Research* 19 (3), 433 – 441. [https://doi.org/10.1016/S0273-1177\(97\)00051-3](https://doi.org/10.1016/S0273-1177(97)00051-3)
199. Schubert, W.H., and Alworth, B.T. (1987) Evolution of potential vorticity in tropical cyclones. *Quarterly Journal of the Royal Meteorological Society*, 113, 147–162.

200. Schultz, D.M., Keyser, D., and Bosart, L.F. (1998) The effect of large-scale flow on low-level frontal structure and evolution of midlatitude cyclones. *Monthly Weather Review*, 126, 1767–1791. [https://doi.org/10.1175/1520-0493\(1998\)126<1767:TEOLSF>2.0.CO;2](https://doi.org/10.1175/1520-0493(1998)126<1767:TEOLSF>2.0.CO;2)
201. Setvak, M., Rabin, R.M., and Wang, P.K. (2007) Contribution of the MODIS instrument to observations of deep convective storms and stratospheric moisture detection in GOES and MSG imagery. *Atmospheric Research* 83, 505–518. <https://doi.org/10.1016/j.atmosres.2005.09.015>
202. Shapiro, L.J., and Franklin, J.L. (1999) Potential Vorticity Asymmetries and Tropical Cyclone Motion. *Monthly Weather Review*, 127, 124–131. [https://doi.org/10.1175/1520-0493\(1999\)127<0124:PVAATC>2.0.CO;2](https://doi.org/10.1175/1520-0493(1999)127<0124:PVAATC>2.0.CO;2)
203. Shapiro, L.J. (1996) The motion of Hurricane Gloria: A potential vorticity diagnosis. *Monthly Weather Review*, 124, 2497–2508.
204. Shapiro, M.A., and Keyser, D. (1990) Fronts, jet streams and the tropopause. Extratropical Cyclones, The Erik Palmén Memorial Volume, C. W. Newton and E. O. Holopainen, Eds., *American Meteorological Society*, 167–191. <https://doi.org/10.1007/978-1-944970-33-8>
205. Skamarock, W. C., Klemp, J. B., Dudhia, J., Gill, D. O., and co-authors (2019) *A Description of the Advanced Research WRF Model Version 4* (No. NCAR/TN-556+STR). doi:10.5065/1dfh-6p97
206. Skamarock, W.C., and coauthors (2008) A description of the Advanced Research WRF version 3. NCAR Tech. Note NCAR/TN-475+STR, 113 pp., doi:<https://doi.org/10.5065/D68S4MVH>
207. Sobrino, J.A., and Romaguera, M. (2004) Land surface temperature retrieval from MSG1-SEVIRI data. *Remote Sensing of Environment*, 92(2), 247–254. <https://doi.org/10.1016/j.rse.2004.06.009>
208. Sprenger, M., Wernli, H. and Bourqui, M. (2007) Stratosphere–Troposphere Exchange and Its Relation to Potential Vorticity Streamers and Cutoffs near the Extratropical Tropopause. *Journal of the Atmospheric Sciences*, 64, 1587–1602. <https://doi.org/10.1175/JAS3911.1>
209. Staelin, D., Barrett, A., Rosenkranz, P., Barath, F., Johnson, E., Waters, J., Wouters, A., and Lenoir, W. (1975) The scanning microwave spectrometer (scams) experiment. *The Nimbus-6 Users Guide*, pp 59–86.
210. Steeneveld, G.J., Ronda, R.J., Holtslag, A.A.M. (2015) The challenge of forecasting the onset and development of radiation fog using mesoscale atmospheric models. *Boundary Layer Meteorology*, 154 (2), 265–289, doi:10.1007/s10546-014-9973-8
211. Stensrud, D.J. (2007) *Parameterization Schemes. Keys to Understanding Numerical Weather Prediction Models*. Cambridge University Press.
212. Stephens, GL, and Kummerow, C.D. (2007) The remote sensing of clouds and precipitation from space: a review. *Journal of the Atmospheric Sciences*, 64(11), 3742–3765.
213. Stoelinga, M.T. (1996) A Potential Vorticity-Based Study of the Role of Diabatic Heating and Friction in a Numerically Simulated Baroclinic Cyclone. *Monthly Weather Review* 124, 849–874. [https://doi.org/10.1175/1520-0493\(1996\)124<0849:APVBSO>2.0.CO;2](https://doi.org/10.1175/1520-0493(1996)124<0849:APVBSO>2.0.CO;2)
214. Susskind, J., Rosenfield, J., Reuter, D., Chahine, M. (1984) Remote sensing of weather and climate parameters from hirs2/msu on tiros-n. *Journal of Geophysical Research: Atmospheres* (1984-2012) 89(D3):4677-4697

215. Tao, C., and Jiang, H. (2015) Distributions of shallow to very deep precipitation-convection in rapidly intensifying tropical cyclones. *Journal of Climate*, 28, 8791–8824. doi:<https://doi.org/10.1175/JCLI-D-14-00448.1>
216. Tian, B., Soden, B.J., and Wu, X. (2004) Diurnal cycle of convection, clouds, and water vapor in the tropical upper troposphere: Satellites versus a general circulation model. *Journal of Geophysical Research*, 109, D10101. <https://doi.org/10.1029/2003JD004117>
217. Tory, K.J., Montgomery, M.T., and Davidson, N.E. (2006) Prediction and Diagnosis of Tropical Cyclone Formation in an NWP System. Part I: The Critical Role of Vortex Enhancement in Deep Convection. *Journal of the Atmospheric Sciences*, 63, 3077–3090. <https://doi.org/10.1175/JAS3764.1>
218. Tourville, N., Stephens, G., DeMaria, M., and Vane, D. (2015) Remote sensing of tropical cyclones: Observations from CloudSat and A-Train profilers. *Bulletin of the American Meteorological Society*, 96 (4), 609–622. <https://doi.org/10.1175/BAMS-D-13-00282.1>
219. Tous, M., Zappa, G., Romero, R., Shaffrey, L., and Vidale, P.L. (2016) Projected changes in medicanes in the HadGEM3 N512 high-resolution global climate model. *Climate Dynamics* 47, 1913–1924. <https://doi.org/10.1007/s00382-015-2941-2>
220. Tous, M., and Romero, R. (2013) Meteorological environments associated with medicane development. *International Journal of Climatology*, 33, 1-14. <https://doi.org/10.1002/joc.3428>
221. Tous, M., Romero, R., and Ramis, C. (2012) Surface heat fluxes influence on medicane trajectories and intensification. *Atmospheric Research*, 123, 400–411. <https://doi.org/10.1016/j.atmosres.2012.05.022>
222. Trenberth, K.E. (2005) Uncertainty in hurricanes and global warming. *Science*, 308, 1753–1754.
223. Trigo, I. F., Bigg, G.R., and Davies, T.D. (2002) Climatology of Cyclogenesis Mechanisms in the Mediterranean. *Monthly Weather Review*, 130, 549–569. [https://doi.org/10.1175/1520-0493\(2002\)130<0549:COCMIT>2.0.CO;2](https://doi.org/10.1175/1520-0493(2002)130<0549:COCMIT>2.0.CO;2)
224. Uppala, S. M., and Coauthors, (2005) The ERA-40 Re-Analysis. *Quarterly Journal of the Royal Meteorological Society*, 131, 2961–3012.
225. van Delden, A. (1989) On the deepening and filling of balanced cyclones by diabatic heating. *Meteorology and Atmospheric Physics*, 41, 127–145. <https://doi.org/10.1007/BF01043132>
226. Vangasse, P., Charlton, J., Jarrett, M. (1996) Characterization of the advanced microwave sounding unit, AMSU-B. *Advances in Space Research*, 17,75-78, [https://doi.org/10.1016/0273-1177\(95\)00451-J](https://doi.org/10.1016/0273-1177(95)00451-J)
227. Verezhenskaya, P., Tilinina, N., Gulev, S., Renfrew, I. A., and Lazzara, M. (2017) Southern Ocean mesocyclones and polar lows from manually tracked satellite mosaics. *Geophysical Research Letters*, 44, 7985–7993. <https://doi.org/10.1002/2017GL074053>
228. Walsh, K., Giorgi, F. and Coppola, E. (2014) Mediterranean warm-core cyclones in a warmer world. *Climate Dynamics* 42, 1053. <https://doi.org/10.1007/s00382-013-1723-y>
229. Wang, C., and Rogers, J. C. (2001) A Composite Study of Explosive Cyclogenesis in Different Sectors of the North Atlantic. Part I: Cyclone Structure and Evolution. *Monthly Weather Review*, 129, 1481–1499. [https://doi.org/10.1175/1520-0493\(2001\)129<1481:ACSOEC>2.0.CO;2](https://doi.org/10.1175/1520-0493(2001)129<1481:ACSOEC>2.0.CO;2)

230. Wernli, H., Dirren, S., Liniger, M.A., and Zillig, M. (2002) Dynamical aspects of the life cycle of the winter storm ‘Lothar’ (24–26 December 1999). *Quarterly Journal of the Royal Meteorological Society*, 128: 405-429. doi:10.1256/003590002321042036
231. Wernli, H., and Bourqui, M. (2002) A Lagrangian “1-year climatology” of (deep) cross-tropopause exchange in the extratropical Northern Hemisphere. *Journal of Geophysical Research*, 107(D2), doi:10.1029/2001JD00812
232. Whitehead, J.P., Jablonowski, C., Kent, J., and Rood, R.B. (2015) Potential vorticity: Measuring consistency between GCM dynamical cores and tracer advection schemes. *Quarterly Journal of the Royal Meteorological Society*, 141, 739-751. doi:10.1002/qj.2389
233. Wilcox, E.M. (2003) Spatial and temporal scales of precipitating tropical cloud systems in satellite imagery and the NCAR CCM3. *Journal of Climate*, 22, 3545–3559. [https://doi.org/10.1175/1520-0442\(2003\)016%3C3545:SATSOP%3E2.0.CO;2](https://doi.org/10.1175/1520-0442(2003)016%3C3545:SATSOP%3E2.0.CO;2)
234. Winstanley, D. (1970) The north African flood disaster, September 1969. *Weather* 25, 390–403. <https://doi.org/10.1002/j.1477-8696.1970.tb04128.x>
235. Wu, C.-C., and Kurihara, Y. (1996) A numerical study of the feedback mechanisms of hurricane-environment interaction on hurricane movement from the potential vorticity perspective. *Journal of the Atmospheric Sciences*, 53, 2264–2282.
236. Wu, Q., and Ruan, Z. (2016) Diurnal Variations of the areas and temperatures in tropical cyclone clouds. *Quarterly Journal of the Royal Meteorological Society*, 142, 700, 2788-2796. <https://doi.org/10.1002/qj.2868>
237. Yang, G.Y., and Slingo, J. (2001) The diurnal cycle in the Tropics. *Monthly Weather Review* 129, 784–801. [https://doi.org/10.1175/1520-0493\(2001\)129<0784:TDCITT>2.0.CO;2](https://doi.org/10.1175/1520-0493(2001)129<0784:TDCITT>2.0.CO;2)
238. Yuan, J., and Wang, D. (2014) Potential vorticity diagnosis of tropical cyclone Usagi (2001) genesis induced by a mid-level vortex over the South China Sea. *Meteorology and Atmospheric Physics*, 125, 75–87. <https://doi.org/10.1007/s00703-014-0316-6>
239. Zhang, W., Villarini, G., Scoccimarro, E., and Napolitano, F. (2020) Examining the Precipitation Associated with Medicanes in the High-Resolution ERA-5 Reanalysis Data. *International Journal of Climatology*. Accepted Author Manuscript. <https://doi.org/10.1002/joc.6669>

Titre : Contribution de la convection profonde à l'intensification des cyclones méditerranéens

Mots clés : convection profonde, médicanes, cyclones subtropicaux, méditerranée, télédétection

Résumé : Le rôle de la convection profonde dans l'intensification des cyclones subtropicaux méditerranéen (médicanes) est examiné dans le cadre de cette thèse. Alors que la plupart des cyclones méditerranéens présentent un cycle de vie barocline typique, où la cyclogenèse est principalement déclenchée par les perturbations situées dans la haute troposphère, le rôle de la convection profonde sur le développement des cyclones a été peu abordé jusqu'ici. Afin d'étudier la contribution de celle-ci sur l'intensification de neuf médicanes entre 2005 et 2018, l'accent a été mis sur le bassin méditerranéen central et oriental moins étudié que celui de la Méditerranée occidentale.

Dans une première partie, la relation entre la convection profonde et la formation et l'intensification des cyclones est étudiée à l'aide de techniques de télédétection par une approche multi-satellites dans l'infrarouge et les micro-onde. Des observations provenant des radiomètres micro-ondes AMSU-B et MHS volant à bord de plusieurs satellites opérationnels (NOAA16 à NOAA19; MetOpA / B), ainsi que l'imageur visible et infrarouge SEVIRI installé à bord des satellites géostationnaires Meteosat-8 à 11 ont été utilisées. Les canaux humidité sondant autour de 183 GHz des capteurs AMSU-B / MHS et les canaux infrarouges de SEVIRI ont été utilisés pour détecter la convection profonde durant le cycle de vie des médicanes. De plus, le cisaillement vertical du vent et l'inclinaison du vortex ont été calculés en utilisant les réanalyses ERA5 afin d'étudier l'évolution de la structure du cyclone. Les résultats fournissent des informations inédites sur les relations entre la convection profonde et l'évolution des cyclones: ainsi il est montré que seule une fraction des cyclones étudiés subissent une activité convective intense près de leurs centres et qu'une convection profonde persistante dans les secteurs où le cisaillement est positif mène à des périodes d'intensification.

L'activité convective des secteurs où le cisaillement est négatif n'est pas liée à des périodes d'intensification, tandis que les structures de courte durée de type ouragans se développent uniquement pendant l'activité convective symétrique, ce qui peut conduire à une intensification des cyclones dans certains cas. En raison de ces comportements variés, les neuf médicanes étudiés ont été groupés en trois familles en fonction des caractéristiques de leur cycle de vie.

Dans un deuxième temps, pour aborder l'impact de la thermodynamique à fine échelle en lien avec la convection profonde et expliquer l'activité convective observée, une modélisation atmosphérique a été effectuée. Pour cela on a utilisé le modèle de recherche et de prévisions météorologiques WRF à une résolution spatiale fine (3 km). Les simulations numériques ont été forcées par les réanalyses ERA5. Pour tenir compte des effets de libération de chaleur latente, des traceurs de vorticit  potentielle (PV) ont été utilisés à chaque pas de temps du modèle. De plus, une version modifi e de l' quation de tendance de pression a  t e utilis e pour post-traiter les r sultats num riques afin d' tudier la dynamique atmosph rique li e   six m dicanes. Les r sultats ont montr  que les changements d'intensit  des cyclones n' taient que partiellement expliqu s par l'activit  de la convection profonde, les facteurs principaux  tant les champs de PV de basse couche et le chauffage diabatique. L'environnement barocline dans lequel ces cyclones se sont d velopp s pr sentait finalement tr s peu de similitudes avec les cyclones tropicaux. Les r sultats num riques appuient en partie notre hypoth se issue du travail men  sur les observations selon laquelle les m dicanes feraient bien partie de la famille des cyclones m diterran ens, mais qu'ils poss dent  galement certaines caract ristiques particuli res,   savoir la contribution des processus diabatiques et baroclines lors de leur d veloppement et au stade mature.

Title : Contribution of deep convection in the intensification of Mediterranean Tropical-Like Cyclones

Keywords : deep convection, medicanes, subtropical cyclones, Mediterranean, remote-sensing

Abstract : The role of deep convection in the intensification of Mediterranean tropical-like cyclones is examined in this thesis. While most of the Mediterranean cyclones present a common baroclinic life cycle where cyclogenesis is mainly triggered by upper tropospheric systems, the role of deep convection on cyclone development has only been addressed by few studies in the recent past. In order to investigate the contribution of deep convection in the intensification of 9 Mediterranean tropical-like cyclones between 2005 and 2018, the emphasis has been put on the Central and Eastern Mediterranean basin where these cyclones have received less attention than those in the Western Mediterranean.

In a first part, the relation of deep convection with cyclones formation and intensification is investigated using remote sensing techniques, through a multi-satellite approach, with observations in the infrared and microwave spectrum. Observations derived from the Advanced Microwave Sounding Unit (AMSU-B) and the Microwave Humidity Sounder (MHS) on several operational satellites (NOAA16 through NOAA19); MetOpA/B, as well as the Spinning Enhanced Visible and Infrared Imager (SEVIRI) onboard the geostationary satellites Meteosat-8 to 11 have been used. The humidity sounding channels around 183 GHz from the AMSU/MHS sensors and a method of infrared channel differencing from SEVIRI were used to detect deep convection during the Mediterranean tropical-like cyclones. Moreover, vertical wind shear and vortex tilt were calculated by ERA5 reanalysis data to study the cyclone structure evolution. Results provide new insights about the relations between deep convection and cyclone evolution, with only a fraction of the studied cyclones experiencing intense convective activity close to their centres and persistent deep convection in the upshear quadrants leads to intensification periods.

Convective activity solely in the downshear quadrants is not linked to intensification periods, while short-lived hurricane-like structures develop only during symmetric convective activity, leading to cyclone intensification in some of the cases. For this reason, the Mediterranean tropical-like cyclones have been divided into 3 groups based on distinct differences during their lifetime.

As a second step, to address the impact of fine-scale thermodynamics related to deep convection and explain the observed convective activity, atmospheric modeling is employed, using the Weather Research and Forecast model (WRF) with a fine spatial resolution (3 km). The numerical simulations are forced by ERA5 reanalysis data with a high temporal resolution. To account for the effects of latent heat release during deep convection, online potential vorticity (PV) tracers are used at every model time step. In addition, a modified version of the classical pressure tendency equation (PTE) is used to post-process the numerical results to study the atmospheric dynamics related to 6 Mediterranean tropical-like cyclones. Results show that cyclone intensity changes are only partly explained by deep convection activity, with an emphasis given on the diabatically-induced low-level PV fields and diabatic heating. The baroclinic environment into which these cyclones develop has very few similarities with tropical cyclones. The numerical findings partially support our hypothesis in the observational study that the Mediterranean tropical-like cyclones may be part of a continuous spectrum of Mediterranean cyclones, but they are also distinct differences among them, namely the contribution of diabatic and baroclinic processes at their developing and mature stages.